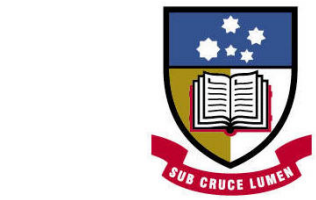

THE UNIVERSITY of ADELAIDE

DEFINING THE NEUROPATHOLOGICAL IMPACT OF HETEROZYGOSITY IN THE GENE ENCODING SULFAMIDASE, A LYSOSOMAL DEGRADATIVE ENZYME

Mohd Nazzmer Mohd Nazri

School of Biomedicine,
Faculty of Health and Medical Sciences, The University of Adelaide
and
Childhood Dementia Research Group,
College of Medicine and Public Health, Flinders University

Thesis submitted for the degree of Doctor of Philosophy

Supervised by Professor Kim Hemsley and Dr. Nicholas Smith
March 2023

Table of Contents

List of Abbreviations

Acid sphingomyelinase	ASM
Adenosine Triphosphate	ATP
Alpha-N-acetylglucosaminidase	NAGLU
Alzheimer's Disease	AD
Amyloid beta	Aβ
Analysis of variance	ANOVA
Beta-galactosylceramidase	GALC
Bicinchoninic Acid (BCA) Protein Assay	BCA
Blood Brain Barrier	BBB
Brown adipose tissue	BAT
Carbonyl cyanide-4-phenylhydrazone	FCCP
Cathepsin D	CTSD
Central Nervous System	CNS
Ceroid lipofuscinosis 2	CLN2
Coefficient of variation	CV
Coordinated lysosomal expression and regulation	CLEAR
Cytosine arabinoside	Ara-C
Dithiothreitol	DTT
Endoplasmic reticulum-associated degradation	ERAD
Endosomal lysosomal network	ELN
Endosomes	EE
Enzyme replacement therapy	ERT
Extracellular vesicles	EV
Fetal Bovine Serum	FBS
Flavin adenine dinuecleotide	FAD
Frontotemporal lobar degeneration	FTLD
Gaucher's disease	GD
Gene therapy	GT
Gene-set enrichment analysis	GSEA
Genome-wide association study	GWAS
Glucocerebrosidase	Gcase
Glucosylceramide	GlcCer
Glucosylceramide beta-1	GBA1
Granulin	GRN
Graphical User Interface	GUI
Green fluorescence proteins	GFP
Haematopoietic stem cell transplantation	HSCT
Heparan sulfate acetyl-CoA:a-glucosaminide N-acetyltransferase	HGSNAT
Hexosaminidase B	HEXB
High-performance liquid chromatography	HPLC

Huntington's Disease	HD
Hyperspectral Imaging	HS
Krabbe disease	KD
Kyoto Encyclopedia of Genes and Genomes	KEGG
Late endosomes	LE
Light emitting diodes	LED
Liquid chromatography	LC
Liquid Chromatography-Mass Spectrometry	LC-MS
Lysosomal Storage Disorders	LSDs
Lysosome related organelles	LRO
Lysosome-associated membrane protein 1	LAMP1
Major histocompatibility complex	MHC
Mannose-6-phosphate	M6P
Microphthalmia-associated transcription factor	MITF
Mitochondrial membrane potential	$\Delta\Psi m$
Mucopolysaccharidosis type III	MPS III
Multi-electrode array	MEA
Multiple Sclerosis	MS
N-sulfoglucosamine sulfohydrolase	SGSH
Neurofibrillary tangles	NFT
Neuronal ceroid lipofuscinosis	NCL
Nicotinamide Adenine Dinucleotide Hydrogen	NADH
Nicotinamide Adenine Dinucleotide Phosphate Hydrogen	NADPH
Niemann-Pick disease	NPD
NPC intracellular cholesterol transporter 1	NPC1
Optical redox ratio	ORR
Oxidative Phosphorylation	OxPhos
Oxygen consumption rate	OCR
Parkinson's Disease	PD
Penicillin/Streptomycin	PenStrep
Peripheral nervous system	PNS
Pharmcological chaperone therapy	PCT
Phosphate Buffered Saline	PBS
phosphatidylinositol 4,5-biphosphate	PI(4,5)P2
Phosphatidylinositol signalling pathway	PIP
Phosphatidylinositol-3-phosphate	PI3P
Poly-L-Lysine	PLL
Polymerase chain reaction	PCR
Post-translational modifications	PTM
Region of Interest	ROI
Rotenone and antimycin A	Rot/AA
Sandhoff disease	SD
Single nucleotide polymorphism	SNP

Soluble N-ethylmaleimide-sensitive factor attachment protein receptors	SNARE
Sphingomyelin phosphodiesterase 1	SMPD1
Standard error of the mean	SEM
Substrate reduction therapy	SRT
Tandem mass tags-based	TMT
TAR DNA-binding protein 43	TDP-43
Tetraethylbenzimidazolylcarbocyanine iodide	JC-1
Thymus cell antigen 1	Thy1
Transcription factor EB	TFEB
Tricarboxylic acid cycle	TCA
Trifluoroacetic acid	TFA
United States Food and Drug Administration	US-FDA
Vacuolar-type proton adenosine triphosphatase	v-ATP
Women's and Children's Hospital	WCH

Thesis Abstract

Neurodegenerative lysosomal storage disorders typically arise from homozygous autosomal recessive mutations in genes encoding catabolic lysosomal proteins, while heterozygous individuals have largely been regarded as clinically unaffected carriers. However, recent genome-wide association study data suggests that carriers of *GBA*, *NPC1*, *SMPD1*, *NAGLU*, and *SGSH* mutations may be at increased risk of later-onset neurological conditions such as Parkinson's disease. This is exemplified in carriers of mutations in the glucosylceramide beta-1 and granulin genes, who are at increased risk of developing Parkinson's disease and frontotemporal lobar degeneration, respectively. With an estimated carrier frequency of 1 in 40 in the general population, heterozygous mutations in one or more lysosomal pathway genes are potentially important contributors to the global burden of later-onset neurodegenerative disease. Here, we sought to define the neuropathological impact of carrying a D31N missense mutation in the sulfamidase gene, which encodes the lysosomal sulfatase, N-sulfoglucosamine sulfohydrolase (*Sgsh*). Homozygous mutations in the *Sgsh/SGSH* gene leads to Sanfilippo syndrome (Mucopolysaccharidosis type IIIA), a childhood-onset dementia. Recent studies in *Sgsh* D31N heterozygous ($Sgsh^{+/D31N}$) mice revealed mildly impaired motor function, and subtle structural changes in pyramidal neurons in 84 weeks old mouse motor cortex, suggesting that carriers of *Sgsh* gene mutations may be susceptible to neurodegeneration, however, the molecular mechanisms contributing to the development of this subtle neuronal phenotype remain to be elucidated.

In this study, an $Sgsh^{+/D31N}$ mouse model was utilised to:

1. Study the temporal impact of *Sgsh* D31N heterozygous mutations upon the mouse cortical proteome.

2. Assess the impact of the D31N *Sgsh* heterozygous mutation on motor cortex pyramidal neuron morphology and cortical neural function.

3. Investigate the impact of heterozygous mutations on the metabolic profile of D31N *Sgsh* heterozygous mouse and *SGSH* heterozygous human fibroblast cells.

The hypothesis tested was that carriers of a mutation in the *Sgsh* gene exhibit aberrations in neuron structure, biochemistry, and/or metabolism, which may cause or predispose them to impaired neurological function.

Assessment of the proteome in the motor cortex of *Sgsh* D31N heterozygotes revealed differentially synthesised proteins in all time-points assessed (0-, 3-, 6-, 12-, 24-, and 48- weeks of age). Of the proteins identified, the majority were commonly involved either in neurodegenerative or energy-related pathways such as Oxidative Phosphorylation, Glycolysis, and Pyruvate Metabolism. Moreover, significantly enriched Kyoto Encyclopedia of Genes and Genomes (KEGG) pathways were identified at 0-, 6-, 24- and 48- weeks, indicating perturbed pathways in early developmental stage and in adulthood. No pathway clusters were detected in 3-week-old mouse motor cortex, and no statistically significant pathway changes were found in 12-week mice based on Gene-set Enrichment analysis. This finding suggests that *Sgsh* D31N heterozygotes have variable changes in protein production early in life but exhibit more significant changes in protein production with age, indicative of a possible developing disease mechanism that exists as a continuum. Hence, future studies are required to assess the impact of *Sgsh* D31N heterozygotes mouse cortical proteome at older timepoint beyond 48 weeks of age, in order to gain insight into any potential pathological processes that may be unfolding.

Whilst subtle morphological changes had previously been observed in other dendrite structure in $Sgsh^{+/D31N}$, here for the first time, we report that there was no alteration in overall dendritic spine density in the $Sgsh^{+/D31N}$ mouse motor cortex, with immature (filopodia and thin) and mature (stubby and mushroom) spine sub-types exhibiting equal numbers and maturity in 24-week-old $Sgsh^{+/D31N}$ compared to $Sgsh^{+/+}$ mice. Surprisingly, electrophysiological recordings carried out on neural cultures from day 0 mouse brain tissue exhibited a decreased spiking rate and delayed neural burst in $Sgsh^{+/D31N}$ samples, suggesting impaired neuronal function. However, $Sgsh^{+/D31N}$ mouse neural cultures exposed to an environmental oxidative stress (via application of the mitochondrial toxin, rotenone) showed conflicting data. Though, network burst duration in 0.1nM rotenone treated neural cultures showed a decline in neural activity, indicative of a worsening neural function. These findings suggest that $Sgsh^{+/D31N}$ cortical neural cells may potentially be susceptible to the effects of rotenone compared to $Sgsh^{+/+}$ cultures, however, a repeat study is required to confirm these observations. The findings also suggest that pyramidal neurons in $Sgsh^{+/D31N}$ motor cortex develop normal numbers of dendritic spines which mature appropriately, and the dysfunction observed in neural cultures could potentially

be associated with impairment in synaptic transmission or mitochondrial function, as suggested by the results of the proteomic studies.

An assessment of mitochondrial health also revealed that *Sgsh*$^{+/D31N}$ mouse fibroblasts had increased mitochondrial membrane potential above wildtype animals; a phenomenon that was not evident in human fibroblasts carrying different *SGSH* mutations, suggesting potential for mutation specific effects (albeit the possibility of species intrinsic differences cannot be discounted). In addition, no significant differences in metabolic parameters (e.g., basal respiration, maximal respiration, proton leak, spare respiratory capacity, non-mitochondrial oxygen consumption, and ATP-production coupled respiration) assessed using the Seahorse Mito Stress test were observed between genotypes in mouse fibroblasts, while human *SGSH* heterozygous and MPS IIIA fibroblasts showed perturbation in some metabolic parameters. These results suggest that mitochondrial dysfunction in human *SGSH* heterozygotes and MPS IIIA may be mutation dependent. Further, supporting this, optical imaging of cellular autofluorescence in *SGSH* heterozygous human fibroblasts showed impaired cellular metabolism in channels corresponding to NAD(P)H. Together, these findings indicate aberrant cellular energy metabolism in human *SGSH* heterozygous and human MPS IIIA fibroblasts, while no changes in cellular autofluorescence were observed in *Sgsh*$^{+/D31N}$ and *Sgsh*$^{D31N/D31N}$ mouse fibroblasts.

The findings, coupled with the existing literature, indicate that D31N heterozygous mutations in *Sgsh* may potentially be susceptible to impaired neurological function later in life due to disrupted energy metabolism and the phenotypic changes observed in individuals with heterozygous mutations in lysosomal genes may be enzyme/mutation dependent. However, further studies are required to validate these findings.

Declaration

I certify that this work contains no material which has been accepted for the award of any other degree or diploma in my name, in any university or other tertiary institution and, to the best of my knowledge and belief, contains no material previously published or written by another person, except where due reference has been made in the text. In addition, I certify that no part of this work will, in the future, be used in a submission in my name, for any other degree or diploma in any university or other tertiary institution without the prior approval of the University of Adelaide and where applicable, any partner institution responsible for the joint award of this degree.

I give permission for the digital version of my thesis to be made available on the web, via the University's digital research repository, the Library Search and also through web search engines, unless permission has been granted by the University to restrict access for a period of time.

……

Mohd Nazzmer Mohd Nazri

31st of March 2023

Acknowledgements

I would like to express my deepest gratitude to my supervisors, **Professor Kim Hemsley** and **Dr Nicholas Smith** for their expert guidance throughout my research years. To Kim, for all her patience, encouragement, and consistently pushing me for improvements. To Nick, for his kind words of encouragement, support, and enthusiasm. I am also thankful to them for bringing me to the world of Childhood Dementia and for giving me the opportunity to complete a fascinating and at times challenging PhD journey. Without their incredible and timely wisdom and counsel, my thesis would have been a frustrating and overwhelming pursuit.

Many thanks to members of the Childhood Dementia Research group, **Dr. Adeline Lau, Dr. Siti Mubarokah, Dr. Karissa Barthelson, Helen Beard, Barbara King, Leanne Winner and Tabitha Lance**, for all their guidance, support, and willingness to answer countless questions regarding experimental procedures. To past members of the group, **Dr. Andrew Shoubridge, Daniel Neumann, Sarah Tamang, and Meghan Douglass** for teaching me animal husbandry, experimental procedures, and for their friendship.

Thank you to my collaborators – **Professor Mark Hutchinson** for welcoming me to the CNBP team and allowing me to use the Hyperspectral imaging; **Dr. Lachlan Jolly** for his expert guidance and advice on electrophysiology experiments; **Drs. Marten Snel, Paul Trim and Sushma Rao** for working with me on the data analysis for proteomics.

I would also like to acknowledge the **Sanfilippo Children's Foundation** who provided me with a Top-up Scholarship as well as the Adelaide Graduate Research Scholarship from the **University of Adelaide** which I received. Thank you to the **Adelaide Graduate Centre** and **Seaneen Hopps** from the International Student Support Office for their advice and help during my candidature. Thank you to the University of Adelaide and Flinders University for the financial and technical support during my candidature, and for providing me the opportunity to study in excellent research facilities.

Last but not least, I am greatly indebted to my family and friends outside of work for their constant encouragement, unconditional love, care, and unyielding support throughout the years, especially during the difficult times when I was not well or home sick. Without their mental support and kind companionship in this long journey, I would not have been able to finish my study. Special thanks to my brother **Nazzeef Nazri,** and my partner **Darren Chow**, I cannot express how grateful I am for your unwavering support and encouragement throughout my journey. Thank you for being my rock and for always being there for me.

Chapter 1: Introduction

1.0 The Lysosome

Lysosomes are ubiquitous organelles that were first described in the 1950s by Christian de Duve (1). Since then, the lysosome has been known as a membrane enclosed organelle that degrades a wide range of biological macromolecules, including proteins, lipids, carbohydrates, and nucleic acids (2, 3). The lysosome receives these macromolecules or substrates via endocytosis, phagocytosis or autophagy for degradation within the lysosomal lumen, which has a pH range of 4.5-5.0. The lysosome's acidity stabilises and mediates the activity of more than 60 luminal hydrolytic enzymes. These enzymes are manufactured in the rough endoplasmic reticulum and transported to the trans-golgi network via the Golgi apparatus (4). The acidic environment is regulated through the activity of proton-pumping vacuolar-type proton adenosine triphosphatase (v-ATPase), which utilises energy from hydrolysing ATP (Figure 1) (5). Outside of its primary catabolic function, the lysosome is a highly active organelle with multiple regulatory functions; other significant proteins in the lysosome include structural proteins like lysosome-associated membrane protein 1 (LAMP1), trafficking and fusion proteins such as soluble N-ethylmaleimide-sensitive factor attachment protein receptors (SNAREs) and RAB GTPase, LAMP2 transporters (which play a role in chaperone-mediated autophagy), and ion channels CIC7 (a chloride channel), and mucolipin 1, which is a cation channel and member of the transient receptor potential family (6, 7).

Moreover, lysosome-related organelles (LROs), such as melanosomes, lytic granules, major histocompatibility complex (MHC) class II compartments and platelet-dense granules complement the catabolic function of the lysosomes (8). Many LROs act as specialised secretory organelles and share characteristics similar to the lysosome, such as an acidic environment, lysosomal membrane proteins, and the ability to fuse with phagosomes (9). Additionally, LROs have unique properties based on their specific cargoes, such as melanosomes containing melanosome-specific transmembrane glycoprotein or granzyme and perforin containing granules intrinsic to cytotoxic T-cells (9). The mechanisms behind the biogenesis and secretion of LROs are not fully understood, but genetic defects in LROs are linked to rare genetic disorders that can result in reduced pigmentation, such as Chediak-Higashi disease (10). Both the lysosome and LROs play important roles in a variety of

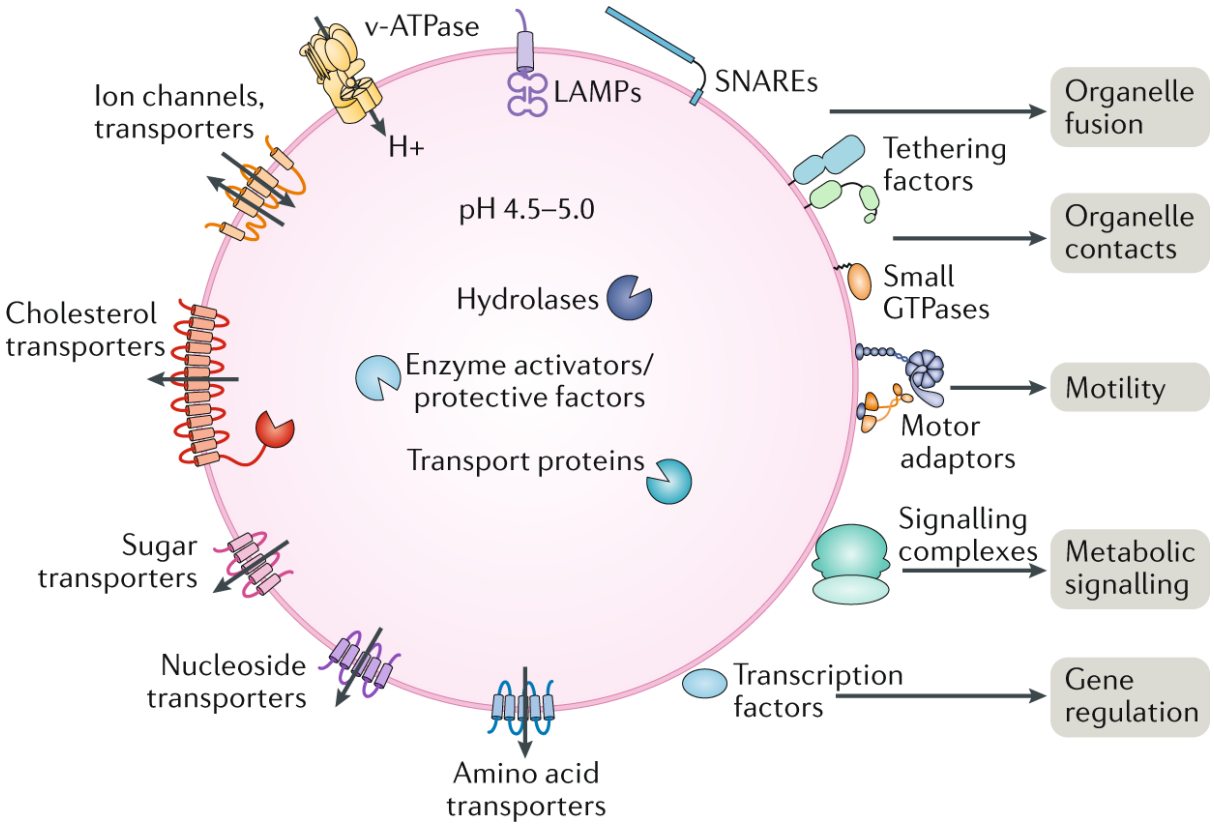

Figure 1. Characteristics of lysosomal function. The lysosome is a cellular organelle that contains acid hydrolases and protective factors in its lumen to aid in substrate degradation. The lysosomal lumen acidic pH is maintained by a v-ATPase in the limiting membrane, and the lysosomal membrane contains lysosome-associated membrane proteins, ion channels, transporters, solute carriers, and SNAREs for functions such as protecting the membrane, maintaining ion balance, and facilitating the export of degradation products. Diagram obtained from (11).

physiological processes, including cholesterol homeostasis, plasma membrane repair, immune system regulation, energy metabolism, cell death, and cellular signalling (3, 12).

The lysosomal membrane also contains approximately 25 lysosomal membrane proteins, which include transporters, fusion machinery, ion channels, and structural proteins that are essential for lysosomal membrane integrity and trafficking, luminal acidification, and protein translocation (3, 13). Moreover, ions and ion channels within the lysosome are essential for maintaining lysosomal pH and its function (14).

1.1 Lysosome biogenesis

The lysosome originates from the Golgi apparatus and is regulated by the coordinated lysosomal expression and regulation (CLEAR) network and its master regulator transcription factor EB (TFEB), which is a member of the microphthalmia-associated transcription factor (MITF) subfamily of transcription factors (15). TFEB has been shown to play a positive role in regulating the expression of lysosomal genes, which helps control the lysosome population and promotes the degradation of lysosomal substrates (16, 17). Specifically, TFEB activates the transcription of genes that encode proteins involved in range of operations related to cellular clearance, such as lysosomal biogenesis, autophagy, and endocytosis, as well as other lysosome-related processes, including phagocytosis, immune response mechanism, and lipid catabolism (16). Similarly, the CLEAR network is also involved in the regulation of lysosomal trafficking, fusion, and degradation of lysosomal substrates, which is crucial for maintaining cellular homeostasis and preventing the accumulation of toxic waste products (17).

Moreover, there are several models of lysosomal formation (Figure 2). The first model describes the formation of early endosomes (EEs) from the plasma membrane, and their progression towards late endosomes (LEs) and lysosomes (18, 19). The second model involves the vesicular transport, with endosomal carrier vesicles or multivesicular bodies transferring cargo either from early to LEs before reaching the lysosome, or directly from the mature LEs to the lysosome (18, 19). The third model represents the “kiss and run” mechanism, where the LEs establish a point of contact with lysosomes for the transfer of cargo, followed by the separation of the lysosomes and LEs (18, 19). The fourth model of lysosome formation involves a fusion-fission process where LEs and lysosome combine to form hybrid organelles, followed by lysosome re-formation.

1.2 The endosomal-lysosomal network

The endosomal-lysosomal network (ELN) is a group of organelles in the endocytic pathway that internalise, recycle, and modulate various cargo molecules required for normal cellular function (20). Endocytosis, autophagy, and phagocytosis are the three pathways by which macromolecules and transmembrane proteins enter the ELN (21, 22). Engulfment of macromolecules via endocytosis is transported to the lysosome for removal and recycling. LEs and lysosomes fuse via the recruitment of several proteins such as GTPase Rab7, vacuolar protein sorting-associated protein 18, vacuolar protein sorting-associated protein 39, and pleckstrin homology domain-containing protein family member 1 (12). The fusion of lysosome and autophagosomes plays a role in the degradation of macromolecules, mainly through the process of autophagy and formation of autophagosomes (23).

Moreover, autophagy is activated during cellular starvation and following other endogenous and exogenous cellular stressors promoting the capture and removal of damaged cell components, and precipitating their degradation in the lysosome (24). The subsequent fusion process occurs effectively, resulting in the transportation of both lysosomes and autophagosomes to the area surrounding the nucleus within the cell, which then triggered by the rise in the intracellular pH during periods of starvation (12). The autophagosomes interacts through the homotypic fusion and vacuole protein sorting complex, Rab7, and pleckstrin homology domain-containing protein family member 1 (12). Furthermore, the SNARE complex promotes the fusion of autophagosomes and lysosomes by forming STX17-VAMP8-SNAP29 complex (25). Hence, the degradative pathway is crucial for cellular homeostasis and changes to these pathways can have severe impacts on the health of the cell.

1.3 Mannose-6 phosphate receptors

Most of the acid hydrolases are modified with mannose-6-phosphate (M6P) residues, which allows them to be recognised by M6P receptors in the Golgi complex and transported to the ELN (26). The asparagine-linked oligosaccharides of these enzymes are then selectively recognised by two enzymes i.e., the UDP-N-acetylglucosamine 1 phosphotransferase and N-acetylglucosamine-1-phosphodiester α-N-acetyl-glucosaminidase, which results in the generation of M6P markers on the enzymes (4). The modified enzymes are then recognised by

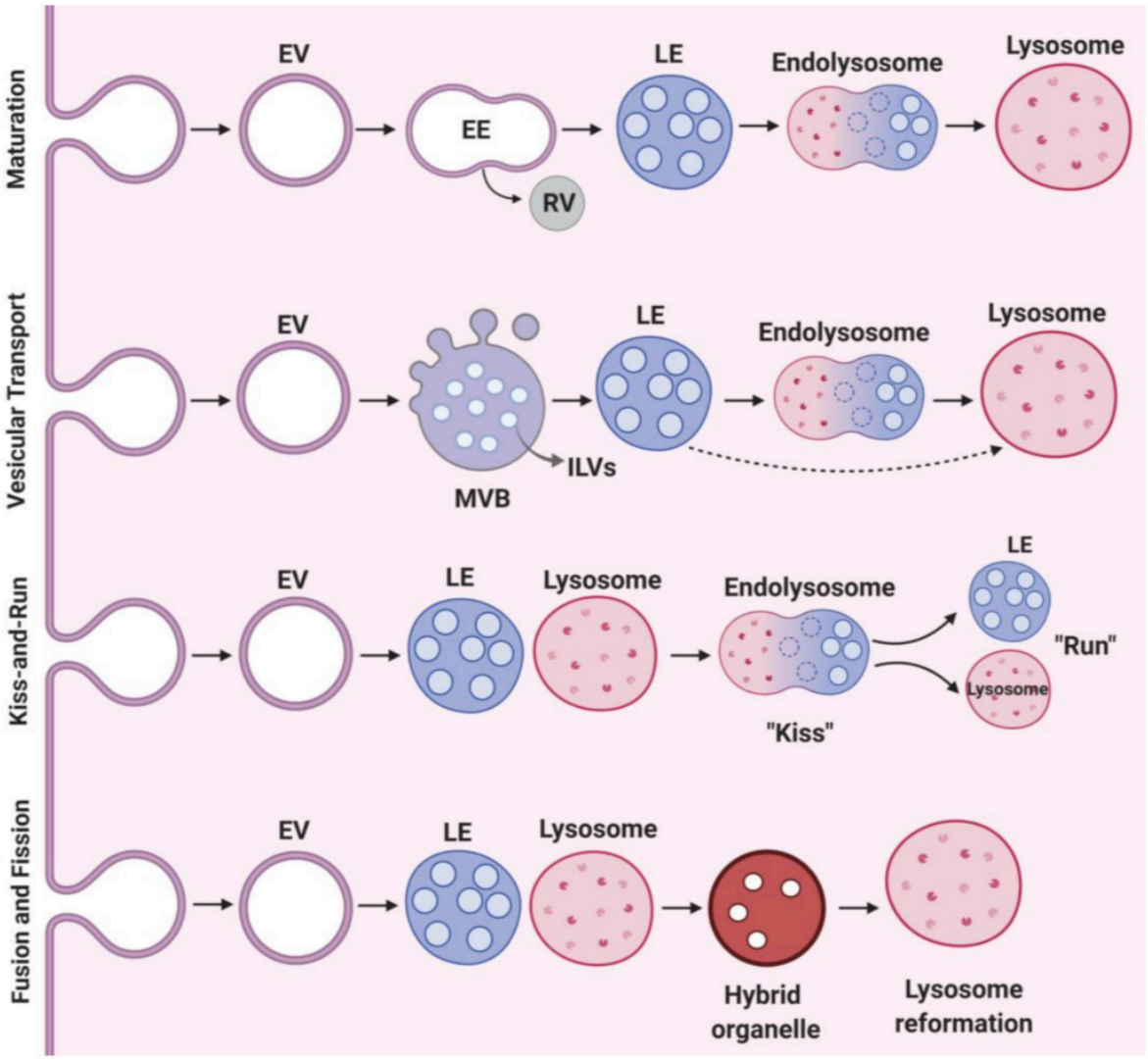

Figure 2. Lysosomal biogenesis models. Diagram shows the proposed mechanism for the transport of cargo to and from the lysosome through endocytic vesicles originating from the plasma membrane. Abbreviations used in the figure: Early endosome (EE), endocytic vesicles (EV), intraluminal vesicles (ILV), late endosome (LE), multi-vesicular bodies (MVB), recycling vesicles (RV). Diagram obtained from (12).

two independent transmembrane M6P receptors in the trans-Golgi network, which bind the M6P residue of the newly synthesised lysosomal hydrolases. Finally, the ligand-receptor complex is encapsulated in clathrin-coated transport vesicles and delivered to endosomes and lysosomes where the hydrolases can start digesting the endocytosed material (4, 26).

EEs have an acidic pH within their lumen, which helps to separate ligands from the M6P receptors and enables them to move towards LEs and lysosomes (20). Unbound M6P receptors are either returned from endosomes to the trans-Golgi network via endosomal vacuoles or are recycled through tubular sorting endosomes (27, 28). The retrograde movement of M6P receptor from endosomes to the trans-Golgi network takes place through "retromer", a five-unit structure that encodes vacuolar protein sorting genes (28). A retromer is comprised of a pair of sorting nexin proteins, such as SNX1/2 (known as Vps5-Vps17 in yeast), a group of three proteins called Vps35-VPS29-Vps26 that form a selective complex of transporting cargo (29). Retromer' association with EEs is regulated by monomeric G protein like RAB GTPase (e.g., Rab5 and Rab7) (30). The loss of Rab7 function leads to destabilisation of the retromer structure, resulting in impaired recycling of M6P receptors, acid hydrolase sorting, maturation of EEs to lysosome, and degradation of cargo (31). Moreover, unlike hydrolases that bind with M6P receptors, lysosomal membrane proteins can be delivered directly to endosome and lysosomes through the direct pathway or to the plasma membrane and then to endosomes and lysosomes through the indirect/salvage pathway (26).

The sorting of acid hydrolases and lysosomal membrane proteins involves the use of the heterotetrameric adaptor protein complex which is composed of four separate adaptin subunits: AP1, AP2, AP3, and AP4 (reviewed in (12)). AP1 is found in the trans-Golgi network and endosomes, and aids in the recycling of M6P receptors within the network. AP2 is present on the plasma membrane and endosomes, while AP3 is found on endosomes, and plays a crucial role in the transportation of lysosomal membrane proteins to the lysosome. Loss of AP3 function affects the sorting of M6P receptors and lysosomal membrane proteins and in turn, formation of lysosomes, as observed in Hermansky-Pudlak syndrome, where redistribution of lysosomal membrane proteins to the plasma membrane occurs, leading to impaired lysosome formation in melanosomes and platelet dense granules (32, 33).

1.4 Lysosomal storage disorders (LSDs)

Lysosomal storage disorders (LSDs) are a group of more than 70 monogenic diseases that are caused by genetically inherited homozygous mutations in genes encoding lysosomal enzymes or proteins (Table 1) (34). Most LSDs are inherited by an autosomal recessive trait, but three are X-linked: Fabry disease, Hunter syndrome (MPS II), and Danon disease (34, 35). The genetic mutations result in insufficient levels of lysosomal enzymes or proteins being synthesised leading to progressive accumulation of incompletely degraded substrates in the cells throughout the body, resulting in lysosomal dysfunction, impaired cell signalling and deterioration of cellular function (36). LSDs can be further subclassified into broad classes (i.e., mucopolysaccharidosis, sphingolipidoses, and glycoproteinoses) according to the type of stored material that is present in the body (34, 37, 38). However, it is notable that in many cases, multiple substrate types accumulate in a single enzyme deficiency. This is exemplified in the case of MPS IIIA, where critical sphingolipids accumulate in addition to the primary enzymatic substrate, the glycosaminoglycan, heparan sulphate.

1.4.1 Epidemiology

Individual LSDs are rare, with an estimated prevalence ranging from 1 in 50000 to 1 in 200000 live births (39, 40). Whilst higher specific disease frequencies are observed among various founder communities (34, 41-44). Collectively LSDs have an estimated combined incidence of 1 in 7000 - 1 in 8000 live births, presenting a significant individual and societal health burden (39, 40, 45). Notably, these disease estimates are likely underestimated, due to misdiagnosis that results from a lack of clinical awareness and are compounded by an increasing number of individuals with attenuated disease phenotypes, not previously identified (46).

1.4.2 Signs and symptoms

LSDs are genetically and clinically heterogeneous disorders but two-third present as paediatric neurodegenerative disorders, with variable symptoms, severity, and age of onset (47). Neurocognitive delays and behavioural abnormalities including aggression and hyperactivity are common (34, 35). Additionally, LSD patients often experience multisystem pathology with

Table 1. List of lysosomal and lysosomal related organelle genes that are associated with human Lysosomal Storage Disorders.

Gene name	Lysosomal Storage Disorders	Human Locus	OMIM	Inheritance
Aspartylglucosaminidase, AGA	Aspartylglucosaminuria	4q34	208400	AR
Arylsulfatase A, ARSA	Metachromatic Leukodystrophy	22q13	250100	AR
Arylsulfatase B, ARSB	Mucopolysaccharidosis VI	16q24	253200	AR
N-acylsphingosine amidohydrolase 1, ASAH1	Farber Lipogranulomatosis	8p22	228000	AR
Ceroid lipofuscinosis 1/Pamitoyl protein thioesterase 1, CLN/PPT1	Neuronal Ceroid Lipofuscinosis	1p34	256730	AR
Ceroid lipofuscinosis 2/Tripeptidyl Peptidase I, CLN/TPP1	Neuronal Ceroid Lipofuscinosis	11p14	204500	AR
Ceroid lipofuscinosis 3, CLN3	Neuronal Ceroid Lipofuscinosis	16p12	204200	AR
Ceroid lipofuscinosis 4/DNAJ Subfamily C, Member 5, CLN4/DNAJC5	Neuronal Ceroid Lipofuscinosis	15q23	204300	AR
Ceroid lipofuscinosis 5, CLN5	Neuronal Ceroid Lipofuscinosis	13q22	256731	AR
Ceroid lipofuscinosis 6, CLN6	Neuronal Ceroid Lipofuscinosis	15q23	601780	AR
Ceroid lipofuscinosis 7/Major facilitator superfamily domain-containing protein 8, CLN7/MFSD8	Neuronal Ceroid Lipofuscinosis	4q28	610951	AR
Ceroid lipofuscinosis 8, CLN8	Neuronal Ceroid Lipofuscinosis	8p23	600143	AR
Ceroid lipofuscinosis 9, CLN9	Neuronal Ceroid Lipofuscinosis	NM	609055	AR
Ceroid lipofuscinosis 10/Cathepsin D, CLN10/CTSD	Neuronal Ceroid Lipofuscinosis	11p15	610127	AR
Ceroid lipofuscinosis 11/Granulin, CLN11/GRN	Neuronal Ceroid Lipofuscinosis	17q21	614706	AR
Ceroid lipofuscinosis 12/ATPase 13A2, CLN12/ATP13A2	Kufor-Rakeb Syndrome	1p36	606693	AR

Gene name	Lysosomal Storage Disorders	Human Locus	OMIM	Inheritance
Ceroid lipofuscinosis 13/Cathepsin F, CLN13/CTSF	Neuronal Ceroid Lipofuscinosis	11q13	615362	AR
Ceroid lipofuscinosis 14/ Potassium channel tetramerisation domain containing protein 7, CLN14/KCTD7	Neuronal Ceroid Lipofuscinosis	7q11	611726	AR
Cystinosin, CTNS	Cystinosis	17p13	219800	AR
Cathepsin A, CTSA	Galactosialidosis	20q13	25640	AR
Fucosidase, FUCA1	Fucosidosis	1p36	230000	AR
Acid α-glucosidase, GAA	Pompe disease	17q25	232300	AR
Galactosylceramidase, GALC	Krabbe disease	14q31	245200	AR
Galactosamine-6-sulfatase, GALNS	Mucopolysaccharidosis type IVA	16q24	253000	AR
β-galactosidase, GLB1	Mucopolysaccharidosis type IVB	3p22	253010	AR
Glucosylceramidase β-1, GBA	Gaucher's	1q21	230900	AR
α-galactosidase A, GLA	Fabry	Xq22	301500	XL
N-acetylglucosamine-1-phosphotransferase, α/β subunits, GNPTAB	Mucolipidosis II alpha/beta, I-cell disease	12q23	252500	AR
N-acetylglucosamine-1-phosphotransferase, α/β subunits, GNPTAB	Mucolipidosis II alpha/beta, pseudo Hurler polydystrophy	12q23	252600	AR
N-acetylglucosamine-1-phosphotransferase, γ subunit, GNPTG	Mucolipidosis III γ, variant pseudo-Hurler polydystrophy	16p13.3	252605	AR
β-glucuronidase, GUSB	Mucopolysaccharidosis VII	7q11	253220	AR
Hexosaminidase A, HEXA	GM2 Gangliosidosis, Tay Sach's disease	15q23	272800	AR
Hexosaminidase B, HEXB	GM2 Gangliosidosis Sandhoff's disease	5q13	268800	AR
β-galactosidase, GLB1	GM1 Gangliosidosis	3p22	230500	AR
GM2 activator, GM2A	GM2 Gangliosidosis	5q33	272750	AR
HPS1 biogenesis of lysosomal organelles complex 3, subunit 1, HPS1	Hermansky-Pudlak type 1	10q24	203300	AR
β-3A subunit of the AP3 complex, AP3B1	Hermansky-Pudlak type 2	5q14	608233	AR
HPS3 biogenesis of lysosomal organelles complex 2, subunit 1, HPS3	Hermansky-Pudlak type 3	3q24	614072	AR

Gene name	Lysosomal Storage Disorders	Human Locus	OMIM	Inheritance
HPS4 biogenesis of lysosomal organelles complex 3, subunit 2, HPS4	Hermansky-Pudlak type 4	22q12	614073	AR
HPS5 biogenesis of lysosomal organelles complex 2, subunit 2, HPS5	Hermansky-Pudlak type 5	11p15	614074	AR
HPS6 biogenesis of lysosomal organelles complex 2, subunit 3, HPS6	Hermansky-Pudlak type 6	10q24	614075	AR
Dystrobrevin-binding protein 1, DTNBP1	Hermansky-Pudlak type 7	6p22	614076	AR
Biogenesis of lysosome-related organelles complex 1, subunit 3, BLOC1S3	Hermansky-Pudlak type 8	19q13	614077	AR
Biogenesis of lysosome-related organelles complex 1, subunit 6, BLOC1S6	Hermansky-Pudlak type 9	15q21	614171	AR
Adaptor-related protein complex 3, δ-1 subunit, AP3D1	Hermansky-Pudlak type 10	19p13	617050	AR
Biogenesis of lysosome-related organelles complex 1, subunit 5, BLOC1S5	Hermansky-Pudlak type 11	6p24	619172	AR
Hyaluronoglucosaminidase 1, HYAL	Mucopolysachharidosis type IX	3p21	601492	AR
Iduronate 2-sulfatase, IDS	Hunter syndrome	Xq28	309900	XLR
α-L-iduronidase, IDUA	Hurler syndrome	4p16	607014	AR
Lysosome-associated membrane protein 2, LAMP2	Danon disease	Xq24	300257	XLD
Lipase A, LIPA	Lysosomal acid lipase deficiency (Wolman)	10q23	278000	AR
Mannosidase-α class 2B member 1, MAN2B1	α-Mannosidosis	19p13	248500	AR
Mannosidase-β A, MANBA	β-Mannosidosis	4q24	248510	AR
Mucolipin, MCOLN1	Mucolipidosis type IV	19p13	252650	AR
Myosin VA, MYO5A	Griscelli syndrome type 1	15q21	214450	AR
Ras-asociated protein RAB27A, RAB27A	Griscelli syndrome type 2	15q21	607624	AR
Melanophilin, MLPH	Griscelli syndrome type 3	2q37	609227	AR
α-N-acetylgalactosaminidase, NAGA	Schindler	22q13	609241	AR
Sulphamidase, SGSH	Mucopolysaccharidosis type IIIA	17q25	252900	AR

Gene name	Lysosomal Storage Disorders	Human Locus	OMIM	Inheritance
N-acetyl-α-D-glucosaminidase, NAGLU	Mucopolysaccharidosis type IIIB	17q21	252920	AR
Acetyl-CoA:α-glucosaminide N-acetyltransferase, HGSNAT	Mucopolysaccharidosis type IIIC	8p11	252930	AR
N-acetylglucosamine-6-sulfatase, GNS	Mucopolysaccharidosis type IIID	12q14	252940	AR
Neuraminidase 1, NEU1	Sialidosis type 1 and 2	6p21	256550	AR
NPC intracellular cholesterol transporter 1, NPC1	Niemann-Pick type C1	18q11	257220	AR
NPC intracellular cholesterol transporter 2, NPC2	Niemann-Pick type C2	14q24	607625	AR
Scavenger receptor class B, member 2, SCARB2	Myoclonus-renal failure syndrome	4q21	254900	AR
Solute carrier family 17, member 5, SLC17A5	Sialic Acid Storage	6q13	269920	AR
Sphingomyelin phosphodiesterase 1, SMPD1	Niemann-Pick type A and B	11p15	257200 607616	AR
Sulfatase-modifying factor 1, SUMF1	Multiple Sulfatase Deficiency	3p26	272200	AR
Prosaposin A, PSAP-A	Atypical Krabbe	10q22	611722	AR
Prosaposin B, PSAP-B	Metachromatic Leukodystrophy due to Saposin B	10q22	249900	AR
Prosaposin C, PSAP-C	Atypical Gaucher	10q22	610539	AR
Prosaposin D, PSAP-D	Not known	10q22	-	AR
Prosaposin, PSAP	Combined Saposin deficiency	10q22	611721	AR

AR = Autosomal recessive; XL = X-linked; XLR = X-linked recessive; X-linked dominant = XLD

visceromegaly (abnormal enlargement of the organs in the abdomen) and skeletal dysmorphia (abnormal shape and size of the bone) (34, 35). The symptoms of LSDs are invariably progressive, resulting in multi-organ system dysfunction and premature death – in many cases reflecting central nervous system neurodegeneration. The average age of death for LSDs varies depending on the types, severity, and progression rates.

1.4.3 Treatments

Over the past decade, the number of clinical trials of treatments for LSDs has dramatically increased. Enzyme replacement therapy, substrate reduction therapy, and gene therapy are amongst those being explored (reviewed in (34)). Despite this progress, the efficacy of these therapies remains limited, particularly when treating the CNS.

1.4.4 Enzyme replacement therapy

Predicated upon chaperoned delivery of recombinant produced lysosomal enzymes to their site of action within the lysosome (utilising mannose-6-phosphate dependent transport mechanisms), enzyme replacement therapy (ERT) acts to surplant dysfunctional endogenous protein (48). However, therapy is quite invasive and requires repeat administration via systemic and, at times, intrathecal routes of delivery. Intravenously administered ERT has been shown to be effective in reducing lysosomal storage material in mucopolysaccharidoses I, II, IV, VI, and VII disorders and ameliorating clinical symptoms such as organomegaly and even improving organ function (34, 48). Moreover, Brineura, a drug that is recently approved by the United States Food and Drug Administration (US-FDA) to treat Ceroid lipofuscinosis 2 (CLN2) has been shown to be successful in attenuating disease progression, specifically in motor and language decline in children with CLN2 following intrathecal delivery (49). Indeed, the inability of ERT to cross the blood brain barrier and target the nervous system presents a significant clinical limitation. Hence, there remains a need to develop further a novel treatment that is less invasive that could also cross the blood- brain barrier (BBB).

1.4.5 Substrate reduction therapy

Substrate reduction therapy (SRT) is a therapeutic approach with the aim of retarding the production of target macromolecules and reducing the catabolic burden upon endogenous lysosomal enzymes (50). Examples of therapies that have shown to have clinical efficacy are N-butyldeoxynojirimycin, which inhibits ceramide glucosyltransferase, the enzyme that is responsible for synthesizing glucosylceramide, the storage compound in Gaucher disease (51, 52). SRT can be administered orally, does not trigger an immune response and can cross the BBB. However, SRT is only approved for use in two LSDs (Gaucher's disease and Fabry disease), and further research is required to determine the efficacy of SRT in other LSD.

1.4.6 Gene therapy

Gene therapy (GT) is administered in two general ways, *in vivo* and *ex vivo* for the treatment of metabolic diseases. GT is delivered by introducing genetic material into an individual's cells and tissues aimed at correcting the inherited genetic defect in order to restore the normal function of the gene and ameliorate the clinical phenotype (53). The use of GT has been reported in several studies, primarily due to its capability in reaching the central nervous system of patients with LSD. This is the case where studies conducted by Tardieu et al. have shown effective gene delivery and expression after injection into the central nervous system of MPS IIIA children (54). Based on these preclinical studies, MPS IIIA children aged two and six years showed improvement in attention skills, behaviour and sleep after receiving intracerebral injection of an AAV vector carrying complementary DNA encoding the *SGSH* gene (54). Similarly, in children affected by metachromatic leukodystrophy, the introduction of normal Arylsulfatase A into CD34-positive hematopoietic stem cells by lentiviral vector that was re-introduced to patients showed no decline in motor and cognitive function over a period of 24 months (55). Previous studies in MPS IIIB, Pompe disease and Fabry disease also showed encouraging results in patients that were treated with GT (56-58). However, despite these promising results the research on long-term safety and efficacy of GT are warranted.

1.5 Heterozygosity in lysosomal degradative genes and other neurodegenerative disorders

Although they have historically been considered to be unaffected, recent attention has focused upon the potential for neurological dysfunction amongst carriers of heterozygous mutations in lysosomal genes. Indeed, this is exemplified in the case of *GBA1* mutations which give rise to Gaucher's disease in their homozygous form, carrier status (mutations in a single allele) has been identified as the most common genetic risk factor for late-onset neurodegenerative pathology similar to Parkinson's disease (PD) and Lewy body dementia with the suggestion of class effects in a number of cognate lysosomal disorders (59-61). Based on recent genome-wide association study (GWAS), other lysosomal degradative genes such as sphingomyelin phosphodiesterase 1 (*SMPD1*), NPC intracellular cholesterol transporter 1 (*NPC1*), granulin (*GRN*), and cathepsin D (*CTSD*) have been associated with common neurological disorders (59, 62, 63). However, the disease mechanisms sub-serving these observations remain undefined, and it is unclear whether heterozygosity in lysosomal gene mutations confers a neurological or cellular phenotype across the spectrum of lysosomal degradative pathway genes. Further, the contribution of different mutation types, for example, null (normal protein produced) or missense mutations in which misfolded, mutant proteins are produced, remains largely unexplained, although a toxic gain of function is a possibility.

The literature describing what is currently known about the impact of heterozygous mutations in lysosomal genes and the link to neurodegenerative diseases has been reviewed and a manuscript drafted (section 1.6).

1.6 Review Article: Heterozygosity in lysosomal genes and neurodegenerative diseases: a chamber of secrets?

Statement of Authorship

Title of Paper	Heterozygosity in lysosomal genes and neurodegenerative diseases: a chamber of secrets?
Publication Status	☐ Published ☐ Accepted for Publication ● Unpublished and Unsubmitted work written in manuscript style ☐ Submitted for Publication
Publication Details	Unpublished review article.

Principal Author

Name of Principal Author (Candidate)	Nazzmer Nazri		
Contribution to the Paper	Performed the literature review and wrote the review article		
Certification:	This paper reports on original research I conducted during the period of my Higher Degree by Research candidature and is not subject to any obligations or contractual agreements with a third party that would constrain its inclusion in this thesis. I am the primary author of this paper.		
Signature		Date	

Co-Author Contributions

By signing the Statement of Authorship, each author certifies that:

i. the candidate's stated contribution to the publication is accurate (as detailed above);

ii. permission is granted for the candidate in include the publication in the thesis; and

iii. the sum of all co-author contributions is equal to 100% less the candidate's stated contribution.

Name of Co-Author	Nicholas Smith		
Contribution to the Paper	Reviewed and edited the manuscript		
Signature		Date	30/3/2023

Name of Co-Author	Kim Hemsley		
Contribution to the Paper	Reviewed and edited the manuscript		
Signature		Date	31/3/23

Heterozygosity in lysosomal genes and neurodegenerative diseases: a chamber of secrets?

Nazzmer Nazri[1,2], Nicholas JC Smith[3,4], Kim M Hemsley[1,2]

1. Childhood Dementia Research Group, College of Medicine and Public Health, Flinders Health & Medical Research Institute, Flinders University, Bedford Park, Adelaide, 5042, South Australia
2. Discipline of Paediatrics, Adelaide Medical School, The University of Adelaide, North Terrace, Adelaide, 5000, South Australia
3. Paediatric Neurodegenerative Diseases Research Group, Discipline of Paediatrics, Adelaide Medical School, The University of Adelaide, North Terrace, Adelaide, 5000, South Australia
4. Department of Neurology and Clinical Neurophysiology, Women's and Children's Hospital, Adelaide, 5006, South Australia

Corresponding Author

Kim M Hemsley

kim.hemsley@flinders.edu.au

Abstract

The monogenic lysosomal storage disorders (LSDs) are a group of diseases typically arising from autosomal recessive or X-linked mutations in genes encoding catabolic lysosomal enzymes or proteins. Mutations in these genes result in inactive, absent or misfolded proteins and reduced enzymatic activity. The lack of enzyme activity leads to progressive accumulation of undegraded substrates, perturbation of cellular function, and a condition known as LSD, two thirds of which occur as paediatric neurodegenerative disorders. While paediatric neurodegenerative phenotypes are prominent amongst the LSDs, individuals with heterozygous mutations in lysosomal protein genes have largely been considered to be clinically unaffected. However, recent genome wide association study data suggests that some heterozygous mutations may confer an increased risk of developing a later-onset neurological condition. This is evident in carriers of mutations in the glucosylceramide beta-1 (*GBA*), NPC intracellular cholesterol transporter 1 (*NPC1*), and granulin (*GRN*) genes, which respectively increase an individual's risk of developing Parkinson's disease, dementia with Lewy bodies, and frontotemporal lobar degeneration. Heterozygous mutations in other lysosomal genes such as sphingomyelin phosphodiesterase 1 (*SMPD1*), Cathepsin D (*CTSD*), beta-galactosylceramidase (*GALC*), Hexosaminidase B (*HEXB*), alpha-N-acetylglucosaminidase (*NAGLU*), and N-sulfoglucosamine sulfohydrolase (*SGSH*) may also confer an increased risk based on genome-wide association studies. Given there are more than 70 lysosomal protein-encoding genes, access to molecular profiling is expanding, and that therapies targeting disorders of lysosomal catabolism are emerging, defining the clinical significance of heterozygous mutations in lysosomal genes holds increasing importance. Here we review the current evidence for, and mechanisms attributed to predisposition to late-onset neurodegenerative disease in carriers of heterozygous mutations in genes encoding lysosomal proteins.

Keywords Lysosomal storage disorders, haploinsufficiency, heterozygous mutation, carriers, lysosomal genes, neurodegenerative diseases, Parkinson's disease

Introduction

Lysosomal storage disorders (LSDs) are a group of more than 70 monogenic diseases that are individually associated with specific deficiencies of a lysosomal catabolic function. The majority are consequent to autosomal recessive loss of function mutations, resulting in a deficiency of enzyme activity and impairment in the breakdown of macromolecular substrates within the cells. The progressive accumulation of these incompletely undegraded cellular substrates leads to perturbation of critical cellular function and eventually leads to cell death. The symptoms are invariably progressive, resulting in multi-organ system dysfunction and premature death. Early onset neurodegeneration is prominent across many of the LSDs and while the pathological mechanisms remain incompletely understood, it is notable that histopathological features congruent with common later-onset neurodegenerative diseases have been reported (48, 64, 65). For example, histopathological assessment of post-mortem brain tissue from severe patients with Gaucher's disease or NPC1 disease has revealed the presence of lesions reactive for α-synuclein and/or amyloid beta (Aβ), in addition to Lewy bodies and neurofibrillary tangles (NFT), which are hallmarks of Parkinson's disease (PD) and Alzheimer's disease (AD) (66-70). The accumulation of these protein aggregates in the brain is suggested to be due to impairment of the endosomal-lysosomal network (ELN) which plays an important role in removing unwanted materials and maintaining cell homeostasis (71).

However, recognition now exists that heterozygous mutations in lysosomal genes may also predispose to clinical disease, albeit in a modified or attenuated form from the manifesting homozygous state (Figure 1) (72). To date, the level of lysosomal enzyme activity in heterozygous carriers has typically been considered sufficient to prevent disease. However, genome wide association study (GWAS) data (59, 62, 63, 73), suggest that individuals heterozygous for pathogenic mutations in lysosomal pathway genes are at increased risk of developing a range of late-onset neurological conditions, with potential cumulative risk when mutations are present in more than one lysosomal gene (63). This is exemplified by mutations in glucosylceramidase beta-1 (*GBA1)*, NPC intracellular cholesterol transporter 1 (*NPC1*), and granulin (*GRN*), which increase an individual's risk of developing PD, dementia with Lewy bodies, and frontotemporal lobar degeneration (FTLD) respectively (70, 74, 75). Similarly, mutations in the N-sulphoglucosamine sulfohydrolase (*SGSH*) and N-acetylglucosaminidase (*NAGLU*) genes (which, in their homozygous form lead to Sanfilippo syndrome) have also been recognised as risk factors for the development of Parkinson's disease (67).

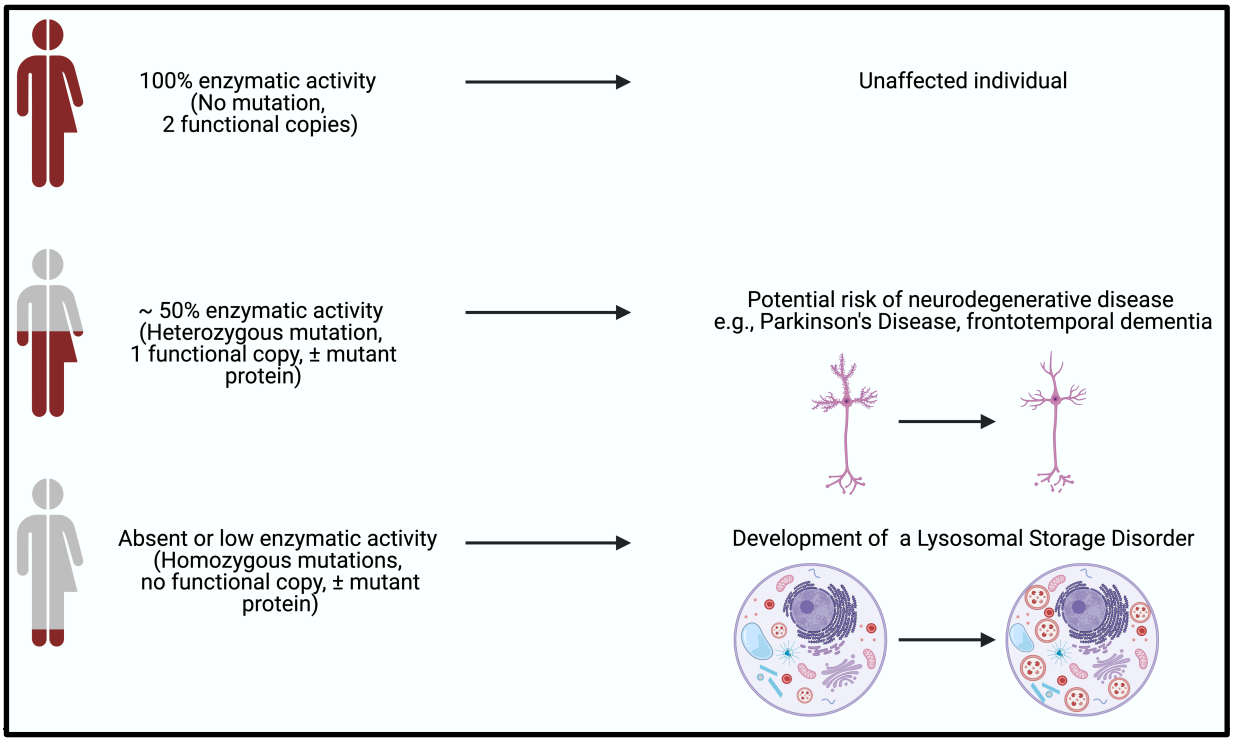

Figure 1. Diagram illustrating the potential risk associated with heterozygous and homozygous mutations in lysosomal genes. Individuals with two functional copies of lysosomal enzyme/protein-encoding genes can produce a normal amount of lysosomal enzyme or protein to degrade macromolecules. Heterozygous individuals with one functional copy of the lysosomal genes are only able to produce approximately half the normal amount of enzyme/protein and are thought to be at increased risk of neurodegeneration (± mutant protein). Homozygous individuals inherit mutations that lead to completely absent or low amount of enzymatic activity to degrade macromolecules and are known to cause dysfunctional lysosomes, which ultimately leads to LSDs.

With an estimated carrier frequency of 1 in 40 (calculated based on Hardy-Weinberg equation) in the general population, heterozygous mutations in one or more lysosomal pathway genes are potentially important contributors to the global burden of later-onset neurodegenerative disease. Recognition of these associations holds particular importance, given the increasing access to molecular phenotyping, including identification of mutations amongst phenotypically normal carriers via pre-conception programmes (76-78) and increasing community access to screening through commercial platforms (e.g. ancestry.com.au and 23andme.com) (59). Moreover, understanding clinically relevant associations between carrier status and disease extends beyond predictions of population risk, with potential to inform therapeutic design and extrapolate mechanistic approaches being developed for homozygous LSD states to heterozygous carriers. Here we seek to review the current literature pertaining to manifesting neurodegenerative disease amongst individuals who are carriers of heterozygous mutations in lysosomal enzyme or protein-encoding genes.

Glucosylceramidase beta-1 (*GBA*)

The human *GBA* gene [chromosome: 1q21] encodes the lysosomal enzyme glucocerebrosidase (GCase), which is responsible for hydrolysis of the sphingolipid, glucosylceramide (GlcCer) to liberate glucose and ceramide (79); deficiency of enzyme activity results in accumulation of GlcCer, its derivatives and upstream precursors (80). Biallelic mutations in *GBA* give rise to Gaucher's disease (GD), a multisystem disorder, typified by aberrant sphingolipid accumulation within the cells of the macrophage-monocyte lineage, with pathology prominent within the reticuloendothelial system (e.g., bone marrow, spleen, and liver) (81, 82). Central nervous system pathology is also present across the clinical disease subtypes, though historically considered isolated to mutation dependent neuronopathic subtypes presenting in infancy and later childhood (Type 2 and 3 GD) (83). Clinical symptoms of GD vary according to disease type, including but not limited to enlargement of the spleen and liver, cytopenia, skeletal deformities, and neurological impairment (84). The variability of clinical representations of GD may be explained by the different pathogenic mutations on both alleles of the *GBA* gene (82). GD is classically divided into three main types on the basis of clinical symptoms and neuronal involvement: type 1 is termed non-neuronopathic, type 2 and 3 are termed neuronopathic due to involvement of the central nervous system (85). Indeed, the predominant mutant allele among type 1 Gaucher disease patients, N370S, is often cited as neuroprotective (86), though studies are limited.

Historically, the link between *GBA* and the development of Parkinson's disease and related Lewy body disorders was first discovered in the 1990's with the identification of patients with GD who also developed PD (87-89). This was further validated in clinical and epidemiological studies where it was observed that *GBA* mutations were significantly prevalent in PD patients, occurring in approximately 5-20% of individuals with PD (90-93). Neuropathological assessment in *GBA* mutation carriers has also confirmed hallmark pathological features of α-synuclein pathology and neocortical Lewy body pathology (Figure 2) (94). Previous studies also reported prodromal signs of PD in *GBA* mutation carriers where clinical signs and symptoms of autonomic dysfunction (i.e., urinary dysfunction, orthostatic hypotension), fatigue, anxiety, changes in REM sleep behaviour and cognitive decline were found to be more frequent in carriers of *GBA* mutations compared to individuals with non-*GBA* associated PD (95, 96). Recent studies showed that mutations in the *GBA* gene can promote the dysregulation of extracellular vesicles (EV) (97). Neuroblastoma (SH-SY5Y) cells overexpressing alpha-synuclein were used to assess the ability of patient derived small EVs from PD patients with or without *GBA* mutations to affect alpha-synuclein. Cerri and colleagues reported that EVs derived from PD patients with *GBA* mutations promote the release of EVs, independently of mutation severity (97). Moreover, EVs released from the cells of PD patients with *GBA* L444P missense mutations (producing misfolded protein) increased the intra-cellular levels of phosphorylated alpha-synuclein, indicating that dysregulation of EV trafficking may play a role in *GBA* associated PD. Additionally, Gatto and colleagues observed that patients with the L444P mutations have the highest risk of developing early onset *GBA* PD, and more rapid cognitive decline, while other mutations e.g., N370S and E326K missense mutations (both produced misfolded protein, but the extend of misfolding is variable) have been reported to confer an intermediate to low risk, respectively (61, 98). Hence, the severity of *GBA* PD related cases appears dependent on the type of *GBA* variants inherited, contributing to the risk of PD and dementia in carriers of *GBA* mutations (99).

Studies using flies carrying *Gba* mutations have also been reported, with transgenic flies expressing the human N370S, L444P, or 84GG (deletion mutation; truncated proteins) mutations (100). Experiments conducted with these Drosophila models revealed that production of misfolded GCase in dopaminergic neurons can lead to the development of PD signs, manifested by death of dopaminergic cells and decreased mobility (Figure 3). Further, there were mutation-specific decreases in lifespan, loss of dopaminergic neurons, and impaired motor activity, with L444P mutations resulting in the most severe phenotype. Hence, the study

suggests that the presence of misfolded GCase in dopaminergic cells results in the development of parkinsonian signs.

A range of heterozygous *Gba* murine models (101-103) have also been evaluated. In 2011, a study conducted by Sardi and colleagues examined hippocampal α-synuclein levels and memory function in GD mice with either the D409H mutation or with the *Gba* gene knocked out (104). The study reported that $Gba^{D409H/+}$ and $Gba^{+/-}$ mice showed no accumulation of glucosphingolipid in the brain, suggesting that one functional copy of the wildtype *Gba* allele is sufficient to maintain normal Gba function and prevent the build-up of incompletely degraded GlcCer substrate. However, $Gba^{D409H/+}$ (but not $Gba^{+/-}$) mice exhibited α-synuclein-reactive lesions in the hippocampus at 6 months of age, suggesting that the presence of mutant misfolded GCase protein might impair alpha-synuclein trafficking and/or degradation (104). Curiously, $Gba^{D409H/+}$ mice did not exhibit any memory deficits when subjected to the novel recognition test, suggesting that accumulation of α-synuclein in the hippocampus is not sufficient to cause memory loss at the age the mice were tested. A separate study by Kim and colleagues using $Gba^{D409H/+}$ mice crossed with A53T α-synuclein mice investigated the potential influence of *Gba* mutations on the disease progression of PD. Crossed mice exhibited loss of dopaminergic neurons in the substantia nigra, increased activation of glial cells, and motor abnormalities (105). Notably, inducing expression of D409H *Gba* led to reduced lifespan, indicating that the D409H mutation may impact upon the age of disease onset and the severity of disease in A53T α-synuclein mice. Recent studies have also shown mice heterozygous for other *Gba* variants (E326K, N370S and L444P) also display α-synuclein-reactive lesions and loss of dopaminergic neurons (103, 106-108). Perturbed mitochondrial function, disrupted mitophagy and increased oxidative stress has been observed in the central nervous system in mice carrying the L444P allele (109, 110).

Additionally, knockout heterozygous mutations in *Gba* appear to negatively modify the neurodegenerative course, with earlier onset of PD symptoms in a murine model of PD which overexpresses the human transgene $SNCA^{A53T}$ (101). This study explains how the combination of multiple genetic factors can potentially lead to an early-onset and worsening neurodegenerative condition. Of note, lipidomic studies in these animals confirmed an absence of glucosylceramide and glucosylsphingosine accumulation, suggesting that the changes in the clinical course were not due to substrate deposition (102). The findings of Ikuno and colleagues are somewhat contradictory. In their hands, knockout *Gba* heterozygous mice producing human α-synuclein demonstrated a reduction in dopaminergic neurons within the substantia

nigra pars compacta, however increased levels of the lysolipid glucosylsphingosine were noted in the brain, suggesting that perturbed lipid metabolism as a consequence of GCase deficiency, may have a pathogenic role in disease (101, 102).

Although the genetic link between GD and PD is well established, we lack an understanding of why carriers of *GBA* mutations are prone to neurodegeneration, emphasising the need to further explore the pathobiological mechanisms underpinning these emerging associations.

Sphingomyelin phosphodiesterase 1 (*SMPD1*) & *NPC* intracellular cholesterol transporter 1 (*NPC1*)

Niemann-Pick disease (NPD) is a group of autosomal recessively inherited disorders associated with neurological impairment and the storage of lipids, including sphingomyelin and cholesterol (111). NPD is characterised by hepatosplenomegaly and neurological signs, including ataxia, cognitive decline, and seizures. Many intermediate cases have been reported with mild-to-moderate neurological presentation (112). NPD is divided into two major subcategories, neuronopathic (type A and C) and non-neuronopathic (type B). NPD type A and B are caused by homozygous mutations in the *SMPD1* gene, which encodes for acid sphingomyelinase (ASM) (111). The mutation in *SMPD1* results in a deficiency of ASM required to degrade sphingomyelin to phosphocholine and ceramide in late endosomes and lysosomes (47, 111). Homozygous mutations in *NPC1* result in the accumulation of unesterified cholesterol in late endosomes and lysosomes of cells due to impaired cholesterol transport (113, 114). As a result, accumulation of lipid storage bodies, dendritic and axonal abnormalities, and ultimately cell death is seen (115). The loss of neurons and the presence of hyperphosphorylated tau and the formation of NFTs are standard neuropathological features seen in NPD diseased brain (47, 70, 115).

Similar to the *GBA* PD association, carriers of mutations in *SMPD1* have previously been shown to be at increased risk for the development of PD (59, 63, 116). However, due to the rarity of *SMPD1* mutations in the population, there is a lack of research examining the aetiology of *SMPD1* and PD association. Gan-or and colleagues reported that L302P missense mutation, which results in the production of misfolded protein in *SMPD1* gene was strongly associated with increased risk of developing PD based on a population study (117). Similarly, carriers of the R591C (missense; misfolded protein) and fsP330 (frameshift; truncated protein) mutations are also known to confer an increased risk of PD. Interestingly, the R496L missense

mutation (produced misfolded protein), which is the most common point mutation in *SMPD1* was not associated with an increased risk of developing PD (116, 118, 119). However, given the limited existing evidence on the relationship of *SMPD1* and PD, further research is required to determine the correlation and elucidate the underlying mechanism of neurodegeneration and how it predisposes carriers of *SMPD1* mutations to an increased risk of developing neurodegenerative diseases.

A detailed review of clinical and diagnostic features of heterozygosity in NPD type C can be found elsewhere (120) but briefly, carriers of heterozygous *NPC1* gene mutations have been shown to have an increased risk of developing PD (121) and AD (122). Moreover, family members of several NPC patients, have presented with symptoms of parkinsonism, suggesting a possible genetic link to PD (123). Prodromal signs such as autonomic dysfunction (hyposmia, orthostatic hypotension, urinary incontinence), changes in REM sleep behaviour, and impotence were present (Figure 2) (123). Individuals with heterozygous mutations in *NPC1* also exhibited similar pathology to that seen in NPD type C, with splenomegaly and abnormal filipin staining observed (120, 124). Electrophysiological recordings using transcranial magnetic stimulation demonstrated impaired intracortical facilitation, short afferent inhibition, and long-term potentiation like plasticity in symptomatic *NPC1* mutation carriers (125). Atrophy of the cerebral cortex and midbrain using MRI have also been observed (121). A recent study by Bremova-Ertl and colleagues also reported that *NPC1* heterozygotes showed characteristics of NPD type C disease such as oculomotor abnormalities, hepatosplenomegaly, and impaired cognitive function (126). Positron emission tomography imaging also revealed significantly abnormal metabolic rates in half of the participants, affecting cerebellar, anterior cingulate, parieto-occipital, and temporal regions.

Furthermore, studies investigating the impact of heterozygosity in knockout murine *Npc1* gene on phenotype reported motor function impairment and increased anxiety-like behaviour by nine weeks of age (Figure 3) (127). The authors also noted knockout $Npc1^{+/-}$ mice showed no improvement in motor coordination and balance on the negative geotaxis test over time in comparison to wildtype mice, suggesting carriers of *Npc1* mutations could potentially be susceptible to developing motor disorders (127). Purkinje cell loss is apparent in the brain of aged $Npc1^{+/-}$ cats and mice, with significant accumulation of glycolipids and hyperphosphorylation of tau (128, 129), suggesting that carrying a *Npc1* mutation leads to impaired lipid metabolism. Collectively, these studies demonstrate reduced production of *Npc1* with or without mutant protein production impairs neuronal architecture, cellular function and lipid metabolism and provides some evidence that carriers of *Npc1* mutations may potentially

have a greater risk of developing neurodegenerative disorders, or more specifically, PD. Nevertheless, more research is required to assess the aetiology and mechanism(s).

Beta-galactosylceramidase (*GALC*)

The β-galactocerebrosidase (*GALC*) gene is found on the long arm of human chromosome 14 (14q31.3) and encodes for the lysosomal enzyme β-galactosylceramidase, which functions to remove galactose from ceramide derivatives, for example galactosylceramide, galactosylsphingosine, and lactosylceramide. Homozygous mutations in this gene cause Krabbe disease (KD), also known as galactosylceramide lipidosis or globoid cell leukodystrophy. Loss of residual enzyme activity leads to accumulation of toxic substrates - galactosylcerebroside and galactosylsphingosine in oligodendrocytes in the CNS and Schwann cells in the peripheral nervous system (PNS) (130). Consequently, this increases recruitment and infiltration of macrophages and microglial cells to phagocytose the non-degraded substrates, ultimately forming multi-nucleated globoid cells (131, 132). Due to their respective role in regulating signal transduction in the CNS and PNS, accumulation of toxic galactoyslsphingosine in the oligodendrocytes and Schwann cells leads to demyelination (133), and altered neuronal conduction that is a key identifying hallmark of KD pathology. Approximately 70 disease-causing mutations in *GALC* have been identified (134). Similar to other LSDs, KD has different clinical forms that are usually described according to the age of onset (135). Children affected with the infantile form, which accounts for 95% of all cases are typically diagnosed within the first six months of life and have a shorter lifespan (136). The late-onset forms of KD are much more variable and categorized into two subgroups: late infantile and juvenile (137, 138), based upon observed clinical symptoms. Common symptoms include increased irritability, spasticity, cognitive decline, seizures, and motor dysfunction along with unexplained fever, blindness, and deafness (139, 140). Interestingly, late-onset forms of KD typically exhibit slower disease progression, and may even exclude peripheral neuropathy in some cases (141).

Individuals with heterozygous *GALC* mutations exhibit an increased risk for the development of diseases such as open angle glaucoma (142), pulmonary artery enlargement (143), and late-onset synucleopathies like PD (144). Furthermore, sporadic PD patients identified with p.Phe596Ser and pTrp132* mutations have been found to exhibit reduced

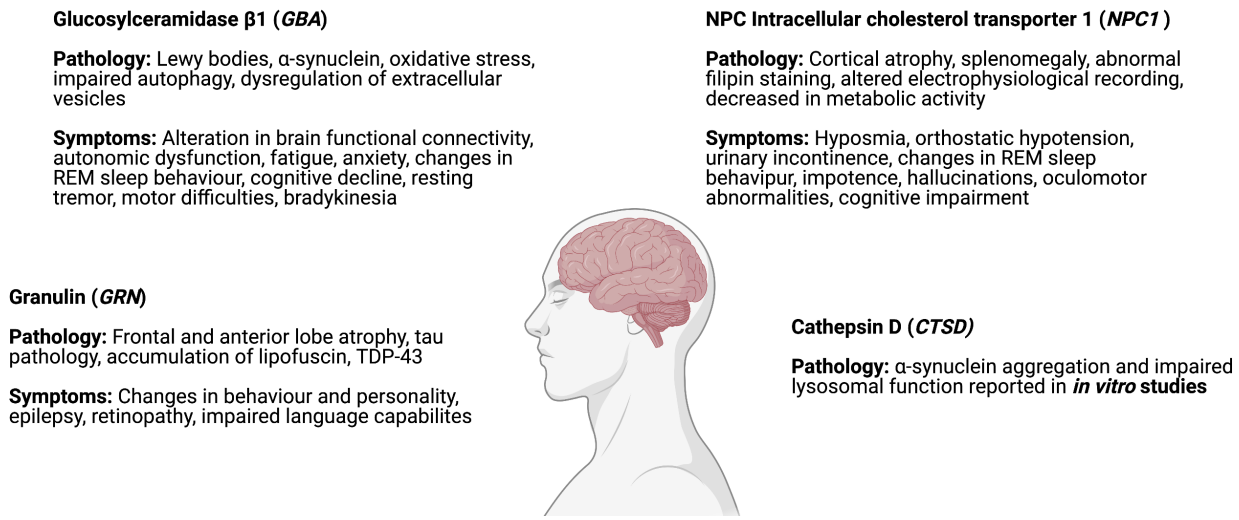

Figure 2. Reported neuropathology and clinical symptoms in carriers of mutations in lysosomal genes. Heterozygous mutations in *GBA*, *NPC1*, *CSTD,* and *GRN* have been associated with neuropathology and symptoms of Parkinson's disease and Frontotemporal Lobar Degeneration (75, 95, 96, 120, 145-148).

GALC activity and sphingolipid accumulation when compared to healthy controls, suggesting a role for *GALC* mutations in the onset of PD (149). Interestingly, the loss of *GALC* activity is also apparent with normal aging (149), indicating age may be a compounding factor to heterozygous *GALC* mutations in the development of PD.

Recent GWAS studies have also demonstrated that mutations in *GALC* are a genetic risk factor for multiple sclerosis (MS) (150, 151). A study by Scott-Hewitt and colleagues provides some evidence of the relationship between *Galc* mutations and aberrant myelination of neuronal cells (152). The authors utilised cuprizone, a highly selective and sensitive copper-chelating agent that produces toxic demyelination that resembles the demyelination commonly seen in MS and found no difference in the amount of corpus callossum myelin, number of oligodendrocytes and motor behaviour as examined by several gait parameters that are normally altered in homozygous *Galc* animals (152). However, Scott-Hewitt and colleagues reported defects in heterozygous in *Galc* mice in repairing myelin damage caused by cuprizone exposure during the recovery phase where fewer oligodendrocytes and less myelin staining was observed when compared to recovery-matched wildtype littermates (152). Defects in remyelination were present up to 4 weeks after restoration to a cuprizone free diet. Moreover, defects in clearing myelin debris were also reported in heterozygous *Galc* mice, indicating impaired phagocytosis and microglial function. The authors also found that the microglia in wildtype mice appeared more ramified while the heterozygous *Galc* microglia appeared stunted with less complex processes (152). This study suggests heterozygous mutations in *Galc* may increase the likelihood of neurodegeneration, however, there exists a need for more studies to be conducted to elucidate whether failure of remyelination due to *Galc* mutations directly contributes to the development of MS in humans, and whether carriers of β-galactocerebrosidase mutations are susceptible to an increased risk of developing other neurological diseases.

α-N-acetylglucosaminidase (*NAGLU*)

The *NAGLU* gene can be found on human chromosome 17q21.2 and encodes *α*-N-acetylglucosaminidase, a lysosomal enzyme responsible for the removal of N-acetylglucosamine from the glycan derivatives, resulting in the breakdown of heparan sulfate (HS). Genetic mutations in *NAGLU* are responsible for one of the four types of mucopolysaccharidosis type III (MPS III) termed MPS IIIB. Other subtypes of MPS III are attributed to sulphamidase (MPS IIIA), heparan acetyl-CoA: a-N-acetyltransferase (MPS IIIC),

and N-acetylglucosamine 6-sulfatase deficiency (MPS IIID) (153-156). Mutations in one of these genes leads to a deficiency in the corresponding lysosomal enzymatic activity which is critical in the degradation of HS, causing subsequent accumulation of incompletely degraded HS in the cells (157). Common symptoms of MPS III include but are not limited to delayed cognitive development, behavioural abnormalities, speech impairment, skeletal pathology, and hepatosplenomegaly (158, 159).

The impact of carrying a heterozygous mutation in *NAGLU* is not well understood at present, however a study by Winder-Rhodes and colleagues reported that *NAGLU* mutations are common genetic variants associated with PD (67). Further, a GWAS study has also identified *NAGLU* to be a novel locus associated with PD risk (160). However, more research is required to fully explore the relationship between *NAGLU* mutations and neurodegenerative (and other) disease susceptibility.

N-sulfoglucosamine sulfohydrolase (*SGSH*)

The *SGSH* gene found on the human chromosome 17q25.3 encodes for the lysosomal enzyme sulphamidase, which plays an important role in the breakdown of long-chain GAGs via the removal of the N-sulfate group at the end of the GAG chain (34). Homozygous mutations in *SGSH* leads to MPS IIIA. A recent study by Douglass and colleagues observed that mice carrying a missense D31N mutation in heterozygous *Sgsh* (*Sgsh*$^{+/D31N}$) mice (producing misfolded protein) exhibit mildly impaired motor function, as indicated by the number of falls in the negative geotaxis test (Figure 3) (161). Interestingly, whilst the brain of *Sgsh* mutation carriers was subjected to a battery of markers for neurodegenerative disease lesions, only subtle changes in motor cortex pyramidal neuron morphology were noted (161), indicating that overt disease lesions and phenotypic changes observed in individuals with heterozygous mutations in lysosomal enzyme genes may be enzyme or mutation dependent. Nonetheless, more research is required to fully elucidate if heterozygous mutations in *Sgsh*/SGSH gene confer an increased risk of neurodegenerative or other clinical diseases.

Granulin (*GRN*)

Apart from Parkinson's disease, there is increased risk of developing frontotemporal lobar degeneration (FTLD) in carriers of mutations in the lysosomal gene, granulin (*GRN*). The *GRN* gene is found on human chromosome 1p34.2 and it encodes the lysosomal enzyme progranulin.

Progranulin plays a role in regulating cellular growth, division, and survival of rapidly-dividing cells, such as skin cells (fibroblasts), immune cells, and neuronal cells (162). In the brain, neurons and microglia produce progranulin, which helps to regulate neuronal survival, neurite outgrowth, synaptogenesis, as well as neuroinflammation (162-165). Homozygous *GRN* mutations lead to development of neuronal ceroid lipofuscinosis (NCL; also known as Batten's disease). NCL are characterized by progressive cognitive and psychomotor deterioration, seizures, and in some cases death in early childhood (166). NCL are caused by pathogenic mutations in one of at least 14 different genes, with deposition of lipofuscin. Classification of NCL disorders is based on age of onset (infantile, late infantile, juvenile, and adult) and the gene involved (each disease type is given the designation "CLN", meaning ceroid lipofuscinosis, and then a number to indicate its subtype). Other genetic variants of CLN such as *CLN5, CLN6, CLN7/MFSD8, CLN8, CLN4/DNAJC5, CLN11/GRN, CLN12/ATP13A2, CLN13/CTSF,* and *CLN14/KCTD17* have also been identified based on recent advances in whole-exome sequencing (166).

FTLD is an incurable neurodegenerative disease characterized by the progressive degeneration of the frontal and anterior temporal lobes (167) and is the second most common cause of dementia under the age of 60 years (75, 168, 169). Haploinsufficiency in *GRN* is the leading risk factor for the pathogenesis of FTLD (75, 145-147). Common clinical symptoms include a progressive change in behaviour and personality, including social disinhibition, epilepsy, and retinopathy, as well as a gradual decline in language capabilities (170). Histopathological features of FTLD include inclusion bodies positive for tau, accumulation of lipofuscin, auto-fluorescent lipid, and ubiquitinated TAR DNA-binding protein 43 (TDP-43) (167, 171).

More than 60 mutations that result in progranulin deficiency have been identified (162). Individuals with genetic polymorphism in *GRN* are at increased risk for developing AD, PD, progressive nonfluent aphasia, and corticobasal syndrome (172-175). The mean age of onset for *GRN* mutation carriers is 60 years (176). Perry and colleagues reported two patients with novel *GRN* mutations who presented with clinical features similar to AD. One patient aged 65 years showed evidence of amyloid aggregation on positron emission tomography whilst another patient aged 54 years presented with logopenic progressive aphasia with TDP-43 inclusions post-mortem (175). Furthermore, about nine to seventeen percent of carriers of *GRN* mutations present with an AD phenotype (177). Interestingly, individuals haploinsufficient for *GRN* have also been reported to have similar clinicopathological features to those with NCL,

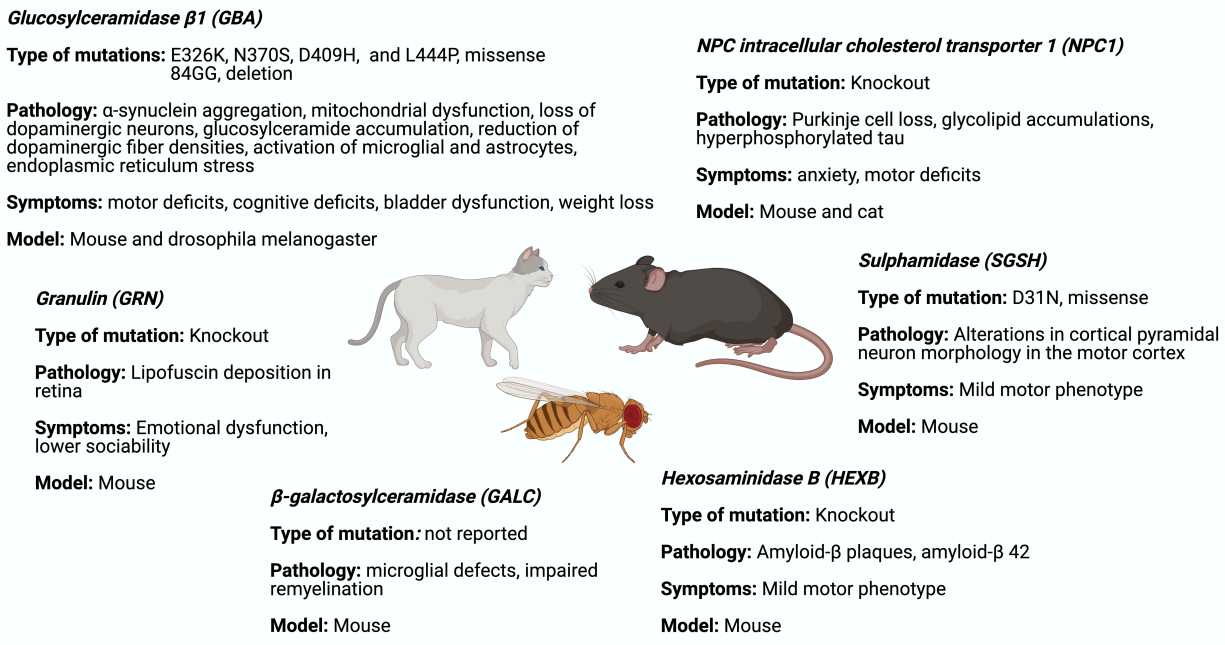

Figure 3. Summary of reported pathology and symptoms in animals who have heterozygous mutations in lysosomal genes. Reduced production of lysosomal proteins in heterozygous animals leads to variable disease pathologies and alteration in behaviour (101-103, 106-108, 127-129, 152, 161, 178-181).

with the presence of autofluorescent NCL-like storage material seen in the frontal cortex (169). Impairment of lysosomal protease activity in carriers of *GRN* mutations also results in substrate accumulation in lymphoblasts, increased levels of the pro-inflammatory cytokine interleukin-6 and decreased cytokine interluekin-10 in macrophages (182, 183).

Whilst haploinsufficient knockout *Grn* mice exhibit no accumulation of lipofuscin in the brain (i.e., thalamus, hypothalamus, and amygdala) (179, 180), deposits have been noted in retina, consistent with human studies (Figure 2 and 3) (169). Filiano and colleagues found no significant changes in neuroinflammatory markers (e.g. Iba1, TNF-alpha, GFAP) nor any evidence of microgliosis and astrocytosis in *Grn* mouse brain (179), despite this, haploinsufficent knockout *Grn* mice display a change in social interaction by six months of age, with reduced sociability and emotional dysfunction (179). Minami and colleagues also reported that reduced *Grn* leads to impaired phagocytosis, cognitive deficits, and increase in amyloid plaques (181). The functional impact of *GRN* haploinsufficiency and any link to the development of FTLD and AD or other disorders requires considerable research.

Cathepsin D (CTSD)

The *CTSD* gene (chromosome: 11p15) encodes a soluble lysosomal aspartic endopeptidase. *CTSD* has numerous physiological functions, including regulation of apoptosis, activation of enzymatic precursors and degradation of cytoskeletal proteins (184). Congenital NCL type-10 (*CLN10/CTSD*) is an early-onset form of Batten's disease caused by homozygous mutations in the *CTSD* gene. Human studies have shown that reduced *CTSD* activity is associated with the development of AD and PD (185), but studies on haploinsufficiency in *CTSD* are limited. A study by Bae and colleagues generated a *CTSD* knockout cell line (148). The study revealed that knockout *CTSD* haploinsufficiency results in impaired lysosomal degradation activity as shown in neuroblastoma cells with nonsense mutations in *CTSD*. As a consequence, α-synuclein accumulated at higher levels in haploinsufficient cells compared to normal cells, suggesting that partial loss of *CTSD* activity is sufficient to cause a significant decline in lysosomal function, which in turn accelerate the propagation of α-synuclein (148). The role of *CTSD* in the development of clinical diseases requires further assessment to determine whether haploinsufficienct individuals are at risk in developing a clinical phenotype.

Hexosaminidase B (HEXB)

The human *HEXB* gene is located on chromosome 5q13.3 and encodes β-hexosaminidase that is responsible for the degradation of GM2 gangliosides into GM3 by removing the N-acetylgalactosamine residue (186). Homozygous mutations in *HEXB* are associated with the development of Sandhoff disease (SD), which is a form of GM2 gangliosidosis. Defective β-hexosaminidase leads to accumulation of GM2 ganglioside in the cells throughout the body, resulting in typical clinical presentation of early onset LSD such as hepatosplenomegaly, coarse facies, and bone abnormalities (187). The clinical manifestation of SD is classified clinically into three forms, infantile, juvenile, and adult. Common symptoms of SD includes developmental delays and regression, cherry red spots in ophthalmic examination, and organomegaly (188). The association between heterozygous mutations in *HEXB* and neurodegenerative disease is not well studied. However, a study conducted by Whyte and colleagues reported the role of *Hexb* heterozygosity in the development of AD. Studies shown that knockout $Hexb^{+/-}$ mice crossed with AD mice showed no substantial memory impairment or upregulation of neuropathological markers, suggesting that deficient β-hexosaminidase activity is not the main factor in the progression of AD (178). Interestingly, knockout $Hexb^{+/-}$ mice exhibited amyloid-β plaques in the cortex and hippocampus at 46 weeks of age and amyloid-β 42 in the hippocampus with mild impairments in behaviour activity (Figure 3) (178). Given the preliminary nature of the findings, more research is required to evaluate the role of *HEXB* mutation and the potential risk for the development of AD or other neurological disease.

Discussion

It is increasingly evident that carrying a single genetic mutation in a gene associated with an autosomal recessive disorder may, in some circumstances at least, increase a person's risk of developing a clinical disorder of the central nervous system. The type, severity, and age of onset of the conditions appear dependent on the number and nature of the genetic mutation(s) inherited. This is particularly evident in humans with *GBA* mutations where the L444P mutation for instance leads to the development of PD with earlier age of onset and rapid progression whereas the N370S polymorphism results in an attenuated form of PD. It is speculated that the production of misfolded proteins from these mutations compared to a null mutation exacerbate the disease process due to changes in the protein's amino acid sequence,

structure and ultimately impacting its function in the CNS (189). Additionally, dysfunction of endoplasmic reticulum-associated degradation (ERAD) can lead to the accumulation of misfolded proteins, which can overwhelm the ubiquitin-proteasome system (UPS) to degrade and remove misfolded or damaged proteins from the cells (190). As a consequence, accumulation of misfolded proteins can lead to the formation of toxic aggregates and inclusion bodies that disrupt cellular function. Thus, dysregulation of ERAD can indirectly affect the function of UPS, further contributing to the accumulation of misfolded proteins and the development of neurodegenerative disease (191).

Whilst studies on *GBA* are well-advanced, detailed research on the impact of heterozygous mutations in many/most of the other 70 genes associated with LSDs is severely lacking. This therefore means there is a significant gap in our knowledge and a need to understand the etiopathogenesis of potential neurodegeneration in carriers of lysosomal gene mutations.

A comprehensive review and proposed mechanism of neurodegeneration in carriers of *GBA* mutations has been reported (192). The deleterious effects of the mutant *GBA* gene are thought to be the main contributor to the development of PD in carriers of mutations in lysosomal genes (100). The *GBA* mutations can cause structural changes in the GCase protein, leading to decreased enzymatic activity, loss of function or toxic gain of function. These changes can result in substrate accumulation, altered lipid metabolism, and lysosomal dysfunction, all of which have been linked to PD pathogenesis (68, 193). However, it should be noted that substrate accumulation has not been recorded in carriers of *GBA* mutations, although minor accumulation of GlcCer has been reported in inducible pluripotent stem cells heterozygous for *GBA* mutations (194, 195). Moreover, while perturbation of lipid metabolism has been suggested to be one of the mechanism of neurodegeneration in PD, impairment of the endosomal-lysosomal network (ELN) has also been implicated, as the degradative pathway play a crucial role in the removal of alpha-synuclein in the brain (68, 194, 196).

In support of the concept that toxic gain of function may hasten disease, a recent study by Pan and colleagues demonstrated that MPS IIIC mice with P304L mutations in the heparan sulfate acetyl-CoA:α-glucosaminide N-acetyltransferase (*HGSNAT*) gene and knockout mice showed similar levels of HGSNAT activity (197). However, mice homozygous for the *Hgsnat*^{P304L} mutation producing misfolded protein show an earlier onset of behavioural changes with reduced lifespan, increased neuroinflammation, and defects in synaptic neurotransmission (197), suggesting that the mutation that leads to product of a mutant

misfolded proteins hastens the disease pathology and infers a toxic gain of function. However, due to limited studies, more research is required to support this hypothesis as the differences in neuropathology may also be enzyme dependent.

It has also been hypothesised that the development of a neurological disease may potentially be due to mutations in more than one gene, resulting in a cumulative effect that may increase the risk of a clinical disease. This was suggested in a study conducted by Robak and colleagues where 56% of the PD cases analysed had at least one mutation in a gene that is involved in lysosomal function, and 21% had more than one genetic risk factor (73). It was also suggested that multiple genetic hits may act in combination to impair overall lysosomal function, which in turn could enhance susceptibility to neurological diseases. Further, chronic diseases like AD, PD, and MS are thought to result from a combination of genetics and environmental factors, a concept commonly referred to as the multiple-hit hypothesis (198-201).

As more carriers of lysosomal gene mutations who are potentially at risk of neurological diseases are identified through carrier screening projects (e.g., Mackenzie's Mission in Australia), therapeutic options will need to be investigated. Current LSD treatment in development for homozygous lysosomal disease, might be considered as therapeutic strategies in an effort to mitigate risk of late-onset neuropathology in heterozygous state.

In conclusion, carriers of mutations in some lysosomal genes appear to be at increased risk of neurological disease; however, our understanding of the biological basis underlying such increased vulnerability remains limited as does our knowledge about the broader applicability of these associations.

1.7 Research significance and hypothesis

Carriers of mutations in some lysosomal degradative genes are at an increased risk of developing common neurological disorders. There is a need to understand the underlying mechanism of disease development in carriers of mutations in lysosomal genes and the breadth of the impact. This project seeks to define pathological consequences of haploinsufficiency in the lysosomal degradative gene, *Sgsh/SGSH*, and further elucidate and add to the existing literature on the mechanism and biology of heterozygosity and how it influences the individual's risk of potentially developing a neuropathology. Additionally, this work will reinforce the prognostic significance of *Sgsh/SGSH* mutation carrier status in the context of late-onset neurodegenerative disease risk and underpin rationale for prophylactic therapeutic intervention amongst mutation carriers.

The hypothesis tested is that:

Carriers of a mutation in the N-sulfoglucosamine sulfohydrolase (*Sgsh*) gene exhibit aberrations in neuron structure, biochemistry and/or metabolism, which may predispose them to impaired neurological function.

1.8 Aims of the study

The overall aim of this project was to define the morphological, biochemical, and functional neuronal consequences of heterozygosity in the lysosomal degradative gene, *Sgsh*; in both an authentic murine model arising from a D31N mutation, which leads to production of mutant (misfolded) enzyme and decreased activity in affected animals and in heterozygous human cell lines.

The specific objectives of the study were to;

1. Study the temporal impact of the D31N *Sgsh* heterozygous mutation upon the mouse cortical proteome.

2. Assess the impact of the D31N *Sgsh* heterozygous mutation on motor cortex pyramidal neuron morphology and cortical neural function.

3. Investigate the impact of heterozygous mutations in the metabolic profile of D31N *Sgsh* heterozygous mouse and *SGSH* heterozygous human fibroblast cells.

Chapter 2: Materials and Methods

2.1 Materials

2.1.1 Animal Husbandry

Item	Product Code	Source
1.5mL Eppendorf Tube	0030120086	Eppendorf, NSW, Australia
100% Ethanol	EL027-10LP	ChemSupply, SA, Australia
Rodent Ear Punch	AS500077	AbleScientific, SA, Australia

2.1.2 Genotyping

Item	Product Code	Source
1.5mL Eppendorf Tube	0030120086	Eppendorf, NSW, Australia
MicroAmp Adhesive Film Applicator	4333183	ThermoFisher Scientific, MA, USA
MicroAmp Optical Adhesive Film	4311971	ThermoFisher Scientific, MA, USA
MicroAmp Support Base	4379590	ThermoFisher Scientific, MA, USA
MicroAmp Optical 384-Well Reaction Plate	4309849	ThermoFisher Scientific, MA, USA
Sterile Water	2037157	Clifford Hallam Healthcare, SA, Australia
Chelex 100 Resin	142-1253	BioRad Laboratories, CA, USA
2x Taqman Gene Expression Master Mix	4369016	ThermoFisher Scientific, MA, USA
2x Taqman Genotyping Master Mix	4371353	ThermoFisher Scientific, MA, USA
40x Custom MPS IIIA Assay	CCU001SNR	ThermoFisher Scientific, MA, USA

Custom SNP Assay for GFP	CCU001S	ThermoFisher Scientific, MA, USA
Custom Taqman Copy Number Assay for GFP	4331348	ThermoFisher Scientific, MA, USA
Taqman Copy Number Reference Assay	4458366	ThermoFisher Scientific, MA, USA

2.1.3 Tissue Collection

Item	Product Code	Source
Anodised Aluminium Brain Slicer	-	Braintree Scientific, MA, USA
GEM Stainless Steel Blades	-	Adelab Scientific, SA, Australia
23G Butterfly Needle	-	Hamilton Company, NV, USA
Paraformaldehyde	P6148	Sigma-Aldrich, NSW, Australia
Phosphate Buffered Saline (10x Stock) Sodium Chloride Potassium Chloride Disodium Hydrogen Orthophosphate	 465-2.5KG 383-500G 391-500G	 Science Supply, VIC, Australia Science Supply, VIC, Australia ChemSupply, SA, Australia

2.1.4 Histology

Item	Product Code	Source
Anodised Aluminium Brain Slicer	-	Braintree Scientific, MA, USA
GEM Stainless Steel Blades	-	Adelab Scientific, SA, Australia

23G Butterfly Needle	-	Hamilton Company, NV, USA
Shandon Embedding Cryomold	E6032-1CS	Sigma-Aldrich, NSW, Australia
Double-edge Stainless Blades	82133316	Wilkinson Sword, UK
Superfrost Plus Coverslips	-	Menzel-Glaser, Germany
Superfrost, Plus Microscope Slides	-	Menzel-Glaser, Germany
Paraformaldehyde	P6148	Sigma-Aldrich, NSW, Australia
100% Ethanol	EL027-10LP	ChemSupply, SA, Australia
bisBenzimide H33342 trihydrochloride (Hoechst)	14533	Sigma-Aldrich, NSW, Australia
Acetone	AA008-2.5L	ChemSupply, SA, Australia
Low Melt Agarose	1613111	BioRad Laboratories, CA, USA
Triton-X 100	X100	Sigma-Aldrich, NSW, Australia
Cubic Reagent Urea Quadrol Triton-X100	 U5378 122262 X-100	 All products obtained from Sigma-Aldrich, NSW, Australia
Phosphate Buffered Saline (10x Stock) Sodium Chloride Potassium Chloride Disodium Hydrogen Orthophosphate	 465-2.5KG 383-500G 391-500G	 Science Supply, VIC, Australia Science Supply, VIC, Australia ChemSupply, SA, Australia

2.1.5 Mass Spectrometry

Item	Product Code	Source
1.5mL Eppendorf Tube	0030120086	Eppendorf, NSW, Australia
Acetone	AA008-2.5L	ChemSupply, SA, Australia
Methanol	MA0O4-2.5L-P	ChemSupply, SA, Australia
Ammonium Bicarbonate	A6141	Sigma-Aldrich, NSW, Australia
Dithiothreitol	D9760	Sigma-Aldrich, NSW, Australia
Iodoacetamide	I1149	Sigma-Aldrich, NSW, Australia
Trifluoroacetic Acid	TS181-100M	ChemSupply, SA, Australia
Formic Acid	AC10760050	ChemSupply, SA, Australia
Acetonitrile	34967-2.5L	Fisher Scientific, VIC, Australia
RapiGest Surfactant	186002123	Waters™, NSW, Australia
Non-binding 96-well plate	CLS3370	Interpath Sevices, VIC, Australia
Bicinchoninic Acid Protein Kit	23235	ThermoFisher Scientific, MA, USA

2.1.6 Tissue Culture

Item	Product Code	Source
Dulbecco/s Modified Eagle's Media (DMEM)	11965092	ThermoFisher Scientific, MA, USA
Ham's nutrient F12	11765054	ThermoFisher Scientific, MA, USA
Fetal Bovine Serum	FBSFR-S00FU	Bovogen, Biologicals, VIC, Australia
Penicillin/Streptomycin (10,000 U/mL)	15140122	ThermoFisher Scientific, MA, USA

Trypsin-EDTA (0.5%), no phenol red	15400054	ThermoFisher Scientific, MA, USA
Glutamax Supplement (100X)	35050061	ThermoFisher Scientific, MA, USA
Dulbecco Phosphate Buffered Saline (1x)	14190136	ThermoFisher Scientific, MA, USA
Corning 5mL Sterile Pipettes	CNG4487	Adelab Scientific, SA, Australia
Corning 10mL Sterile Pipettes	CNG4488	Adelab Scientific, SA, Australia
Corning 25mL Sterile Pipettes	CNG4489	Adelab Scientific, SA, Australia
229mm Glass Pasteur Pipettes	HIR92601.01	Adelab Scientific, SA, Australia
Corning T25 Flask	CNG430639	Adelab Scientific, SA, Australia
Corning T75 Flask	CNG4306411U	Adelab Scientific, SA, Australia
100% Ethanol	EL027-10LP	ChemSupply, SA, Australia
Sodium Hypochlorite	ST044-5L	ChemSupply, SA, Australia
Mycoplasma PCR detection kit	G238	Apploed Biological Materials, Richmond, Canada

2.1.7 Electrophysiology

Item	Product Code	Source
Neurobasal-A Media	10888022	ThermoFisher Scientific, MA, USA
Hank's Balanced Salt Solution	14175095	ThermoFisher Scientific, MA, USA
1M HEPES	15630080	ThermoFisher Scientific, MA, USA

B27 Supplement	17504044	ThermoFisher Scientific, MA, USA
DNase I	D5025	Sigma-Aldrich, NSW, Australia
Poly-L-Lysine	P6282	Sigma-Aldrich, NSW, Australia
24-well plate with Pedot Electrode on Glass	24W300/30G-288	Multi-Channel Systems, Germany
Rotenone	R8875-1G	Sigma-Aldrich, NSW, Australia
Borate Buffer Boric Acid Sodium Tetraborate Decahydrate Sodium Chloride	 B6768 B3545 465-2.5KG	 Sigma-Aldrich, NSW, Australia Sigma-Aldrich, NSW, Australia Science Supply, VIC, Australia

2.1.8 Mitochondrial Assay

Item	Product Code	Source
Seahorse XF Cell Mito Stress Test Kit	103015-100	Agilent, CA, USA
Seahorse XFe96 Fluxpak mini with PDL plates	103729-100	Agilent, CA, USA
Seahorse XF DMEM media	103680-100	Agilent, CA, USA
Seahorse XF Glucose	17504044	Agilent, CA, USA
Seahorse XF Pyruvate	D5025	Agilent, CA, USA
Seahorse XF L-Glutamine	103579-100	Agilent, CA, USA
Seahorse Calibrant Solution	100840-000	Agilent, CA, USA
Tetraethylbenzimidazolylcarbocyanine iodide (JC-1)	ab141387	Abcam, Cambridge, UK
DMEM with no phenol red	21063029	ThermoFisher Scientific, MA, Australia

Black, Clear-bottom 96 well-plate	6055300	PerkinElmer, MA, USA

2.1.9 Hyperspectral Imaging

Item	Product Code	Source
Glass Bottom Dish 35mm	81218-200,	DKSH, SA, Australia
DMEM with no phenol red	21063029	ThermoFisher Scientific, MA, USA
Nicotinamide Adenine Dinucleotide + Hydrogen (NADH)	10107735001	Sigma-Aldrich, NSW, Australia
Flavin Mononucleotide (FMN)	F6625-100MG	Sigma-Aldrich, NSW, Australia

2.2 Methods

This section includes methods that are used in multiple Chapters, while methods specific to a single Chapter are provided in that Chapter.

2.2.1 GFP$^{+/-}$-MPS IIIA Mouse Colony Establishment and Maintenance

In the year prior to the commencement of the study, reanimation of transgenic mice (*Sgsh*^{D31N};Tg$^{Thy1\text{-}EGFPLdru}$) was performed by the Australian Phenomics Facility, Australian National University, Canberra. Nine female and ten male GFP hemizygous mice were shipped to the Women's and Children's Hospital (WCH). The mouse line had previously been created by the Childhood Dementia Research Group lab by crossing D31N MPS IIIA mouse with the "M" line (202). The mouse model uses a murine *Thy1* promoter at transgenic (reporter) insertion M to express green fluorescence proteins (GFP) in the central nervous system (CNS) (Figure 2.1). This line is subsequently termed as "*Thy1*-GFP-M" to describe the expression of the fluorescent protein and the location of the insertion in the model (202). The mouse line contains a modified regulatory region of the *Thy1* gene where deletion of exon 3, and the flanking introns upstream of the fluorescent protein sequences resulted in the selective expression of GFP in subsets of neurons in the brain (Figure 2.1). Around 10-30% of sensory neurons found in the dorsal root ganglia are labelled; pyramidal neurons are selectively labelled in the cerebral cortex and hippocampus; mossy fibres are labelled in the cerebellar cortex; and approximately 10-20% retinal ganglion cells are identified and labelled in the retina (202).

All animals were bred, housed, and maintained in the Animal Care Facility of the WCH, with all breeding (AE#1112) and experimental (WCH: AE#1013, University of Adelaide: M-2020-075) procedures undertaken with approval from the Institutional Animal Ethics Committee, according to the guidelines of the National Health and Medical Research Council's Australian Code for the Care and Use of Animals for Scientific Purposes (8th Edition). Gene technology approval (B144/12/2020) was obtained from the Biosafety Committees of the WCH and the University of Adelaide.

All mice were housed in a temperature- and humidity-controlled environment in the WCH Animal Care Facility with a 14-hour light: 10-hour dark cycle and were provided pelleted food and water *ad libitum*. Further, to improve the well-being of the mice, environmental enrichment such as plastic houses, cardboard and tissue paper were provided. These

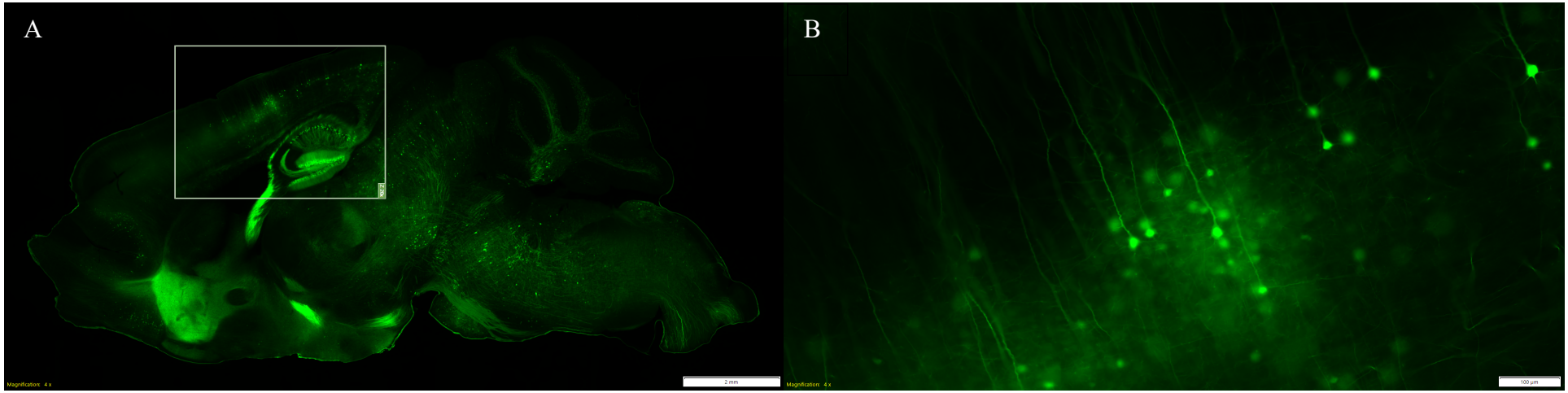

Figure 2.1. Expression of green fluorescent protein in transgenic GFP$^{+/-}$ mouse. (A) Sagittal cut of GFP$^{+/-}$ mouse brain, scale bar 2mm (B) GFP positive pyramidal neuron in layer 5 of the cerebral cortex, scale bar 100µm. Approximately 10-20% of sensory neurons are labelled on the dorsal root ganglia, pyramidal neurons are selectively labelled in the cerebral cortex and in the hippocampus, and approximately 10-30% of retinal ganglion cells are labelled in the retina (202). Scale bar 2mm.

environmental enrichments permitted them to grow, mature, reproduce and maintain good health within the colony. The date of birth was recorded when mouse pups were first observed in the morning following birth. For identification, each mouse had a unique identity number, which corresponds to the number of ear notches it has as shown in Figure 2.2. Notches were placed either on the left or right ear to show the individual mouse number. Mice were ear notched typically between the ages of 19- to 21-days or when the ears are big enough to notch. The notched tissue was subsequently stored in -20^{o}C or immediately used for genotyping (method described in section 2.2.2) to identify its genetic variants. Following ear notch, mice were housed in same-sex groups of similar ages, monitored daily and overall health assessment such as body weight and eye check was conducted weekly.

In this study, a breeding plan was developed to ensure enough mice were born with the desired genotype and that only female mice were utilised. For neuronal morphology study (Chapter 4), wildtype progeny was generated by having one parent with no copies of GFP ($GFP^{-/-}$) while the other parent possess two copies of GFP ($GFP^{+/+}$), and that both parents were homozygous wildtype ($Sgsh^{+/+}$). To produce heterozygous progeny, one parent had to possess zero copies of GFP ($GFP^{-/-}$), the other parent required to have two copies of GFP ($GFP^{+/+}$), and either parent had to be homozygous wildtype ($Sgsh^{+/+}$) or homozygous for the D31N *Sgsh* gene mutation ($Sgsh^{D31N/D31N}$, MPS IIIA). Hence, hemizygous single-copy GFP ($GFP^{+/-}$) with wildtype ($Sgsh^{+/+}$) was classified as wildtype ($Sgsh^{+/+\ EGFP}$), and single-copy $GFP^{+/-}$ with heterozygous ($Sgsh^{+/D31N}$) classified as heterozygous ($Sgsh^{+/D31N\ EGFP}$) mice. A total of 50 transgenic mice aged 0, 3, 6, 12, and 24 weeks old (5 mice/genotype/age) were collected for the neuro-morphological assessment of pyramidal neurons in the cerebral cortex.

2.2.2 Congenic MPS IIIA Mouse Colony

A congenic mouse strain was developed by Crawley and colleagues by backcrossing mice with the MPS IIIA D31N mutation, which were initially on a mixed genetic background, with the inbred C57BL/6 strain (203). The congenic mice (no GFP expression) were utilised and $Sgsh^{+/+}$ classified as wildtype, and $Sgsh^{+/D31N}$ classified as heterozygous. In proteomic study, a total of 60 mice (5 mice/genotype/age) and only female mice were used. Female mice were selected for the proteomic study because group housing is possible, allowing them to be housed in groups up to 48 weeks. In contrast, male mice necessitate individual housing due to welfare concerns, as they tend to engage in aggressive behaviour, which can subsequently affect proteomic outcomes. For electrophysiological recordings, a total of 24 mice (12 mice/genotype)

were used from the congenic colony. However, given that newborn mice were utilised in the assay, identification of gender was unable to be performed. Thus, mice with mixed gender (male and female) were utilised in the electrophysiology experiment.

2.2.3 Mouse Ear-Notching

Prior to ear notching, a clean area in the laboratory was set up with all supplies laid out (70% ethanol, ear punch scissors, tweezers, bench coat sheets, genotyping book to record information, and autoclaved Eppendorf tubes). Mice aged between 19- to 21- days were removed from the mother's cage and placed in a separate cage with soft tissues and environmental enrichment to reduce stress on the animals. Each mouse was then handled on bench coat to identify sex and ear punch scissors was used to perform the ear notch, corresponding to a designated identification number as shown in Figure 2.2. In between mice, the scissors and forceps were sterilised with 70% ethanol and wiped dry to remove any contaminants or leftover tissues. The ear notched tissue was then placed into a sterilised 1.5mL Eppendorf tube and stored on ice until further use. Once all litters had been ear notched, the mice were returned to the mother ahead of weaning and monitoring. The tubes containing the ear tissue were stored in -20^{o}C for long term storage and genotyping.

2.2.3 Genotyping of mice

2.2.3.1 Genomic DNA lysis from mouse tissue

Genomic DNA extraction from mouse tissue was done using 10% (w/v) Chelex-100 solution. Briefly, an aliquot of 10% Chelex-100 was thawed and 100µL of vortexed solution was added to a tube containing the mouse tissue. The tube was subsequently vortexed ensuring the tissue is immersed in the Chelex-100 solution, and then immediately transferred to a 100^{o}C heating block for 20 minutes. The tube was vortexed briefly at the 10-minute mark and returned to the heating block for a further 10 minutes. Following incubation, the tube containing cellular debris and Chelex-100 particles were spun down for 5 minutes at 13, 000 rpm using a bench centrifuge. The supernatant containing genomic DNA was either directly used for Polymerase Chain Reaction (PCR) amplification or stored at -20^{o}C for long term storage.

2.2.3.2 Quantitation of Genomic DNA by Nanodrop

Genomic DNA was quantified using a NanoDrop-1000 Spectrophotometer (ND-1000; ThermoFisher Scienctific, Waltham, MA, USA) loaded with the ND-1000 v3.7.0 software under the "Nucleic Acid" selection. The NanoDrop was calibrated by pipetting 2µL of Milli-Q water onto the pedestal. Following further instruction, the NanoDrop was then "blank" and loaded with a new 2µL of Milli-Q water. Once calibration was completed, the amount of genomic DNA was measured by loading 1µL of genomic DNA onto the pedestal. The amount of DNA was recorded, and the pedestal wiped clean between samples using kimwipes. Prior to genotyping, the final concentration of genomic DNA needed was determined to be 5ng in 1µL of sterile water using the following equation:

- gDNA volume to add (µL)
  200ng/ [neat genomic DNA concentration in ng/µL]

- Water for Injection volume to add (µL)
  40µL – genomic DNA volume in steps above (for 5ng/uL)
  200µL – genomic DNA volume in steps above (for 1ng/uL)

The diluted genomic DNA with final concentration of 1ng/µL and 5ng/µL were used immediately for genotyping or stored at -20°C for long term storage.

2.2.3.3 Genotyping assay

A Taqman custom single nucleotide polymorphism (SNP) genotyping assay was developed by Dr. Adeline Lau (Childhood Dementia Research Group, Flinders University) and used to differentiate wildtype (*Sgsh*$^{+/+}$) and heterozygous (*Sgsh*$^{+/D31N}$) mice (Figure 2.3). Prior to starting genotyping assay, diluted DNA was thawed at room temperature and subsequently kept in the fridge until ready for sampling. A PCR master mix was created in a sterile Eppendorf tube in a designated PCR cabinet. The master mix contained 5µL of 2x Taqman Genotyping Master Mix, 0.25µL of 40x MPS IIIA SNP Custom Assay, and 3.75µL of sterile water as a working stock. Each component was multiplied by the number of samples being tested, which included two negative control samples (sterile water instead of genomic DNA), three positive controls (Wildtype, Heterozygous, and MPS IIIA), and three spares for pipetting error.

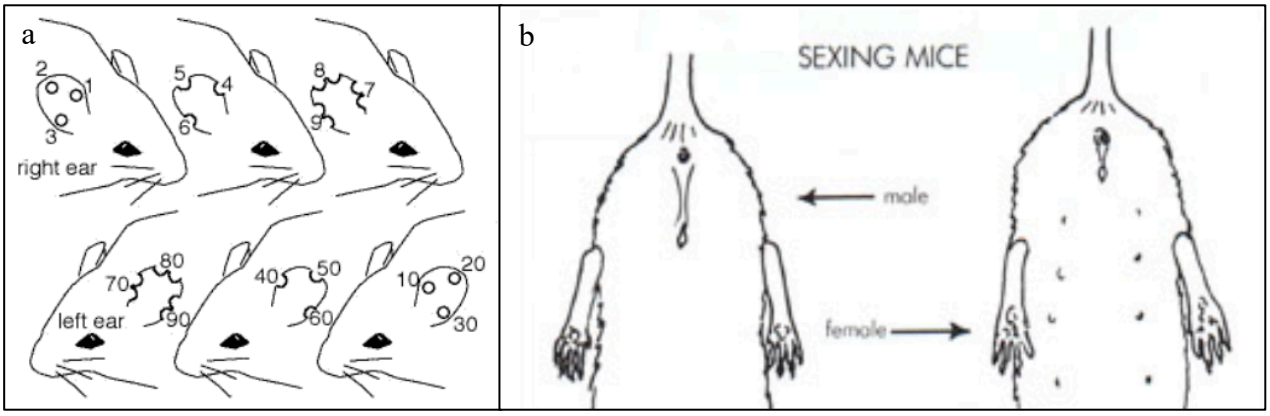

Figure 2.2. Mouse ear notching and sex identification chart. (a) Illustrated guide on marking mice for ear notch. (b) Identification of sex at weaning age.

The MPS IIIA SNP custom assay contained the following primers:

Forward primer: 5' ACG CCC TCT GCT CTG TCT TC 3'

Reverse primer: 5' GCG ATG GCA GTG TTG TTG TAT AC 3'

Wildtype probe: 5' VIC-TCA GCG GAT GAC GG-NFQ-MGB 3'

Mutant probe: 5' FAM-TCA GCG AAT GAC GG-NFQ-MGB 3'

The master mix was then subsequently vortexed to mix the reagents and briefly spun down to ensure no liquids were stuck in the cap. In each well of a 384 well plate, 9µL of master mix was aliquoted, followed by 1µL of the negative control into two of the wells. The plate was then transferred from the PCR hood to a lab bench, where 1µL of genomic DNA (1ng/µL) was added to each assigned well. Once all the samples were loaded with master mix and genomic DNA, the plate was then sealed with an adhesive film and briefly centrifuged for about 10 seconds in a plate centrifuge. The plate was then inserted into Quant Studio 7 Flex Real Time Polymerase Chain Reaction (PCR) System (ThermoFisher Scientific, MA, USA). The conditions used to amplify the targeted sequences are as follows:

60^{O}C	30 seconds	Pre-read stage
95^{O}C	10 minutes	Hold stage
95^{O}C	15 seconds	PCR amplification stage (x40 cycles)
60^{O}C	1 minute	PCR amplification stage (x40 cycles)
60^{O}C	30 seconds	Post-read stage

At the completion of the assay, the data were then exported and analysed with the Quant Studio Real-Time PCR software to determine the genotype of each sample.

2.2.3.4 Genotyping assay for *GFP* in GFP$^{+/-}$-MPS IIIA mice

Similarly, a Taqman custom SNP genotyping assay to differentiate the GFP transgene in GFP$^{+/-}$-MPS IIIA tissue was developed by Dr. Adeline Lau (Childhood Dementia Research Group,

Flinders University) (Figure 2.4, A). A PCR master mix was created in a sterile Eppendorf tube in a designated PCR cabinet. The master mix contained 1.5µL of sterile water, 2.5µL of 2x Taqman Genotyping Master Mix, and 0.25µL of 20x GFP-FAM SNP Custom Assay to make a working stock. Each component was multiplied by the number of samples being tested, which included two negative control samples (sterile water instead of genomic DNA), two positive controls (a hemizygous GFP single copy and a homozygous YFP double copy), and three spares to account for pipetting error.

The GFP-FAM SNP Custom Assay Working Stock contained the following primers;

Forward primer: 5' GCA CCA CCG GCA AGC T 3'

Reverse primer: 5' AGT CGT GCT GCT TCA TGT GGT 3'

GFP probe: 5' FAM-CCA CCC TGA CCT ACG-NFQ-MGB 3'

The master mix was then subsequently vortexed to mix the reagents and briefly spun down to ensure no liquids are stuck in the cap. In each well of a 384 well plate, 4.5µL of master mix was aliquoted, followed by 0.5µL of the negative control into two of the wells. The plate was then transferred from the PCR hood to a lab bench, where 0.5µL of genomic DNA (5ng/µL) was added to each assigned well.

Once all the samples had been loaded with master mix and genomic DNA, the plate was then sealed with an adhesive film and briefly centrifuged for about 10 seconds in a plate centrifuge. The plate was then inserted into Quant Studio 7 Flex Real Time Polymerase Chain Reaction (PCR) System (ThermoFisher Scientific, Waltham, MA, USA). The conditions used to amplify the targeted sequences are as follows:

60^{O}C	30 seconds	Pre-read stage
95^{O}C	10 minutes	Hold stage
95^{O}C	15 seconds	PCR amplification stage (x40 cycles)
60^{O}C	1 minute	PCR amplification stage (x40 cycles)
60^{O}C	30 seconds	Post-read stage

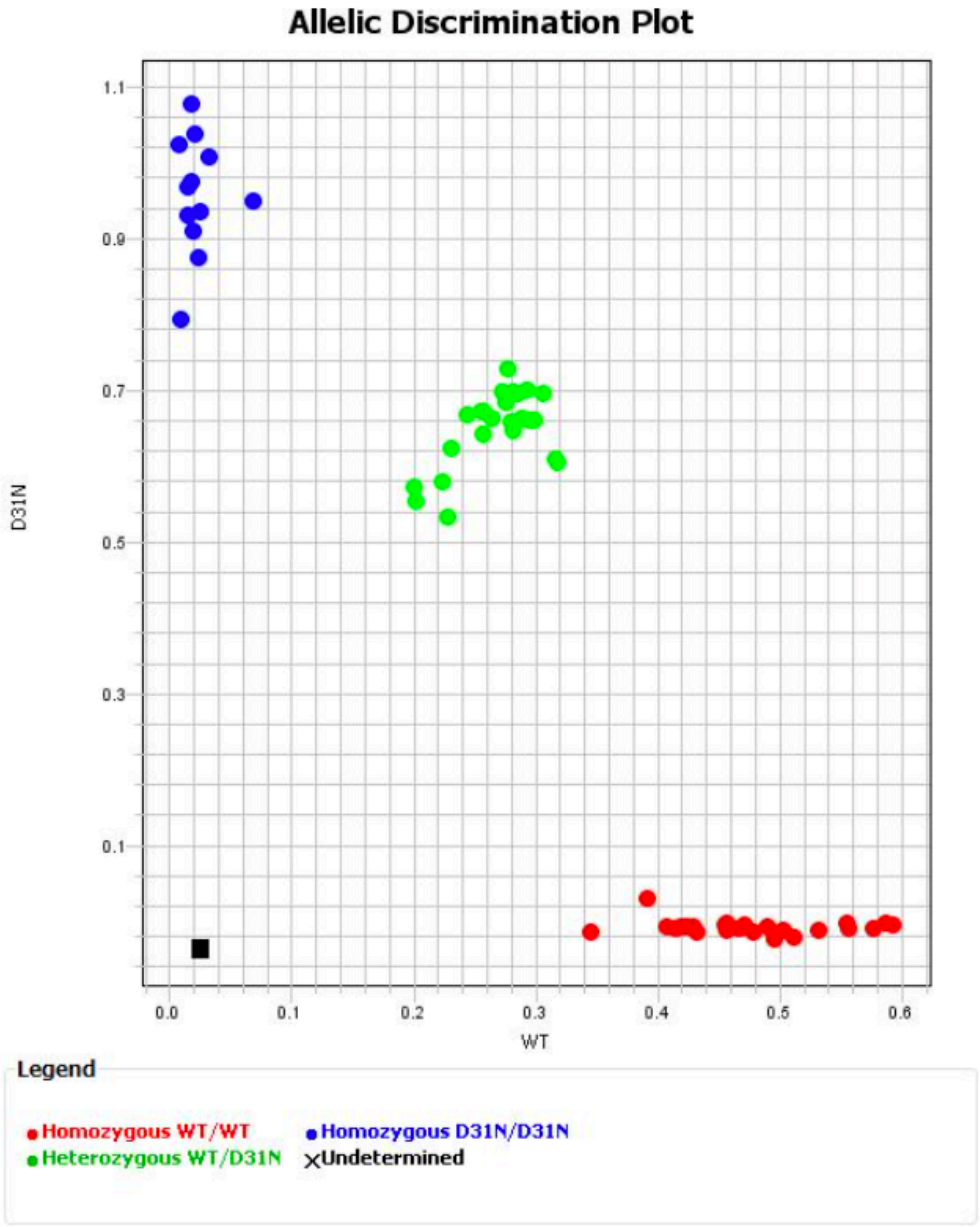

Figure 2.3. An example of an Allelic Discrimination Plot exported from QuantStudio Real-Time PCR Software. The software was used to analyse raw data from genotyping experiments created on a Life Technologies real-time PCR system.

At the completion of the assay, the data were then exported and analysed with the Quant Studio Real-Time PCR software to determine the GFP copy number expressed in each sample.

2.2.3.5 Genotyping assay for *GFP* copy number in GFP$^{+/-}$-MPS IIIA mice

To differentiate between hemizygous GFP single copy from homozygous GFP double copy, a Taqman custom SNP genotyping assay was developed by Dr. Adeline Lau (Childhood Dementia Research Group, Flinders University) (Figure 2.4, B). A PCR master mix was created in a sterile Eppendorf tube in a designated PCR cabinet. The master mix contained 2µL of sterile water, 5µL of 2x Taqman Genotyping Master Mix, 0.5µL of Taqman Copy Number Reference Assay, and 0.5µL of 20x GFP-FAM SNP Custom Assay as a working stock. Each component was multiplied by the number of samples being tested, which included two negative control samples (sterile water instead of genomic DNA), two positive controls (a hemizygous GFP single copy and a homozygous GFP double copy), and three spares for pipetting error.

The GFP-FAM SNP Custom Assay working stock contained the following primers:

Forward primer: 5’ GCA CCA CCG GCA AGC T 3’

Reverse primer: 5’ AGT CGT GCT GCT TCA TGT GGT 3’

GFP probe: 5’ FAM-CCA CCC TGA CCT ACG-NFQ-MGB 3’

The master mix was then subsequently vortexed to mix the reagents and briefly spun down to ensure no liquids are stuck in the cap. In each well of a 384 well plate, 8µL of master mix was aliquoted, followed by 2µL of the negative control into two of the wells. The plate was then transferred from the PCR hood to a lab bench, where 2µL of genomic DNA (5ng/µL) was added to each assigned well. Once all the samples had been loaded with master mix and genomic DNA, the plate was then sealed with an adhesive film and briefly centrifuged for about 10 seconds in a plate centrifuge. The plate was then inserted into Quant Studio 7 Flex Real Time Polymerase Chain Reaction (PCR) System (ThermoFisher Scientific, Waltham, MA, USA).

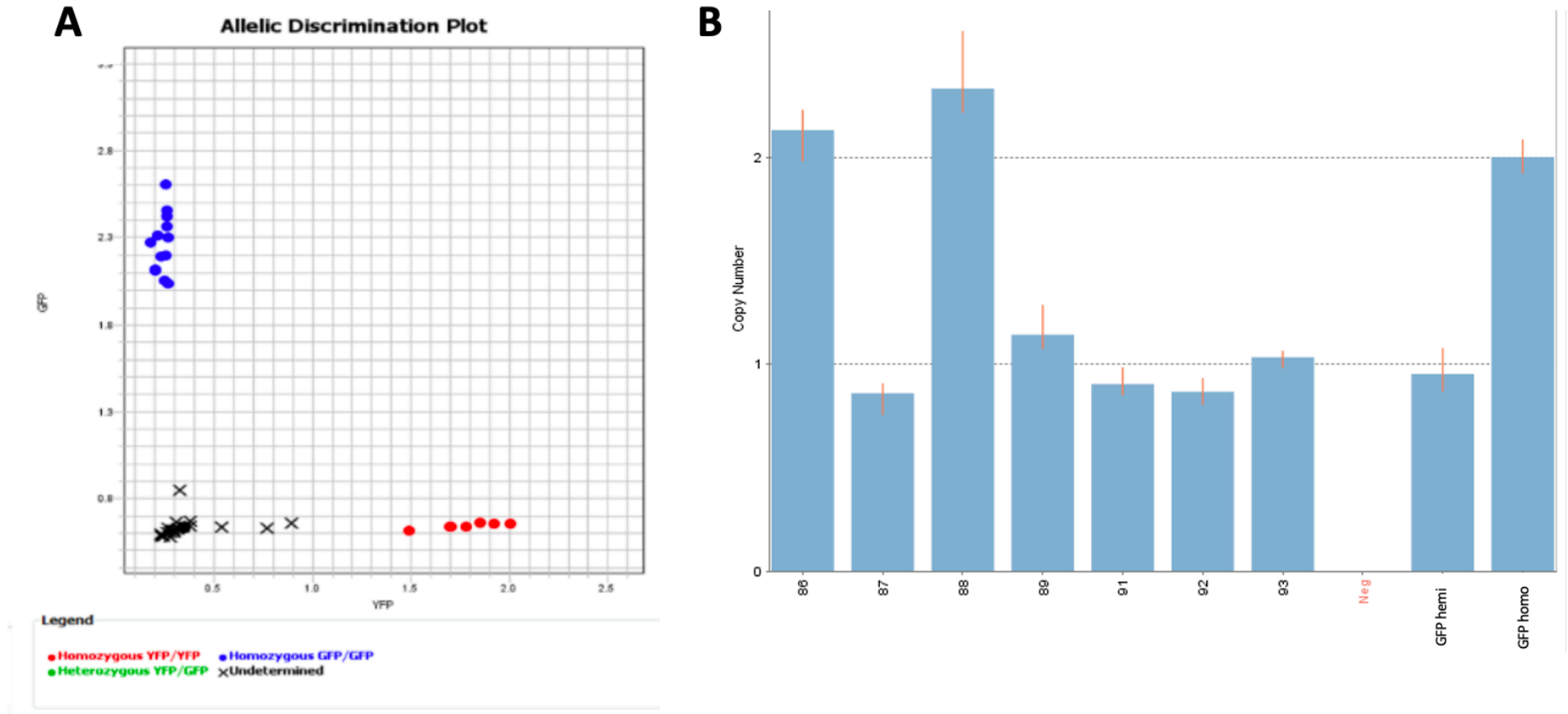

Figure 2.4 Genotyping assay output. (A) identification of positive expression of fluorescence protein in individual mice of GFP (blue), and non-fluorescence (black). (B) The CopyCaller histogram visualises the zygosity of individual mice expressing GFP with copy number presented on the y-axis, and individual samples listed on the x-axis.

The conditions used to amplify the targeted sequences were as follows:

60^{O}C	30 seconds	Pre-read stage
95^{O}C	10 minutes	Hold stage
95^{O}C	15 seconds	PCR amplification stage (x40 cycles)
60^{O}C	1 minute	PCR amplification stage (x40 cycles)
60^{O}C	30 seconds	Post-read stage

At the completion of the assay, the data were then exported and analysed with the Quant Studio Real-Time PCR and CopyCaller v2.1 software to determine the number of GFP copy number in each sample.

2.2.4 Perfusion and fixation

Four percent paraformaldehyde (PFA; w/v) in 1xPBS (pH 7.4) was prepared fresh each morning prior to tissue collection. The fixative was kept at 4ºC or on ice until use. Mice were then humanely euthanised via CO_2 asphyxiation (at a rate of 0.5-1 L/minute), with confirmation of death by a toe pinch. All mice were euthanised humanely in an isolated holding chamber to minimise stress to other animals. Each mouse was then transported to a fume hood, and individual limbs were pinned to a Styrofoam board to stabilise the mouse. Using surgical scissors, the abdominal cavity was cut opened, diaphragm and rib cage were cut away to expose the heart. Using a 23G butterfly needle, the left ventricle of the heart was subsequently punctured to allow the perfusion process to occur. The right auricle was then cut using a surgical scissor to allow for blood to escape and phosphate buffered saline (PBS) to perfuse throughout the body. Approximately 20 mL of PBS was perfused prior to fixation with 4% PFA to ensure blood was cleared from all the tissues in the body. A sample is sufficiently perfused with PBS when the colour of the liver changed from red-brown to pale-brown. Following PBS, approximately 20 mL of 4% PFA was perfused to ensure complete fixation of the tissue. This was confirmed by stiffening of the body, tail and limb twitching during fixation. Once perfusion with both PBS and 4% PFA were completed, the head was decapitated, and the brain swiftly removed. The brain tissue was immediately immersed in 4% PFA overnight at 4ºC and then transferred to 1xPBS for long-term storage at 4ºC.

2.2.5 Statistical Analysis

Most data were analysed using GraphPad Prism software (v9.4.1; GraphPad Prism Software Inc., San Diego, CA, USA), and data are presented as mean ± standard error of the mean (SEM), with statistical significance set as p-value < 0.05. All data were assessed for normality distribution and tests of statistical significance are two-sided. Perseus software (http://maxquant.net) and R (https://www.r-project.org/) were utilised for the analysis of proteomic data. Electrophysiological data were analysed with parametric unpaired t-tests. All hyperspectral data analyses were carried out using Matlab software R2017b (MathWorks, MA, USA). Data were either analysed by unpaired student t-test or Mann–Whitney test (due to data not following a normal distribution). All remaining data were analysed with analysis of variance (ANOVA), followed by *post-hoc* Bonferroni correction to adjust for multiple group comparisons.

Chapter 3: Quantitative Proteomic Analysis of the Motor Cortex in Wildtype and *Sgsh* Heterozygous Mice using Mass Spectrometry

3.1 Introduction

Proteomic analysis (or proteomics) refers to the identification and quantification of the complete complement of proteins from biological samples such as cells, tissues, organs, or biological fluids (reviewed in (204)). Proteomics enables the study of protein synthesis, structure, and function, which aids in identifying proteins that could be involved in human disease. Studies have shown that perturbation in protein production or post-translational modifications (PTMs) contributes to disease pathogenesis in several neurodegenerative diseases including Alzheimer's disease, Parkinson's disease, Amyotrophic lateral sclerosis and Huntington's disease (reviewed in (205)). Hence, proteomic analysis provides a powerful platform technology to inform patho-aetiology and identify temporospatial alterations in protein synthesis across the disease course.

Mass spectrometry (MS) has been developed as an important and widely used method to identify proteins and their isoforms, and measure changes in PTMs (206). Through MS based quantitative proteomics, identification of complete proteins or specific sets of peptides can be determined. Moreover, by incorporating multiple separations and pre-fractionation techniques, MS is able to identify the target protein or peptide with high yield and accuracy (207). For example, liquid chromatography (LC) or high-performance liquid chromatography (HPLC) facilitates the continuous separation of a large number of proteins from complex mixtures and when paired with MS, it forms LC-MS resulting in increased sensitivity and specificity (208, 209).

Moreover, clinical diseases (e.g., cancers and neurodegenerative diseases) in humans are complicated biological processes that are caused by perturbation in protein synthesis and signalling pathways (210). Changes to these signalling pathways results in dysregulation of cellular homeostasis and as a consequent, leading to various pathology to occur (210). Hence, uncovering the specific changes in protein signalling networks provides deeper insight into the molecular mechanism of disease pathogenesis as well as distinctive disease signature to the type or stage of the disease (211-214). Therefore, utilising proteomic analysis can offer insights into the function of proteins and its role in biological pathways.

While genetic associations between haploinsufficient lysosomal gene mutations and late-onset forms of neurodegeneration are well accepted, as described in Chapter 1, the underpinning mechanisms of disease remain poorly defined.

In this study, we employed an existing MPS IIIA mouse model that has been well-characterised to create *Sgsh* heterozygous (*Sgsh*$^{+/D31N}$) mouse model, which exhibits the D31N missense mutation in one copy of the *Sgsh* gene (215, 216). The aspartic acid residues D31 are believed to play an important role in the catalytic activity of the sulfatase family of enzymes, including sulfamidase (216). Specifically, these residues are involved in the coordination of a divalent metal ion such as zinc that is required for the enzyme to function properly (216). Hence, if the D31 residues are impaired or absent, the enzyme may not be able to coordinate the metal ion, leading to its reduced or absent catalytic activity (216). As a consequence, the activity of sulfamidase enzyme is impaired leading to the accumulation of undegraded heparan sulfate within the lysosomes and development of MPS IIIA. Further, the accumulation of heparan sulfate in MPS IIIA has been shown to contribute to cellular dysfunction, tissue damage, and development of neurological symptoms (217). Additionally, altered structure of pyramidal neurons in MPS IIIA mouse cortex has recently been reported supporting interrogation of this target neuronal population (218). The cerebral cortex was studied as it is commonly implicated in neurodegenerative diseases as well as in both mouse and human MPS IIIA due to its involvement in learning, memory formation, and motor function.

Overall, the aim of this study was to investigate the temporal impact of *Sgsh* D31N heterozygous mutation upon the mouse cortical proteome. Hence, the outcome from this experiment will be to expand our understanding on the impact of *Sgsh* heterozygous state in the brain as well as insight to potential disease mechanisms associated with neurodegeneration. To the best of our knowledge, this is the first proteomic study that has been conducted on carriers of any mutation in a lysosomal gene.

3.2 Methods

3.2.1 Sample Preparation

A discovery proteomics experiment was conducted on a set of female mouse motor cortex samples covering six time points (0, 3, 6, 12, 24, 48 weeks) and two genotypes (Wildtype and Heterozygous) with five biological replicates for each genotype and age (n = 5 mice/genotype/age; Figure 3.1). Mouse breeding and genotyping was undertaken by Meghan Douglass (Research Assistant, Childhood Dementia Research Group) as was sample collection. This resulted in 60 samples in total. Details of mouse husbandry and genotyping methods can be found in Chapter 2. All samples (motor cortex) were snap frozen in liquid nitrogen and stored at -80ºC until used. Samples were randomised and blinded prior to tissue homogenisation. Cortical tissue was homogenised in a mixture of methanol and Milli-Q water (MeOH:H_2O) in a ratio of 1:1 for 40 seconds with 30 seconds rest at 6500 revolutions per minute. Five-hundred µL of MeOH:H_2O was then added to each tube containing Precellys bead mill homogeniser, and the total protein concentration of each homogenate using the Bicinchoninic Acid Protein (BCA) method.

3.2.2 Bicinchoninic Acid (BCA) Protein Assay

To determine the total protein content in each cortical tissue, a BCA protein assay was conducted by Meghan Douglass, and performed according to the manufacturer's instructions. A standard curve was first prepared from bovine serum albumin which was then added in duplicate to a non-binding 96-well plate in addition to duplicates of each quality control brain homogenates from MPS IIIA mice. Each cortical homogenate was then diluted in Milli-Q water and was subsequently added to the plate in duplicates. Milli-Q water was added to each well to ensure an equal volume of 100µL for all wells. Subsequently, 100µL of micro-BCA working reagent was administered to each well to give a final volume of 200µL. The plate was then sealed and incubated for two hours at 37°C. After two hours, the plate was then read on the Spectramax iD5 (Molecular Devices, CA, USA); absorbance wavelength at 562nm. To determine the quality of a plate and sample, the calculations from the standard curve presented a coefficient of variation (% CV) and a sample was rejected if the CV value was greater than 10%.

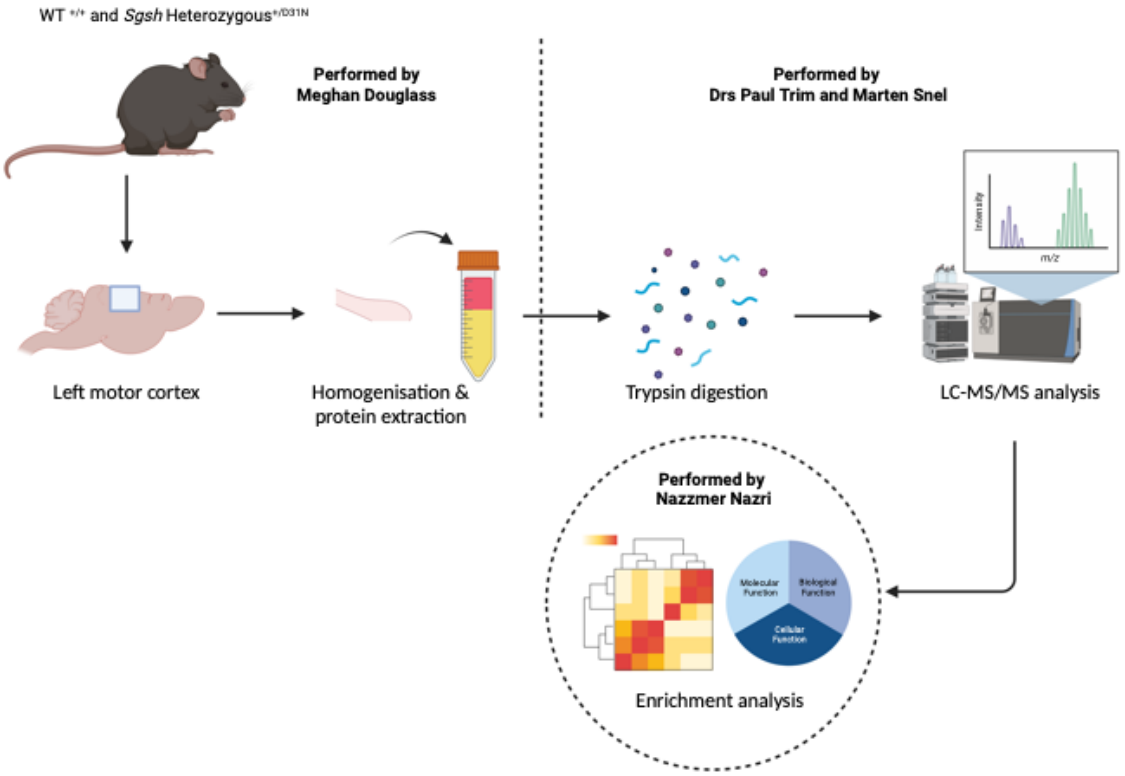

Figure 3.1. A schematic of the experiment to study the proteomic changes in the motor cortex of *Sgsh* heterozygous mice. Cortical tissues from *Sgsh* D31N heterozygous, and wildtype mice were dissected and snap frozen after perfusion with ice cold phosphate buffered saline. The cortical samples were then homogenised in a mixture of methanol and Milli-Q water with a ratio of 1:1. Cortical proteomes were obtained from LC-MS/MS analysis and proteins identified using Progenesis QI for Proteomic software. The full list of proteins was then statistically analysed using Perseus software (http://maxquant.net) and R to determine differentially abundant proteins and biological pathways that could provide insight to risk of neurological disease. (Diagram created by BioRender.com).

3.2.3 Liquid Chromatography-Mass Spectrometry (LC-MS)

The subsequent steps were conducted by Drs. Paul Trim and Marten Snel (SAHMRI). The experimenters were blinded to the samples genotype and age. The samples were randomised and processed by batch on the LC-MS as detailed in Table 3.1. All samples were prepared and loaded into the autosampler simultaneously, and one run was initiated, spanning a total of eight days. Unfortunately, the run was halted twice due to instrument breakdown, which required a restart. Prior to continuing the analysis, additional quality control samples were run to ensure that the performance of the LC-MS had not been affected.

The volume equivalent to 150 µg total protein was placed in a 2 mL Eppendorf tube made up to 350 µL with 50:50 MeOH:H_2O and the protein was precipitated for 1 hour at -20°C using 1600 µL ice cold acetone. Precipitated protein was pelleted by centrifugation (10 min at 12,000 x g) and the pellet was briefly air dried. The protein pellet was resuspended in 25mM ammonium bicarbonate solution, proteins were denatured using 0.05% Rapigest surfactant and incubated at 80°C for 10 mins. Subsequently, proteins were reduced and alkylated by incubating in 2.5 mM Dithiothreitol (DTT) for 10 mins at 60°C followed by incubation with 7.5 mM iodoacetamide (IA) for 30 min at room temperature. The proteins were then enzymatically digested using a 1:100 w/w ratio to trypsin and incubated overnight at 37°C. Following digestion, the samples were acidified with Trifluoroacetic acid (TFA) 0.5% to degrade the Rapigest surfactant followed by centrifugation. The supernatant was retained and transferred to total recovery sample vials and stored in the auto sampler of an Acquity M class UPLC prior to analysis. The final concentration of the sample was equivalent to 1.5 µg/µL starting protein concentration.

All data were acquired on a XEVO G2-XS QT of mass spectrometer equipped with an M-Class ACQUITY LC (both Waters Corp., Milford, MA). For each sample 7.5 µg of total protein was loaded onto a 100 mm x 0.3 mm high strength silica (HSS)-T3 analytical column (Waters™). Tryptic peptides were chromatographically separated using an 80-minute solvent gradient starting at 3% mobile phase B rising to 40% at a flowrate of 7 µL/min. Mobile phases used were A: 0.1% aqueous formic acid and B: 0.1% formic acid in acetonitrile. All solvents used were LC-MS grade. MS analysis was performed in SONAR mode. In this instrument mode a quadrupole window of 30 Da is scanned over 0.5 seconds from 400 Da to 900 Da.

Table 3.1. Samples from wildtype and *Sgsh* D31N heterozygous mice were randomised and analysed by batch on the LC-MS.

Batch 1			Batch 2			Batch 3		
ID number	**Genotype**	**Age (Week)**	**ID number**	**Genotype**	**Age (Week)**	**ID number**	**Genotype**	**Age (Week)**
147	Normal	3	55	Het	12	221	Normal	48
1.1	Het	0	174	Normal	48	125	Het	3
597	Het	24	146	Normal	3	158	Normal	6
144	Normal	3	565	Het	24	82	Het	6
218	Het	48	566	Normal	24	98	Normal	12
188	MPS	48	75	Het	6	216	Het	48
53	Het	12	111	Normal	12	81	Normal	6
84	Het	6	596	Het	24	567	Het	24
72	Het	6	219	Het	3	3.2	Normal	0
152	Het	3	253	Normal	48	217	Het	48
52	Het	12	623	Normal	24	3.1	Normal	0
145	Normal	3	1.5	Het	0	173	Normal	48
3.3	Normal	0	99	Normal	12	96	Normal	12
621	Normal	24	56	Het	12	149	Het	3
1.3	Het	0				85	Normal	6
97	Normal	12				54	Het	12
568	Het	24				181	Het	48
143	Normal	3				254	Normal	48
157	Normal	6				564	Normal	24
238	Het	6				182	Het	48
126	Het	3				622	Normal	24
3.5	Normal	0				83	Normal	6
1.4	Het	0						
3.4	Normal	0						
1.2	Het	0						

Scans alternate between low (5 V) and elevated (15 V to 40 V) collision energies (CE). At low CE predominantly peptide ions are observed and at elevated CE mostly peptide fragment ions are measured. Fragments were linked to peptides based on chromatographic retention time and quadrupole scan position. These two dimensions of separation provided excellent quality fragment ion data with low levels of interference from co-eluting peptides.

3.2.4 Progenesis QI Software for Proteomics Analysis

Following LC-MS analysis, the subsequent steps were conducted by Nazzmer Nazri. The raw data was subsequently processed in Progenesis QI software (Version 2.2) from Nonlinear Dynamics (Durham, NC), which enables the quantification and identification of proteins by using the advantages of label free analysis. The raw data were imported into Progenesis QI for alignment, peak picking, and annotation. Data processing parameters were set identically for all samples to make the results comparable. Default parameters for peak picking (automatic thresholds, minimum peak width = 0.5 minutes) and alignment were applied. Single ion compounds were removed to reduce noise and false discovery. Only ions with a charge state of two to seven were considered and included in the analysis. Peptide ions with a charge state of one and above eight were removed. Moreover, due to technical limitations (i.e., slow processor) with the analysis computer and the time taken to analyse the proteomic data, this necessitates batch analysis of the raw files. This was to prevent the Progenesis QI for Proteomics software from shutting down every couple of days and to allow the processor to work faster. Hence, “0 and 3”, “6 and 12”, and “24 and 48”, week timepoints were paired and analysed together. The total time taken for raw data analysis per group was approximately 3-4 days. Approximately 2000 proteins were identified and relatively quantified. The analysed data were then exported in a pdf (.pdf) format and bioinformatic analysis conducted in Perseus.

3.2.5 MaxQuant – Perseus

All data analysis steps were performed within a graphical workflow (Figure 3.2). Each tab is represented as an entity in the workflow and any matrix or network undergoing analysis becomes a new entity that gets connected to the original data in the workflow. The interactive workflow allows the user to keep track of all steps in the analysis and to navigate through data

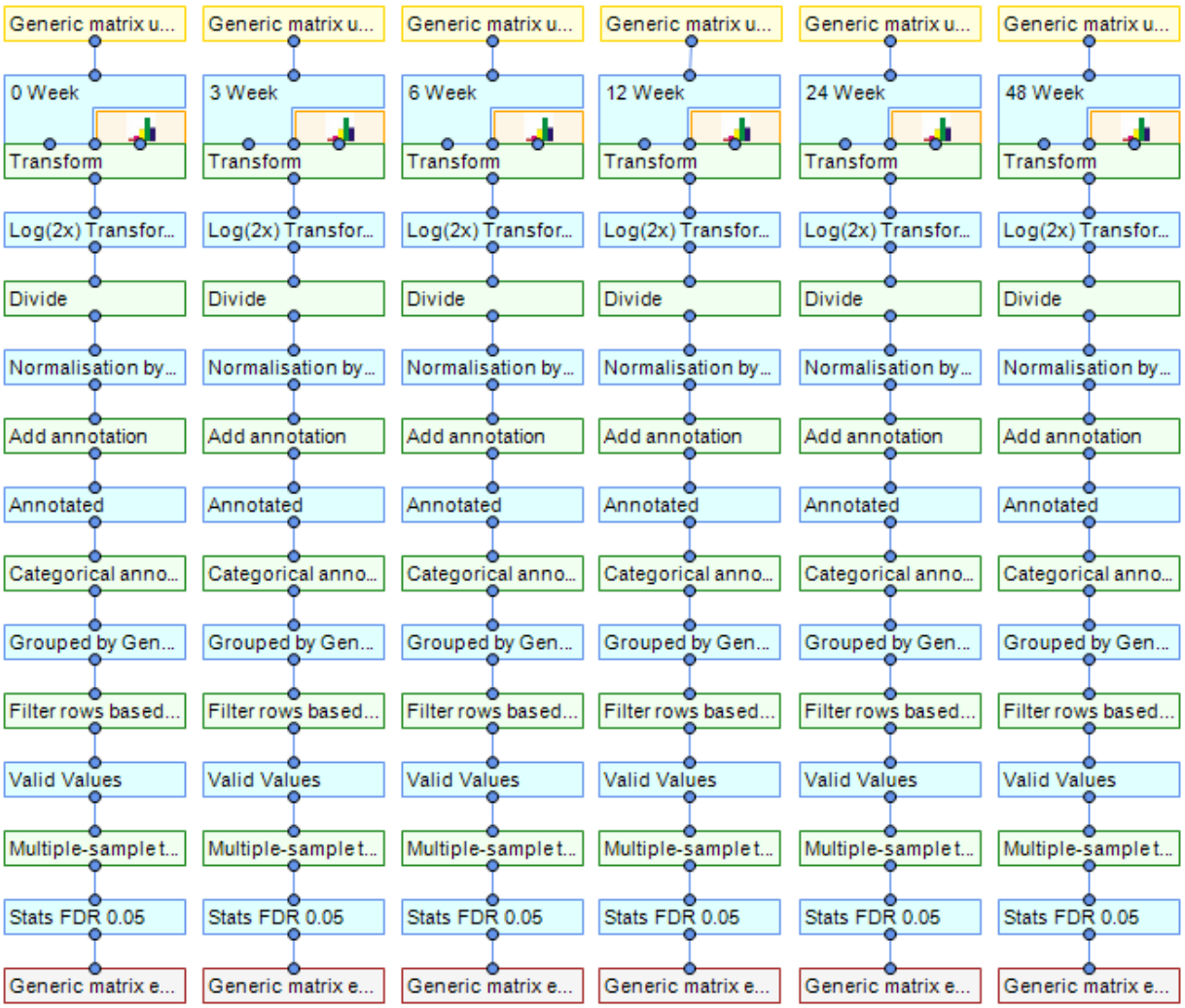

Figure 3.2. Graphical workflow of data processing in Perseus. The interactive workflow allows the user to keep track of all steps in the analysis and to navigate through data matrices and visualisation components. Briefly, the data was log transformed and normalised to sum intensity values. The protein profiles were then compared to the *mus musculus* database for accurate identification of protein IDs. Following this, proteins were individually filtered for each time point to exclude those with missing values. Finally, a multiple sample test correction was conducted using a permutation-based false discovery rate (FDR).

matrices and visualisation components. Every processing step in the analysis is transparent and reproducible.

Data from 0-, 3-, 6-, 12-, 24-, and 48-week-old mice tissues were imported into Perseus (Version 2.0.3) and downstream analysis was performed. Firstly, before the data can be used for subsequent analysis, the data was log transformed and normalised to sum intensity values. Protein profiles were then matched to *Mus musculus* annotation to allow for correct identification of protein ID. Independently for each timepoint, proteins were then filtered to only retain proteins that do not have a missing value. Finally, a multiple sample test correction using a permutation based false discovery rate (FDR) was conducted. This method enables reliable estimation of the percentage of proteins that are mistakenly indicated as differentially abundant. The FDR value was set as 0.05% with the minimum fold change (S_0) set as 0, aiming for a list of differentially abundant proteins in the datasets. These data were then exported for enrichment analysis in R and data visualisation in Prism9 (Version 9.4.1).

3.2.6 Gene-set Enrichment Analysis (GSEA)

Gene-set enrichment analysis (GSEA) was performed under the guidance of Dr. Karissa Barthelson (Childhood Dementia Research Group) using R (https://www.r-project.org/). The KEGG pathways for *Mus musculus* were obtained using the msigdbr package (219). GSEA was implemented using the fgsea R package (220). A directional ranking statistic for each protein in the dataset was compared between *Sgsh*$^{+/D31N}$ and *Sgsh*$^{+/+}$ mice in each timepoint. This was calculated from the differential abundance tests from Perseus by the following R code: sign(logFC)*-Log_{10}(1/p-value). A Kyoto Encyclopedia of Genes and Genomes (KEGG) pathway was considered significant if the Bonferroni-adjusted p-value was < 0.05. Although GSEA is a valuable method for identifying enriched pathways, one limitation of using GSEA is its inability to determine whether a pathway is upregulated or downregulated. Data visualisation was performed using Prism9 (version 9.4.1).

3.3 Results

A total of five biological replicates (one wildtype each from 0-, 3-, and 6- week, and one heterozygous each from 24- and 48- week timepoint) were omitted due to missing lock mass, reducing the number of biological replicates to four in some timepoints. Missing lock mass during MS measurement could potentially be due to instrument malfunction. The lock mass is important as it provides an internal mass standard and is used to adjust the mass calibration for the scan in MS so other mass peaks or peptides can be accurately measured.

3.3.1 Quantitative Proteomic Analysis of LC-MS/MS data

Differential proteomic analyses were carried out using a tandem mass tags-based (TMT) quantitative proteomic approach. The fractions were analysed by Liquid Chromatography-MS/MS individually which led to 14328 peptides from 2020 proteins identified at "0 and 3" weeks; 25131 peptides from 2533 proteins identified at "6 and 12" weeks; and 28470 peptides from 2221 proteins identified at "24 and 48" weeks. The number of peptides identified that contains more than one unique amino acid sequences was 1904, 1856, and 1920 in the "0 and 3", "6 and 12", and "24 and 48" weeks respectively. The acceptable range of missing values in proteomic studies is less than 10-20% (221), however, the number of missing values in this study was 6, 27 and 14 percent in "0 and 3", "6 and 12" and "24 and 48" week group respectively (Table 3.2). There are several reasons for missing values in proteomic studies, including the presence of low abundance proteins, which can make them difficult to detect and quantify. Further, missing values may occur along the analytical pipeline as a result of losses in protein digestion and separation, as well as failure in measurement during mass spectrometry acquisition (222). Typically, if a dataset has more than 20% missing values, imputation is recommended. However, imputation of data can introduce bias because it replaces the missing data with estimated values, which may not reflect the true underlying biological processes, leading to inaccurate conclusions (223). Therefore, no data imputation was conducted in this study. A summary of the number of proteins, unique peptide and peptide counts can be found in Table 3.2.

Of the proteins identified, many proteins were found to be significantly differentially abundant in the *Sgsh*$^{+/D31N}$ mouse motor cortex at all time-points after adjusting for multiple testing. A total of 141, 80, 31, 95, 196, and 204 proteins were dysregulated in the *Sgsh*$^{+/D31N}$ motor cortex at 0-, 3-, 6-, 12-, 24-, and 48- weeks respectively (P-value < 0.05). A volcano plot

representing the log2 fold change distribution of the dysregulated proteins in *Sgsh*$^{+/D31N}$ and *Sgsh*$^{+/D31N}$ mice is shown in Figure 3.3 (A-F). The *Sgsh*$^{+/D31N}$ motor cortex proteome datasets showed 88 upregulated proteins and 54 downregulated proteins at 0-week; 33 upregulated proteins and 47 downregulated proteins at 3-week; 20 upregulated proteins and 11 downregulated proteins at 6-week; 27 upregulated proteins and 68 downregulated proteins at 12-week; 108 upregulated proteins and 89 downregulated proteins at 24-week; and 113 upregulated proteins and 92 downregulated proteins at 48-week. However, no single proteins were found to be dysregulated (statistically significant) with age (or at all timepoints), though, we identified several proteins that appeared in two timepoints, specifically at 24- and/or 48 weeks. These proteins are primarily involved in synaptic transmissions (Table 3.3), oxidative phosphorylation (Table 3.4), proteasome (Table 3.5), and phosphatidylinositol signaling pathways (Table 3.6).

The complete list of these significant differentially abundant proteins in *Sgsh*$^{+/D31N}$ motor cortex can be found in Appendix 1-6 which includes the Swiss-Prot accession code, gene name, protein description, up- or down- regulation information, and p-value for each protein.

Table 3.2. Number of proteins, unique peptides, peptide counts, and missing values identified in all the timepoints between *Sgsh*$^{+/D31N}$ and *Sgsh*$^{+/+}$ mice.

Age (Week)	Number of proteins identified	Proteins with unique peptides >2	Proteins with unique peptides = 1	Peptide count from proteins identified	Percentage of missing values
0 and 3	2020	1510	394	14658	6
6 and 12	2533	1292	564	25131	27
24 and 48	2221	1548	372	28470	14

Table 3.3 Dysregulated proteins associated with synaptic transmission in *Sgsh* D31N heterozygous mouse motor cortex compared to wildtype.

Age (Week)	Swiss-Prot Code	Gene Name	Protein Description	Up- or down-regulation	P-Value
3	Q9Z2Q6	Septin5	Septin-5	↓	0.04288744
12, 48	Q9R1T4	Septin6	Septin-6	↓	0.0318925
12	P42208	Septin2	Septin-2	↓	0.00887606
24	Q8C650	Septin10	Septin-10	↓	0.03948762
24, 48	O55131	Septin7	Septin-7	↓	0.0486011
48	Q8C1B7	Septin11	Septin-11	↓	0.01439375

Table 3.4 Dysregulated proteins associated with oxidative phosphorylation in *Sgsh* D31N heterozygous mouse motor cortex compared to wildtype.

Age (Week)	Swiss-Prot Code	Gene Name	Protein Description	Up- or down-regulation	P-Value
0	Q9Z1G4	Atp6v0a1	V-type proton ATPase 116 kDa subunit a isoform 1	↓	0.03919869
0	Q9WTT4	Atp6v1g2	V-type proton ATPase subunit G 2	↓	0.012717
3	P62814	Atp6v1b2	V-type proton ATPase subunit B, brain isoform	↓	0.02428979
3	P03930	Mtatp8	ATP synthase protein 8	↓	0.03586702
3, 24	Q9CR51	Atp6v1g1	V-type proton ATPase subunit G 1	↓	0.01093093
48	Q9CQ69	Uqcrq	Cytochrome b-c1 complex subunit 8	↓	0.04189749
48	P00416	mt-Co3	Cytochrome c oxidase subunit 3	↓	0.04264393
0	P48771	Cox7a2	Cytochrome c oxidase subunit 7A2, mitochondrial	↑	0.0153701
0	Q9D593	Atp6v1e2	V-type proton ATPase subunit E 2	↑	0.04018359
0	Q9ERS2	Ndufa13	NADH dehydrogenase [ubiquinone] 1 alpha subcomplex subunit 13	↑	0.03813646
0	Q8BK30	Ndufv3	NADH dehydrogenase [ubiquinone] flavoprotein 3, mitochondrial	↑	0.02751149
0	Q9CR68	Uqcrfs1	Cytochrome b-c1 complex subunit 11;Cytochrome b-c1 complex subunit Rieske, mitochondrial	↑	0.03236579
48	Q9Z1W8	Atp12a	Potassium-transporting ATPase alpha chain 2	↑	0.02312761
48	P03888	Mtnd1	NADH-ubiquinone oxidoreductase chain 1	↑	0.03193311
48	P03921	Mtnd5	NADH-ubiquinone oxidoreductase chain 5	↑	0.00951583
48	Q9Z1P6	Ndufa7	NADH dehydrogenase [ubiquinone] 1 alpha subcomplex subunit 7	↑	0.00598861
48	Q91YT0	Ndufv1	NADH dehydrogenase [ubiquinone] flavoprotein 1, mitochondrial	↑	0.01521449

Table 3.5 Dysregulated proteins associated with ubiquitin proteasomal system in *Sgsh* D31N heterozygous mouse motor cortex compared to wildtype.

Age (Week)	Swiss-Prot Code	Gene Name	Protein Description	Up- or down-regulation	P-Value
0	Q9Z2U0	Psma7	Proteasome subunit alpha type-7	↓	0.0440709
0	Q9QUM9	Psma6	Proteasome subunit alpha type-6	↓	0.01166511
12	Q9R0P9	Uchl1	Ubiquitin carboxyl-terminal hydrolase isozyme L1	↓	0.04658101
24	Q9Z2U1	Psma5	Proteasome subunit alpha type-5	↓	0.01785697
24	Q9QUM9	Psma6	Proteasome subunit alpha type-6	↓	0.01166511
48	P49722	Psma2	Proteasome subunit alpha type-2	↓	0.02177988
48	O09061	Psmb1	Proteasome subunit beta type-1	↓	0.00696669
48	Q8BG32	Psmd11	26S proteasome non-ATPase regulatory subunit 11	↓	0.02235092
48	Q9QUM9	Psma6	Proteasome subunit alpha type-6	↓	0.01166511
0	O70435	Psma3	Proteasome subunit alpha type-3	↑	0.01124378
0	P68037	Ube2l3	Ubiquitin-conjugating enzyme E2 L3	↑	0.02083104
3	P14685	Psmd3	26S proteasome non-ATPase regulatory subunit 3	↑	0.04331233
3, 6	Q02053	Uba1	Ubiquitin-like modifier-activating enzyme 1	↑	0.00345846
24	Q9D6P8	Calml3	Calmodulin-like protein 3	↑	0.04235441

Table 3.6 Dysregulated proteins associated with phosphatidylinositol signalling pathways in *Sgsh* D31N heterozygous mouse motor cortex compared to wildtype.

Age (Week)	Swiss-Prot Code	Gene Name	Protein Description	Up- or down-regulation	P-Value
24	P53810	Pitpna	Phosphatidylinositol transfer protein alpha isoform	↓	0.0368898
24	Q8R071	Itpka	Inositol-trisphosphate 3-kinase A	↓	0.03052499
24	Q9Z1B3	Plcb1	1-phosphatidylinositol 4,5-bisphosphate phosphodiesterase beta-1	↓	0.03197723
48	Q9JI46	Nudt3	Diphosphoinositol polyphosphate phosphohydrolase 1	↓	0.02674355
48	Q91XU3	Pip4k2c	Phosphatidylinositol 5-phosphate 4-kinase type-2 gamma	↓	0.02851004
24	P70182	Pip5k1a	Phosphatidylinositol 4-phosphate 5-kinase type-1 alpha	↑	0.02984908
24	Q9EPW0	Inpp4a	Type I inositol 3,4-bisphosphate 4-phosphatase	↑	0.02195163
48	Q8VDP6	Cdipt	CDP-diacylglycerol--inositol 3-phosphatidyltransferase	↑	0.02475217
48	E9Q3L2	Pi4ka	Phosphatidylinositol 4-kinase alpha	↑	0.02483484

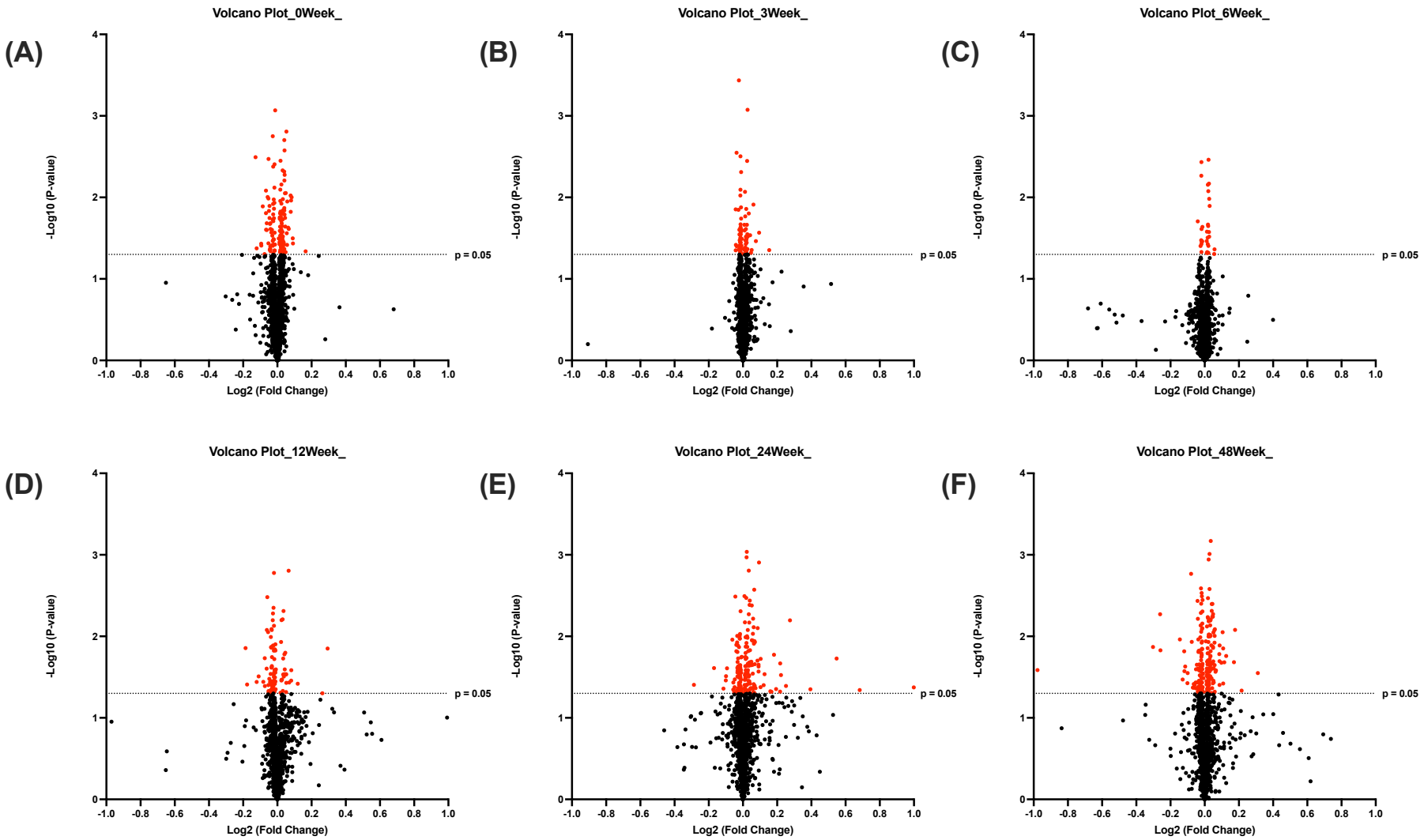
(A)
Volcano Plot_0Week_
(B)
Volcano Plot_3Week_
(C)
Volcano Plot_6Week_
(D)
Volcano Plot_12Week_
(E)
Volcano Plot_24Week_
(F)
Volcano Plot_48Week_
-Log10 (P-value)
Log2 (Fold Change)
p = 0.05

Figure 3.3. Volcano plot of dysregulated proteins identified in the motor cortex of *Sgsh*$^{+/D31N}$ mice at 0, 3, 6, 12, 24, and 48 weeks. (A) 0-week, (B) 3-week, (C) 6-week, (D) 12-week, (E) 24-week, (E) 48-week. The volcano plot displays the results of approximately 2000 proteins in all timepoints. The plot displays two variables on the x- and y- axes: the log2 fold change of each protein and its -log10 p-value. The log2 fold change is a measure of the difference in the production of proteins between two conditions, with positive values indicating an increase in production and negative values indicating a decrease. The -log10 p-value represents the statistical significance of the observed difference in protein synthesis. Proteins that are in red represents dysregulated proteins in *Sgsh*$^{+/D31N}$ mice compared to *Sgsh*$^{+/+}$ mice in each of the timepoints (p-value < 0.05).

3.3.2 Gene-Set Enrichment Analysis (GSEA) of Proteins in *Sgsh*$^{+/D31N}$ Mouse Motor Cortex

GSEA analysis is a powerful analytical method that is commonly performed to associate a disease phenotype to a group of proteins by using quantitative data (224). GSEA analysis ranked all the proteins identified from most up-regulated (enriched, more abundant) to most down-regulated (depletion, less abundant) to detect subtle changes to protein synthesis. The identified proteins are termed leading edge proteins in the GSEA analysis and are the ones which drive the enrichment (statistical significance) of the pathway. Hence, in order to further elucidate the biological implications of the differentially abundant proteins in the *Sgsh*$^{+/D31N}$ mice brain compared to *Sgsh*$^{+/+}$, the whole proteome profile containing the upregulated and downregulated proteins were analysed by GSEA enrichment pathway analysis.

GSEA enrichment pathway analysis revealed enrichment of all five KEGG pathways in the 0-week timepoint. The enriched KEGG pathways identified were Ribosome (p-value = $2.8x10^{-6}$), Long-Term Potentiation (p-value = $4.8x10^{4}$), Proteasome (p-value = 0.003), Spliceosome (p-value = 0.003), and Wnt signaling (p-value = 0.005) (Figure 3.5, A).

At 6-week timepoint, the enriched KEGG pathways identified were Alzheimer's disease (AD; p-value = 0.003), Parkinson's disease (p-value = 0.007), Epithelial cell signaling in helicobacter pylori infection (p-value = 0.008), Peroxisome (p-value = 0.01), and Valine leucine and isoleucine degradation (p-value = 0.013) (Figure 3.5, B). At 24-week timepoint, the enriched KEGG pathways detected were Phosphatidylinositol signaling system (p-value = 0.002), Hungtington's disease (p-value = 0.006), Inositol phosphate metabolism (p-value = 0.001), Oxidative phosphorylation (OxPhos; p-value = 0.013), and peroxisome (p-value = 0.023) (Figure 3.5, D).

At 48-week, only four KEGG pathways were enriched i.e, Glycolysis gluconeogenesis (p-value = 0.003), Pyruvate metabolism (p-value = 0.015), Phosphatidylinositol signaling system (p-value = 0.017), and Antigen processing and presentation (p-value = 0.044) (Figure 3.5, E).

Furthermore, no pathways were identified in the 3-week timepoint based on the GSEA analysis, indicating no subtle changes in pathway detected. Moreover, no pathways were found to be statically enriched at 12-week timepoint, however, the top five pathways identified were Cardiac muscle contraction, Oxidative phosphorylation, Arrhythmogenic right ventricular cardiomyopathy arvc, Parkinson's disease, and long-term depression (all p-value > 0.05)

(Figure 3.5, C). The pathways identified in these timepoints revealed neurodegenerative and cellular energy related pathways to be slightly altered with age.

Moreover, a group of proteins dysregulated in murine *Sgsh*$^{+/D31N}$ mouse motor cortex clustered as "Oxidative Phosphorylation" (Atp12a, Atp6v0a1, Atp6v1b2, Atp6v1e2, Atp6v1g1, Atp6v1g2, Cox7a2, mt-Atp8, mt-Co3, mt-Nd1, mt-Nd5, Ndufa13, Ndufa7, Ndufv1, Ndufv3, Uqcrfs1, Uqcrq), "Glycolysis Gluconeogensis" (Aldoa, Aldob, Aldoc, Dlat, Gpi1, Ldhb, Pfkm, Pfkp, Pklr), and "Pyruvate Metabolism" (Dlat, Ldhb, Pklr). These alterations correlate with the deregulation of the metabolic pathways.

Additionally, dysregulation of proteins involved in neurodegenerative pathways, including "Parkinson's Disease" (Camk2d, Gnai2, Gnai3, Maob, Septin5, Uba1, Ube2l3, Uchl1; Figure 3.4, B), "Alzheimer's Disease" (Akt2, Ctnnb1, Grin2a, Grin2b, Hsd17b10, Mapk1, Mapk3, Plcb1, Rtn4; Figure 3.4, B), and "Hungtinton's Disease" (Slc1a3; Figure 3.4, D) was identified. Furthermore, dysregulated proteins that overlapped in the neurodegenerative pathways was further classified into "Metabolic pathways" (Atp2a1, Atp5e, Cox7a2, Mcu, mt-Atp8, mt-Co3, mt-Nd1, mt-Nd4, mt-Nd5, Ndufa13, Ndufa3, Ndufa7, Ndufa9, Ndufv1, Ndufv3, Uqcrfs1, Uqcrq) and "Ubiquitin-proteasome system (UPS)" (Calml3, Psma2, Psma3, Psma5, Psma6, Psma7, Psmb1, Psmd11, Psmd3, Uba1, Ube213, Uchl1), further suggesting that metabolic pathways and impaired proteasome function may potentially contribute to the pathogenesis of neurodegeneration in *Sgsh* D31N heterozygotes.

Furthermore, dysregulated proteins in phosphatidylinositol signalling pathways (Pitpna, Pip5k1a, Inpp4a, Itpka, Plcb1, Cdipt, Pi4ka, Nudt3, Pip4k2c) were also detected at 24 and 48 weeks in murine *Sgsh*$^{+/D31N}$ mouse motor cortex. Perturbations in this pathway have been associated in several neurodegenerative diseases.

(A)

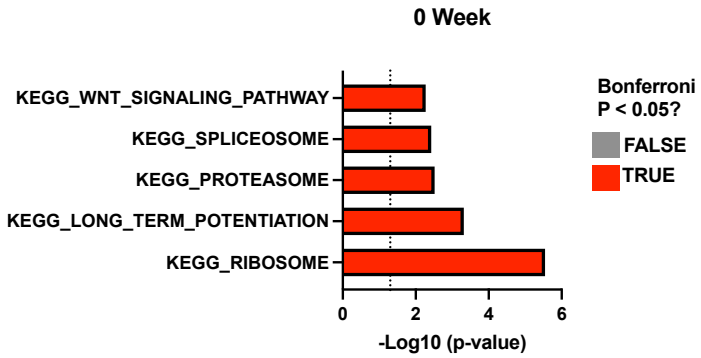
0 Week
KEGG_WNT_SIGNALING_PATHWAY
KEGG_SPLICEOSOME
KEGG_PROTEASOME
KEGG_LONG_TERM_POTENTIATION
KEGG_RIBOSOME
0
2
4
6
-Log10 (p-value)
Bonferroni
P < 0.05?
FALSE
TRUE

(B)

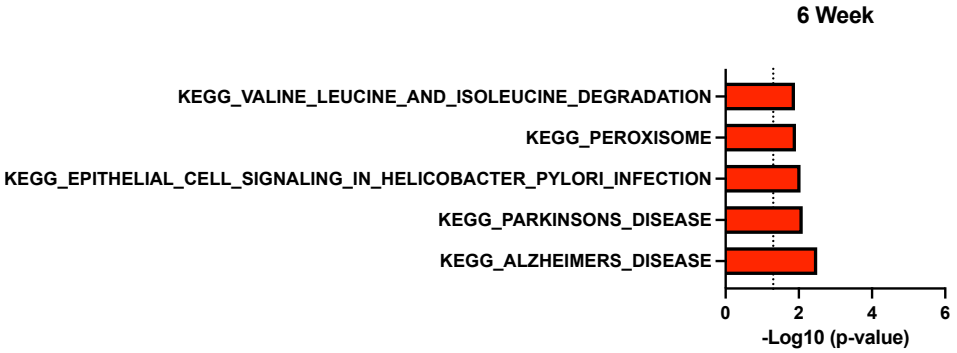
6 Week
KEGG_VALINE_LEUCINE_AND_ISOLEUCINE_DEGRADATION
KEGG_PEROXISOME
KEGG_EPITHELIAL_CELL_SIGNALING_IN_HELICOBACTER_PYLORI_INFECTION
KEGG_PARKINSONS_DISEASE
KEGG_ALZHEIMERS_DISEASE
0
2
4
6
-Log10 (p-value)

(C)

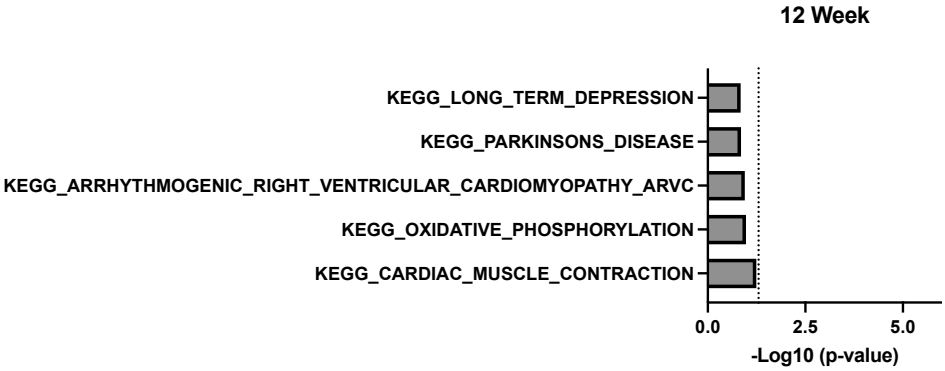
12 Week
KEGG_LONG_TERM_DEPRESSION
KEGG_PARKINSONS_DISEASE
KEGG_ARRHYTHMOGENIC_RIGHT_VENTRICULAR_CARDIOMYOPATHY_ARVC
KEGG_OXIDATIVE_PHOSPHORYLATION
KEGG_CARDIAC_MUSCLE_CONTRACTION
0.0
2.5
5.0
-Log10 (p-value)

(D)

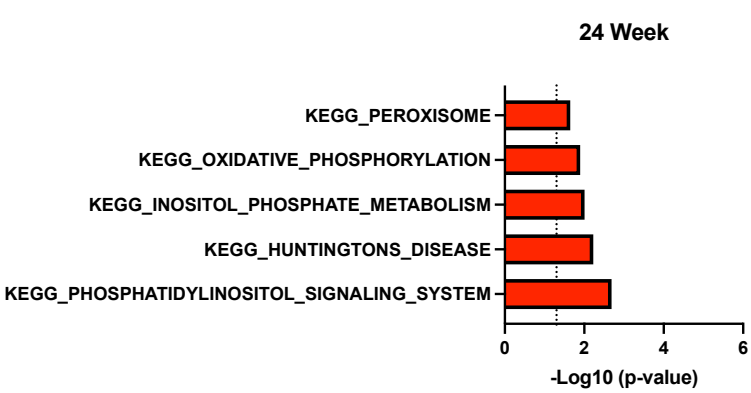
24 Week
KEGG_PEROXISOME
KEGG_OXIDATIVE_PHOSPHORYLATION
KEGG_INOSITOL_PHOSPHATE_METABOLISM
KEGG_HUNTINGTONS_DISEASE
KEGG_PHOSPHATIDYLINOSITOL_SIGNALING_SYSTEM
0
2
4
6
-Log10 (p-value)

(E)

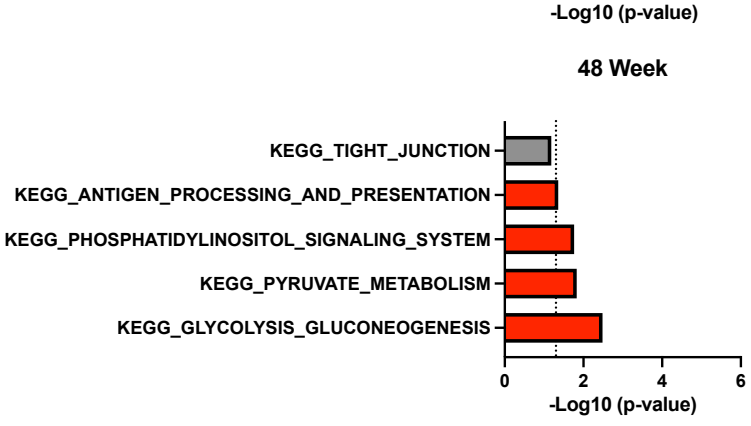
48 Week
KEGG_TIGHT_JUNCTION
KEGG_ANTIGEN_PROCESSING_AND_PRESENTATION
KEGG_PHOSPHATIDYLINOSITOL_SIGNALING_SYSTEM
KEGG_PYRUVATE_METABOLISM
KEGG_GLYCOLYSIS_GLUCONEOGENESIS
0
2
4
6
-Log10 (p-value)

Figure 3.4. Bar charts depicting the top five KEGG pathways identified in *Sgsh*$^{+/D31N}$ mice using GSEA enrichment analysis at different timepoints. (A) KEGG pathways identified at 0-week, (B) KEGG pathways identified at 6-week, (C) KEGG pathways identified at 12-week, (D) KEGG pathways identified at 24-week, and (E) KEGG pathways identified at 48-week. Significantly enriched KEGG pathways were identified at 0-, 6-, 24-, and 48- week timepoint in the motor cortex of *Sgsh*$^{+/D31N}$ mouse. No pathway was identified at 3-week timepoint, and no perturbation of enriched pathways was detected at 12-week based on GSEA analysis. A pathway is significantly enriched if Bonferroni p-value < 0.05.

3.4 Discussion

3.4.1 Proteomic Profiling of *Sgsh*$^{+/D31N}$ Mice Cerebral Cortex

To the best of our knowledge, this is the first proteomic study to be conducted on the brain of mice heterozygous for a mutation in a lysosomal enzyme/protein gene. At the single protein level, differentially abundant proteins in the *Sgsh*$^{+/D31N}$ mouse motor cortex was identified at all timepoints. In this study, 141, 80, 31, 95, 196, and 204 proteins were dysregulated in the *Sgsh*$^{+/D31N}$ mouse motor cortex compared to *Sgsh*$^{+/+}$ at 0-, 3-, 6-, 12-, 24-, and 48- weeks respectively, indicative of changes in protein synthesis with age and between genotypes. Moreover, the differentially abundant proteins detected in this study reflected perturbation of neurodegenerative and energy-related pathways.

3.4.2 Dysregulated proteins involved in metabolic pathways

Oxidative phosphorylation (OxPhos) is a key metabolic pathway that is responsible for the production of ATP (225), which is the primary source of energy for cellular processes. ATP is required for neuronal plasticity, axonal transport, synaptic transmission, and for neurotransmitter release (226). Hence, dysregulation of this pathway or ATP production in *Sgsh* D31N heterozygotes can have significant consequences for cellular metabolism due to production of reactive oxygen species, which can lead to oxidative stress and cell death if not tightly regulated (225). Impairment of OxPhos have been reported in MPS IIIC where a decrease in mitochondrial respiratory chain complex II and IV activities was observed, though, no studies was reported in the heterozygous state (227, 228). Moreover, studies in *Gba1*$^{+/-}$ mice carrying L444P mutations also showed perturbed mitochondrial function, disrupted mitophagy and increased oxidative stress in the central nervous system (109, 110). Together with the current findings, these studies suggest that heterozygous mutations in lysosomal genes may contribute to mitochondrial dysfunction and the severity is dependent on the types of mutations inherited.

Glycolysis and pyruvate metabolism are two closely interconnected metabolic pathways that play a crucial role in cellular metabolism. Glycolysis is a process whereby glucose is broken down into pyruvate, to generate ATP and NADH, whilst Pyruvate metabolism is the process by which pyruvate is converted to acetyl-CoA, lactate and alanine

(229). Dysfunction of these pathways has been implicated in a variety of diseases, including cancer, and neurological disorders (230). Metabolic dysfunction has been recognized as one of the early abnormalities observed in the brain during preclinical stage of dementia such as AD (231, 232). Evidence has shown that in the development of AD, pathophysiological changes can occur up to 20-30 years earlier before clinical symptoms manifest (232, 233). Further, the cerebral metabolic rate of glucose (CMRglc) has been utilised as an indicator of neuronal and synaptic activity (234). From these studies, nearly all clinical AD symptoms are accompanied by reduction of CMRglc with significantly decreased glucose metabolism observed in AD-vulnerable brain regions, such as hippocampus, and the cerebral cortex (232, 235, 236). Related to the present work, proteomic studies in 8-month-old MPS IIIB knockout mouse brain also revealed perturbation in metabolic pathways such as ATP synthesis, Glycolysis, Pyruvate metabolism and Tricarboxylic acid cycle (237). Whilst similar studies have not been published for MPS IIIA brain, similar outcomes would be predicted.

3.4.3 Dysregulated proteins involved in neurodegenerative pathways

Endoplasmic reticulum-associated degradation (ERAD) is a cellular process that targets misfolded and damaged proteins for degradation (190). This process primarily occurs in the endoplasmic reticulum, where the misfolded proteins are recognised and retro-translocated across the endoplasmic reticulum membrane, and then delivered to the ubiquitin-proteasome system (UPS), which resides in the cytoplasm for degradation (190, 238, 239). Dysfunction of ERAD can indirectly affect the function of the UPS, resulting in accumulation of misfolded proteins, which can form aggregates and inclusion bodies that can disrupt cellular function and, ultimately development of neurodegenerative disease (191). One of the altered neurodegenerative pathways observed in *Sgsh*$^{+/D31N}$ mouse motor cortex was the UPS where Calml3, Psma2, Psma3, Psma5, Psma6, Psma7, Psmb1, Psmd11, Psmd3, Uba1, Ube2l3, and Uchl1proteins were found to be perturbed. The UPS mediates the degradation of short-lived proteins and the removal of damaged soluble proteins in eukaryotic cells (240). UPS dysfunction has been shown to induce pathological changes and abnormal brain function in several neurodegenerative diseases such as AD and PD (reviewed in (241)). Further, studies in lysosomal storage disorders (LSD model system) have shown that reduced expression of lysosomal genes leads to impairment of the UPS system (242). This is evident where ubiquitin C-terminal hydrolase (Uchl1) is inhibited in several LSD patients fibroblasts (such as

galactosialidodosis, GM_1 gangliosidosis, Morquio syndrome type A and B, sialidosis, sialic acid storage disease and Gaucher's disease I and II) and in brains of Sandhoff mice (242). Ubiquitinylated protein accumulation has been reported in tissues of mice and humans affected with LSD (243-249). This is the first study to document changes in the UPS in heterozygotes for a lysosomal gene mutation and further research is required to verify the findings, and to determine the cause and ramification of this pathway changes.

Moreover, phosphatidylinositol signalling pathway (PIP) was also found to be altered at 24 and 48 weeks in *Sgsh*$^{+/D31N}$ mouse motor cortex. PIP play a crucial role in the regulation of several cellular processes including endosomal trafficking, autophagy, vesicle trafficking, and neurotransmitter release in the central nervous system (250-253). Dysfunction in PIP have been implicated in several neurodegenerative diseases, including Alzheimer's disease and Parkinson's disease (254). Perturbation in PIP, specifically in phosphatidylinositol-3-phosphate (PI3P) in selected brain regions results in neuronal degeneration and reactive gliosis, which appear to be associated with impaired endosomal system (255, 256). Supporting this, deficiency of PI3P have been reported in the brains of human and murine models of Alzheimer's disease, which exhibit related impairments in the endosomal-lysosomal network (257, 258). Additionally, phosphatidylinositol 4,5-biphosphate (PI(4,5)P2) also plays a crucial role in neurotransmitter receptor signal transduction and maintaining the normal function of numerous ion channels within the central nervous system (reviewed in (259, 260)). Decreased PI(4,5)P2 levels in the brain have been linked to impairments in synaptic transmission (261). Thus, future studies are required to verify if changes in PIP proteins observed at 24 and 48 weeks in *Sgsh* D31N heterozygous mouse could potentially contribute to the risk of neurodegeneration at a later stage.

Notably, Guanosine-5'-triphosphate binding proteins such as Septin 2, Septin 5, Septin 6, Septin 7, Septin 10, and Septin 11 have also been found to be aberrantly produced in *Sgsh*$^{+/D31N}$ mouse motor cortex. Specifically, Septin 7 was found to be dysregulated at 24- and 48- weeks. Septins play a crucial role in axonal transport, vesicular trafficking, regulation of dendritic spine morphology, and neurotransmitter release (262-264). The dysregulation of Septins is associated with several neurological diseases, including Alzheimer's disease, Parkinson's disease, frontotemporal dementia and Down syndrome (265-267). Studies in frontal cortex of frontotemporal dementia patients reported increased levels of truncated forms of Septin 11, which were localised to the superficial cortical layers with the presence of fibrillar thread-like structures of Septin 11 (268). Brain proteome studies in the temporal neocortex of Alzheimer's disease patients also revealed that Septin 2 and 3 levels were increased while

Septin 5 levels was decreased compared to normal patients (269). Changes in the production of Septins may lead to altered synaptic function, therefore studies investigating dendritic spine density and morphology as well as neuronal function are warranted to explore this outcome more in *Sgsh*$^{+/D31N}$ cerebral cortex.

3.4.4 Limitation, and Future Directions

There are some limitations to the study conducted. The number of proteins identified with one unique peptide was approximately 500 proteins in each timepoint and these were included in the proteomic analyses. Identification of proteins with single peptide can make it difficult to confirm the identity of the protein as many proteins have similar or identical peptides, and a single peptide may be shared by multiple proteins (270). Factors that can contribute to proteins with single peptide could be due to sample processing, such as fewer tryptic peptide digestion, or masking by highly abundant proteins in the sample (271). For future studies, to avoid the number of false positive in protein identification, more than two unique peptide within a single protein is recommended (272).

Whilst the number of missing values in this study was within the acceptable range (Table 3.2), this resulted in lower number of proteins identified especially in the "6 and 12" week timepoint where the missing values was at 27 percent. The presence of missing values in quantitative proteomic greatly reduces the completeness of the data and may have contributed to the failure to identify significant changes in KEGG pathways at 12 weeks. A few reasons for this might be related to how the data was analysed, which involved analysing distinct timepoint data in batches rather than all at once. This may have an influence on protein identification since some proteins may not be detected at different timepoints and was not analysed together in the database. Further, as previously described, analysis of all the raw data in a single run was unable to be conducted due to technical issues with the analytics computer. Hence, this can result in missing values for proteins that are present at low levels and are difficult to detect. Moreover, this could potentially contribute to the variable differences observed in each timepoints, thus, there is a need to replicate this study with a refined method with single batch analyses.

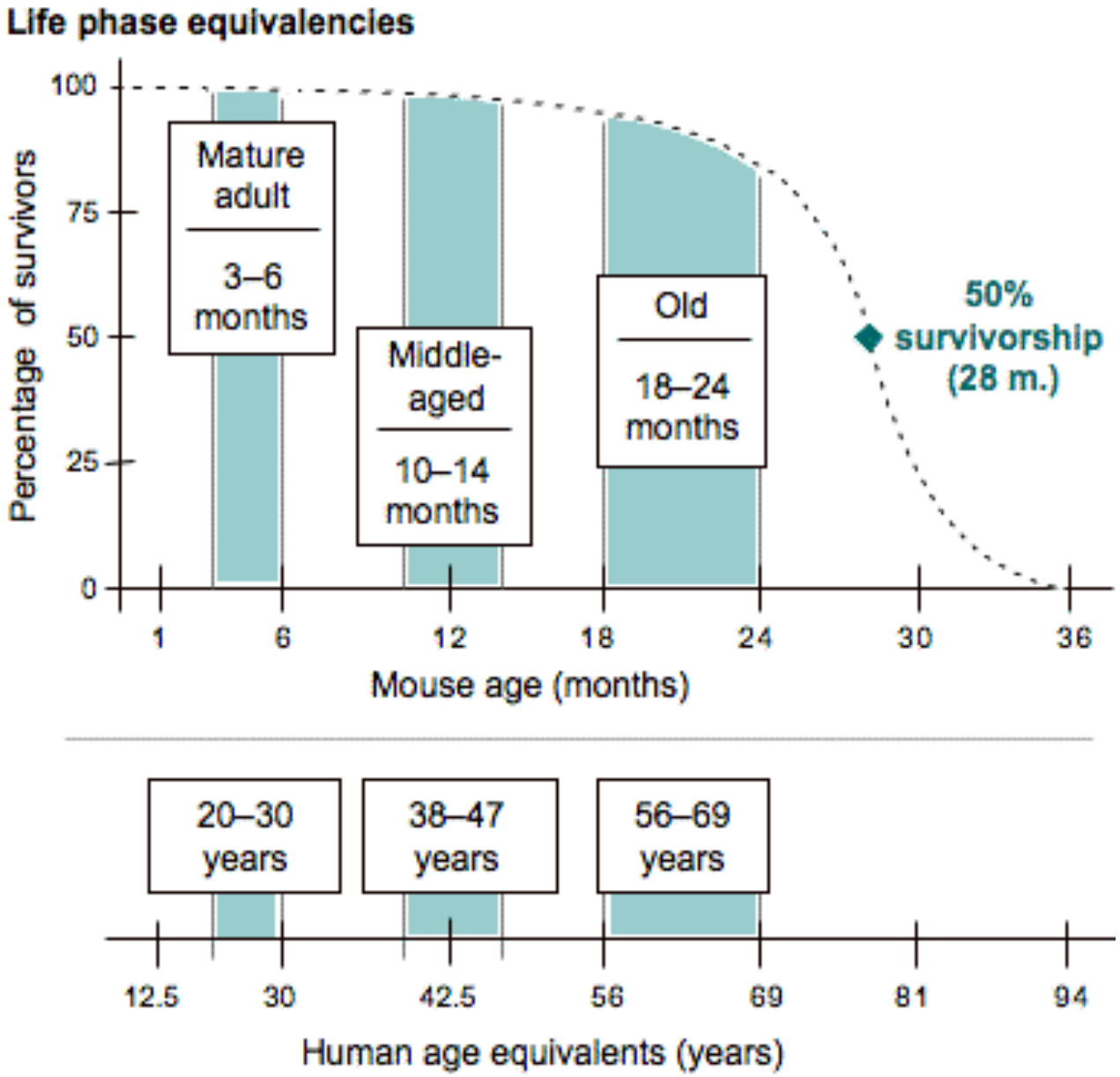

Figure 3.5. Age comparison between C57BL/6 mice to human. Mature adult mice range in age from 3-6 months whilst the human equivalent ranges from 20-30 years. After 6 months of age, the middle-aged mice range from 10-14 months and the human equivalent age ranges from 38-47 years. Mice age ranging from 18-24 months correlate with human age ranging from 56-69 years and are define as "old" where changes in biomarkers of senescence in all animals are often observed. Diagram obtained from (273).

Furthermore, female mice were selected because group housing is possible, and this allowed mice to be housed in groups for up to 11 months. Male mice in contrast, require single housing due to fighting, and various studies have reported alterations in hormones, neurochemistry and metabolism in single-housed mice compared to those in social housing, which can impact proteomic outcomes (274, 275). However, given that neurological diseases affect both males and females, future studies should include both genders for a comprehensive insight to potential disease mechanisms. Supporting this, a proteomic study conducted by Distler and colleagues revealed that male and female mice at 6 weeks old had differentially abundant synaptic proteins (276). The study reported 71 proteins in the hippocampus showed differences in their protein levels between sexes; 28 proteins in the cerebellum was dysregulated in females compared to males and the proteins identified were mainly involved in the neuron projection and synaptic transmission (276). Moreover, in some neurological diseases, the incidence is higher in men compared to women, for example, autism and Parkinson's disease is more common in men whereas depression and multiple sclerosis is more common in women (reviewed in (277)), but this is not the case in autosomal recessive lysosomal storage disorders.

Further, given that the mice age used in this experiment were relatively middle aged (based on Figure 3.5), future proteomic studies using older cohorts of animals might be able to provide further insight to potential mechanism of neurological dysfunction in *Sgsh*$^{+/D31N}$ mice. Additionally, validation studies using western blot to confirm the upregulated and downregulated proteins involved in the perturbed pathways will need to be determined. Hence, future studies utilising western blot or peptide sequencing is required to validate the results.

3.5 Conclusion

In conclusion, this study is the first to provide biological insight to changes in the cortical proteome of *Sgsh*$^{+/D31N}$ mice. Proteomic evaluation of *Sgsh*$^{+/D31N}$ mouse motor cortex revealed perturbations in protein synthesis at all timepoints. When compared with wildtype samples, several pathways were identified based on the GSEA enrichment pathway analysis, with the majority of dysregulated proteins were located in metabolic and neurodegenerative pathways. Predicated upon these findings, assays to interrogate neuronal morphology and electrophysiological function as well as mitochondrial health are presented in Chapter 4 and 5 respectively.

Chapter 4: Structure and function of cortical neurons in *Sgsh* heterozygous mice carrying a D31N mutation

4.1 Introduction

In Chapter 3, dysregulated proteins were identified at all timepoints in *Sgsh*$^{+/D31N}$ mouse motor cortex compared to age-matched wildtype. Septin proteins were found to be reduced at 24- and 48- weeks in the *Sgsh*$^{+/D31N}$ mouse motor cortex (Chapter 3, Table 3.3). Septins are a group of guanosine-5'-triphosphate binding proteins that have been associated with the regulation of dendritic spine morphology and neurotransmitter release (262-264). Specifically, Septin 7 (Sept7) has been shown to play a crucial role in mediating dendritic spine maturation and formation as well as synapse maturation (264, 278). Studies have shown that depletion of Sept7 results in decreased branching of axons and dendrites both *in vitro* and *in vivo* (279, 280). Additionally, an increase in immature filopodia spines on neuronal cell was observed when Sept7 was knocked down (264).

Moreover, a recent study conducted on *Sgsh*$^{+/D31N}$ mice reported mild impairment in motor function and subtle changes in motor cortex pyramidal neuron morphology in 84-week-old mice (161). Further, previous studies in MPS III mice reported perturbation in the architecture and dendritic spine densities of pyramidal neurons as well alteration in synaptic function (218, 281, 282). Studies in MPS IIIA mice showed an overall reduction in dendritic spine densities on cortical pyramidal neurons from 6 weeks, with fewer stubby and mature mushroom spine subtypes seen at 20-weeks of age (Figure 4.1) (218). Similarly, dendritic spine deficiencies in basal and apical dendrites of cortical pyramidal neurons were also observed in MPS IIIB mice at 20-weeks of age (218). Both studies suggest that perturbation in dendritic spine morphology could contribute to the loss of neuronal function associated with MPS III. Supporting this, Para et al. observed reduced levels of synaptic proteins (i.e., vGLUT1 and/or PSD-95) in cultured hippocampal and cortical pyramidal neurons in the MPS IIIC mouse model leading to disruption of synaptic transmission (281, 282). Alterations in excitatory and inhibitory postsynaptic currents was also evident in both MPS IIIA and MPS IIIC (218, 281), further suggesting that the functional and structural changes observed could contribute to the onset of neurological symptoms and cognitive decline seen in MPS III individuals.

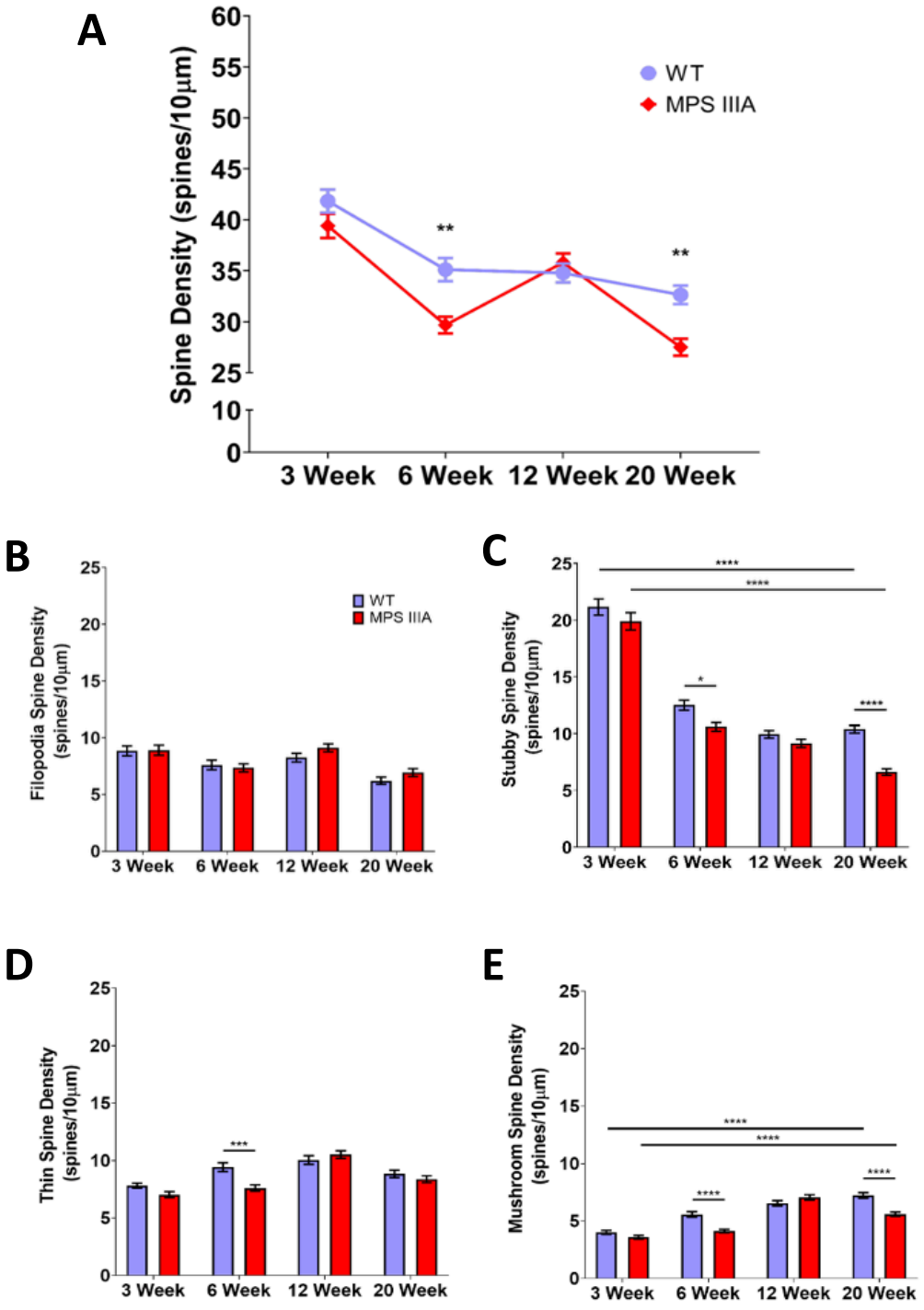

Figure 4.1. Dendritic spine densities in MPS IIIA layer 5 motor cortical neurons. (A) total dendritic spine densities of wildtype and MPS IIIA mice at 3-, 6-, 12- and 20 weeks of age. Spine subtypes were classified into (B) filopodia, (C) stubby, (D) thin, and (E) mushroom. n = 6 dendritic segments per cell; six animals per genotype per age. **p<0.01, ***p<0.001, ****p<0001; Two-way ANOVA. Data are mean ± SEM. Unpublished data obtained from (218).

Analysis in this study focused on the structure of layer 5 pyramidal neurons within the motor cortex. Other than Douglass et al. paper, no other studies in heterozygous mutations in lysosomal genes have looked at this brain region despite motor deficits being observed in animal models of heterozygous mutations in *Gba1*, *Npc1*, and *Hexb* (100, 127, 178). Pyramidal neurons are the most abundant excitatory neurons in the brain regions they inhabit and make up two-thirds of all neurons in the cerebral cortex (283). Due to their role in numerous cognitive processes and motor function, pyramidal neurons have been extensively studied in neurodegenerative diseases. To evaluate dendritic spine density in the $Sgsh^{+/D31N}$ mouse motor cortex, a transgenic MPS IIIA mouse model expressing green fluorescence protein (GFP) was created. This study utilised a reporter strain (*thy1-GFP-M* line) in which layer 5 pyramidal neurons in the cerebral cortex are GFP positive (202). Heterozygous GFP mice were generated by pairing congenic MPS IIIA mice from an in-house colony to produce the $Sgsh^{+/D31N\ EGFP}$ mouse model. Additionally, field potentials (measurement of electrical signals generated by the collective activity of neurons) from neural cultures established from $Sgsh^{+/D31N}$ and $Sgsh^{+/+}$ mouse brain were also evaluated to determine the functional impacts of carriers of *Sgsh* mutations status.

4.2 Methods

4.2.1 Dendritic spine visualisation and quantification

In order to assess dendritic spine density in both *Sgsh*$^{+/+\ EGFP}$ and *Sgsh*$^{+/D31N\ EGFP}$ mice, *Sgsh*$^{+/D31N\ EGFP}$ mice were bred and aged to 24 weeks. Genotyping and tissue collection procedures can be found in Chapter 2. For dendritic spine characterisation, a total of 5 mice per genotype was obtained, however, initial analyses were carried out on three animals per genotype, three dendritic segments per cell and 3 cells per animal given the cost of confocal microscopy.

4.2.1.1 Brain section preparation

Cryomold were placed on a levelled and flat work bench. Six-percent low melt agarose (w/v) in 1xPBS was gently heated in a microwave until dissolved, and mixed. The agarose solution was let to cool to approximately 37^{o}C. Using a brain slicer and a GEM blade, a sagittal cut was made from the midline of the mouse brain, separating the left and right hemisphere. The left hemisphere was used in this study. The brain tissue was then carefully transferred into a cryomold, positioned to the centre of the cryomold, and the cooled agarose was carefully poured until the tissue was covered, taking care to prevent formation of air bubbles around the tissue as this will impact sectioning. Once the agarose cooled and hardened, the embedded tissue was then removed from the cryomold and stored in 1xPBS at 4^{o}C in the dark until further use. Embedded tissue was then fixed to the mounting stage of a Leica VT1000S vibratome (Leica, Germany) with superglue. Once the glue set, the stage was then secured inside the chamber and chilled 1xPBS was poured into the chamber until the tissue was completely submerged. The vibrating blade was programmed to move at a slow speed (1 mm/s) and high frequency (100Hz) to maintain the integrity of the sample. The razor blade was gently and carefully wiped with acetone to remove oil residue, and washed with 100% ethanol to sterilised, then dried before securing in the blade holder. Brain tissues were sectioned at a thickness of 100μm and mounted onto slides with freshly made CUBIC reagent-1 (mixture of urea (25% final concentration), Quadrol (25% final concentration), Triton X-100 (15% final concentration) and Milli-Q water), and cover slipped. Slides were then sealed with nail polish and left to dry overnight in a fume hood before storing at 4^{o}C in the dark.

4.2.1.2 Dendritic spine imaging and data analysis

Mouse genotypes and age data were not available to the candidate during tissue imaging and analysis. Slides were labelled 1-18 by a person not included in the study. To produce a high-resolution image of dendritic spines suitable for evaluating density and morphology, the brain sections were imaged on an Olympus FV3000 spectral confocal microscope (Olympus, Tokyo, Japan) with an oil immersion 63x objective lens and a 2x digital zoom, which increases the magnification to 100x objective. To reduce background noise and improve image quality, the confocal microscopy settings were set: line averaging was accumulated three times, and a final frame average of two times per image acquisition was done. GFP in the tissue sections was excited with a laser tuned to 488nm excitation at 5% power and 510-550nm emission range. Images of three dendritic segments with a length of 40µm were taken from the secondary apical dendrite (Figure 4.2) per neuron, 3 neurons per mouse, and 3 mice per genotype were evaluated. This is a total of 54 images. Z-stacks acquired by confocal microscopy were then exported and processed with Imaris software (Version 9.7.2; Bitplane, Belfast, UK).

4.2.1.3 Automated image analysis using Imaris

In Imaris surpass mode, a new filament was created using the auto path mode and a region of interest (ROI) was selected. To select an ROI, we identified a dendritic region of 40µm that branch off from the primary apical dendrite (Figure 4.2). A minimum dendrite end diameter was measured for each dendrite and a single dendrite starting point was assigned. Automatic thresholds were used for assigning dendrite end points. To trace spines, the maximum length and minimum spine end diameter were set at 3µm and 0.2µm, respectively. This allowed detection of dendritic spine in the subsequent steps. Automatic thresholds were used for generating spine seed points and surface rendering. After generating the trace, a filter was applied to ensure all dendritic protrusions less than 3µm in length were assigned a spine. For each subsequent image processed, an ROI was selected, a dendrite starting point was assigned, and then the trace was built by clicking finish. Spines were classified as stubby, mushroom, thin, and filopodia, using the “Classify Spines” plug-in by MATLAB (vR2017b; MathWorks, MA, USA), following the parameters set in Imaris as shown in Table 4.1. The data were subsequently exported for unblinding and statistical analysis.

4.2.2 Multielectrode Array analysis

4.2.2.1 Newborn pups and primary cortical neuron cultures

24-well MEA plates were sterilised with 70% ethanol and air dried overnight in a laminar flow hood with UV light on for 30 minutes. The plate was subsequently coated with 1mg/ml Poly-L-Lysine and incubated overnight at 37^{o}C. Following day, the substrate was removed from each well and the surface was washed five times with sterile water to remove any unbound PLL. The washed MEA plate was then stored in the 37^{o}C tissue culture incubator with sterile water in each well until further use. Neural feed (Neurobasal-A media, 2% B27 supplement, 1% penicillin/streptomycin (PenStrep)) and Neural seed (neural feed media and 10% FBS) media was made prior to culturing neurons. Neural feed media was subsequently made fresh each week.

A total of 12 newborn mice (postnatal day 0) per genotype were transported via road from CMPH, Flinders University to the University of Adelaide and kept warm during transport. Upon arrival, the pups were humanely euthanised by decapitation with sharp scissors in an animal procedure room, and the brain was removed and put in a 10mL sterile tube containing cold neurobasal-A media and transported to the lab on ice for dissection.

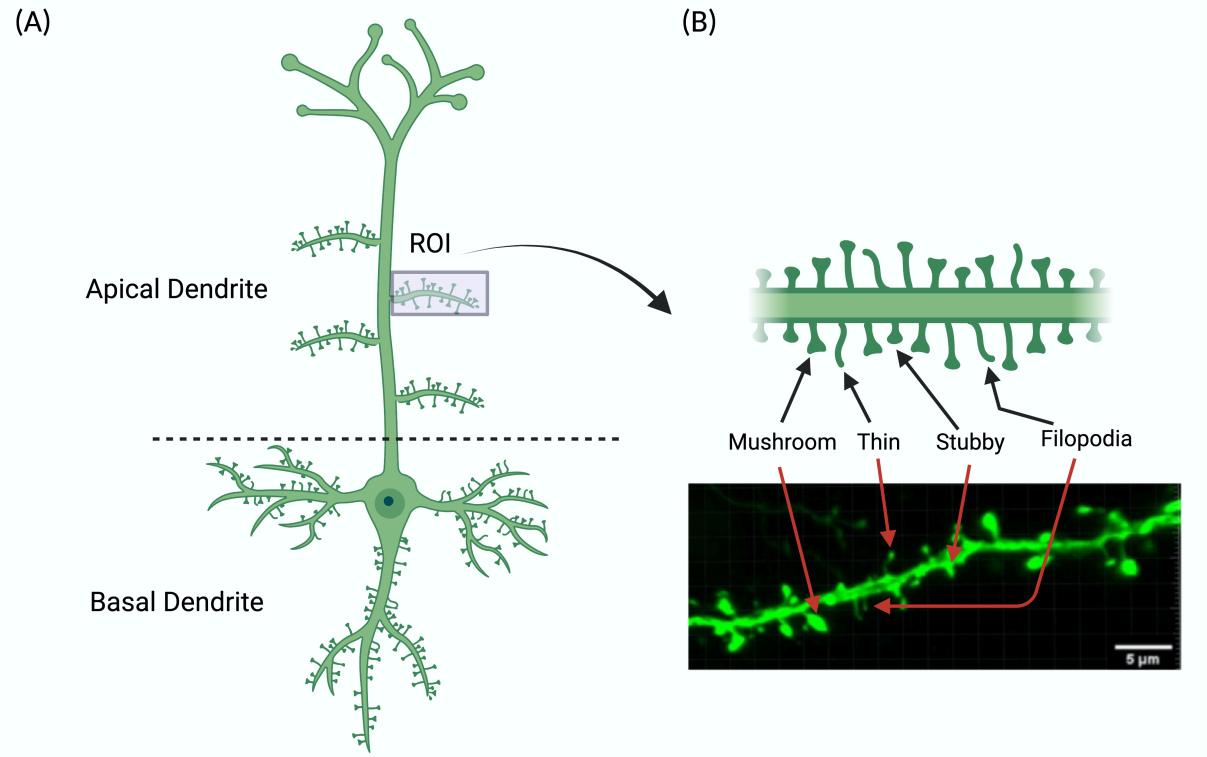

Figure 4.2. Dendritic spine morphologies in the apical dendrite of layer 5 pyramidal neuron. (A) illustrated GFP positive layer 5 pyramidal neurons in the motor cortex and the ROI chosen for dendritic spine assessment, i.e., 40µm from the branch point as shown above, (B) dendritic spine morphology from filopodia to long thin (immature), and stubby to mushroom spines (mature). Scale bar is 5µm.

Table 4.1 Spine classifications parameters from Imaris

Type	Parameters
Long-thin spines	Mean_width(neck)*2 < length(spine) AND mean_width(neck) <= max_width(head)
Mushroom spines	Mean_width(head) > mean_width(neck)
Stubby spines	Length(spine) < 1
Filopodia	Mean_width(head) <= mean_width(neck)

The cerebral cortex was dissected using a pair of super fine forceps in dissection media (made up with 500mL of HBSS, 3.5ml of 1M HEPES buffer, 1% Glutamax and 1% PenStrep, filter sterilised and pH to 7.3). Dissected cerebral cortex was subsequently enzymatically dissociated in trypsin solution containing 1mg/mL DNase I for 25mins, swirled briefly every 5 minutes. The trypsin was then neutralised by the addition of neural seed media supplemented with 10% FBS. The tissue was dissociated mechanically with a fire polished glass pipette and the media was supplemented with 1 mg/mL DNase I. The dissociated cortical cells were then plated at a density of $1x10^6$ cells per well in a 24-well MEA plate. The cells were cultured in neural seed media overnight and the media was changed to neural feed media the following morning.

4.2.2.2 Primary cortical neuron cultures treated with rotenone

Select cultures were also exposed to rotenone, a potent inhibitor of complex I of the mitochondrial respiratory chain. In this instance, a media change to neural feed was supplemented with 0.1nM rotenone made up fresh every three days. The rotenone was resuspended in 100% DMSO and the final concentration of DMSO in media was less than 0.005%. Plates were incubated in a humidified incubator at 37^{o}C supplied with 5% CO_2. The media was changed (50% changed; half old media and half new media) every 3 days thereafter.

4.2.2.2 Dataset and recording set-up

Field potential recordings were conducted at 7, 14, 21, and 28 days *in vitro* (DIV). For the rotenone study, electrophysiological recordings were done at 6, 12, 18, and 24 DIV. Prior to recording, each of the 24-well plate was removed from the incubator and placed in a humidified chamber at 37^{o}C under a constant flow of humidified gas (5% CO_2, 20% O_2, 75% N_2).

Recordings began after 30 minutes of equilibration when the baseline neuronal activity was first recorded. Neuronal activity was measured with the MEA2100-Lite head stage (Multi Channel Systems, Germany) connected to the MCS-IFB interface board (Multi Channel Systems, Germany). Neuronal activities were recorded with a sampling rate of 20 kHz. After filtering, a threshold of ± six standard deviation was set for each channel to reduce the likelihood of detecting spurious/noise signals and activity exceeding this threshold was counted as a spike (284). The settings for burst detection in each electrode were a minimum of four

spikes with a maximum inter-spike interval of 0.l second, which meant that if four or more spikes occurred within a 0.1 second window, they were considered to be part of the same burst. Moreover, the settings were chosen based on previous studies where a minimum of four spikes are considered a burst (284). The burst duration, number of spikes per burst, and interburst interval were analysed by multi-well analyser software (Version 2.0.2.0, Multi-Channel Systems, Germany). The recording lasted for 10 minutes, and all devices were maintained at 37^{o}C under a constant flow of humidified gas to preserve the microenvironment.

To ensure consistency when acquiring MEA data, all the experimental procedures, including the animal dissection, cell counting and plating, medium changes, and recordings were conducted by the same individual. All data were analysed and visualised using Prism9 (Version 9.4.1).

4.3 Results

4.3.1 No change in dendritic spine density or morphology in *Sgsh*$^{+/D31N\ EGFP}$ motor cortical pyramidal neurons

Examples of the images collected of a dendrite segment displaying dendritic spines on the secondary apical dendrite are shown in Figure 4.2 A, B. There were no changes in total dendritic spine density in *Sgsh*$^{+/D31N\ EGFP}$ cortical pyramidal neurons compared to *Sgsh*$^{+/+\ EGFP}$ at 24-weeks of age (Figure 4.3, C). Moreover, classification of dendritic spines based on synaptic maturity (spine subtypes) also showed no statistical significance in spine maturation (Figure 4.3, D).

4.3.2 Electrophysiological recording of primary cortical neural cultures derived from *Sgsh*$^{+/D31N}$ mice show altered network burst activity

Electrophysiological recordings of primary mouse cortical neurons were conducted on the multi-electrode array (MEA) platform to establish if *Sgsh*$^{+/D31N}$ cortical neural cultures have altered neuronal activity. Cortical tissue was harvested from euthanised newborn mice pups (day 0) and neuronal activity was recorded after 7, 14, 21, and 28 DIV. Using the MEA system, the field potentials of mouse primary cortical neurons cultured in 24-well plates were detected (Figure 4.3, A-B). Studies have shown that primary mouse neural cultures start exhibiting global synchronised bursts around 19-20 days of culture and that neural cultures start to deteriorate in day 28 (285). Hence, only day 7, 14, and 21 data are presented.

In Figure 4.4 A and B, representative images show the neural cultures on MEA plates. Bursting activity in *Sgsh*$^{+/D31N}$ primary cortical neural cultures showed reduced spike count (Figure 4.4, C), burst duration (Figure 4.4, E), and interburst interval (Figure 4.4, J) at day 7 *in vitro* compared with *Sgsh*$^{+/+}$ mouse cultures. No changes in burst count, burst spike count, spike rate, burst spike rate, and percentage of spikes in burst were observed at this point. However, in day 14 *in vitro*, a reduced burst count (Figure 4.4, D), and burst duration (Figure 4.4, E) were evident in *Sgsh*$^{+/D31N}$ neurons with no changes observed in the other electrophysiological parameters assessed. Interestingly, no changes in burst activity were found at day 21 *in vitro* except for burst spike rate activity (Figure 4.4, H).

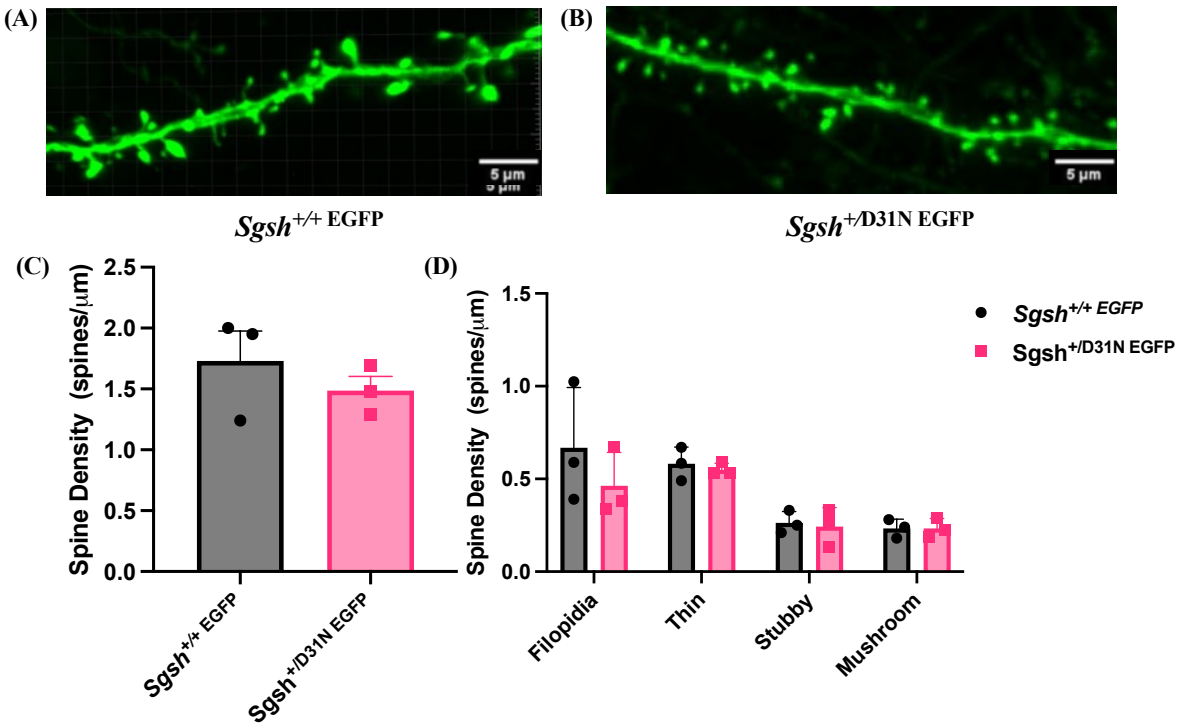

Figure 4.3. Dendritic spine densities on layer 5 pyramidal neurons in the cerebral motor cortex of *Sgsh*$^{+/+\ EGFP}$ and *Sgsh*$^{+/D31N\ EGFP}$ mice aged 24-weeks. (A-B) representative images of dendritic spines in *Sgsh*$^{+/+\ EGFP}$ (A) and *Sgsh*$^{+/D31N\ EGFP}$ pyramidal neuron (B). (C) overall dendritic spine density, (D) Densities of dendritic spine sub-types. Overall, there were no evident changes of spine density in the layer 5 pyramidal neurons between genotypes. n = 3 dendritic segments per cell; 3 cells per animal; 3 animals per genotype. Data are represented as mean ± SEM and individual animal averages are shown as dots. Experimenter was blinded to genotype.

The parameters assessed in Figure 4.5 reflect the neuronal activity of the whole network and measure the degree of synchronisation and coordination between neurons in the network. In Figure 4.5, significant changes in network burst activity were evident in *Sgsh*$^{+/D31N}$ neural cultures at day 21 *in vitro*. A decrease in network burst count (Figure 4.5, A), network burst spike rate (Figure 4.5, D), and percentage spikes in network burst (Figure 4.5, E) was observed. Moreover, the average time between events, which consists of episodes of relatively fast spiking separated by periods of quiescence is decreased as shown in network interburst interval (Figure 4.5, F), indicating altered and delayed neuronal activity in *Sgsh*$^{+/D31N}$ neurons compared to *Sgsh*$^{+/+}$ neurons. However, no changes in network burst duration (Figure 4.5, B) and network burst spike count (Figure 4.5, C) was observed at day 21. Changes in network burst duration and network burst spike count were only apparent at day 7 and day 14 (Figure 4.5, B-C) with *Sgsh*$^{+/D31N}$ recorded to have reduced neuronal activity with shorter burst activity compared to *Sgsh*$^{+/+}$ neural cultures.

4.3.3 Electrophysiological recording on rotenone-treated primary cortical neural cultures in *Sgsh*$^{+/D31N}$ and *Sgsh*$^{+/+}$ mice

To test the multiple hit hypothesis theory, which states that the development of clinical diseases or disorders results from a combination of multiple genetic or environmental factors (286), an environmental insult was introduced into the neural cultures to determine if rotenone would hasten (or worsen) the dysfunction of neuronal network activity in *Sgsh*$^{+/D31N}$ neurons. Rotenone is a commonly used pesticide in the agriculture industry (287-289) and exposure to it has been linked to the development of PD due to its potent inhibition of complex I of the mitochondrial respiratory chain (290). In this study, primary cortical neural cultures established from *Sgsh*$^{+/D31N}$ and *Sgsh*$^{+/+}$ mouse pups (day 0) were treated with 0.1nM rotenone concentration and controls received an equivalent volume of diluent (DMSO). The concentration of rotenone supplied was determined based on previous studies (14, 291, 292) where 0.1nM rotenone have been shown to have the least impact on cell viability as well as apoptosis. Electrophysiological recording of the neurons was undertaken every 6 days up to 24 days *in vitro* (Figure 4.6). However, due to loss of neuronal activity in day 24 cultures, only day 6, day 12, and day 18 cultures were analysed.

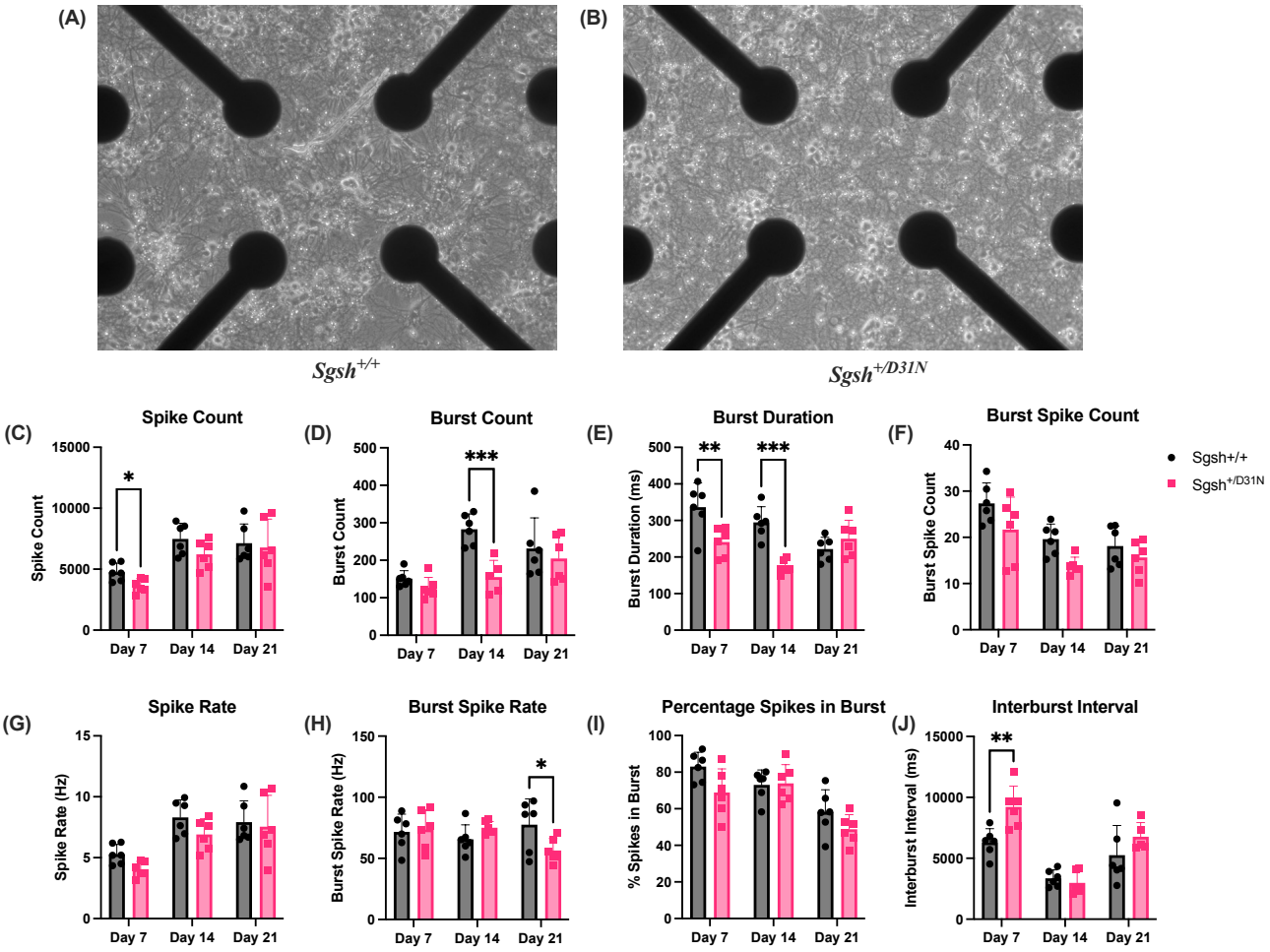

Figure 4.4. Bursting activity in primary cortical neural cultures at Days 7, Day 14, and Day 21 *in vitro*. (A-B) *In vitro* images of *Sgsh*$^{+/+}$ and *Sgsh*$^{+/D31N}$ primary cortical neurons at day 21, (C) spike count, (D) burst count, (E) burst duration, (F), burst spike count, (G) spike rate, (H) burst spike rate, (I) percentage spikes in burst, (J) interburst interval. At day 7, a reduction was observed in the spike count, burst duration, and interburst interval in *Sgsh*$^{+/D31N}$ neurons. On day 14, a decline in burst count, and burst duration was observed. On day 21, the only changes observed was a decline in the burst spike rate, demonstrating a reduction in the overall burst activity of *Sgsh*$^{+/D31N}$ neurons. n = 6 mice/genotype; 4 technical replicate per mice; Each point in the graphs represents one biological replicate; Multiple t-test; *P < 0.05, **P < 0.01, ***P < 0.001. Data are represented as mean ± SEM.

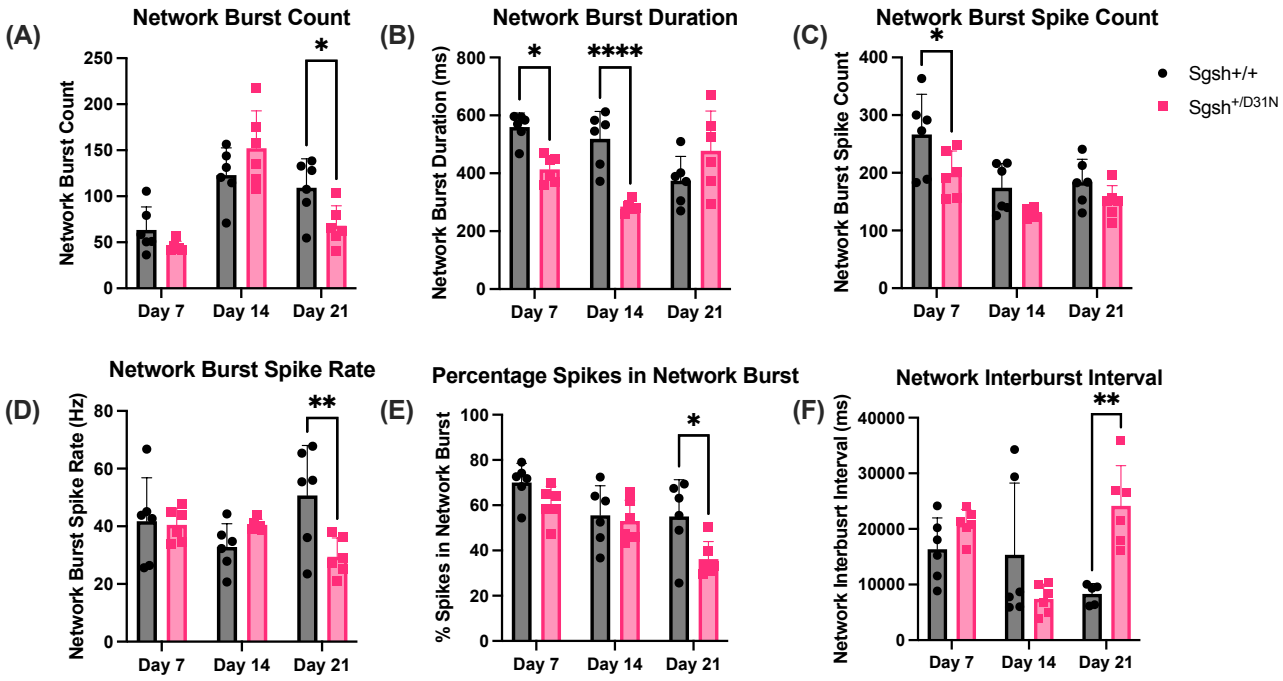

Figure 4.5. Network burst activity in primary neural cultures at Days 7, 14, and 21 *in vitro*. (A) network burst count, (B) network burst duration, (C) network burst spike count, (D) network burst spike rate, (E) percentage spikes in network burst, (F) network interburst interval. *Sgsh*$^{+/D31N}$ neurons show a decrease in network burst count, network burst spike rate, percentage spikes in network burst, and network interburst interval at day 21 *in vitro* with no changes observed in network burst duration and network burst spike count. Changes in network burst duration and network burst spike count was only apparent at day 7 and day 14. n = 6 mice/genotype; 4 technical replicates per mouse; Each point in the graphs represents one biological replicate; Multiple t-test; *P < 0.05, **P < 0.01, ***P < 0.001. Data are represented as mean ± SEM.

In the vehicle control group, network burst duration was found to be significantly decreased in *Sgsh*$^{+/D31N}$ primary neural cultures compared to *Sgsh*$^{+/+}$ cultures at day 18, indicating a decrease excitability and synchronization of neuronal firing (Figure 4.8, B). Interestingly and in contrast to the findings in Figure 4.4 and 4.5, there were no statistically significant changes in other parameters of burst and network burst activity in the vehicle group between *Sgsh*$^{+/D31N}$ primary neural cultures compared to *Sgsh*$^{+/+}$ cultures (Figure 4.7, 4.8).

Sgsh$^{+/D31N}$ neural cultures treated with 0.1nM rotenone exhibited a decrease in burst spike count (Figure 4.7, D), and burst spike rate (Figure 4.7, F) compared to rotenone treated wildtype cultures at day 6. No changes in bursting activity were observed in day 12. However, at day 18, percentage spikes in burst (Figure 4.7, G) showed a decreased in overall firing activity with increased interburst interval (Figure 4.7, H), suggesting *Sgsh*$^{+/D31N}$ neural cultures treated with 0.1nM rotenone had lower spiking activity and delayed burst of electrical activity. Moreover, *Sgsh*$^{+/D31N}$ cultures treated with 0.1nM rotenone also showed a longer time in bursting activity compared to vehicle treated *Sgsh*$^{+/D31N}$ cultures, indicating that treatment with 0.1nM rotenone affects neuronal firing (Figure 4.7, H).

In Figure 4.8, network burst activity in *Sgsh*$^{+/D31N}$ neural cultures treated 0.1nM rotenone exhibited significant reduction in network burst duration (Figure 4.8, B) compared to rotenone treated *Sgsh*$^{+/+}$ cultures at day 6. Interestingly, a shorter network interburst interval was observed at day 12 between rotenone treated *Sgsh*$^{+/D31N}$ neural cultures compared to vehicle treated *Sgsh*$^{+/D31N}$ cultures (Figure 4.8, F), indicative of faster neural firing in the neuronal network. Significantly decreased network burst duration was observed in day 6, and 12 between vehicle treated *Sgsh*$^{+/D31N}$ cultures and rotenone treated *Sgsh*$^{+/D31N}$ cultures, suggesting the treatment with 0.1nM rotenone affects neuronal firing in these neural cultures (Figure 4.8, B).

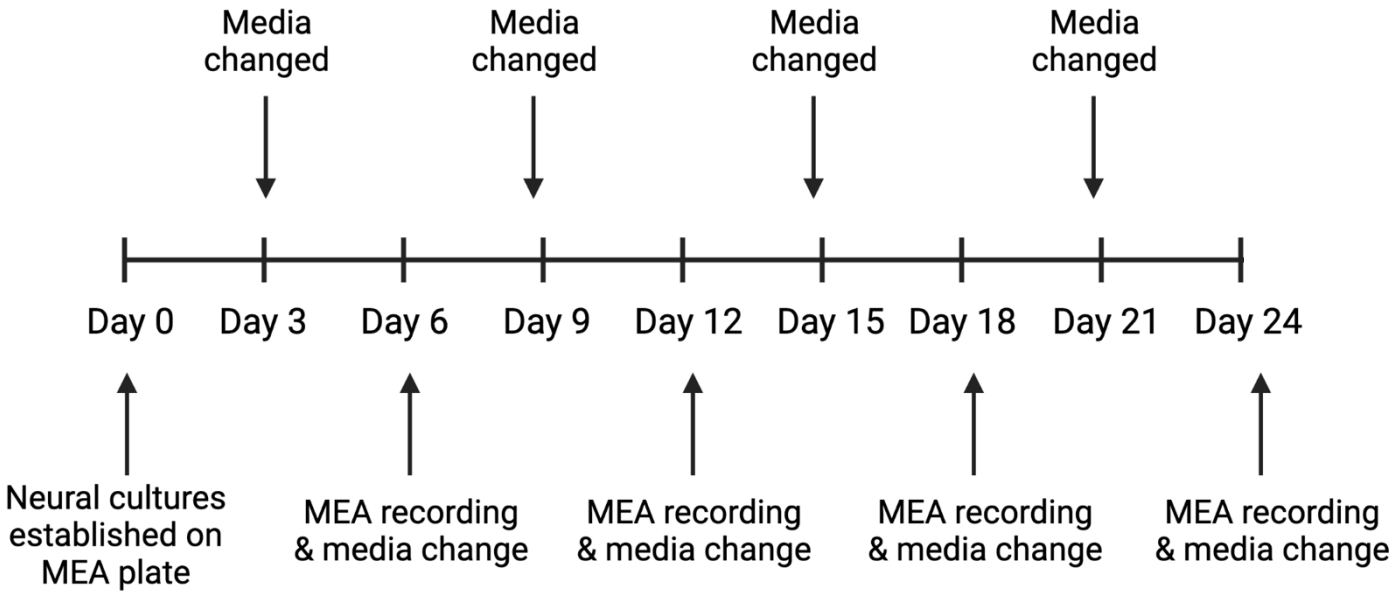

Figure 4.6. Timeline of experimental design for mouse primary cortical neurons treated with 0.1nM rotenone. Primary mouse cortical neural cultures were treated with low dose rotenone (0.1nM) supplemented in media every 3 days. Cell media and rotenone were made up fresh every media change. After the media was changed on day 6, 12, 18 and 24, the plates were returned to the incubator for an hour to allow neural activity to stabilise prior to MEA recording.

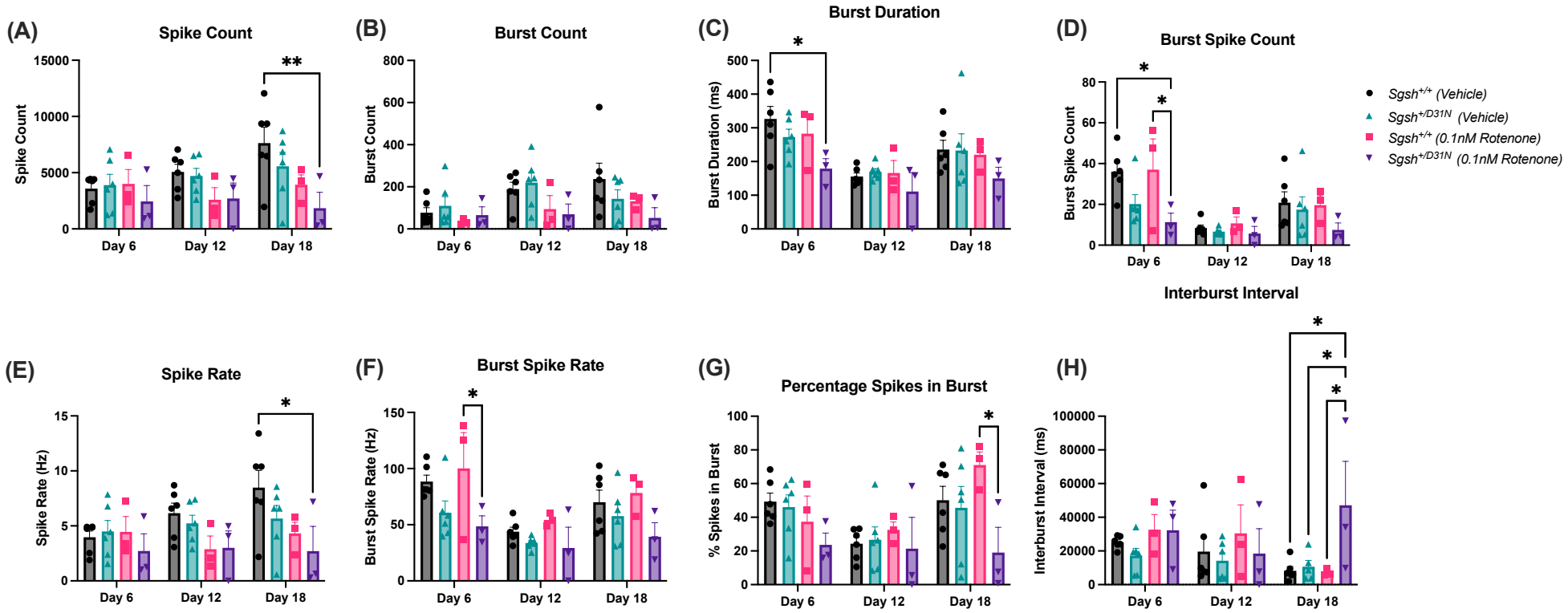

Figure 4.7. Bursting activity in 0.1nM rotenone-treated *Sgsh*$^{+/D31N}$ primary cortical neurons at day 6, 12, and 18 *in vitro*. (A) spike count, (B) burst count, (C) burst duration, (D) burst spike count, (E) spike rate, (F) burst spike rate, (G) percentage spikes in burst, and (H) interburst interval. Primary mouse neural cultures treated with 0.1nM rotenone exhibited perturbation in burst spike count, and burst spike rate at day 6 in *Sgsh*$^{+/D31N}$ neural cultures. No changes in bursting activity was observed at day 12. However, percentage spikes in burst and interburst interval showed alteration in neuronal activity at day 18 in *Sgsh*$^{+/D31N}$ cultures. Interburst interval exhibited a significant delay in network firing in rotenone treated *Sgsh*$^{+/D31N}$ cultures compared to vehicle treated *Sgsh*$^{+/D31N}$ cultures. n = 6 mice/genotype in vehicle treated group, n = 3 mice/genotype in rotenone treated group; n = 3 technical replicates; one-way ANOVA; *P < 0.05, **P < 0.01; Data are represented as mean ± SEM.

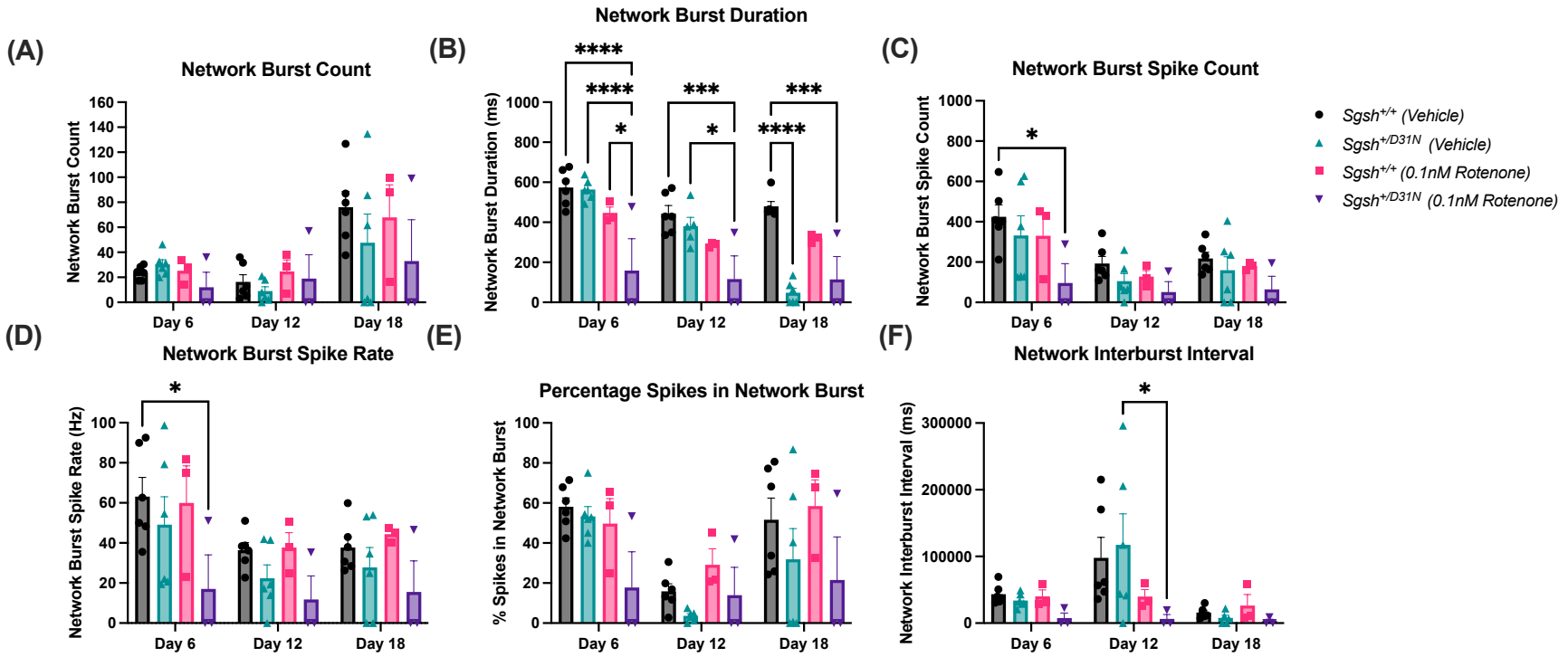

Figure 4.8. Network burst activity in 0.1nM rotenone-treated *Sgsh*$^{+/D31N}$ primary cortical neurons at day 6, 12, and 18 *in vitro*. (A) network burst count, (B) network burst duration, (C) network burst spike count, (D) network burst spike rate, (E) percentage spikes in network burst, (F) network interburst interval. Network burst duration was ignificantly reduced in 0.1nM rotenone treated *Sgsh*$^{+/D31N}$ cultures compared to rotenone treated *Sgsh*$^{+/+}$ cultures at day 6. Network burst duration was significantly reduced in the rotenone treated *Sgsh*$^{+/D31N}$ neural cultures compared to vehicle treated *Sgsh*$^{+/D31N}$ cultures at day 6, and 12. Moreover, rotenone treated *Sgsh*$^{+/D31N}$ neural cultures also showed a faster neural burst in day 12, suggesting *Sgsh*$^{+/D31N}$ neural cultures exhibited a shorter network burst duration with delayed burst. n = 6 mice/genotype in vehicle treated group, n = 3 mice/genotype in rotenone treated group; n = 3 technical replicates; one-way ANOVA; *P < 0.05, ***P < 0.001, ****P < 0.0001; Data are represented as mean ± SEM

4.4 Discussion

4.4.1 No alterations in dendritic spine densities in layer 5 pyramidal neurons in motor cortex of *Sgsh*$^{+/D31N\ EGFP}$ mice

To the best of our knowledge, this is the first study to investigate dendritic spine density and morphology in mice with a heterozygous mutation in a gene encoding a lysosomal enzyme/protein. Whilst Douglass *et al.* reported the presence of subtle structural changes in the dendritic morphology of cortical pyramidal neurons in 84-week-old *Sgsh*$^{+/D31N}$ mice (161), no evaluation of spine density was undertaken. In the present study, no overt changes in dendritic spine maturity or density were observed on layer 5 pyramidal neurons in the motor cortex of 24-week-old *Sgsh*$^{+/D31N\ EGFP}$ mice, indicating that any changes in protein synthesis at 24 weeks does not affect the morphology of these neurons. The impact of carrying this mutation on other neuronal subtypes is unknown. Given that MPS IIIA mice exhibit reduction in dendritic spines in the cerebral cortex, future studies should evaluate the brains of older mice and explore the hypothesis that the dendritic aberration occur on a continuum.

4.4.2 Perturbation of network burst activity in cortical neural cultures

Although no changes in dendritic spine density were seen in the layer 5 pyramidal neurons in the motor cortex of *Sgsh*$^{+/D31N}$ mice, distinct changes in network burst activity were observed in the cortical neural cultures (Figure 4.4). Reduced spiking rate with delayed neural burst activity was evident in *Sgsh*$^{+/D31N}$ neurons compared to *Sgsh*$^{+/+}$, suggesting altered neuronal function. The reduced activity in neuronal networks in *Sgsh*$^{+/D31N}$ neural cultures could be related to the changes observed in the proteomic data in Chapter 3. Specifically, perturbation in proteasome pathway was found to be significantly enriched at 0-week timepoints and play a crucial role in degrading and removing misfolded or damaged proteins from the cells (293). Endoplasmic reticulum-associated degradation (ERAD) and the proteasome are interconnected processes that help maintain protein homeostasis in cells by removing misfolded proteins (190). The ERAD pathway identify and target misfolded or damaged proteins to be retrotranslocated from the ER to the cytosol and then delivered to the proteasome for degradation (190, 238, 239). Hence, perturbation in proteasome pathway can result in the accumulation of misfolded proteins and ER stress, leading to neuronal cell death and impacting

synaptic transmission in the neural cultures (191). Moreover, it was hypothesised that defects in oxidative phosphorylation in neurodegenerative diseases are caused by the accumulation of misfolded proteins (294). Hence, it is not surprising to see that dysregulated proteins involved in oxidative phosphorylation pathway was found to be perturbed at 0-week timepoint in *Sgsh*$^{+/D31N}$ mice (Chapter 3, Table 3.4). Oxidative phosphorylation is the primary site of cellular ATP production within the mitochondria and play a crucial role in maintaining neuronal homeostasis such as generating action potentials, release of neurotransmitters and intracellular signalling (295). Therefore, dysregulation of oxidative phosphorylation may potentially contribute to altered neural network activity in *Sgsh*$^{+/D31N}$ neural cultures. However, a repeat experiment is required to confirm this observation and future studies would include assessment of proteostasis in *Sgsh*$^{+/D31N}$ mouse motor cortex to verify the findings.

4.4.3 Rotenone-treated neural cultures showed alteration in neural activity

Sgsh$^{+/D31N}$ and *Sgsh*$^{+/+}$ primary cortical neural cultures treated with 0.1nM rotenone exhibited conflicting outcomes compared to data observed in section 4.4.2. This is evident where vehicle treated *Sgsh*$^{+/+}$ and *Sgsh*$^{+/D31N}$ neural cultures showed no aberration in network burst activity between genotypes. On the other hand, *Sgsh*$^{+/D31N}$ neural cultures treated with 0.1nM rotenone revealed an effect on network burst activity where a decreased in network burst duration at both day 6 and 12 was observed. This study indicates that the amount of time that the neurons in the network were firing together in a synchronised manner was reduced. These findings suggest that exposure to rotenone leads to a decrease in firing activity within the *Sgsh*$^{+/D31N}$ neural network but not in *Sgsh*$^{+/+}$, indicative of neural damage and susceptibility to the toxic effects of rotenone in *Sgsh*$^{+/D31N}$ neural cultures. The study also showed that rotenone exposure did not further exacerbate the dysfunction of neuronal network activity as hypothesised, though, a dysfunction in network burst duration was observed. Theoretically, rotenone exposure to neurons would increase oxidative stress as well as superoxide radicals, resulting in mitochondrial dysfunction (296). As a consequence, this can lead to the activation of apoptosis pathways, which ultimately results in the death of affected neurons (290). Moreover, rotenone exposure is also associated with the inhibition of proteasome pathway, which is responsible in breaking down and removing damaged or misfolded proteins, including alpha-synuclein (297). Hence, we would anticipate that the inhibition of proteasome system by rotenone might lead to increased accumulation of misfolded sulfamidase proteins in this study due to D31N

mutations, leading to further dysfunction and stress in the neural networks. However, this is not the case in this study and a repeat study is warranted to confirm these observations.

A possible explanation for the conflicting data in 4.4.2 and 4.4.3 could potentially be due to technical errors in culture establishment. Indeed, the mice allocated for this experiment was born on the same day, and a total of 12 mice were euthanised, with neural cultures subsequently established. However, the process of harvesting and isolating neuronal cells from the dissected cerebral cortex took longer than expected, potentially affecting the quality of the cultures. As a result, data variations were evident in the 0.1nM rotenone treated cultures (Figure 4.7 and 4.8). Additionally, the extended duration required to establish the neural cultures from 12 mice may potentially cause the temperature of the cold dissection media, used for dissecting the cerebral cortex to rise in temperature, resulting in accelerated neuronal cell death, thereby further impacting the culture conditions. Hence, a repeat study is required to validate these findings and assess the impact of rotenone exposure on *Sgsh*$^{+/D31N}$ neural cultures as well as the impact it has on synaptic transmission by interrogating changes in synaptic proteins.

4.4.4 Limitations and Future Directions

Given that the equivalent human age for 24-week old mice is around 20-30 years in humans (273), dysfunction of dendritic spine density may not be detected at this timepoint. Hence, future studies, would need to evaluate older timepoints to monitor changes in neuronal morphology and activity in *Sgsh*$^{+/D31N}$ mice neurons and may need a larger sample size to find a statistical difference. Additionally, the current study only looked at changes in the cerebral cortex. Given that neurological diseases affect different parts of the brain, it is important to evaluate other brain areas such as hippocampus to fully understand the risk of *Sgsh* heterozygosity in the CNS.

Primary neurons harvested from newborn mice pups also have some disadvantages. Isolation of healthy neurons is dependent on the user's skills and experience in dissection and preparation of cultures. Primary neurons are also highly sensitive to insult as subtle changes in reagents or environment in cultures can lead to neuronal cell loss (298). Moreover, neurons prepared using these techniques have a higher proportion of non-neuronal cell types compared to cultures that was prepared from embryos due to the developmental stage of the animals. It is estimated that the proportion of glial cells can vary between 10-20% and are relatively present in low numbers compared to neurons (299). Additionally, maintaining healthy cultures

beyond 28 days *in vitro* can be extremely difficult and studies are usually limited to a time period. Hence, to reduce the number of glial cell contamination in cultures, embryonic day 18.5 or earlier is recommended as gliogenesis begins around embryonic day 16 (300). Further, the use of inhibitors, such as cytosine arabinoside (ara-C) can inhibit the growth of dividing non-neuronal cells in long-term cultures.

Finally, assessment of synaptic activity in pre- and post-synaptic markers were unable to be completed due to lower number of isolated neuronal cells harvested from newborn mice pups. Hence, future studies could potentially use brain tissue sections of similar age to assess for pre- and post- synaptic markers to determine synaptic function. Studies have also shown that electrophysiological properties can differ between male and female mice as sex hormones in these animals can have an impact on synaptic plasticity in neurological disease (301, 302). For example, a study conducted by Zhang and colleagues uncovered significant sex differences in input resistance and in the percentage of neurons that displayed post-inhibitory rebound, which was larger in media preoptic area neurons in the hypothalamus in male compared to female mice (303). Moreover, dendritic branching of cells in the prefrontal cortex of female rats showed less apical arbor than males in the agranular insular cortex (304). However, given that newborn mice pups were used, identification of sex was unable to be determined and stratification of electrophysiological data between genders in mice was unable to be analysed. Future studies may also include Y chromosome *in situ* hybridisation to allow for identification of Y chromosome in cells, allowing for separation of data by gender.

4.4 Conclusion

Overall, for the first time, the densities and morphologies of dendritic spines were assessed in the *Sgsh*$^{+/D31N\ EGFP}$ mouse motor cortex. This study shows that layer 5 pyramidal neurons in the motor cortex of *Sgsh*$^{+/D31N\ EGFP}$ mice showed no significant changes in dendritic spine density or maturity at 24-weeks old. However, altered network burst activity was observed in cortical neural cultures derived from newborn *Sgsh*$^{+/D31N}$ mouse brain and maintained to day 21 *in vitro*, suggesting perturbed neuronal function despite no evidence of morphological differences. Further, *Sgsh*$^{+/D31N}$ neural cultures that was treated with rotenone did not further exacerbate the dysfunction in neuronal network activity, potentially due to technical errors in neural cultures establishment. However, a repeat assay is required to confirm this observation. Overall, the data indicate that *Sgsh* D31N heterozygosity may lead to subtle impairment in cortical neural function, which may potentially be hastened by an environmental insult, however, given the preliminary nature of the experiments, further validation studies are needed to confirm the findings.

Chapter 5: Metabolic profile of fibroblasts from *Sgsh* D31N mice and patients carrying disease-causing mutations in *SGSH* gene

5.1 Introduction

Mitochondria are membrane-bound organelles found in most eukaryotic cells and play a crucial role in several metabolic functions. Their primary role is to produce adenosine triphosphate (ATP) through oxidative phosphorylation (OxPhos), which is supported by the tricarboxylic acid cycle (TCA) (305). The process of OxPhos occurs within the inner mitochondrial membrane, where five large-enzymatic complexes are located within the cristae (306). The electron transport chain functions by shuttling electrons along the mitochondrial membrane and pumping protons into the intermembrane space, creating a mitochondrial membrane potential (307). The proton gradient generated by the electron transport chain is used to power the production of ATP from ADP by the ATP synthase (308). A summary of the process is shown in Figure 5.1.

Given their central role in cellular homeostasis, mitochondrial dysfunction is emerging as an important contributory factor to the pathophysiology of several neurodegenerative diseases, including LSDs. The causes of mitochondrial impairment in LSDs are thought to be multifactorial and leads to impaired mitophagy, changes in mitochondrial morphology, decreased mitochondrial membrane potential, and oxidative stress (reviewed in (309)). Moreover, impaired mitochondrial function can directly affect the function of the lysosome by increasing the generation of reactive oxygen species (ROS) and depriving the lysosome of ATP for the maintenance of lysosomal lumen acidity via V-ATPase proton pump (310). Dysregulation of autophagic flux can also have a major impact on mitochondrial function, resulting in impaired clearance of dysfunctional mitochondria.

A study conducted in MPS IIIC mice reported changes in mitochondrial morphology where the mitochondria appeared enlarged, structurally abnormal and swollen with many of them containing disorganised cristae (228). In addition, a decrease in mitochondrial respiratory chain (MRC) complex II and IV activities was observed in isolated mitochondria from the brain of MPS IIIC mice and a deficit in cerebral CoQ10 levels was observed at the latter stages of the disease (227, 228). Interestingly, human MPS IIIC patients were also reported to have a deficit in plasma CoQ10 (311), possibly due to low levels of vitamin B6 detected in these

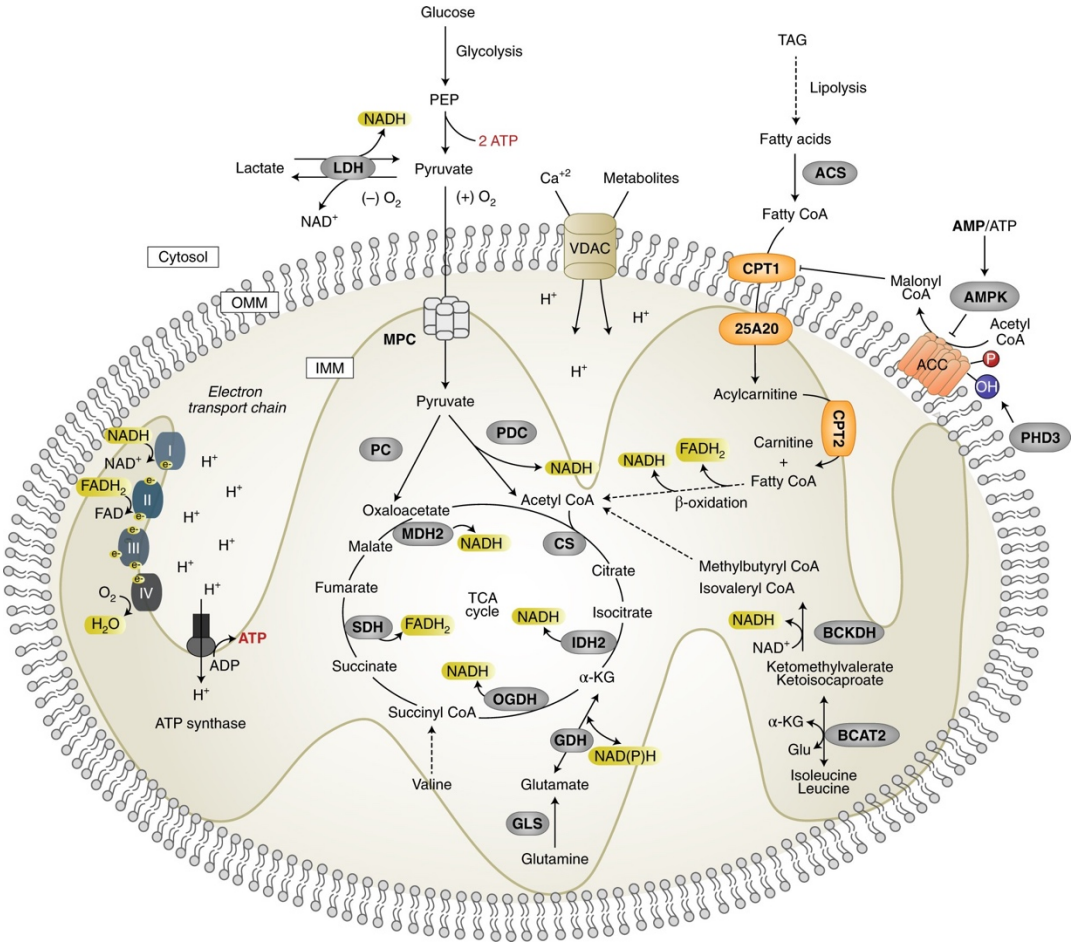

Figure 5.1. Mitochondria are the site of ATP synthesis. Mitochondria are responsible for generating energy in the form of ATP. Glucose, lactate, fatty acids, and amino acids are utilised to create a flow of electrons through the NADH and $FADH_2$ carriers. These electrons then travel to the electron transport chain, where they are used to produce ATP through a process called oxidative phosphorylation. This process is facilitated by several proteins, including, voltage-dependent anion channel, isocitrate dehydrogenase 2, α-ketoglutarate dehydrogenase, succinate dehydrogenase, branched-chain amino transferase and acyl CoA synthetase. Electrons and reducing equivalents are depicted in yellow. Diagram obtained from (306).

patients. Furthermore, studies on MPS IIIA mice revealed impaired mitophagy and significant accumulation of mitochondria in brown adipose tissue (BAT) (312). This correlated with a significant accumulation of mitochondrial markers such as TOMM20 and cytochrome b-c1 complex subunit 1 in MPS IIIA mice compared to wildtype controls. Additionally, the study also revealed a significant increase in the number of mitophagosomes in MPS IIIA BAT (312). This study suggests that the increased mitochondrial activity in BAT and the persistent rise in energy demand in MPS IIIA mice was driven by a reduced ability to generate energy. Moreover, proteomic studies in the MPS IIIB mouse model revealed alterations in metabolic pathways such as ATP synthesis, glycolysis, pyruvate metabolism and TCA cycle, thus, further suggesting that the metabolism associated proteins may contribute to the pathogenesis of neuropathology in MPS III (237). Trudel and colleagues have also suggested that oxidative stress may be a direct result of cellular heparan sulfate accumulation in MPS IIIB mice, although the mechanism is yet to be elucidated. Given that the mitochondria play an important role in cellular homeostasis, and the maintenance of healthy neurons, there is a lack, and a need to explore mitochondrial health in human Sanfilippo patient and whether there are dosage effects in carriers of *SGSH* gene mutations. One promising approach to explore this area is through the use of hyperspectral imaging microscopy.

Hyperspectral imaging is a novel technology which examines endogenous fluorophores and non-invasively assesses the molecular composition of cells and tissues using a wide spectrum of light (Figure 5.2) (313). This type of imaging uses multiple light-emitting diodes with different excitation and emission wavelengths to capture endogenous auto-fluorescent signatures (314, 315). The broad-spectrum approach, which covers excitation wavelengths from 340nm to 750nm, enables the detection of variety of endogenous fluorophores integral to cellular metabolism, including but not limited to NADH and FAD, thereby providing insight into cellular respiration (314). NADH and FAD are involved in oxidative phosphorylation and serve as valuable markers for cellular metabolism, with increased FAD abundance indicating higher metabolism and increased NADH abundance signifying lower metabolism (316). Hyperspectral imaging has been used in medical research such as in reproduction, cancer, and in neuroscience (313, 317, 318). Evidently, hyperspectral imaging can detect subtle alterations in metabolic signatures between disease and healthy states as shown in pancreatic cancer cells (314), olfactory cells (315), and articular cartilage tissue (313). Moreover, the use of hyperspectral imaging in reproductive biology was able to discern between good and poor-quality bovine embryos (316, 319). Positioning, hyperspectral imaging as a promising

technology with potential to inform changes of cellular metabolic activity through the analysis of biomarker fluorophores specific to various metabolic pathways, for example, FAD and NADH, which are involved in the generation of energy through oxidative phosphorylation.

Overall, the experiments in this Chapter aimed to explore general metabolic and specific mitochondrial health in *Sgsh*$^{+/D31N}$ mouse and *SGSH* heterozygous human fibroblast carrying disease causing *SGSH* mutation. *SGSH* homozygous cells from patients with MPS IIIA were included as a positive control sample for comparison. The investigations focused on examining the metabolic parameters in both mouse and human Sanfilippo fibroblasts by utilising mitochondrial assays (tetraethylbenzimidazolylcarbocyanine iodide (JC-1) dye and Seahorse Mito Stress test) and hyperspectral microscopy. JC-1 dye is a mitochondrial membrane potential-sensitive dye, which exhibits a shift in fluorescence from green to red as the membrane potential increases, allowing for the assessment of mitochondrial health in cells whilst the Seahorse Mito Stress test is an assay that measures oxygen consumption rate in cells to assess mitochondrial respiration using specific modulators of electron transport chain complexes to interrogate several metabolic parameters of mitochondrial activity *in vitro* (320, 321). Hence, this study aimed to provide insight into the specific nature of mitochondrial dysfunction in Sanfilippo type A cells as well as whether gene dosage effects were seen in cells with heterozygous *Sgsh/SGSH* gene mutations.

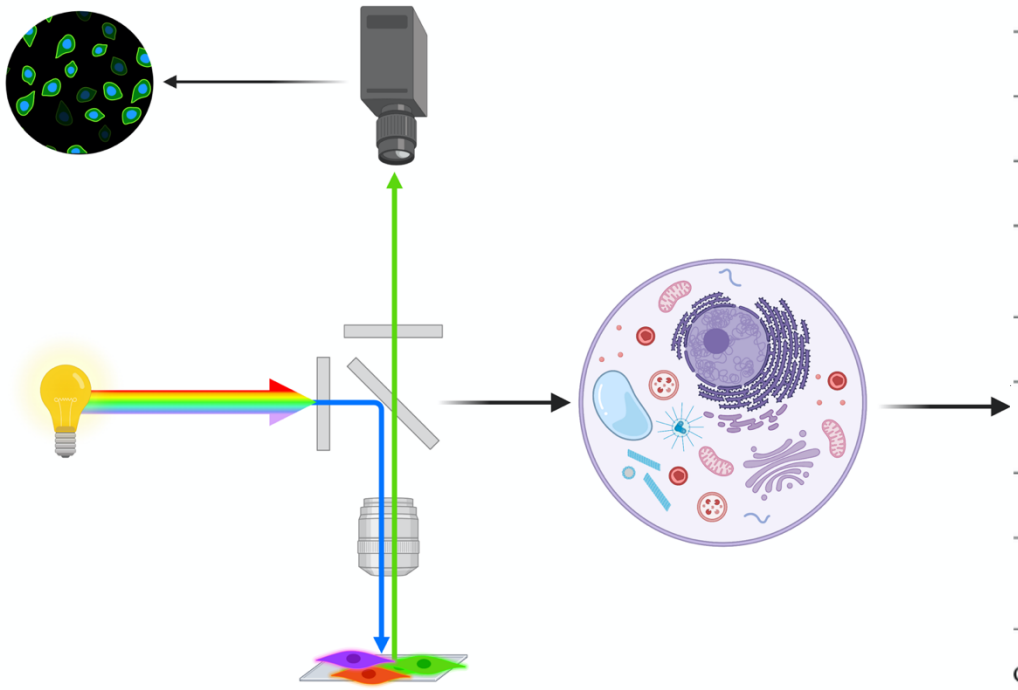

Fluorophore	Function	Excitation (nm)	Emission (nm)	Diagnostic Value, Esp. Changes Depending on Progress of Disease
Collagen	Structural protein in ECM	330–340	400–410	Altered in neoplastic lesions or fibrotic states, e.g., in liver fibrosis
Elastin	Structural protein in ECM	350–420	420–510	Altered expression in invasive tumors
Keratin	Structural protein in ECM	355–405	420–480	Altered expression in invasive tumors, delineate tumor borders
NAD(P)H	Cofactor in redox reactions	330–380	440 (bound); 462 (unbound)	Biomarkers of energy metabolism and redox state
FAD	Cofactor in redox reactions	440–450	525	Biomarker of energy metabolism and redox state e.g., in cancer formation
Porphyrin	Formation of heme	405	630–700	Altered in dental caries and neoplastic lesions
Lipofuscin	End product of lysosomal digestion	400–500	480–700	Biomarker of degenerative diseases
AGEs	Metabolic by-products	300–420	420–600	Accumulate with age and progressive degenerative diseases
Amino acids, e.g., Tyrosin, Tryptophan	Protein metabolism	<310	>500	Altered abundance in invasive tumors
Calcium-sensing receptor	Regulation of parathyroid hormone (PTH) secretion	785	822	Postulated candidate fluorophore for parathyroid AF, distinguishing between parathyroid and surrounding tissues

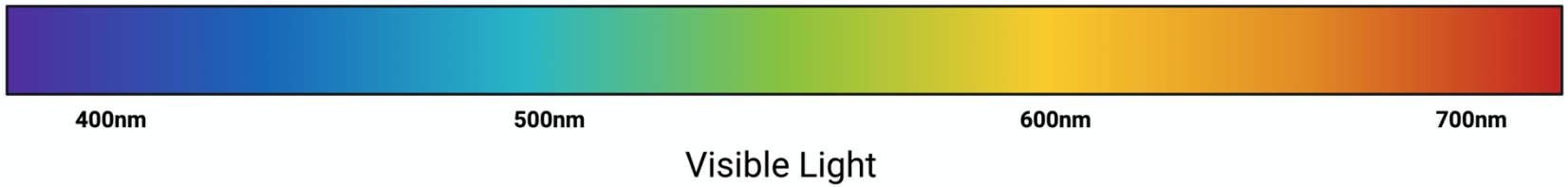

Figure 5.2. Overview of hyperspectral imaging and commonly known endogenous fluorophores. Hyperspectral imaging is a novel technology which utilises endogenous fluorophores to non-invasively assess the molecular composition of cells and tissues. All wavelengths are approximate values of the optimal excitation and emission spectra of fluorophores found in cells. Table in the figure obtained from (322). ECM = Extracellular matrix; NAD(P)H = Nicotinamide adenine dinucleotide phosphate hydrogen; FAD = Flavin adenine dinucleotide; AGEs = Advanced glycation end-products.

5.2 Methods

5.2.1 Mitochondrial assays

5.2.1.1 Cell Culture Lines

Established mouse fibroblast cell lines were obtained from the Childhood Dementia Research Group, Flinders University. Cells were used at passage 6 and 14 in these experiments and cultured at 37°C with 5% CO_2 in DMEM and Ham's nutrient F12 (50:50) media supplemented with 20% v/v Fetal Bovine Serum (FBS), 1% Glutamax, and 1% Penicillin-Streptomycin (PenStrep).

Human fibroblast cell lines were purchased from the Coriell Institute for Medical Research (New Jersey, United States) and were all examined at passage 12. The cells were cultured at 37°C with 5% CO_2 in DMEM media supplemented with 20% v/v FBS, 1% Glutamax, and 1% PenStrep. Information on both mouse and human fibroblast cell lines can be found in Table 1 and 2. All cell lines were negative for mycoplasma as determined using Mycoplasma PCR detection kit by the candidate.

5.2.1.2 Mitochondrial membrane potential (ΔΨm)

Changes in the mitochondrial membrane potential (ΔΨm) in both mouse and human fibroblast were assessed using the fluorescent reagent tetraethylbenzimidazolylcarbocyanine iodide (JC-1) mitochondrial membrane potential dye following the manufacturer's protocol. Fibroblast cells were seeded at a density of $3x10^4$ cells per well and allowed to adhere overnight in a black, clear-bottom 96 well plate. The following day, cells were incubated with 5µM JC-1 dye in DMEM media with no phenol red for 15 minutes at 37 °C, protected from light. JC-1 dye was then removed, and cells were washed twice with preheated media. 100µL of DMEM media with no phenol red was then added to each well and read on iD5 SpectraMax (Molecular Devices, CA, USA) plate reader using the red fluorescence in excitation/emission (530/590nm) and green fluorescence excitation (475/530nm). The ratio of red over green fluorescence intensity was analysed, and data visualisation was performed in Prism9 (Version 9.4.1).

5.2.1.3 Metabolic Flux Analysis

To assess for mitochondrial bioenergetics, mouse and human fibroblasts were assayed using a Seahorse Bioscience XF Analyser and Mito Stress kit according to manufacturer's protocol (Agilent Technologies, User Guide Kit 103015-100). Prior to the assay, cells were plated at $3x10^4$ cells per well in a Seahorse XFe96 cell culture microplate, n = 3 cell lines were used per genotype with each sample plated in 10 technical replicates. Cells were left at room temperature for 1 hour to reduce the "edge" effect and incubated overnight at 37 °C, 5% CO_2 prior to analysis to facilitate cell attachment. Hydration of the sensor cartridge was done overnight using Seahorse XF calibrant media at 37 °C in a non-CO_2 incubator. The following day, three pharmacological compounds were administered sequentially: oligomycin (1.5µM), FCCP (1.0µM), and rotenone/antimycin A (0.5µM). Three measurement cycles at five-minute intervals were performed prior to the first compound injection and following every compound injection, as is standard practise for metabolic analysis. Upon assay completion, the plates were then fixed with 4% PFA and stained with Hoechst. A cell count was conducted using the well-scan mode on the CLARIOstar plus (BMG Labtech, VIC, Australia) plate reader as per (323). This method measures the fluorescence of Hoechst-stained nuclei and was used for cell normalisation between wells in each plate. The data was then imported to Seahorse Analytics (available online: seahorseanalytics.agilent.com) for calculations of metabolic capacity.

5.2.2 Hyperspectral Imaging

5.2.2.1 Culturing mouse and human fibroblasts for hyperspectral imaging

Mouse and human fibroblasts (Table 1 and 2) were cultured and maintained in 5% CO2 at 37^{o}C. Using a 35mm glass bottom dish, $1x10^5$ cells were plated in each dish and cultured overnight to allow the cells to adhere to the glass. Prior to imaging, the cells were washed twice with PBS without calcium and magnesium and cells were imaged in Hank's balanced salt solution supplemented with 1M of HEPES buffer.

Table 5.1. Human fibroblasts obtained from the Coriell Institute for Medical Research

No	Genotype	Cell ID	Age	Mutation	Type of mutation/protein	Passage
1	Normal/unaffected	GM 38	9, Female	n/a	Normal	12
2	Normal/unaffected	GM 3349	10, Male	n/a	Normal	12
3	Normal/unaffected	GM 3377	7, Male	n/a	Normal	12
4	Heterozygous	GM 886	19, Female	E447k or R245H	E447K: Missense, misfolded R245H: Missense, misfolded	12
5	Heterozygous	GM 1095	n/a, Female	9-BP-DEL or NT1307	9-BP-DEL: Deletion, truncated NT1307: Missense, misfolded	12
6	Heterozygous	GM1096	n/a, Male	9-BP-DEL or NT1307	9-BP-DEL: Missense, misfolded NT1307: Missense, misfolded	12
7	MPS IIIA	GM 629	10, Male	S66W	Missense, misfolded	12
8	MPS IIIA	GM6110	6, Female	R245H	Missense, misfolded	12
9	MPS IIIA	GM879	3, Female	E447K/R245H	E447K: Missense, misfolded R245H: Missense, misfolded	12

Note: the exact mutation in heterozygous individuals is unknown. It can only be inferred based on the mutations found in their offspring, who has MPS IIIA.

Table 5.2. Mouse fibroblast obtained from the Childhood Dementia Research Group, Flinders University

No	Genotype	Cell ID	Age	Mutation	Type of mutation/protein	Passage
1	Normal/Wildtype	288.1	Day 0	nil	Normal	6
2	Normal/Wildtype	288.2	Day 0	nil	Normal	6
3	Normal/Wildtype	935.5	Day 0	nil	Normal	6
4	Heterozygous	935.4	Day 0	+/D31N	Missense, misfolded	6
5	Heterozygous	935.8	Day 0	+/D31N	Missense, misfolded	6
6	Heterozygous	935.9	Day 0	+/D31N	Missense, misfolded	6
7	MPS IIIA	183.1	Day 0	D31N/D31N	Missense, misfolded	6
8	MPS IIIA	183.2	Day 0	D31N/D31N	Missense, misfolded	6
9	MPS IIIA	333.1	Day 0	D31N/D31N	Missense, misfolded	6

5.2.2.2 Hyperspectral imaging and brightfield imaging

To allow the capture of autofluorescence or native endogenous fluorophores found within cells, a standard fluorescence microscope (Nikon Eclipse TiE, 40 objective, NA = 1.3) that had been modified and fitted with a multi-LED light source (Prizmatix Ltd, Givat-Shmuel, Israel) was utilised. This newly built microscope had an excitation lamp (QuantativeTM, Australia) comprising of multiple low-powered light emitting diodes (LEDs) with selected bands of excitation wavelengths (centred at 348, 369, 371, 376, 384, 390,394, 407, 420, 423, 432, 447, 449, 471, 476, 480, 499, 507, 522, 531, 563, 597, 625, and 649nm) used to excite cellular autofluorescence. Three epifluorescence filter cubes with long pass emission bands centred at 442 nm, 560 nm and 695 nm allowed the measurement of autofluorescence signals in cell samples in a number of defined narrow bands. The modifications enabled generation of specific and defined spectral channels (Appendix 7), covering excitation range of between 348-649nm and emission range of 450-715nm wavelength. In total, 55 spectral channels were available to measure autofluorescence signals in a biological sample. However, a modified protocol was utilised due to no autofluorescence signal detected in channels 33-39. Images were then captured by a digital camera C1140, OCRA Flash 4.0 (Hamamatsu, Shizuoka, Japan). Image acquisition times of up to 3-5 seconds per channel, with 3-5 times averaging was used to optimise the image quality in each channel. A total of four images per dish were captured from the four corners of the glass bottom dish. Each data set was supplemented with a brightfield image of the sample which was used as a broad reference.

5.2.2.3 Hyperspectral data analysis

Images obtained from the hyperspectral were then processed using a custom-made Graphical User Interface (GUI) softwares (GUI_Visual (324), GUI_Preparation v3.12 (313) and GUI_Segmentation). First, image preparation was carried out to remove any image artefacts, this includes background fluorescence, Poisson's noise, dead or saturated pixels. At the beginning of each experiment, two calibration images (a culture dish with Milli-Q water, and another with calibration fluid containing NADH and riboflavins were taken using the hyperspectral system to act as a background reference.

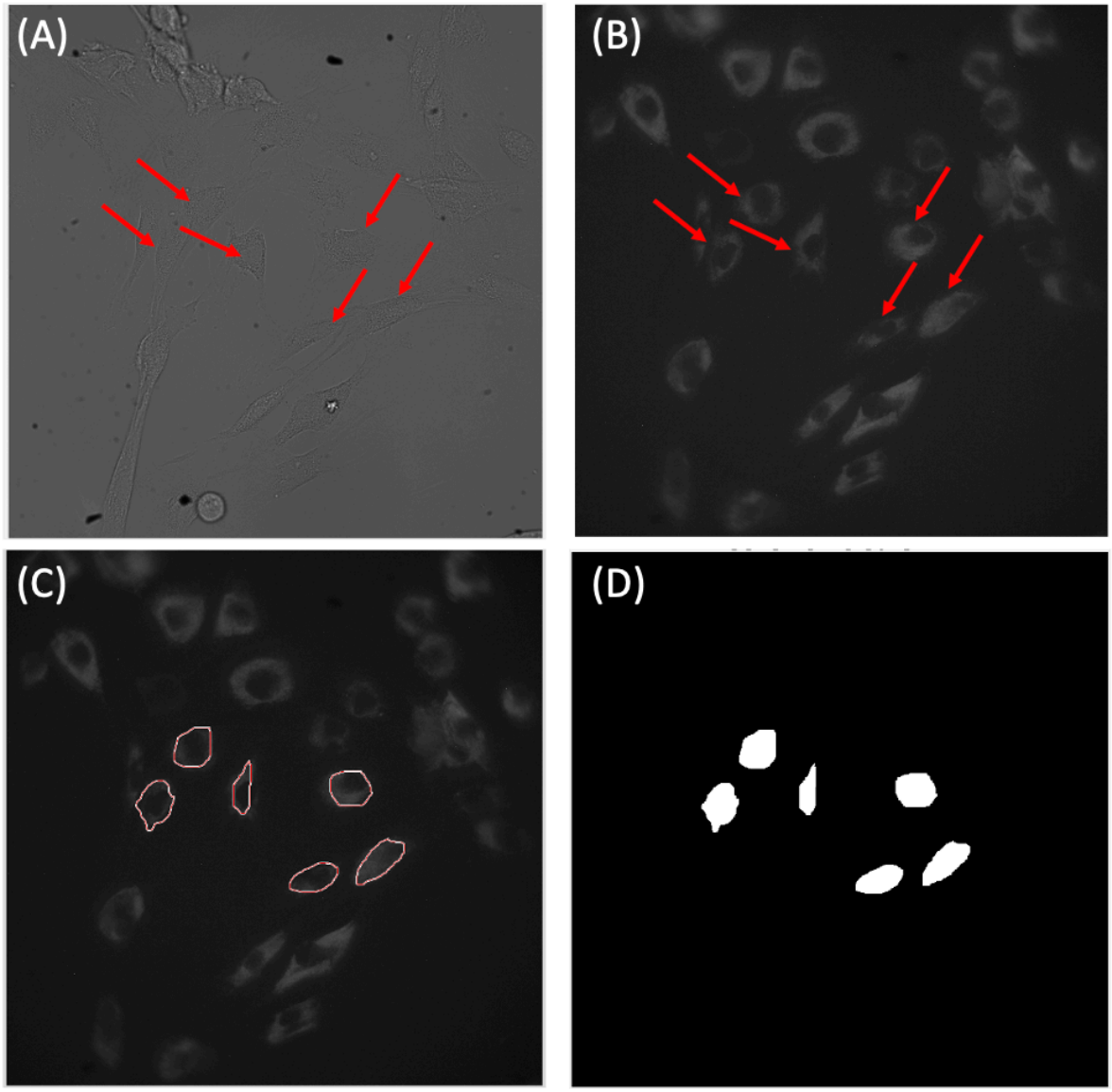

Figure 5.3. Representative images of the region of interest drawn using GUI segmentation software. (A) Brightfield image, (B) representative image of channel 8, (C) region of interest drawn around the cell, (D) cell masks. Fibroblast cell membranes were manually segmented to create a region of interest/cell mask using the spectral channels prior to further analysis using GUI preparation to determine the level of fluorescence intensity. Images taken using x40 objectives.

The background reference image (Milli-Q water and calibration fluid) was included and subtracted from all images with cells to remove any potential background signals generated from the glass bottom dish or potentially due to fluorescence contamination from microscopic optics that may increase fluorescence intensity in all spectral images.

The microscope was calibrated with a mixture of 30mM NADH and 18mM riboflavins whereby their spectrum span across all spectral channels. The excitation and emission spectra of this calibration fluid was measured using a fluorimeter (FluroMax Plus-c, Horiba, Japan) and imaged on the hyperspectral microscope across all spectral channels. The calibration images were then used to correct the same spectrum measured with the hyperspectral system by utilising GUI preparation software. Finally, fibroblasts were manually segmented/drawn using the brightfield image taken concurrently with the hyperspectral images, creating a region of interest (ROI)/cell mask (Figure 5.3). For fibroblast, the ROI was drawn around the cell membrane that was clearly visible on the spectral channel.

Moreover, presence of an artefacts (ring effect) during imaging made it difficult to obtain an accurate readout of fluorescence intensity in all the spectral channels. The artefacts can obscure signals from the cells, resulting in potentially inaccurate intensity measured. Hence, in order to work around the artefacts and to keep the analysis consistent, cells within the artefacts was analysed throughout the study. Also, due to time constraints, the HS machine and the presence of artefact was unable to be fix, and the data collected for mouse and human fibroblasts contains the artefact in the background image during analysis.

5.3 Results

5.3.1 Evaluation of ΔΨm using JC-1 dye in MPS IIIA *and Sgsh/SGSH* heterozygous fibroblasts

To determine whether *Sgsh*$^{D31N/D31N}$ and *Sgsh*$^{+/D31N}$ fibroblast had an altered mitochondrial activity, the fibroblasts were stained with JC-1 dye and the fluorescence intensity was quantified using a microplate reader. The JC-1 dye allows for the detection of altered mitochondrial membrane potential through the accumulation of dye within the mitochondria in a healthy cell, and lack thereof in an unhealthy cell, thus reflecting changes in mitochondrial function within a cell. Specifically, the JC-1 dye actively accumulates in the energised mitochondria (negatively charged mitochondrial membrane), forming large aggregates that fluorescence in the red wavelength range. On the other hand, unhealthy cells are typically associated with increased membrane permeability and loss of electrochemical gradient (320), therefore the JC-1 dye will passively enter the mitochondria to a lesser degree. In this condition, JC-1 retains its monomer state and remains in the cytoplasm, which emits its original green fluorescence. The ratiometric difference in red over green fluorescence reflects the changes in mitochondrial membrane potential (ΔΨm), and thus of mitochondrial function.

As shown in Figure 5.4 (A), no statistically significant difference in ΔΨm was observed when comparing *Sgsh*$^{D31N/D31N}$ and *Sgsh*$^{+/+}$ mouse fibroblast. However, MPS IIIA human fibroblasts exhibited a significant decrease in ΔΨm when compared to normal human fibroblasts, potentially indicating defective mitochondrial function (Figure 5.4, B). On the other hand, *Sgsh*$^{+/D31N}$ mouse fibroblast exhibited a statistically significant increase in ΔΨm, potentially indicating an increase in mitochondrial activity compared to *Sgsh*$^{+/+}$ mouse fibroblasts. No perturbation in ΔΨm was noted across *SGSH* heterozygous human fibroblast, regardless of the type of *SGSH* mutation (Figure 5.4, B).

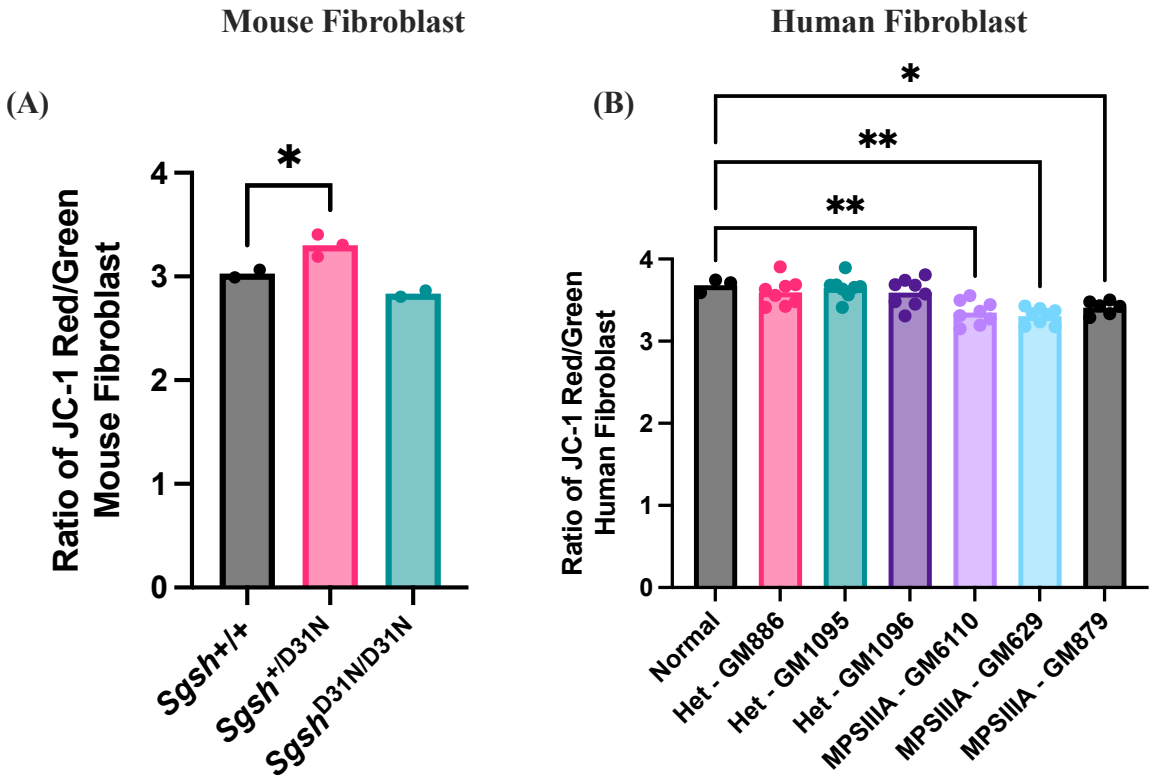

Figure 5.4 Assessment of mitochondrial membrane potential using JC-1 dye in mouse and human fibroblast. Changes in the red (~590nm) / green (~529nm) fluorescence intensity ratio is indicative of disruption of the mitochondrial membrane potential. (A) *Sgsh*$^{+/D31N}$ mouse fibroblasts show a significant higher JC-1 fluorescence intensity ratio compared to *Sgsh*$^{+/+}$; however, no significant changes were observed in *Sgsh*$^{D31N/D31N}$ cells compared to *Sgsh*$^{+/+}$. (B) No significant changes can be observed in the heterozygous human cell lines, but human MPS IIIA fibroblasts show a decrease in JC- 1 fluorescence intensity ratio compared to normal human fibroblast. The sample size for mouse fibroblast: n = 2 wildtype and *Sgsh*$^{D31N/D31N}$ and n = 3 *Sgsh*$^{+/D31N}$ fibroblast cell lines with 10 technical replicates; sample size for human fibroblast: n = 3 normal human fibroblast with 8 technical replicates, and n = 1 heterozygous and MPS IIIA fibroblast cell lines carrying different mutations, with 8 technical replicates; All mouse fibroblasts were utilised at passage 6 and all human fibroblasts were utilised at passage 12 at the time of experiment; *P < 0.05; **P < 0.01; one-way ANOVA; Data are represented as mean ± SEM.

5.3.2 Mitochondrial profiles of mouse *Sgsh* and human *SGSH* heterozygous fibroblast

To assess cellular respiration in the fibroblasts, the Seahorse Mito Stress Test was used to measure the key parameters of mitochondrial function by sequentially blocking the different OxPhos complexes. Oligomycin is the first compound that was injected into the Seahorse plate. Oligomycin is an ATP-synthase inhibitor that reduces the influx of electrons, ultimately reducing ATP production and forcing the cell to consume oxygen via OxPhos (325). As a consequence, oxygen consumption rate (OCR) is expected to decrease upon exposure to oligomycin. Following oligomycin treatment, carbonyl cyanide-4-phenylhydrazone (FCCP) is injected. FCCP is an uncoupling agent that collapses the proton gradient, leading to a disruption in ATP synthesis. OCR is expected to significantly increase following the administration of this compound. Finally, a drug cocktail of rotenone and antimycin A (Rot/AA) is injected. Rot/AA shuts down mitochondrial respiration by inhibiting OxPhos complexes I and III respectively. The addition of this drug is expected to significantly decrease the OCR of cells following FCCP addition. The sequential addition of these drugs allows for the calculation of metabolic parameters by observing the changes to OCR (Figure 5.5).

Basal respiration provides the baseline of mitochondrial respiration of the cells in a standard assay condition prior to adding any drug compounds (326). Maximal respiration represents the maximum theoretical volume of mitochondrial respiration that the cell can achieve whilst FCCP uncouples the proton gradient in the OxPhos (326). Proton leak represents the diffusion of proton across the inner membrane independently of ATP synthase, resulting in continued consumption of mitochondrial oxygen in the presence of oligomycin. Hence, proton leak can be an indicator of mitochondrial membrane damage (326). Non-mitochondrial oxygen consumption measures the consumption of oxygen that is occurring outside of the mitochondria, such as the cell surface via transplasma membrane electron transport, or by a subset of cellular enzymes such as nicotinamide adenine dinucleotide phosphate hydrogen (NADPH) oxidase (327). ATP-production coupled respiration is defined as the oxygen consumption driven by ATP synthesis in the mitochondria to meet the energetic needs of the cell. Spare respiratory capacity represents the cell's ability to respond to increase in energy demand as well as how well the cell can respire to its theoretical maximum. Changes to this parameter can indicate alterations in mitochondrial biogenesis or mass.

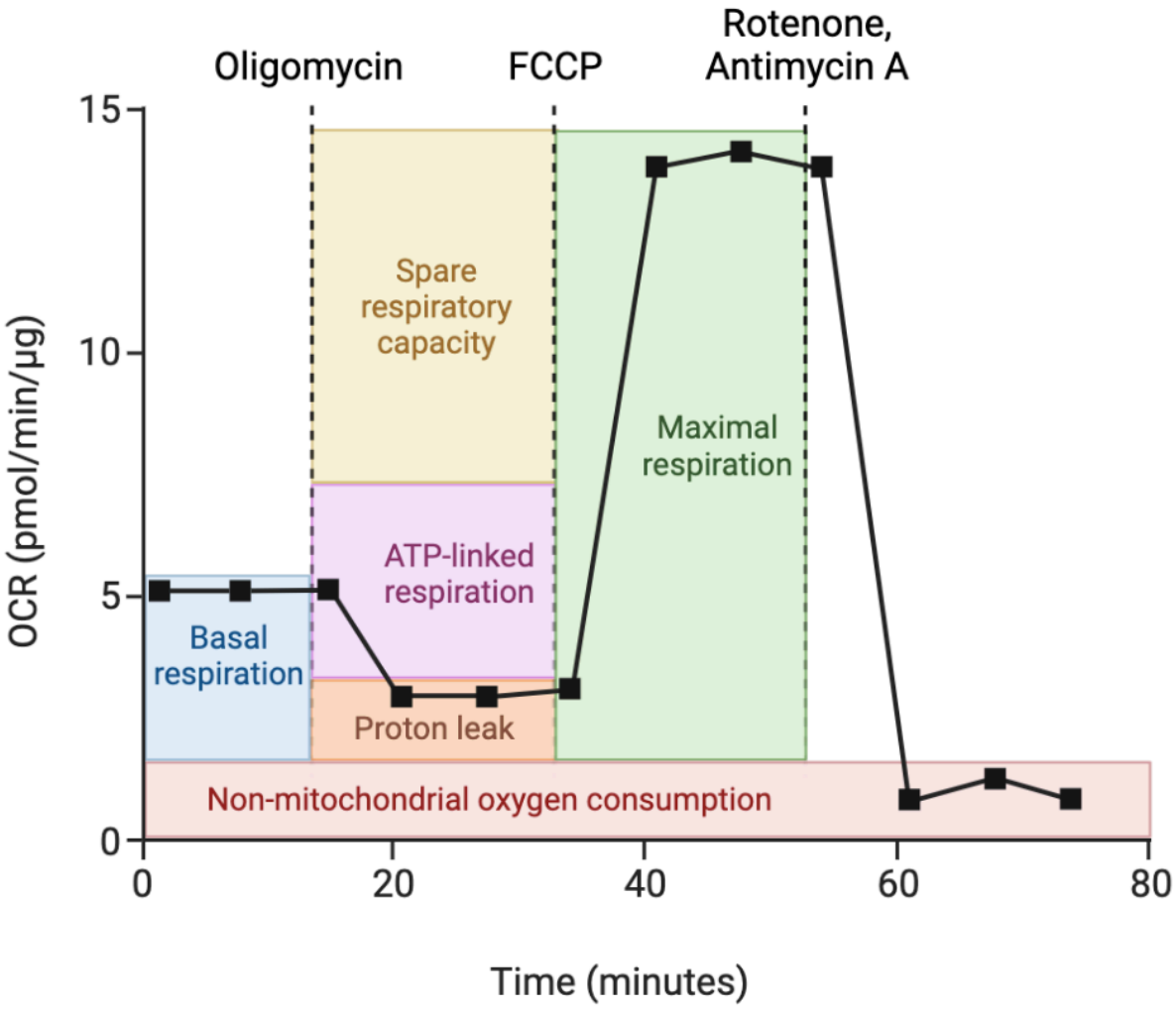

Figure 5.5. Predicted changes in OCR due to mitochondrial and non-mitochondrial-related metabolism. Different colours have been used to represent the different OCR parameters. Graph obtained from BioRender.com

To determine whether specific mitochondrial and non-mitochondrial metabolic pathways are impacted in *Sgsh*$^{D31N/D31N}$ and *Sgsh*$^{+/D31N}$ fibroblasts, the Seahorse Mito Stress Test was used to measure the oxygen consumption rate (OCR) in fibroblasts following sequential treatment with metabolic inhibitor drugs. In Figure 5.6 (A-F), no significant perturbation of OCR was found across all metabolic parameters assessed. However, there was a notable decrease in OCR in *Sgsh*$^{D31N/D31N}$ mouse fibroblasts across all metabolic parameters, albeit not quite reaching statistically significance.

In Figure 5.7 (A), the heterozygous GM886 fibroblast cell line shows a significant increase while heterozygous GM1096 fibroblast showed a significant decrease in basal mitochondrial respiration compared to normal human fibroblasts. This finding suggests that different mutations in the *SGSH* gene may be associated with distinct mitochondrial phenotype. In contrast, all MPS IIIA human fibroblast displayed a significant reduction in proton leakage, regardless of the types of *SGSH* gene mutations (Figure 5.7, B). No statistically significant effect on proton leakage was observed for *SGSH* heterozygous human fibroblast (Figure 5.7, B). Similarly, no significant impact was observed in human fibroblasts on non-mitochondrial oxygen consumption activity between genotypes (Figure 5.7, C).

When assessing the maximal respiration rate, only heterozygous GM1096 fibroblast OCR was significantly reduced when compared normal fibroblasts (Figure 5.7, D). Likewise, both MPS IIIA GM629 and GM879 fibroblasts exhibited a significant reduction in maximal respiration rate compared to normal fibroblast. Similarly, a trend was seen in MPS IIIA GM6110 (Fig 5.7, D). The same outcome was observed when assessing for the spare respiratory capacity where heterozygous GM1096 fibroblast and MPS IIIA GM629 and GM879 were found to have significantly decreased OCR compared to normal fibroblast with MPS IIIA GM6110 exhibiting a trend in the same direction (Figure 5.7, E). In contrast, ATP-production coupled respiration was significantly increased in heterozygous GM886, but it was significantly decreased in heterozygous GM1096 fibroblast when compared to normal human fibroblast (Figure 5.7, F). No changes were seen in the MPS IIIA cell lines.

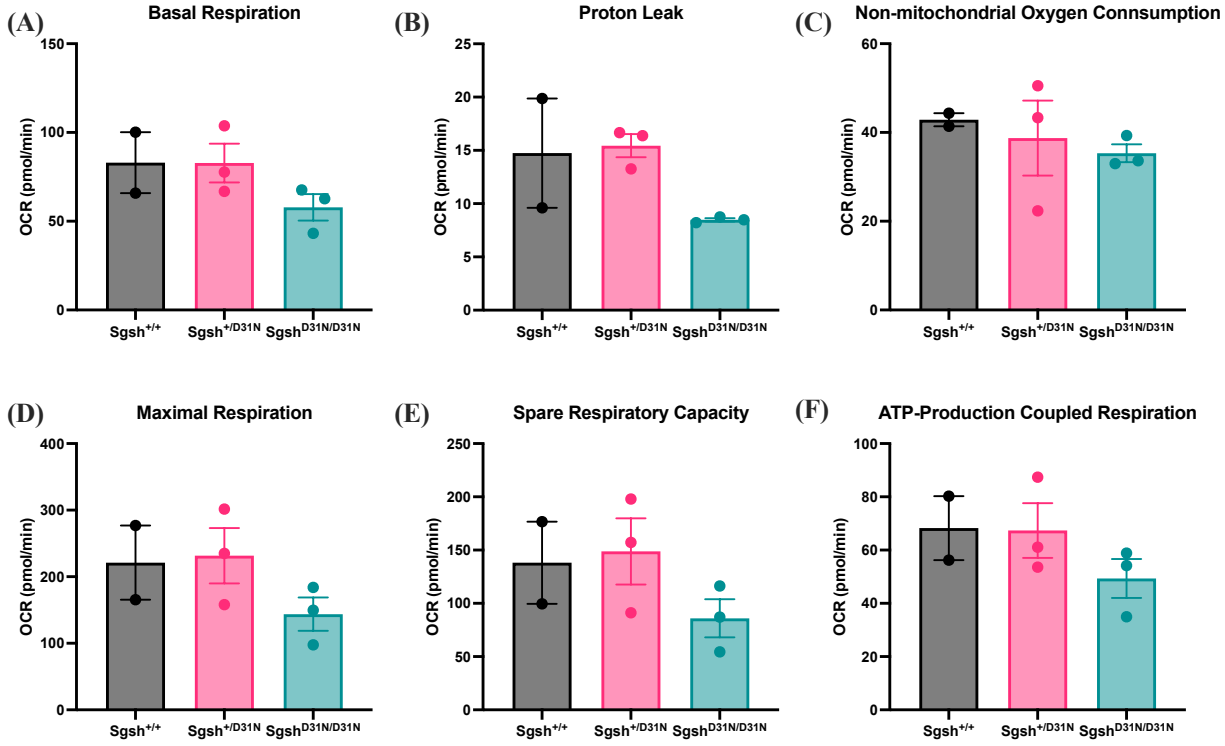

Figure 5.6 OCR-related metabolic parameters in *Sgsh*$^{+/D31N}$ and *Sgsh*$^{D31N/D31N}$ mouse fibroblasts. (A) basal respiration; (B) proton leak; (C) non-mitochondrial oxygen consumption; (D) maximal respiration; (E) spare respiratory capacity; and (F) ATP-production coupled respiration were calculated from measurements obtained using the Seahorse Mito Stress test. There were no significant changes between genotypes in the metabolic parameters assessed, although, *Sgsh*$^{D31N/D31N}$ fibroblasts showed reduced OCR in all metabolic parameters. n = 2 *Sgsh*$^{+/+}$ and n = 3 *Sgsh*$^{+/D31N}$ and *Sgsh*$^{D31N/D31N}$ fibroblasts with 10 technical replicates; One wildtype fibroblast was omitted due to low cell density at the time of experiment; All mouse fibroblasts were utilised at passage 10; one-way ANOVA; Data are represented as mean ± SEM.

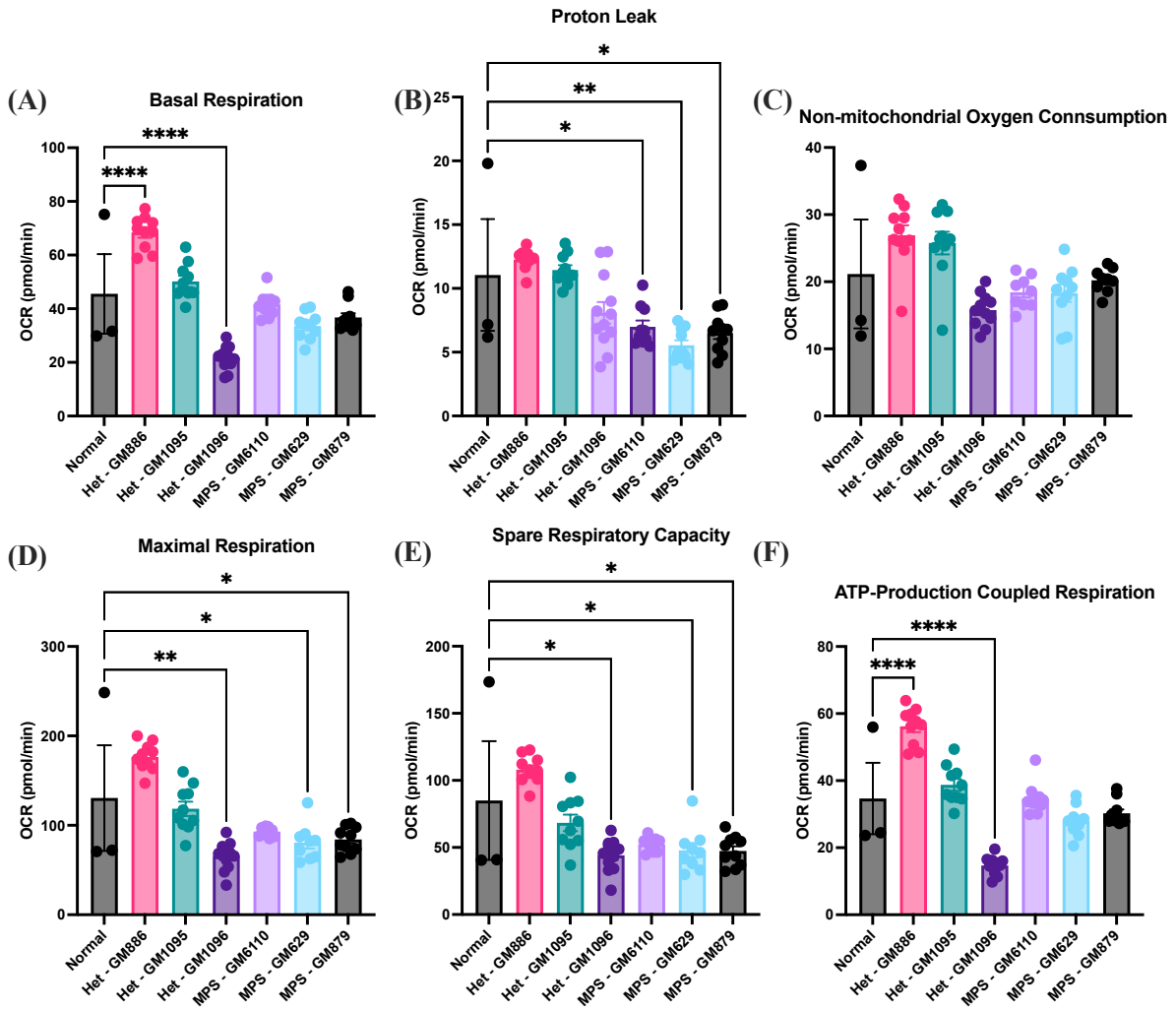

Figure 5.7 OCR-related metabolic parameters in human fibroblasts from patients carrying single or homozygous *SGSH* mutations. (A) basal respiration; (B) proton leak; (C) non-mitochondrial oxygen consumption; (D) maximal respiration; (E) spare respiratory capacity; and (F) ATP-production coupled respiration were calculated from measurements obtained using the Seahorse Bioscience Metabolic Flux Analyser Mito Stress test. Asterisk (*) represents statistically significance difference with normal fibroblast control. Each data point in the graphs above for normal fibroblast represents one biological replicate with 10 technical replicate at the time of assay; each data point for heterozygous and MPS IIIA fibroblasts represent technical replicates; n = 3 normal human fibroblast, n = 1 heterozygous and MPS IIIA fibroblast carrying different mutations; 10 technical replicates per genotype; all human fibroblasts were utilised at passage 13 at the time of experiment. *P < 0.05; **P < 0.01; ****P < 0.0001; one-way ANOVA; Data are represented as mean ± SEM.

5.3.3 Hyperspectral microscopy detects subtle metabolic changes in human fibroblasts carrying single or homozygous *SGSH* mutation

Fixed human fibroblast imaging (in Figure 5.8), shows representative images taken in spectral channels 1-5, demonstrating the changes seen in normal, *SGSH* heterozygous, and MPS IIIA human fibroblast.

When fixed mouse fibroblasts were imaged (Figure 5.9, A, B, C, D, E), no statistically significant changes in signal intensity were detected in *Sgsh*$^{+/D31N}$ and *Sgsh*$^{D31N/D31N}$ mouse fibroblasts compared to wildtype across all hyperspectral channels. The result suggests that the signal detected in both *Sgsh*$^{+/D31N}$ and *Sgsh*$^{D31N/D31N}$ mouse fibroblasts exhibit no aberrant changes in endogenous fluorophores.

On the other hand, endogenous fluorophores detected by hyperspectral imaging in both fixed human heterozygous (GM886 and GM1095) fibroblasts were higher in Channels 2-10 (Figure 5.10, A), 11 (Figure 5.10, B), 30 (Figure 5.10, C), 31-40 (Figure 5.10, D), 41-44 and 46-47 (Figure 5.10, E), with an exception at Channel 45 (Figure 5.10, E) where signal intensity was significantly lower compared to wildtype fibroblasts. Additionally, only heterozygous GM886 fibroblasts were significantly higher in Channel 19 compared to wildtype fibroblasts. All three MPS IIIA GM629, GM6110, and GM879 human fibroblast cell lines have significantly higher signals detected in Channel 31 (Figure 5.10, D), 41, 42, 44, 45, and 47 (Figure 5.10, E) compared to wildtype human fibroblast. Notably, MPS IIIA GM629 and GM879 fibroblasts have significantly higher signal intensity in Channel 11 (Figure 5.10, B), whilst signal intensity detected was significantly lower in Channel 43 for MPS IIIA GM6110 and GM879 fibroblasts (Figure 5.10, E). Overall, it appears that both *SGSH* heterozygous human fibroblasts GM886 and GM1095 have consistently higher signal intensity detected across most, if not all hyperspectral channels, while signals detected for all three MPS IIIA human fibroblasts were highly variable, and in most cases, were similar to wildtype human fibroblasts.

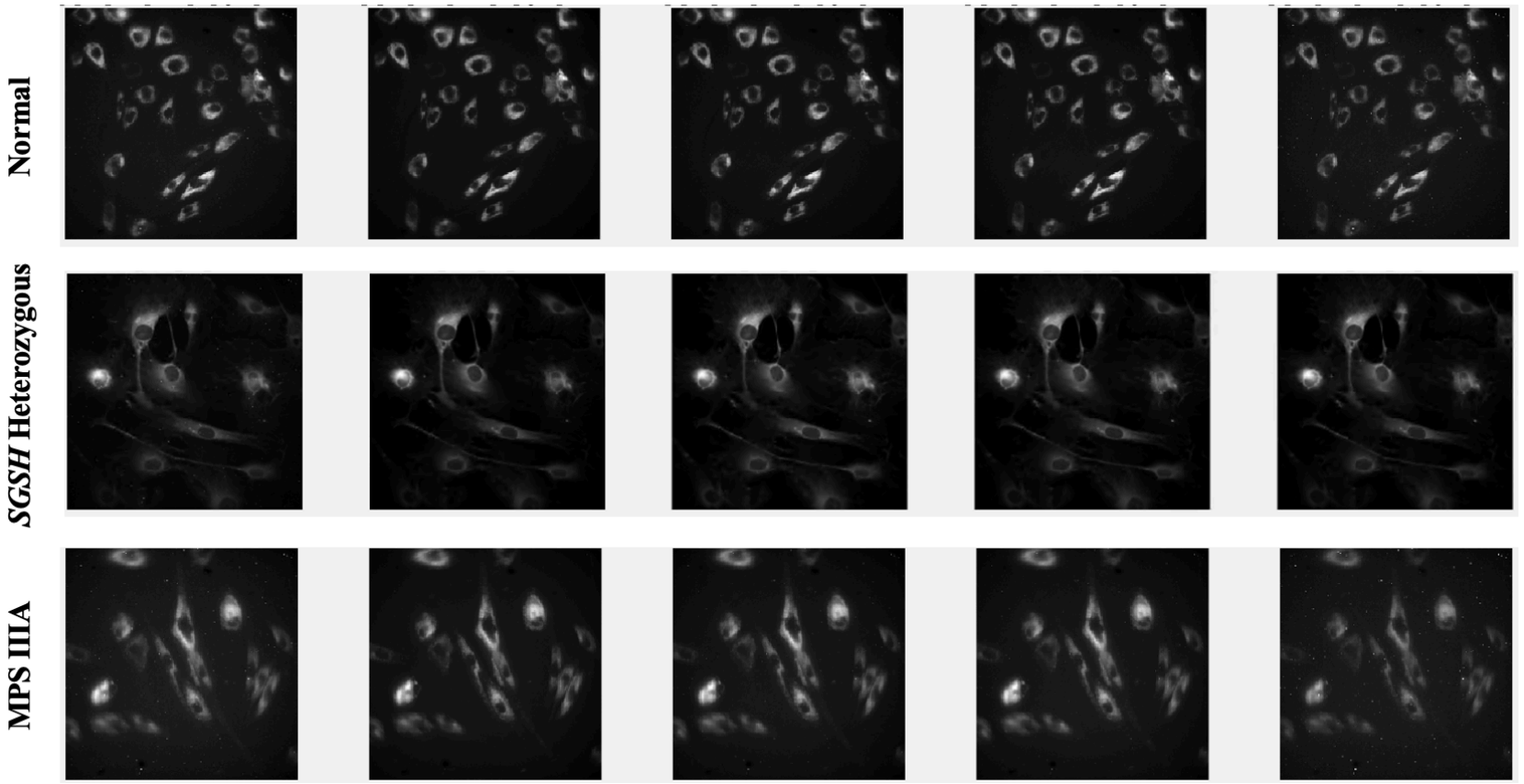

Figure 5.8 Representative images acquired from hyperspectral channels 1 to 5 of human fibroblasts from normal, *SGSH* heterozygous, and MPS IIIA. Changes in autofluorescence were analysed using GUI software.

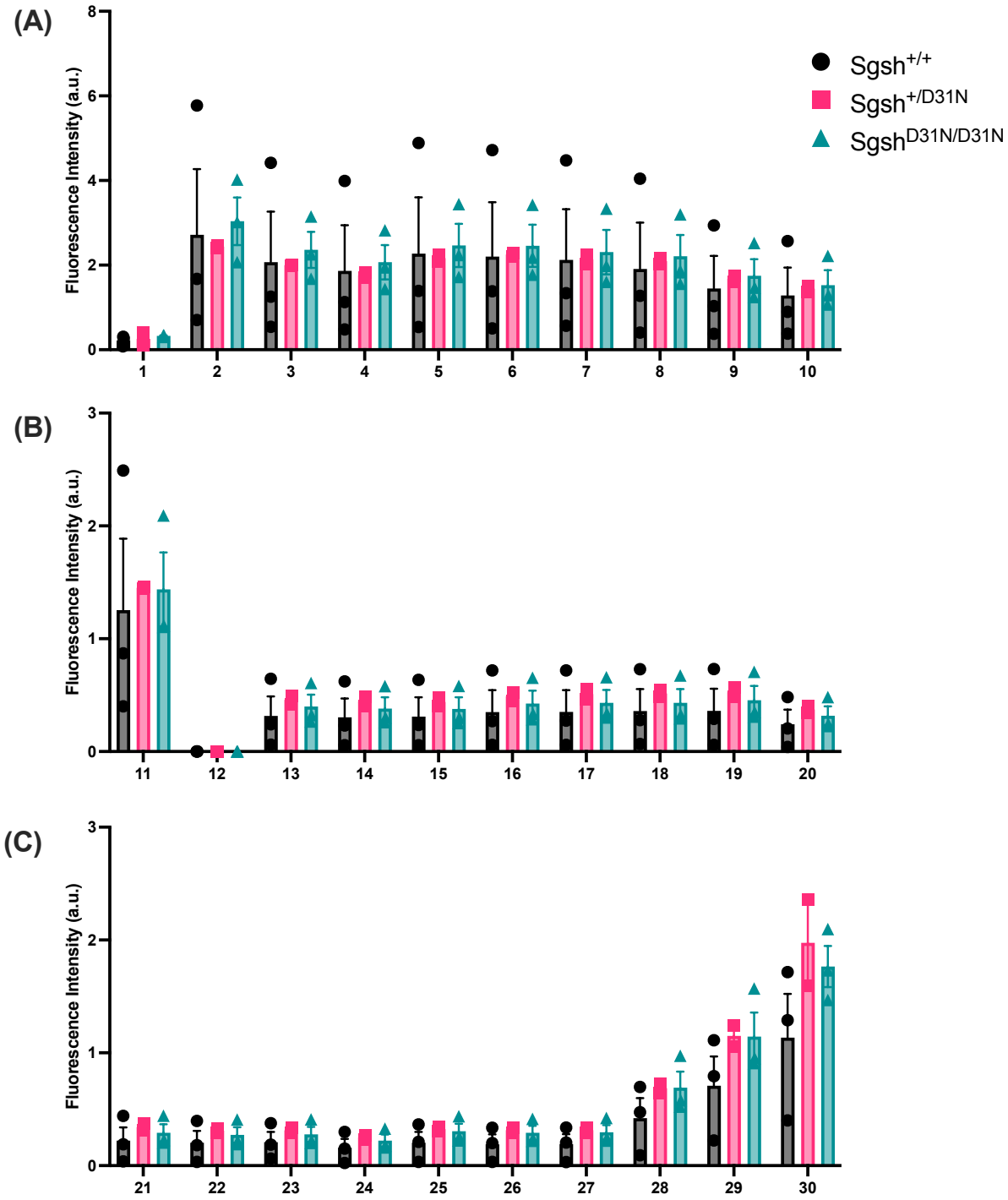
(A)
(B)
(C)
Fluorescence Intensity (a.u.)
Sgsh+/+
Sgsh+/D31N
SgshD31N/D31N

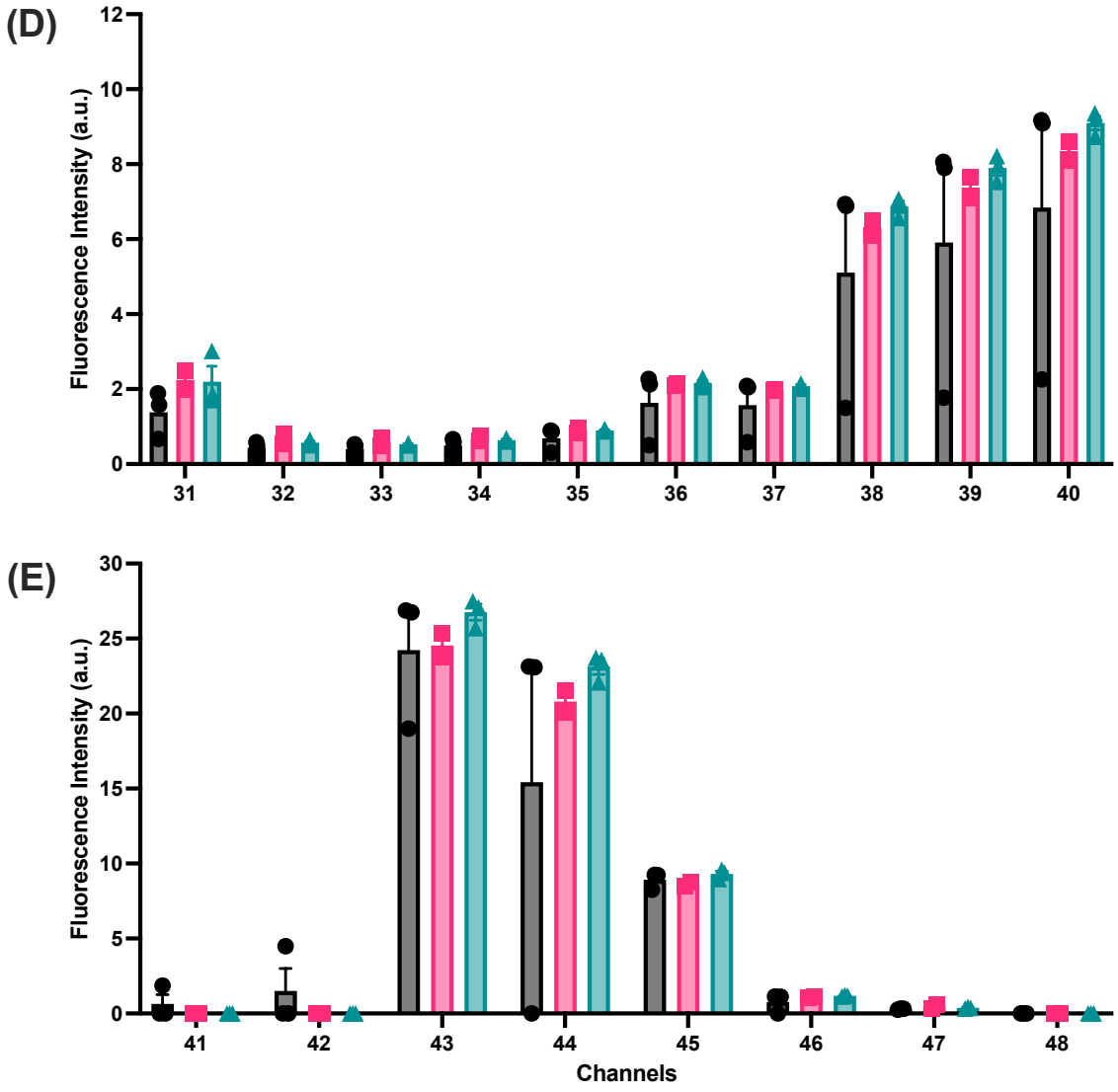

Figure 5.9 Hyperspectral microscopy revealed no changes in endogenous autofluorescence in fixed *Sgsh*$^{+/D31N}$ mouse fibroblasts. (A, B, C, D, E) bar graphs of spectral channels. No changes in autofluorescence intensity were found in the spectral channels in mice of different genotypes. n = 3 *Sgsh*$^{+/+}$ and *Sgsh*$^{D31N/D31N}$ fibroblasts and n = 2 *Sgsh*$^{+/D31N}$; 3 technical replicate per genotype; 4 images per technical replicate; One heterozygous fibroblast was omitted due to low cell density at the time of experiment; Data are represented as mean ± SEM.

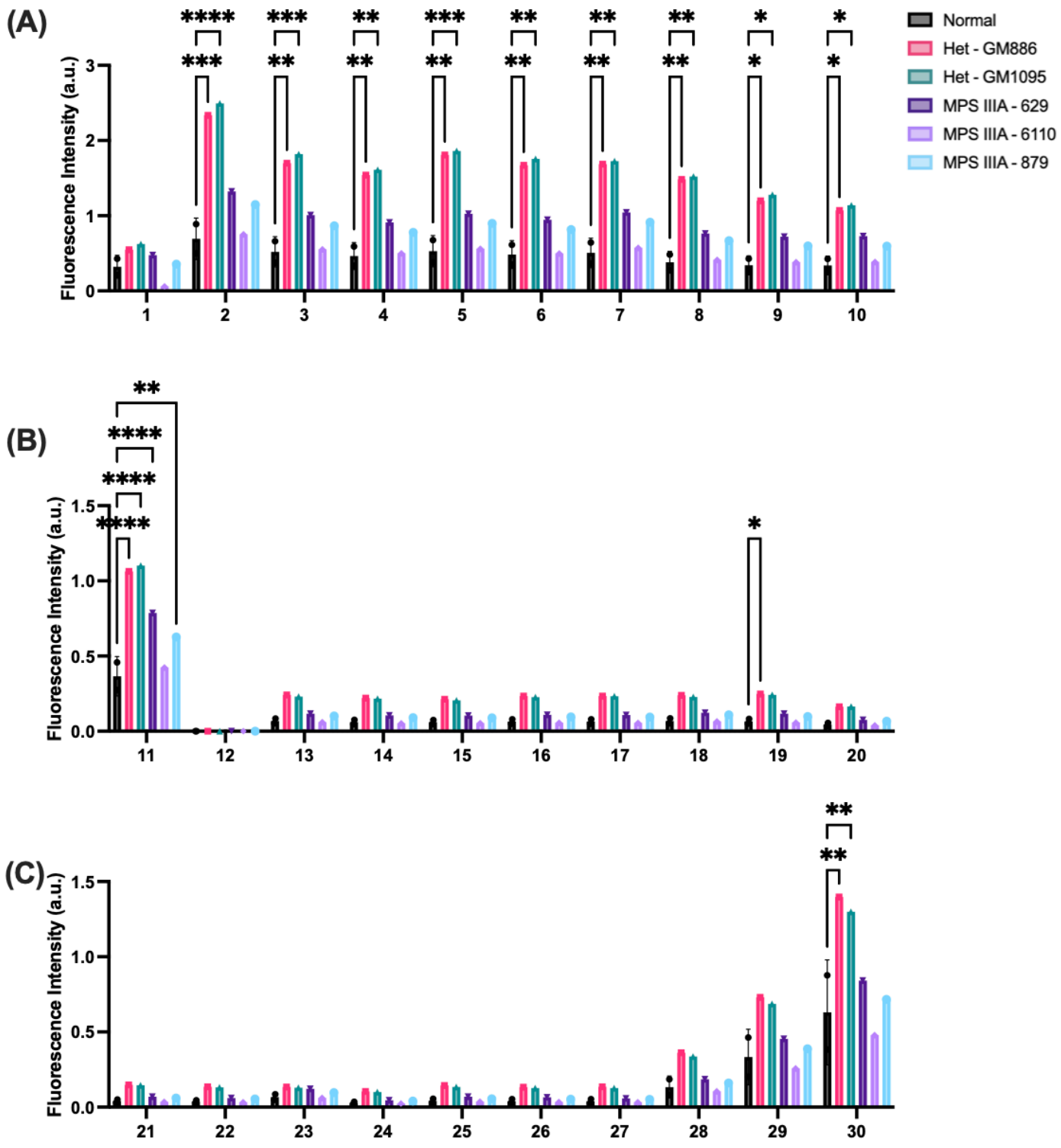
(A)
Fluorescence Intensity (a.u.)
Normal
Het - GM886
Het - GM1095
MPS IIIA - 629
MPS IIIA - 6110
MPS IIIA - 879
(B)
Fluorescence Intensity (a.u.)
(C)
Fluorescence Intensity (a.u.)

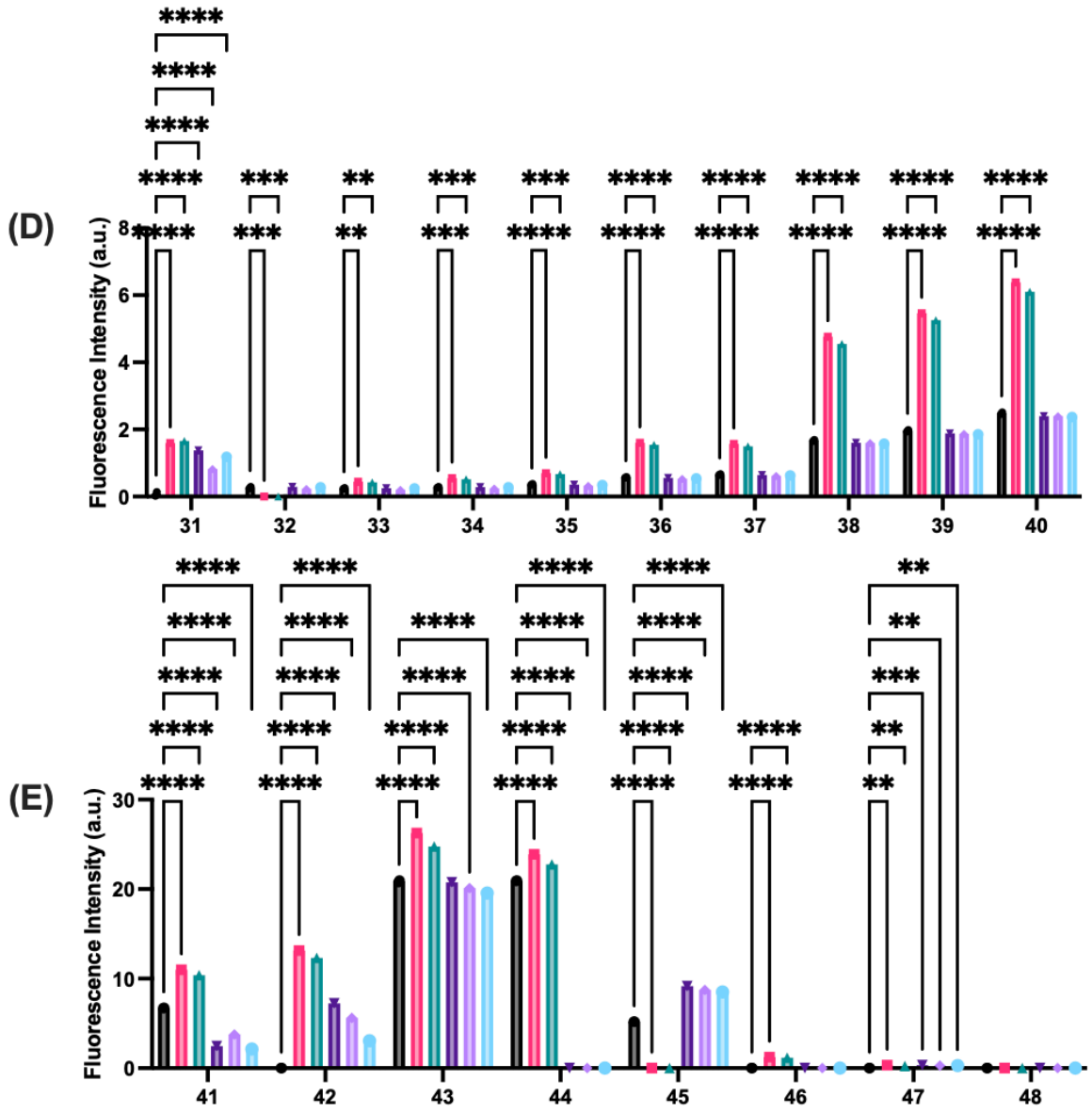

Figure 5.10 Hyperspectral microscopy detects metabolic changes in human fibroblasts. (A, C, E, G, I) bar graphs of spectral channels (B, D, F, H, J) spectral line graph. Autofluorescence intensity was statistically significant between genotypes as observed in some spectral channels. n = 2 normal and heterozygous and n = 3 MPS IIIA fibroblasts; 3 technical replicates per genotype; 4 images per technical replicate; One wildtype and one heterozygous fibroblast was omitted due to low cell density at the time of experiment; *P<0.05; **P<0.01; ***P<0.00l, ****P<0.0001; Two-way ANOVA; Data are represented as mean ± SEM.

5.4 Discussion

In this study, skin fibroblasts derived from mice and patients with MPS IIIA and from murine and human carriers of mutations in the *Sgsh/SGSH* gene were used as cell models in which to examine changes in metabolic activity. Skin fibroblasts have been suggested as a useful strategy to investigate and detect early mitochondrial abnormalities in neurodegenerative diseases such as Alzheimer's disease, Parkinson's disease, and Huntington's disease (328-330). Skin fibroblasts obtained from these patients can be reprogrammed into neuronal cells and the metabolic changes observed are similar to those seen in the skin fibroblasts (328-330). Importantly, mitochondrial dysfunction that is commonly found in neurodegenerative diseases such as oxidative stress, reduced ATP levels, and altered mitochondrial morphology have been reported in skin fibroblasts derived from human patients (331-335). Hence, fibroblasts represent a novel and accessible cell model in which to study the progression of mitochondrial dysfunction and other metabolic abnormalities in neurological diseases.

5.4.1 Changes in ΔΨm in *Sgsh* mouse and *SGSH* human fibroblast carrying single or homozygous mutations

Stability of intracellular ATP and ΔΨm is required for normal cellular functioning (336, 337). Prolonged perturbation of these factors can contribute to loss of cell viability, resulting in pathological consequences (reviewed in (338)). Recent findings have also indicated that ΔΨm plays an important role in mitochondrial viability and elimination of dysfunctional mitochondria (reviewed in (339)). Hence, altered ΔΨm has been widely used as an indicator of mitochondrial function prior to deeper investigation into mitochondrial bioenergetics.

In this study, the ΔΨm in MPS IIIA human fibroblasts was significantly lower compared to that in normal fibroblasts, with no changes observed in ΔΨm in human *SGSH* heterozygous fibroblasts. The human fibroblast data are consistent with previous studies where mitochondrial dysfunction was reported in MPS III mice (227, 228, 311, 340). Decrease in ΔΨm in MPS IIIA human fibroblasts suggest that the mitochondria could be bioenergetically stressed due to ATP depletion as a decrease in ΔΨm is associated with reduced ATP production. Decreased ATP in MPS III could potentially be a result of impaired OxPhos where a decrease in complex II and IV activities was observed in MPS IIIC. (228). This is further supported by proteomic studies in MPS IIIB mouse model where mitochondrial proteins such

as NADH dehydrogenase, ATP synthase, and pyruvate dehydrogenase were found to be downregulated, hence, impacting ATP synthesis (237). It is important to note that while the above findings shed light on the mitochondrial dysfunction in MPS IIIA, the focus of this study is on *SGSH* heterozygous human fibroblasts. Despite observing parallel changes in the disease state, the specific assays used in this study did not reveal similar alterations in the *SGSH* heterozygotes human fibroblasts. This discrepancy could potentially be attributed to the low sample size, sensitivity of the assay, or ΔΨm is unaffected in *SGSH* heterozygous human fibroblasts.

Moreover, murine *Sgsh*$^{+/D31N}$ mouse fibroblasts unexpectedly exhibit a significantly higher levels of JC-1 fluorescence intensity ratio, indicative of increased ΔΨm in the fibroblast. Increased in ΔΨm is typically associated with an upregulation of ATP production. However, given that the study is underpowered, a repeat study is required to confirm this observation. The potential reason for increased ΔΨm in mouse *Sgsh*$^{+/D31N}$ fibroblasts are unclear but it could potentially be due several factors such as a compensatory need for an increase in energy demand or for mitochondrial biogenesis (341). An increase in ΔΨm can also be a sign of mitochondrial stress and dysfunction as a result of increased production of ROS due to excessive ATP production (342). As a consequence, production of ROS can lead to deleterious effect in cells such as damage to cellular proteins and DNA (343). Intriguingly, no changes in ΔΨm were observed in *Sgsh*$^{D31N/D31N}$ mouse fibroblast compared to wildtype, suggesting that mitochondrial function is unperturbed. However, previous studies conducted on MPS III mouse models revealed that mitochondrial dysfunction is affected (227, 237, 312). These studies observed alterations in mitochondrial morphology, decrease in OxPhos, impaired mitophagy, and perturbed mitochondrial pathways, as determined by proteomic analyses (227, 228, 237, 312). These various non-significant and variably contradictory findings could potentially be due to low sample size in the *Sgsh*$^{+/+}$ and *Sgsh*$^{D31N/D31N}$ cell line, thus affecting statistical power in the study. Hence, future studies will need to include more cell lines to increase statistical power. Moreover, measurement of ATP production and ROS is required to validate the findings in *Sgsh*$^{+/D31N}$ and *Sgsh*$^{D31N/D31N}$ mice fibroblasts as well as human fibroblasts carrying single or homozygous *SGSH* mutations.

5.4.2 Assessment of mitochondrial bioenergetics in mouse and human fibroblast

Following from the determination of ΔΨm, a Seahorse Mito Stress Test was utilised to study the potential causes of mitochondrial dysfunction, while hyperspectral imaging was used to detect alterations in metabolic activity in mouse and human fibroblast cells.

In this study, human MPS IIIA fibroblasts showed a reduction in maximal respiration, spare respiratory capacity, and proton leak. The decreased OCR rate in maximal respiration and spare respiratory capacity suggest that human MPS IIIA cells (GM629 and GM879) have an impaired response to satisfy an increased in energy demand and a loss in reserve capacity. These findings support those in a recent study conducted by Tillo et al. where they found that MPS IIIA mice exhibited impaired mitophagy in BAT, resulting in accumulation of dysfunctional mitochondria and an increase in ROS production (312). The study suggests that the impaired mitochondrial activity in BAT may contribute to the metabolic abnormalities observed and that the persistent rise in energy demand could indicate the reduced capability to generate ATP in MPS IIIA. Moreover, impair mitophagy in MPS IIIA mice could potentially be a result of defective lysosomal function, specifically autophagy (344). Autophagy is the cellular process in which damaged or cellular components are degraded and recycled while mitophagy is responsible for the removal of damaged or dysfunctional mitochondria for degradation (345). In MPS IIIA, the production of SGSH misfolded proteins due to the missense mutations (shown in Table 5.1) can affect protein folding and stability. As a result, accumulation of misfolded proteins as well as heparan sulfate occurs in the lysosome leading to impaired autophagy, and the removal of defective mitochondria via mitophagy. Hence, a build-up of defective mitochondria in the cells can lead to impaired ATP production and increased generation of ROS that can damage cellular components (346). Furthermore, under certain conditions, the cells in the body can require an increased amount of ATP, in response to cellular stress or increased in workload (347). However, if the spare respiratory capacity of the cell is unable to provide the required ATP as shown in MPS IIIA, this will result in cellular senescence and ultimately, cell death (348). Additionally, depletion of spare respiratory capacity has been associated with various diseases including cardiovascular and neurodegenerative diseases (349-351).

Also, accumulation of toxic molecules such as lipids and ceramides in LSDs have also been shown to impair mitochondrial function by interfering with mitochondrial electron transport chain, mitochondrial respiration, OxPhos, and ATP production (352). Hence, a decreased in both maximal respiration and spare respiratory capacity in MPS IIIA human

fibroblast reflects unhealthy mitochondria. Moreover, proton leak was also found to be significantly altered in all three human MPS IIIA fibroblast suggesting mitochondrial membrane damage. Studies have shown that damage in the mitochondrial membrane can result in altered mitochondrial morphology and loss of electrochemical gradient (as shown in Figure 5.4, B) (353), which ultimately can cause impair activity of the electron transport chain and decrease ATP production.

On the other hand, *SGSH* heterozygous human fibroblasts showed perturbation in basal respiration and ATP-production coupled respiration. An increased in basal respiration compared to normal fibroblast suggest that basal respiration is almost entirely driven by ATP coupled respiration and the decreased in basal respiration indicate that the cells may utilise a different metabolic pathway for ATP synthesis. This is evident in Chapter 3 where KEGG glycolysis pathway was found to be perturbed from 12 weeks of age. Moreover, the three *SGSH* heterozygous human fibroblast exhibit different mitochondrial phenotypes, suggesting the perturbed changes in mitochondrial respiration could potentially be due to the type of mutations inherited (Table 5.1). NT1307, E447K, and R245H mutations are missense mutations, producing misfolded SGSH proteins whereas 9-BP-DEL mutation is deletion producing truncated SGSH protein. However, the effect of the mutations on SGSH protein and mitochondrial health is not well characterised and further work is required to fully comprehend the effects of misfolded proteins in mitochondrial function.

In contrast, mouse $Sgsh^{D31N/D31N}$ and $Sgsh^{+/D31N}$ fibroblast did not show any significant changes in any of the mitochondrial parameters assessed. However, a trend towards a reduction in mitochondrial respiration can be seen in all the parameters in $Sgsh^{D31N/D31N}$ mouse fibroblast. The non-significant findings in this study could potentially be due to low sample size in the experiments, thus, impacting statistical power in determining a statistical significance. Moreover, both mouse *Sgsh* heterozygous and MPS IIIA fibroblast carry an *Sgsh* D31N mutation and no studies have reported mitochondrial dysfunction in this mouse model.

Whilst spectral unmixing was unfortunately not possible in this study, based on previous studies, channels 1 and 2 correspond to the spectral properties of NADH and NADPH (318, 354). However, as both NADH and NADPH share near identical spectral properties, they are collectively referred to as NAD(P)H to represent their combined signals (355). Moreover, channels 24 and 25 correspond to the spectral properties of flavin adenine dinuecleotide (FAD) (318, 354). The metabolic coenzymes NADH and FAD are autofluorescent and can be monitored non-invasively using optical techniques. Typically, the intensity of NADPH divided by the intensity of FAD is referred to as the optical redox ratio (ORR) (356) which is commonly

used to detect metabolic shifts in cells (357, 358). Hence, changes in these channels can only indicate a potential change in metabolic activity and are used to confirm the observation seen in the mitochondrial assays.

The results of this study revealed that human *SGSH* heterozygous fibroblasts showed increased autofluorescence intensity in channel 2 and no changes in channels 24 and 25 between genotypes, indicative of NAD(P)H perturbation but not FAD. These results further support the idea of impaired mitochondrial respiration in heterozygous human fibroblasts as shown in Figure 5.7. Changes in these metabolic coenzymes can directly impact the level of ATP production. Moreover, studies have shown that increased in NAD(P)H and FAD is associated with increased metabolic cellular activity whilst a decrease implies impaired cellular metabolic activity. Furthermore, given that no studies have reported changes in the other spectral channels and spectral unmixing was unable to be done, we can only speculate that the changes observed in the earlier channels (1-25 and 32-39) corresponds to changes in collagen, elastin, keratin, amino acids, and mitochondrial proteins such as NADH and FAD whereas the later channels (26-31 and 40-55) correspond to changes in vitamins, flavins, porphyrin, lipopigments and lipids such as lipofuscin that is commonly seen in LSDs (Figure 5.2; spectral channel excitation/emission wavelength can be found in Appendix 7).

In contrast, mitochondrial assays conducted in mouse *Sgsh*$^{+/D31N}$ fibroblasts showed no apparent changes in mitochondrial activity, further suggesting that the D31N missense mutation, do not have a pathogenic effect on mitochondrial function, although, perturbations of dysregulated proteins in energy-related pathways were identified in Chapter 3. However, further studies are required to confirm this observation.

Overall, the relationship between different mutations in *Sgsh/SGSH* gene and mitochondrial function remains to be elucidated. However, it is clear that lysosomal dysfunction can have an impact on mitochondria, and that maintaining proper protein folding and quality control within both organelles is critical for maintaining cellular health. Hence, to better understand the underlying mechanism behind mitochondrial dysfunction in MPS IIIA and *Sgsh/SGSH* heterozygotes, future studies will need to investigate for changes in mitochondrial DNA to determine mitochondrial biogenesis, the number of mitochondria per cell as well as fission and fusion processes in the mitochondria. More importantly, given that these assays only looked at aerobic respiration (oxidative phosphorylation), mitochondrial assays looking at changes in different metabolic pathway such as glycolysis and fatty acid metabolism needs to be investigated. Moreover, hyperspectral imaging was able to detect changes in metabolic activity in the human fibroblasts, confirming the findings from the

mitochondrial assays. However, due to technical issues, endogenous fluorophores in other spectral channels were unable to be identified by linear unmixing. Therefore, for future studies, spectral unmixing and validation studies are required to determine the changes observed in these spectral channels to provide thorough insight to the biological changes that are occurring within these cells.

5.4.3 Limitations

There are several limitations to this study. Firstly, in the mitochondrial experiments, a small sample size was used due to lack of available cell lines in both mouse and human fibroblast. This is especially true where all human *SGSH* heterozygous and MPS IIIA fibroblasts carry a different mutation. Hence, reducing the biological replicate to one. However, establishment of new mouse and human fibroblasts lines are possible for future studies in order to increase the statistical power of the experiment.

Additionally, normal human fibroblasts used in this experiment showed a lower OCR rate that are similar to the disease state. These fibroblasts could potentially harbor unknown mitochondrial mutations, hence impacting the mitochondrial assay readout. Therefore, future studies might need to include for genetic screening or karyotyping prior to mitochondrial assays to detect any abnormalities in the fibroblasts. Moreover, the human fibroblasts obtained from the cell repository (Coriell Institute) were of from different age-groups (Table 5.1) and may potentially have an impact on data analyses. Hence, increasing the biological replicates or screening for potential mutations in mitochondrial DNA and using age-matched controls to control for the effects of aging in the study can improve the readout of the mitochondrial assay.

Additionally, fixed fibroblast instead of live cells were used for the hyperspectral imaging experiments. The reason being fixed cells are more stable, easier to handle and allow for long-term storage. However, the disadvantage of using fixed cells is that it can potentially lead to altered cellular structure, thus impacting the readout of the hyperspectral imaging data. Also, fixed cells do not reflect the normal cellular environment of the disease state. Hence, future studies should consider utilising live cells for hyperspectral imaging.

5.5 Conclusion

In conclusion, this study found no perturbation in ΔΨm and in the mitochondrial parameters assessed using the Seahorse analysis in the mouse *Sgsh*$^{D31N/D31N}$ fibroblasts, suggesting that homozygous D31N mutations in the *Sgsh* gene do not affect mitochondrial function in this mouse model. On the other hand, altered mitochondrial activity was seen in human MPS IIIA fibroblasts. The results in human MPA IIIA studies are more consistent with prior reports of mitochondrial dysfunction in MPS III as previously reported. However, human *SGSH* heterozygous fibroblasts showed subtle changes in metabolic activity, but these changes seem mutation-dependent. Interestingly, *Sgsh*$^{+/D31N}$ mouse fibroblasts had higher ΔΨm, indicating increased in mitochondrial activity, however, similar to *Sgsh*$^{D31N/D31N}$ mouse fibroblasts, *Sgsh*$^{+/D31N}$ fibroblasts showed no changes in the mitochondrial parameters assessed using the Seahorse Mito Stress test.

The changes in mitochondrial activity observed in *SGSH* heterozygous human fibroblasts were supported by cellular autofluorescence measurement with hyperspectral imaging, which detected differences in NADPH but not FAD levels. For the first time, hyperspectral imaging of cells from mice and patients carrying single or homozygous *Sgsh/SGSH* mutations was carried out. Whilst more work is required, the study outcomes indicate that *SGSH* heterozygous and MPS IIIA human fibroblast have altered metabolic activity. While *Sgsh*$^{+/D31N}$ and *Sgsh*$^{D31N/D31N}$ mouse fibroblasts did not show an overt mitochondrial dysfunction. Nonetheless, more research is required to validate these findings to better understand the mechanism of mitochondrial dysfunction in *Sgsh/SGSH* heterozygotes and MPS IIIA.

Chapter 6: Discussion

6.1 Project significance

As described in Chapter 1, the association between heterozygous *GBA1* mutations and the increased risk of Parkinson's disease has been extensively studied, highlighting the potential link between carriers of lysosomal gene mutations and neurodegeneration. In addition to *GBA1,* the risk for neurodegeneration has also been associated with carriers of other lysosomal gene mutations, such as *NPC1*, *SMPD1*, *GRN*, *CTSD*, *NAGLU*, *HEXB*, and *SGSH*. With an estimated carrier frequency of 1 in 40 (calculated based on Hardy-Weinberg equation) in the general populations, heterozygous mutations in one or more lysosomal pathway genes are potentially important contributors to the global burden of later-onset neurodegenerative disease. Recent studies have found pathological changes in the post-mortem brains of human patients carrying lysosomal gene mutations, including the accumulation of lipofuscin, alpha-synuclein, and TDP-43 pathology in heterozygotes of *GBA1*, *NPC1*, and *GRN* mutations (94, 121, 148, 169, 171). Similarly, current studies in animal models have demonstrated neuropathological changes and neuronal cell loss in carriers of lysosomal gene mutations, along with motor deficits (100, 104, 105, 127, 161). Despite these findings, the impact of heterozygosity within the *SGSH* gene carrying disease-causing mutations on the development of neurological conditions has received limited attention, and the underlying mechanism remains unclear.

Hence, the overall aim of this project was to define the morphological, biochemical, and functional neuronal consequences of heterozygosity in the lysosomal degradative gene, *Sgsh*; in both an authentic murine model arising from a D31N mutation, which leads to mutant (misfolded) enzyme production and decreased activity in affected animals and in *SGSH* heterozygous human cell lines. The overarching hypothesis is that heterozygotes carrying *Sgsh* gene mutations will exhibit significant alterations in the cortical proteome, neuronal morphology, and function, as well as perturbation in mitochondrial bioenergetics due to reduced sulfamidase enzyme activity.

The specific objectives of the study were to;

1. Study the temporal impact of the D31N *Sgsh* heterozygous mutation upon the mouse cortical proteome.

2. Assess the impact of the D31N *Sgsh* heterozygous mutation on motor cortex pyramidal neuron morphology and cortical neural function.

3. Investigate the impact of heterozygous mutations in the metabolic profile of D31N *Sgsh* heterozygous mouse and *SGSH* heterozygous human fibroblast cells.

6.2 Impact of carrying a D31N *Sgsh* mutation on mouse cortical proteome, cortical neuron structure and cell function

A summary of experimental outcomes utilising murine *Sgsh*$^{+/D31N}$ and *Sgsh*$^{D31N/D31N}$ mouse models can be found in Table 6.1.

Table 6.1. Summary of experimental outcomes utilising murine *Sgsh*$^{+/D31N}$ and *Sgsh*$^{D31N/D31N}$ mouse models

Experiment	**Outcomes**
Proteomic analysis	Dysregulated proteins were identified in all timepoints (0-, 3-, 6-, 12-, 24-, and 48-weeks) in *Sgsh*$^{+/D31N}$ mice compared to *Sgsh*$^{+/+}$. Majority of the dysregulated proteins identified were clustered in neurodegenerative (Alzheimer's disease, Parkinson's disease, Huntington's disease) and energy-related pathways (Oxidative phosphorylation, Glycolysis, Pyruvate metabolism). Moreover, phosphatidylinositol signalling pathway and proteins involved in Ubiquitin-Proteasomal System and synaptic transmission were found to be perturbed in *Sgsh*$^{+/D31N}$ mice.
Dendritic spine assessment	No significant changes in dendritic spine density or maturity in layer 5 pyramidal motor cortex neurons at 24-week-old *Sgsh*$^{+/D31N}$ mice.
Multi-electrode array (MEA) recording	MEA recording revealed aberrations in network burst activity in *Sgsh*$^{+/D31N}$ cortical neural cultures compared to *Sgsh*$^{+/+}$ neural cultures. However, neural cultures treated with 0.1nM rotenone exhibited conflicting outcomes compared to previous data. Vehicle treated *Sgsh*$^{+/+}$ and *Sgsh*$^{+/D31N}$ neural cultures showed no aberration in network burst activity between genotypes. Moreover, neural cultures treated with 0.1nM rotenone revealed a decreased in network burst duration in *Sgsh*$^{+/D31N}$ neural cultures at day 6 and 12 *in vitro*.

Measurement of mitochondrial membrane potential (ΔΨm)	*Sgsh*$^{+/D31N}$ mouse fibroblasts show a significant higher ΔΨm compared to *Sgsh*$^{+/+}$; however, no significant changes were observed in *Sgsh*$^{D31N/D31N}$ mouse fibroblasts compared to *Sgsh*$^{+/+}$ fibroblasts.
Seahorse Mito stress test	There were no significant changes between genotypes in the metabolic parameters assessed based on Seahorse Mito Stress test assay.
Hyperspectral imaging	*Sgsh*$^{+/D31N}$ and *Sgsh*$^{D31N/D31N}$ mouse fibroblast showed no changes in the channels corresponding to NADPH and FAD between genotypes. No changes in other spectral channels observed.

Cortical pyramidal neuron structure in *Sgsh*$^{+/D31N}$ mouse brain

The proteomic evaluation of the *Sgsh*$^{+/D31N}$ mouse motor cortex revealed significant reductions in septin proteins in 3, 12, 24 and 48-week-old *Sgsh*$^{+/D31N}$ mice (Chapter 3, Table 3.3). Septins are postulated to have a significant roles in macroautophagy (reviewed in (359)) and contribute to neurite outgrowth, synapse formation and regulation (reviewed in (360)). Whilst the change in septin protein production may be relevant to the previous report of aberrant dendritic structure in 84-week-old *Sgsh*$^{+/D31N}$ mouse pyramidal neurons (161), we observed no differences in dendritic spine number or maturation on motor cortex pyramidal neurons in *Sgsh*$^{+/D31N}$ mice, to at least 24-weeks of age. In contrast, *Sgsh*$^{D31N/D31N}$ mice exhibit reduced dendritic spine numbers from 12 weeks of age (unpublished data, (218)). It is currently unknown whether dendritic spine loss or impairment in spine maturation occurs beyond this timepoint, necessitating further investigation. However, if *Sgsh*$^{+/D31N}$ mice exist on a continuum with *Sgsh*$^{D31N/D31N}$ mice, and depending on the mechanism responsible for the reduced spine numbers in the affected *Sgsh*$^{D31N/D31N}$ mouse brain, it could be postulated that with time, a reduction in spine number occurs in *Sgsh*$^{+/D31N}$ mouse pyramidal neurons in the motor cortex.

Whilst cortical pyramidal neuron architecture was unaffected, neural cultures from *Sgsh*$^{+/D31N}$ mouse cerebral cortex exhibit aberrant neuronal firing.

Considering the aforementioned observation that dendritic spine density in layer 5 motor cortex pyramidal neuron was not affected in *Sgsh*$^{+/D31N}$ mice, it was rather unexpected to find that the firing activity in *Sgsh*$^{+/D31N}$ cortical neural cultures was somewhat reduced (Chapter 4, Figure 4.4). Moreover, the co-ordination of neural network firing activity exhibited significant

impairments (Chapter 4, Figures 4.5, 4.8), particularly at later timepoints in culture. Whilst studies of mitochondrial function were not able to be undertaken in neural cell cultures, the proteomic study found evidence suggestive of dysregulated oxidative phosphorylation in *Sgsh*$^{+/D31N}$ mouse brain (Chapter 3, Table 3.4). Further, increased mitochondrial membrane potential was recorded in three independent *Sgsh*$^{+/D31N}$ mouse skin fibroblast cell lines (Chapter 5, Figure 5.4A), indicative of aberration in cell metabolism and impairment of the mitochondrial redox state, which requires further exploration.

The mitochondrial redox state or optical redox ratio (ORR) has been extensively used as an indicator of cellular dysfunction (361). The ORR is the balance between the fluorescence intensity of two essential cellular metabolic enzymes: NADH and FAD (361). Perturbation in the levels of NADH and FAD can have significant consequences such as dyshomeostasis of cellular redox state, contributing to oxidative stress as well as reduced ATP production, impacting overall cellular function and viability (362). As a consequence, impacting mitochondrial function in maintaining action potentials, release of neurotransmitters and intracellular signalling in the central nervous system (295). Hence, dysregulation of oxidative phosphorylation, specifically in the two essential cellular metabolic enzymes NADH and FAD may potentially contribute to altered neural network activity observed in *Sgsh* D31N heterozygous neural cultures. However, optical imaging showed no differences in cellular autofluorescence corresponding to NADPH and FAD in *Sgsh*$^{+/D31N}$ mouse skin fibroblast cell lines. This may be attributed to the limitations discussed in Chapter 5, where the presence of artefacts during data analysis could hinder the detection of autofluorescence signals in channels corresponding to NADPH and FAD. Hence, a repeat study is required to validate these findings after resolving the technical challenges associated with hyperspectral imaging.

6.3 Impact of carrying a mutation in *SGSH* on human skin fibroblast cell metabolism

A summary of experimental outcomes utilising human *SGSH* heterozygous, and MPS IIIA fibroblast cell lines can be found in Table 6.2.

Table 6.2. Summary of experimental outcomes utilising human *SGSH* heterozygous, and MPS IIIA fibroblast cell lines.

Experiment	**Outcomes**
Measurement of mitochondrial membrane potential (ΔΨm)	No significant changes in ΔΨm in human *SGSH* fibroblast cell lines. However, all three human MPS IIIA fibroblast cell lines showed significant reduction in ΔΨm compared to normal fibroblasts.
Seahorse Mito stress test	MPS IIIA and *SGSH* heterozygous fibroblast cell lines showed a reduction in mitochondrial respiration. However, no changes in mitochondrial respiration was observed in one *SGSH* heterozygous fibroblasts compared to normal fibroblasts.
Hyperspectral imaging	*SGSH* heterozygous fibroblasts exhibit changes in autofluorescence in channel 2 and no changes in channels 24 and 25, suggesting NADPH is increased with no changes in FAD. No changes in channels 1, 2, 24, 25 was detected in MPS IIIA fibroblasts. However, *SGSH* heterozygous and MPS IIIA human fibroblasts exhibited alterations in endogenous fluorophores in other spectral channels, indicative of perturbation in other cellular physiological processes.

Mutation-dependent changes in mitochondrial function and endogenous fluorescence in human *SGSH*-deficient fibroblasts.

Mitochondrial membrane potential, mitochondrial respiration and expression of endogenous autofluorescence was examined in multiple human MPS IIIA and heterozygous *SGSH* mutation-carrying fibroblast cell lines (Chapter 5, Figures 5.4, 5.7 and 5.10, respectively). Mutation type did not appear to significantly affect mitochondrial assay outcomes in human MPS IIIA skin fibroblasts, with equivalent reductions in mitochondrial membrane potential and respiration seen in the three MPS IIIA cell lines (Chapter 5, Figure 5.4, 5.7), however oxygen consumption rate in particular was obviously different between cell lines from the three different *SGSH* mutation carriers. Significantly elevated basal and ATP-coupled respiration were seen in a carrier of an E447K or R245H mutation in *SGSH* (Chapter 5, Figure 5.7), whereas significantly reduced respiration parameters were observed in a carrier expressing either a 9-BP deletion mutation in *SGSH* (1307 del 9; (363)) or an unknown mutation. Unfortunately, it is not known precisely which *SGSH* mutation these cell lines exhibit; carrier status is predicted by the mutations found in cells from the proband's offspring. Given the current findings, future studies would involve mutational analysis, in addition to the collection and analysis of cell lines from a larger number of *SGSH* mutation carriers.

It is important to note that the type of mutation plays a significant role in the development, progression, and severity of genetic diseases. It is hypothesised that different types of mutations can have varying impacts on the function of the affected gene, leading to diverse clinical manifestations and consequences. Evidently, missense mutations can have minimal or no effect on protein function, while others can lead to a loss of function, gain of function, or altered protein function, resulting in clinical disease (364). For example, in a study conducted in MPS IIIC mouse models carrying P304L mutations or knockout *Hgsnat* gene exhibited different phenotype despite producing similar levels of HGSNAT activity (197). Mice homozygous for the *Hgsnat*^{P304L} mutation producing misfolded protein show an earlier onset of behavioural changes with reduced lifespan, increased neuroinflammation, and defects in synaptic neurotransmission (197), suggesting that the mutation that leads to product of a mutant misfolded proteins hastens the disease pathology and infers a toxic gain of function. Moreover, the three *SGSH* heterozygous human fibroblast exhibit different mitochondrial phenotypes, suggesting the perturbed changes in mitochondrial respiration could potentially be due to the type of mutations inherited (Chapter 5, Table 5.1). Moreover, it is also plausible that the small sample size in this study is diminishing its statistical power, which may, in turn, affect the outcomes of the mitochondrial assays. Nevertheless, given the limited number of studies available, further research is needed to substantiate this hypothesis, as the differences in pathology could also be enzyme-dependent.

Paucity of models in which to study impact of *SGSH* mutation heterozygosity

Whilst the models utilised herein, all represent heterozygosity for the *Sgsh/SGSH* gene, there are obvious differences in the outcomes obtained from the various mouse and human cell lines and the mouse model which make definitive conclusions difficult at this point. A mouse model exhibiting a human mutation (R245H) in the *Sgsh* gene is presently under construction (K Hemsley, personal communication), and collection, banking and examination of further samples from *SGSH* mutation carriers is necessary in order to fully determine the impact of *Sgsh/SGSH* mutation type, if any, towards deleterious cell or organ function.

The use of induced pluripotent stem cells (IPSCs) and neuronal models have emerged as a valuable tool for modelling various diseases, including neurological disorders (365). IPSCs can be generated by reprogramming adult somatic cells such as skin fibroblasts into pluripotent state, which enables them to differentiate into various cell types, including neurons (366). Hence, the development of IPSC-derived neuronal models from a large collection of *SGSH*

mutation heterozygotes represents a promising future direction in research. By generating IPSCs, we can gain valuable insights into the molecular, cellular and functional consequences of these mutations in *SGSH* heterozygotes with deficient sulfamidase enzyme. Future studies such as comparative transcriptome, proteome, electrophysiological function of these IPSC-derived neuronal models will allow insight to the molecular and cellular basis of *SGSH*-related diseases, if any. Hence, this knowledge can better inform the development of new novel therapies and potentially act as “vaccine” to reduce the risk of a clinical disease.

6.3 Conclusion

In conclusion, the findings collectively reported in this thesis contribute new knowledge to the rapidly expanding literature investigating the underlying mechanism of potential neurological dysfunction in carriers of lysosomal gene mutations, specifically in *Sgsh/SGSH* gene. The findings highlight that *Sgsh*$^{+/D31N}$ mouse motor cortex proteome is perturbed from infancy to adulthood with neurodegenerative and energy-related pathways were found to be impacted. Furthermore, although, no aberration in dendritic spine density or maturity in layer 5 motor cortical pyramidal neurons were observed at 24-weeks old, *Sgsh*$^{+/D31N}$ neural cultures exhibited impaired neuronal network activity. However, these data need to be interpreted with caution due to conflicting data obtained from the rotenone treated neural cultures and a repeat assay is required to validate these findings. Investigation of mitochondrial function in *Sgsh*$^{+/D31N}$ mouse fibroblasts also showed subtle changes in metabolic activity. On the other hand, changes in mitochondrial activity, specifically in the *SGSH* heterozygous human fibroblasts seem to be mutation dependent with endogenous fluorophores NADPH found to be altered compared to normal and MPS IIIA human fibroblasts. It is also important to note that the age of mice utilised in this study corresponds to around 30-40 years in humans where pathologies might not yet be present, and pathological changes could develop later in life. Therefore, future studies utilising older mice may provide valuable insights into potential neurological dysfunction in *Sgsh* heterozygotes carrying disease-causing mutations.

Overall, our understanding of the biological basis underlying such increased vulnerability still remains limited. We hypothesised that heterozygous mutations in lysosomal genes are best conceptualised as a biological clinical continuum based on current evidence. This corresponds to disease progression from the asymptomatic to the preclinical to the symptomatic phase, where changes continue, and symptoms of cognitive and functional impairment becomes evident. It is also important to note that not all carriers of lysosomal gene mutations will develop a neurological condition, and other factors such as environmental or epigenetic changes may play a significant role in increasing the risk of clinical disease. Despite the extensive knowledge acquired about lysosomal gene mutation pathogenicity, particularly in the heterozygous state, there is still much to explore on the impact of *Sgsh/SGSH* mutations. The potential involvement of other organ systems warrants further investigations but should not detract from the main focus on understanding the neurological implications of carrying *Sgsh/SGSH* gene mutations.

Appendices

Appendix 1. Dysregulated proteins in *Sgsh* D31N heterozygous mouse motor cortex compared to wildtype at 0 Week.

Swiss-Prot Code	Gene Name	Protein Description	Up- or Down-regulation	P-Value
Q02780	Nfia	Nuclear factor 1 A-type	↑	0.04586215
P97863	Nfib	Nuclear factor 1 B-type	↑	0.03675959
Q9WUK6	Zbtb18	Zinc finger and BTB domain-containing protein 18	↑	0.03178816
Q61390	Cct6b	T-complex protein 1 subunit zeta-2	↑	0.00995502
Q6PE01	Snrnp40	U5 small nuclear ribonucleoprotein 40 kDa protein	↑	0.01093218
Q60625	Icam5	Intercellular adhesion molecule 5	↑	0.01501847
Q8VE37	Rcc1	Regulator of chromosome condensation	↑	0.00947436
P09602	Hmgn2	Non-histone chromosomal protein HMG-17	↑	0.02433915
O70591	Pfdn2	Prefoldin subunit 2	↑	0.0235222
O70435	Psma3	Proteasome subunit alpha type-3	↑	0.01124378
Q91V81	Rbm42	RNA-binding protein 42	↑	0.03821496
Q8BK30	Ndufv3	NADH dehydrogenase [ubiquinone] flavoprotein 3, mitochondrial	↑	0.02751149
Q9CQF9	Pcyox1	Prenylcysteine oxidase	↑	0.00155584
Q62241	Snrpc	U1 small nuclear ribonucleoprotein C	↑	0.00886083
Q9CQB5	Cisd2	CDGSH iron-sulfur domain-containing protein 2	↑	0.04687138
P62307	Snrpf	Small nuclear ribonucleoprotein F	↑	0.02281593
Q9CRB2	Nhp2	H/ACA ribonucleoprotein complex subunit 2	↑	0.01788332
P62827	Ran;Rasl2-9	GTP-binding nuclear protein Ran;GTP-binding nuclear protein Ran, testis-specific isoform	↑	0.00890739
Q5SQM0	Eml6	Echinoderm microtubule-associated protein-like 6	↑	0.00529462
O88477	Igf2bp1	Insulin-like growth factor 2 mRNA-binding protein 1	↑	0.00265474
Q61545	Ewsr1	RNA-binding protein EWS	↑	0.01625294

P61957	Sumo2;Sumo3	Small ubiquitin-related modifier 2;Small ubiquitin-related modifier 3	↑	0.00621438
Q8C7Q4	Rbm4;Rbm4b	RNA-binding protein 4;RNA-binding protein 4B	↑	0.01449669
P31786	Dbi	Acyl-CoA-binding protein	↑	0.01350332
P97825	Hn1	Hematological and neurological expressed 1 protein;Hematological and neurological expressed 1 protein, N-terminally processed	↑	0.00198037
O35286	Dhx15	Pre-mRNA-splicing factor ATP-dependent RNA helicase DHX15	↑	0.04294161
Q9CQ22	Lamtor1	Ragulator complex protein LAMTOR1	↑	0.0048279
Q9WTR5	Cdh13	Cadherin-13	↑	0.0368246
P59708	Sf3b6	Splicing factor 3B subunit 6	↑	0.04545502
Q8R2Y8	Ptrh2	Peptidyl-tRNA hydrolase 2, mitochondrial	↑	0.04627426
P84104	Srsf3	Serine/arginine-rich splicing factor 3	↑	0.03557428
Q9ERS2	Ndufa13	NADH dehydrogenase [ubiquinone] 1 alpha subcomplex subunit 13	↑	0.03813646
Q9JIK5	Ddx21	Nucleolar RNA helicase 2	↑	0.01438199
O70194	Eif3d	Eukaryotic translation initiation factor 3 subunit D	↑	0.01583444
Q60899	Elavl2	ELAV-like protein 2	↑	0.03935939
Q61937	Npm1	Nucleophosmin	↑	0.04027972
Q8K4Z5	Sf3a1	Splicing factor 3A subunit 1	↑	0.01050494
Q9QXT0	Cnpy2	Protein canopy homolog 2	↑	0.03382839
Q99P88	Nup155	Nuclear pore complex protein Nup155	↑	0.03017667
Q60634	Flot2	Flotillin-2	↑	0.00466535
P62313	Lsm6	U6 snRNA-associated Sm-like protein LSm6	↑	0.01864629
P12815	Pdcd6	Programmed cell death protein 6	↑	0.02654855
Q8BK67	Rcc2	Protein RCC2	↑	0.04683187
O55128	Sap18	Histone deacetylase complex subunit SAP18	↑	0.03130063
Q9D593	Atp6v1e2	V-type proton ATPase subunit E 2	↑	0.04018359
Q3UHX2	Pdap1	28 kDa heat- and acid-stable phosphoprotein	↑	0.02256048
Q9CQE8	Rtraf	UPF0568 protein C14orf166 homolog	↑	0.0379237
O08583	Alyref;Alyref2	Aly/REF export factor 2;THO complex subunit 4	↑	0.03239668

Q8VH51	Rbm39	RNA-binding protein 39	↑	0.04575445
P68037	Ube2l3	Ubiquitin-conjugating enzyme E2 L3	↑	0.02083104
P29595	Nedd8	NEDD8	↑	0.0310039
Q9ESX5	Dkc1	H/ACA ribonucleoprotein complex subunit 4	↑	0.02902403
Q8R464	Cadm4	Cell adhesion molecule 4	↑	0.00695691
Q8CGF7	Tcerg1	Transcription elongation regulator 1	↑	0.01548578
Q9JKC8	Ap3m1	AP-3 complex subunit mu-1	↑	0.01193256
Q62446	Fkbp3	Peptidyl-prolyl cis-trans isomerase FKBP3	↑	0.04791747
Q921M3	Sf3b3	Splicing factor 3B subunit 3	↑	0.02479576
O08756	Hsd17b10	3-hydroxyacyl-CoA dehydrogenase type-2	↑	0.0451337
Q80YP0	Cdk3	Cyclin-dependent kinase 3	↑	0.01937114
P35802	Gpm6a	Neuronal membrane glycoprotein M6-a	↑	0.02705752
Q6ZWM4	Lsm8	U6 snRNA-associated Sm-like protein LSm8	↑	0.04098188
P55258	Rab13;Rab8a	Ras-related protein Rab-13;Ras-related protein Rab-8A	↑	0.03992539
Q68FL4	Ahcy;Ahcyl2	Adenosylhomocysteinase;Putative adenosylhomocysteinase 3	↑	0.01730525
P15116	Cdh2	Cadherin-2	↑	0.03260721
P35700	Prdx1	Peroxiredoxin-1	↑	0.01576939
P48771	Cox7a2	Cytochrome c oxidase subunit 7A2, mitochondrial	↑	0.0153701
Q6ZWV7	Rpl35	60S ribosomal protein L35	↑	0.01492587
P35235	Ptpn11	Tyrosine-protein phosphatase non-receptor type 11	↑	0.01809286
Q9CY58	Serbp1	Plasminogen activator inhibitor 1 RNA-binding protein	↑	0.0464965
Q9CQD1	Rab5a	Ras-related protein Rab-5A	↑	0.03476037
Q9Z0X1	Aifm1	Apoptosis-inducing factor 1, mitochondrial	↑	0.00355419
P35803	Gpm6b	Neuronal membrane glycoprotein M6-b	↑	0.01105791
Q6A068	Cdc5l	Cell division cycle 5-like protein	↑	0.00803331
Q6ZWN5	Rps9	40S ribosomal protein S9	↑	0.04430932
Q9D0S9	Hint2	Histidine triad nucleotide-binding protein 2, mitochondrial	↑	0.02948879
O08579	Emd	Emerin	↑	0.01569638

P35278	Rab5c	Ras-related protein Rab-5C	↑	0.03567857
Q8CC88	Vwa8	von Willebrand factor A domain-containing protein 8	↑	0.03334593
Q9CY50	Ssr1	Translocon-associated protein subunit alpha	↑	0.02285707
Q9CR68	Uqcrfs1	Cytochrome b-c1 complex subunit 11;Cytochrome b-c1 complex subunit Rieske, mitochondrial	↑	0.03236579
P56812	Pdcd5	Programmed cell death protein 5	↑	0.04675579
Q9Z0H8	Clip2	CAP-Gly domain-containing linker protein 2	↑	0.03224432
P15532	Nme1	Nucleoside diphosphate kinase A	↑	0.02570382
Q8BKC5	Ipo5	Importin-5	↑	0.01831997
Q9D0L7	Armc10	Armadillo repeat-containing protein 10	↑	0.01757899
P63318	Prkcg	Protein kinase C gamma type	↑	0.03552422
Q9CQI3	Gmfb	Glia maturation factor beta	↑	0.03745108
Q9DCN2	Cyb5r3	NADH-cytochrome b5 reductase 3	↑	0.031884
Q8JZK9	Hmgcs1	Hydroxymethylglutaryl-CoA synthase, mitochondrial	↓	0.00085672
Q920I9	Wdr7	WD repeat-containing protein 7	↓	0.03788167
Q8QZY1	Eif3l	Eukaryotic translation initiation factor 3 subunit L	↓	0.04511473
P46935	Nedd4	E3 ubiquitin-protein ligase NEDD4	↓	0.02706558
Q8VDM6	Hnrnpul1	Heterogeneous nuclear ribonucleoprotein U-like protein 1	↓	0.00392909
Q61548	Snap91	Clathrin coat assembly protein AP180	↓	0.04480189
O88712	Ctbp1;Ctbp2	C-terminal-binding protein 1;C-terminal-binding protein 2	↓	0.00759955
Q9QUM9	Psma6	Proteasome subunit alpha type-6	↓	0.01166511
Q5SQX6	Cyfip2	Cytoplasmic FMR1-interacting protein 2	↓	0.0137793
Q3V3R1	Mthfd1l	Monofunctional C1-tetrahydrofolate synthase, mitochondrial	↓	0.01800445
Q6R0H7	Gnal;Gnas	Guanine nucleotide-binding protein G(olf) subunit alpha	↓	0.03268713
Q8JZU2	Slc25a1	Tricarboxylate transport protein, mitochondrial	↓	0.01061454
P84084	Arf5	ADP-ribosylation factor 5	↓	0.03267707
Q922Q1	37316	Mitochondrial amidoxime reducing component 2	↓	0.03764158
Q99JY8	Ppap2b	Lipid phosphate phosphohydrolase 3	↓	0.03322637

Q8VD37	Sgip1	SH3-containing GRB2-like protein 3-interacting protein 1	↓	0.04852253
Q91WC3	Acsl6	Long-chain-fatty-acid--CoA ligase 6	↓	0.01958107
Q7TSJ2	Map6	Microtubule-associated protein 6	↓	0.00420014
Q8R0Y6	Aldh1l1	Cytosolic 10-formyltetrahydrofolate dehydrogenase	↓	0.01614558
P62774	Mtpn	Myotrophin	↓	0.01204276
Q9Z1G4	Atp6v0a1	V-type proton ATPase 116 kDa subunit a isoform 1	↓	0.03919869
P35486	Opa3;Pdha1	Optic atrophy 3 protein homolog;Pyruvate dehydrogenase E1 component subunit alpha, somatic form, mitochondrial	↓	0.00177443
P97496	Smarcc1	SWI/SNF complex subunit SMARCC1	↓	0.03413907
Q7TQF7	Amph;Bin2	Amphiphysin;Bridging integrator 2	↓	0.01877625
Q9CR95	Necap1	Adaptin ear-binding coat-associated protein 1	↓	0.02948905
Q63844	Mapk3	Mitogen-activated protein kinase 3	↓	0.02502531
P48036	Anxa5	Annexin A5	↓	0.03865549
Q8BML2	Oacyl	O-acyltransferase like protein	↓	0.02693369
Q61207	Psap	Prosaposin	↓	0.02441452
Q8CH09	Sugp2	SURP and G-patch domain-containing protein 2	↓	0.02075365
P46425	Gstp2	Glutathione S-transferase P 2	↓	0.04555314
O88384	Vti1b	Vesicle transport through interaction with t-SNAREs homolog 1B	↓	0.04358169
Q9DD18	Dtd1	D-tyrosyl-tRNA(Tyr) deacylase 1	↓	0.04014775
P62631	Eef1a2	Elongation factor 1-alpha 2	↓	0.04283618
Q2NL51	Gsk3a	Glycogen synthase kinase-3 alpha	↓	0.02114214
Q9Z2U0	Psma7	Proteasome subunit alpha type-7	↓	0.0440709
Q3UHL1	Camkv	CaM kinase-like vesicle-associated protein	↓	0.01789469
Q9WTT4	Atp6v1g2	V-type proton ATPase subunit G 2	↓	0.012717
P56564	Slc1a3	Excitatory amino acid transporter 1	↓	0.01464726
P62962	Pfn1	Profilin-1	↓	0.00338022
Q61490	Alcam	CD166 antigen	↓	0.01033172
Q8VE62	Paip1	Polyadenylate-binding protein-interacting protein 1	↓	0.03665866

Q9D892	Itpa	Inosine triphosphate pyrophosphatase	↓	0.00990965
Q91Z69	Srgap1	SLIT-ROBO Rho GTPase-activating protein 1	↓	0.0251482
P34884	Mif	Macrophage migration inhibitory factor	↓	0.02074164
P20108	Prdx3	Thioredoxin-dependent peroxide reductase, mitochondrial	↓	0.02486906
Q3V1L4	Nt5c2	Cytosolic purine 5'-nucleotidase	↓	0.01561227
P70324	Tbx3	T-box transcription factor TBX3	↓	0.00826322
Q9WUB3	Pygm	Glycogen phosphorylase, muscle form	↓	0.04969882
Q9WTL7	Lypla2	Acyl-protein thioesterase 2	↓	0.01289199
Q6PHZ2	Camk2d	Calcium/calmodulin-dependent protein kinase type II subunit delta	↓	0.03895368
Q62426	Cstb	Cystatin-B	↓	0.03703075
P50543	S100a11	Protein S100-A11	↓	0.04220812
Q8BGT8	Phyhipl	Phytanoyl-CoA hydroxylase-interacting protein-like	↓	0.00321306

Appendix 2. Dysregulated proteins in *Sgsh* D31N heterozygous mouse motor cortex compared to wildtype at 3 Week.

Swiss-Prot Code	Gene Name	Protein Description	Up- or Down-regulation	P-Value
Q9DCL9	Paics	Multifunctional protein ADE2; Phosphoribosylaminoimidazole carboxylase;Phosphoribosylaminoimidazole-succinocarboxamide synthase	↑	0.04439635
Q9JIX0	Eny2	Transcription and mRNA export factor ENY2	↑	0.02711346
O88271	Cfdp1	Craniofacial development protein 1	↑	0.03444175
Q03958	Pfdn6	Prefoldin subunit 6	↑	0.0122755
P28667	Marcksl1	MARCKS-related protein	↑	0.04426448
Q91WM1	Strbp	Spermatid perinuclear RNA-binding protein	↑	0.0477613
Q9CR51	Atp6v1g1	V-type proton ATPase subunit G 1	↑	0.0291143
Q9WUC3	Ly6h	Lymphocyte antigen 6H	↑	0.01577459
Q99PL5	Rrbp1	Ribosome-binding protein 1	↑	0.03030296
P62869	Tceb2	Transcription elongation factor B polypeptide 2	↑	0.00084293
A2A8L1	Chd5	Chromodomain-helicase-DNA-binding protein 5	↑	0.0431332
Q8K341	Atat1	Alpha-tubulin N-acetyltransferase 1	↑	0.02828131
P60122	Ruvbl1	RuvB-like 1	↑	0.00357921
Q9D7S7	Rpl22l1	60S ribosomal protein L22-like 1	↑	0.02172006
Q62446	Fkbp3	Peptidyl-prolyl cis-trans isomerase FKBP3	↑	0.03599367
Q91WJ8	Fubp1	Far upstream element-binding protein 1	↑	0.03297629
Q5M8N0	Cnrip1	CB1 cannabinoid receptor-interacting protein 1	↑	0.04653384
Q9CZX0	Elp3	Elongator complex protein 3	↑	0.01385098
P70441	Slc9a3r1	Na(+)/H(+) exchange regulatory cofactor NHE-RF1	↑	0.03287527
Q91VM5	Rbmxl1	RNA binding motif protein, X-linked-like-1	↑	0.03038863
Q99L45	Eif2s2	Eukaryotic translation initiation factor 2 subunit 2	↑	0.0244244
P17156	Hspa2	Heat shock-related 70 kDa protein 2	↑	0.03731997
P16045	Lgals1	Galectin-1	↑	0.0337983

Q921L3	Tmco1	Transmembrane and coiled-coil domain-containing protein 1	↑	0.04124753
P14685	Psmd3	26S proteasome non-ATPase regulatory subunit 3	↑	0.04331233
Q8CCK0	H2afy2	Core histone macro-H2A.2	↑	0.0170983
Q6ZWY3	Rps27l	40S ribosomal protein S27-like	↑	0.00854959
P53657	Pklr	Pyruvate kinase PKLR	↑	0.04467587
Q6A068	Cdc5l	Cell division cycle 5-like protein	↑	0.02548154
Q9QZM0	Ubqln2	Ubiquilin-2	↑	0.04205106
P84104	Srsf3	Serine/arginine-rich splicing factor 3	↑	0.02168029
P62264	Rps14	40S ribosomal protein S14	↑	0.04958758
P62305	Snrpe	Small nuclear ribonucleoprotein E	↑	0.0430609
Q3ULJ0	Gpd1l	Glycerol-3-phosphate dehydrogenase 1-like protein	↓	0.03233159
Q8CIE6	Copa	Coatomer subunit alpha;Proxenin;Xenin	↓	0.03909837
P60843	Eif4a1	Eukaryotic initiation factor 4A-I	↓	0.02487222
Q61187	Tsg101	Tumor susceptibility gene 101 protein	↓	0.0048945
P40124	Cap1	Adenylyl cyclase-associated protein 1	↓	0.01822375
P06745	Gpi	Glucose-6-phosphate isomerase	↓	0.026053
Q68FL4	Ahcy;Ahcyl2	Adenosylhomocysteinase;Putative adenosylhomocysteinase 3	↓	0.04276753
Q9WUA3	Pfkp	ATP-dependent 6-phosphofructokinase, platelet type	↓	0.01327687
Q8BLQ9	Cadm2	Cell adhesion molecule 2	↓	0.02838115
P03930	Mtatp8	ATP synthase protein 8	↓	0.03586702
Q9CYT6	Cap2	Adenylyl cyclase-associated protein 2	↓	0.02553047
P14824	Anxa6	Annexin A6	↓	0.02669608
P10922	H1f0	Histone H1.0;Histone H1.0, N-terminally processed	↓	0.02440936
Q9R226	Khdrbs3	KH domain-containing, RNA-binding, signal transduction-associated protein 3	↓	0.03174911
O08599	Stxbp1	Syntaxin-binding protein 1	↓	0.04850827
Q9R0Q7	Ptges3	Prostaglandin E synthase 3	↓	0.02140888

Q8BMF4	Dlat	Dihydrolipoyllysine-residue acetyltransferase component of pyruvate dehydrogenase complex, mitochondrial	↓	0.02328757
P19536	Cox5b	Cytochrome c oxidase subunit 5B, mitochondrial	↓	0.03128842
P07758	Serpina1a	Alpha-1-antitrypsin 1-1	↓	0.00312911
P46096	Syt1;Syt5	Synaptotagmin-1;Synaptotagmin-5	↓	0.04951045
D3Z7P3	Gls	Glutaminase kidney isoform, mitochondrial	↓	0.04702066
P39053	Dnm1	Dynamin-1	↓	0.03151544
P61922	Abat	4-aminobutyrate aminotransferase, mitochondrial	↓	0.04731234
Q640R3	Hepacam	Hepatocyte cell adhesion molecule	↓	0.00805722
Q9JIA1	Lgi1	Leucine-rich glioma-inactivated protein 1	↓	0.04059328
P84091	Ap2m1	AP-2 complex subunit mu	↓	0.009474
P62814	Atp6v1b2	V-type proton ATPase subunit B, brain isoform	↓	0.02428979
Q9Z2Y3	Homer1	Homer protein homolog 1	↓	0.04560812
P35802	Gpm6a	Neuronal membrane glycoprotein M6-a	↓	0.04656328
Q02053	Uba1	Ubiquitin-like modifier-activating enzyme 1	↓	0.02423344
Q9Z2Q6	Septin5	Septin-5	↓	0.04288744
P68368	Tuba4a	Tubulin alpha-4A chain	↓	0.02885014
P15105	Glul	Glutamine synthetase	↓	0.04237688
P05064	Aldoa	Fructose-bisphosphate aldolase A	↓	0.03536956
Q8BTI9	Pik3cb	Phosphatidylinositol 4,5-bisphosphate 3-kinase catalytic subunit beta isoform	↓	0.04149403
Q4FZC9	Syne3	Nesprin-3	↓	0.03879581
P47857	Pfkm	ATP-dependent 6-phosphofructokinase, muscle type	↓	0.0335335
P11499	Hsp90ab1	Heat shock protein HSP 90-beta	↓	0.02846113
P07901	Hsp90aa1	Heat shock protein HSP 90-alpha	↓	0.02501624
Q3UYV9	Ncbp1	Nuclear cap-binding protein subunit 1	↓	0.00036734
P62482	Kcnab2	Voltage-gated potassium channel subunit beta-2	↓	0.04380456
P26443	Glud1	Glutamate dehydrogenase 1, mitochondrial	↓	0.01418879

Q923S9	Rab30	Ras-related protein Rab-30	↓	0.03976379
P16125	Ldhb	L-lactate dehydrogenase B chain	↓	0.00283298
P02088	Hbb-b1;Hbb-b2	Hemoglobin subunit beta-1;Hemoglobin subunit beta-2	↓	0.03823049
Q99MN9	Pccb	Propionyl-CoA carboxylase beta chain, mitochondrial	↓	0.04459239
P62075	Timm13	Mitochondrial import inner membrane translocase subunit Tim13	↓	0.0140395

Appendix 3. Dysregulated proteins in *Sgsh* D31N heterozygous mouse motor cortex compared to wildtype at 6 Week.

Swiss-Prot Code	Gene Name	Protein Description	Up- or Down-regulation	P-Value
P09581	Csf1r	Macrophage colony-stimulating factor 1 receptor	↑	0.04338024
Q9D7H3	RtcA	RNA 3'-terminal phosphate cyclase	↑	0.04950323
Q61207	Psap	Prosaposin	↑	0.01274305
P16125	Ldhb	L-lactate dehydrogenase B chain	↑	0.01043188
Q9R0Q7	Ptges3	Prostaglandin E synthase 3	↑	0.03034319
Q8CAA7	Pgm2l1	Glucose 1,6-bisphosphate synthase	↑	0.00678091
Q9CWS0	Ddah1	N(G),N(G)-dimethylarginine dimethylaminohydrolase 1	↑	0.02663273
Q02053	Uba1	Ubiquitin-like modifier-activating enzyme 1	↑	0.00345846
P10637	Mapt	Microtubule-associated protein tau	↑	0.04793912
Q9Z0Y1	Dctn3	Dynactin subunit 3	↑	0.03934962
Q9DBP5	Cmpk1	UMP-CMP kinase	↑	0.00838698
P16858	Gapdh	Glyceraldehyde-3-phosphate dehydrogenase	↑	0.02247099
P31938	Map2k1	Dual specificity mitogen-activated protein kinase kinase 1	↑	0.02154008
Q8BFZ3	Actbl2	Beta-actin-like protein 2	↑	0.00698826
P07901	Hsp90aa1	Heat shock protein HSP 90-alpha	↑	0.03745138
P50396	Gdi1	Rab GDP dissociation inhibitor alpha	↑	0.03121237
Q8CCK0	H2afy2	Core histone macro-H2A.2	↑	0.04690994
P26618	Pdgfra	Platelet-derived growth factor receptor alpha	↑	0.02636185
Q3UHJ0	Aak1	AP2-associated protein kinase 1	↑	0.04818148
O54967	Tnk2	Activated CDC42 kinase 1	↑	0.03444202
E9PY46	Ift140	Intraflagellar transport protein 140 homolog	↓	0.02303274
P22723	Gabrg2	Gamma-aminobutyric acid receptor subunit gamma-2	↓	0.03467072
A6PWD2	Fhad1	Forkhead-associated domain-containing protein 1	↓	0.03526765
Q91YQ5	Rpn1	Dolichyl-diphosphooligosaccharide--protein glycosyltransferase subunit 1	↓	0.02448012
P05532	Kit	Mast/stem cell growth factor receptor Kit	↓	0.04682028

Q9QYA2	Tomm40	Mitochondrial import receptor subunit TOM40 homolog	↓	0.03739625
Q9D8W7	Ociad2	OCIA domain-containing protein 2	↓	0.00368823
Q8R404	Qil1	Protein QIL1	↓	0.00542165
P62774	Mtpn	Myotrophin	↓	0.0335645
Q922D8	Mthfd1	C-1-tetrahydrofolate synthase, cytoplasmic	↓	0.03952776
Q8BLK3	Lsamp	Limbic system-associated membrane protein	↓	0.01969143

Appendix 4. Dysregulated proteins in *Sgsh* D31N heterozygous mouse motor cortex compared to wildtype at 12 Week.

Swiss-Prot Code	Gene Name	Protein Description	Up- or Down-regulation	P-Value
O54946	Dnajb6	DnaJ homolog subfamily B member 6	↑	0.01409778
Q925U4	Edem1	ER degradation-enhancing alpha-mannosidase-like protein 1	↑	0.04991812
Q8BIG7	Comtd1	Catechol O-methyltransferase domain-containing protein 1	↑	0.03810874
Q8BXV2	Bri3bp	BRI3-binding protein	↑	0.02600105
Q9DCV7	Krt7	Keratin, type II cytoskeletal 7	↑	0.03494393
Q3TMP8	Tmem38a	Trimeric intracellular cation channel type A	↑	0.03691437
P03911	Mtnd4	NADH-ubiquinone oxidoreductase chain 4	↑	0.0015647
Q8CHK3	Mboat7	Lysophospholipid acyltransferase 7	↑	0.03723546
Q9QYA2	Tomm40	Mitochondrial import receptor subunit TOM40 homolog	↑	0.02933137
Q8C7M3	Trim9	E3 ubiquitin-protein ligase TRIM9	↑	0.04825715
Q8BLK3	Lsamp	Limbic system-associated membrane protein	↑	0.02912636
Q8K1M6	Dnm1l	Dynamin-1-like protein	↑	0.0159213
Q9CTY5	Micu3	Calcium uptake protein 3, mitochondrial	↑	0.02548092
P61329	Fgf12	Fibroblast growth factor 12	↑	0.01661583
P85094	Isoc2a	Isochorismatase domain-containing protein 2A, mitochondrial	↑	0.02916116
Q9DC69	Ndufa9	NADH dehydrogenase [ubiquinone] 1 alpha subcomplex subunit 9, mitochondrial	↑	0.03109557
P35283	Rab12	Ras-related protein Rab-12	↑	0.00489565
Q8CC35	Synpo	Synaptopodin	↑	0.01870624
Q99L04	Dhrs1	Dehydrogenase/reductase SDR family member 1	↑	0.029454
P48318	Gad1	Glutamate decarboxylase 1	↑	0.04678416
Q925N0	Sfxn5	Sideroflexin-5	↑	0.00619271
Q8VHH5	Agap3	Arf-GAP with GTPase, ANK repeat and PH domain-containing protein 3	↑	0.03401174
P35436	Grin2a	Glutamate receptor ionotropic, NMDA 2A	↑	0.03420376
Q80ZW2	Them6	Protein THEM6	↑	0.00632735

Q01097	Grin2b	Glutamate receptor ionotropic, NMDA 2B	↑	0.03483445
P17809	Slc2a1	Solute carrier family 2, facilitated glucose transporter member 1	↑	0.01173993
Q3UMR5	Mcu	Calcium uniporter protein, mitochondrial	↑	0.04912421
Q99P72	Rtn4	Reticulon-4	↓	0.02544697
P05063	Aldoc	Fructose-bisphosphate aldolase C	↓	0.04458668
Q3UHL1	Camkv	CaM kinase-like vesicle-associated protein	↓	0.02613371
Q78ZA7	Nap1l4	Nucleosome assembly protein 1-like 4	↓	0.01251451
Q9DCW4	Etfb	Electron transfer flavoprotein subunit beta	↓	0.03578655
Q61792	Lasp1	LIM and SH3 domain protein 1	↓	0.01492048
P45591	Cfl2	Cofilin-2	↓	0.027889
Q9R1T4	Septin6	Septin-6	↓	0.0318925
P80316	Cct5	T-complex protein 1 subunit epsilon	↓	0.0382546
P08752	Gnai2	Guanine nucleotide-binding protein G(i) subunit alpha-2	↓	0.01444168
Q8R429	Atp2a1	Sarcoplasmic/endoplasmic reticulum calcium ATPase 1	↓	0.04445455
P29319	Epha3	Ephrin type-A receptor 3	↓	0.04728632
Q9Z2H5	Epb41l1	Band 4.1-like protein 1	↓	0.02595
Q99MI1	Erc1	ELKS/Rab6-interacting/CAST family member 1	↓	0.0475088
P39054	Dnm2	Dynamin-2	↓	0.01903169
Q9R0Q7	Ptges3	Prostaglandin E synthase 3	↓	0.03576443
Q99LX0	Park7	Protein deglycase DJ-1	↓	0.03483953
P60335	Pcbp1	Poly(rC)-binding protein 1	↓	0.0280571
P62281	Rps11	40S ribosomal protein S11	↓	0.00166662
P31324	Prkar2b	cAMP-dependent protein kinase type II-beta regulatory subunit	↓	0.00742508
Q8BP86	Snapc4	snRNA-activating protein complex subunit 4	↓	0.03146003
P63005	Pafah1b1	Platelet-activating factor acetylhydrolase IB subunit alpha	↓	0.01496697
P60487	Pdxp	Pyridoxal phosphate phosphatase	↓	0.02939483
P68033	Acta1	Actin, alpha cardiac muscle 1	↓	0.00446273
P05064	Aldoa	Fructose-bisphosphate aldolase A	↓	0.04054146

Q99PT1	Arhgdia	Rho GDP-dissociation inhibitor 1	↓	0.0130616
P56399	Usp5	Ubiquitin carboxyl-terminal hydrolase 5	↓	0.01297727
Q61699	Hsph1	Heat shock protein 105 kDa	↓	0.00524091
Q9R0P9	Uchl1	Ubiquitin carboxyl-terminal hydrolase isozyme L1	↓	0.04658101
Q8VDI1	Epsti1	Epithelial-stromal interaction protein 1	↓	0.04712573
Q9WUM3	Coro1b	Coronin-1B	↓	0.0063505
Q8K424	Trpv3	Transient receptor potential cation channel subfamily V member 3	↓	0.03792958
P04925	Prnp	Major prion protein	↓	0.04197534
Q9D9T8	Efhc1	EF-hand domain-containing protein 1	↓	0.04334903
P51660	Hsd17b4	(3R)-hydroxyacyl-CoA dehydrogenase;Enoyl-CoA hydratase 2;Peroxisomal multifunctional enzyme type 2	↓	0.04865089
Q920P5	Ak5	Adenylate kinase isoenzyme 5	↓	0.01796962
Q8R1U1	Cog4	Conserved oligomeric Golgi complex subunit 4	↓	0.02391319
Q8C854	Myef2	Myelin expression factor 2	↓	0.04953073
Q9QXS6	Dbn1	Drebrin	↓	0.0232065
P61759	Vbp1	Prefoldin subunit 3	↓	0.00835417
Q61316	Hspa4	Heat shock 70 kDa protein 4	↓	0.01378693
P22682	Cbl	E3 ubiquitin-protein ligase CBL	↓	0.00815089
P58389	Ppp2r4	Serine/threonine-protein phosphatase 2A activator	↓	0.02424606
O70310	Nmt1	Glycylpeptide N-tetradecanoyltransferase 1	↓	0.0393781
Q9D8Y0	Efhd2	EF-hand domain-containing protein D2	↓	0.03553068
Q91Y97	Aldob	Fructose-bisphosphate aldolase B	↓	0.01352704
O08967	Cyth3	Cytohesin-3	↓	0.01368675
P46097	Syt2	Synaptotagmin-2	↓	0.03760539
Q8CC88	Vwa8	von Willebrand factor A domain-containing protein 8	↓	0.01017708
Q6ZWX6	Eif2s1	Eukaryotic translation initiation factor 2 subunit 1	↓	0.04569198
P51863	Atp6v0d1	V-type proton ATPase subunit d 1	↓	0.02893515
P11983	Tcp1	T-complex protein 1 subunit alpha	↓	0.03679331

O08810	Eftud2	116 kDa U5 small nuclear ribonucleoprotein component	↓	0.0362677
P61082	Ube2m	NEDD8-conjugating enzyme Ubc12	↓	0.03325949
O08917	Flot1	Flotillin-1	↓	0.04916274
Q8C7K6	Pcyox1l	Prenylcysteine oxidase-like	↓	0.0469611
P61294	Rab6a/b	Ras-related protein Rab-6A;Ras-related protein Rab-6B	↓	0.0396241
P42208	Septin2	Septin-2	↓	0.00887606
Q8K3H0	Appl1	DCC-interacting protein 13-alpha	↓	0.00330526
Q8C0E2	Vps26b	Vacuolar protein sorting-associated protein 26B	↓	0.00837189
Q8CDL9	Ccdc87	Coiled-coil domain-containing protein 87	↓	0.02490057
Q9DD18	Dtd1	D-tyrosyl-tRNA(Tyr) deacylase 1	↓	0.04068889
Q61166	Mapre1	Microtubule-associated protein RP/EB family member 1	↓	0.01853727
P32921	Wars	T1-TrpRS;T2-TrpRS;Tryptophan--tRNA ligase, cytoplasmic	↓	0.03613524
Q8C263	Ska3	Spindle and kinetochore-associated protein 3	↓	0.03100982
Q91VM9	Ppa2	Inorganic pyrophosphatase 2, mitochondrial	↓	0.03627919
P48758	Cbr1	Carbonyl reductase [NADPH] 1	↓	0.0389799
Q0VE82	Cpne7	Copine-7	↓	0.01392201

Appendix 5. Dysregulated proteins in *Sgsh* D31N heterozygous mouse motor cortex compared to wildtype at 24 Week.

Swiss-Prot Code	Gene Name	Protein Description	Up- or Down-regulation	P-Value
Q9D6P8	Calml3	Calmodulin-like protein 3	↑	0.04235441
Q9Z100	Cpxm1	Probable carboxypeptidase X1	↑	0.04560659
Q80VY2	Fam212b	Protein FAM212B	↑	0.01872554
P68134	Acta1	Actin, alpha skeletal muscle	↑	0.04457274
Q91X78	Erlin1	Erlin-1	↑	0.00636583
Q8K0D0	Cdk17	Cyclin-dependent kinase 17	↑	0.0406154
P70182	Pip5k1a	Phosphatidylinositol 4-phosphate 5-kinase type-1 alpha	↑	0.02984908
Q8BHE8	Maip1	Uncharacterized protein C2orf47 homolog, mitochondrial	↑	0.02151642
Q8BUR9	Mzt1	Mitotic-spindle organizing protein 1	↑	0.04773739
Q91WU0	Ces1f	Carboxylic ester hydrolase	↑	0.04438731
Q8R4U7	Luzp1	Leucine zipper protein 1	↑	0.0168297
Q60900	Elavl3	ELAV-like protein 3	↑	0.04789197
Q9D1J3	Sarnp	SAP domain-containing ribonucleoprotein	↑	0.04717127
Q920F6	Smc1b	Structural maintenance of chromosomes protein 1B	↑	0.02913799
P62307	Snrpf	Small nuclear ribonucleoprotein F	↑	0.03973212
Q9D4J1	Efhd1	EF-hand domain-containing protein D1	↑	0.01891516
P60824	Cirbp	Cold-inducible RNA-binding protein	↑	0.0420428
P41216	Acsl1	Long-chain-fatty-acid--CoA ligase 1	↑	0.00124326
Q7TT50	Cdc42bpb	Serine/threonine-protein kinase MRCK beta	↑	0.02343875
Q8R0S4	Cacnb4	Voltage-dependent L-type calcium channel subunit beta-4	↑	0.02234284
Q8BXZ1	Tmx3	Protein disulfide-isomerase TMX3	↑	0.02705968
Q3V3R1	Mthfd1l	Monofunctional C1-tetrahydrofolate synthase, mitochondrial	↑	0.00792089
P62073	Timm10	Mitochondrial import inner membrane translocase subunit Tim10	↑	0.01985235
Q8BJD1	Itih5	Inter-alpha-trypsin inhibitor heavy chain H5	↑	0.04322838
Q91W34	Rusf1	RUS1 family protein C16orf58 homolog	↑	0.0117644

Q9EPW0	Inpp4a	Type I inositol 3,4-bisphosphate 4-phosphatase	↑	0.02195163
Q62418	Dbnl	Drebrin-like protein	↑	0.04037138
O54950	Prkag1	5'-AMP-activated protein kinase subunit gamma-1	↑	0.01145401
Q6PE15	Abhd10	Mycophenolic acid acyl-glucuronide esterase, mitochondrial	↑	0.0492625
Q4ACU6	Shank3	SH3 and multiple ankyrin repeat domains protein 3	↑	0.00267521
Q99NB5	Gsdmc	Gasdermin-C	↑	0.01230699
Q64314	Cd34	Hematopoietic progenitor cell antigen CD34	↑	0.00773888
P70379	Fgf14	Fibroblast growth factor 14	↑	0.04209562
Q9D7J9	Echdc3	Enoyl-CoA hydratase domain-containing protein 3, mitochondrial	↑	0.03861881
P61967	Ap1s1	AP-1 complex subunit sigma-1A	↑	0.04390049
P14431	H2-Q9	H-2 class I histocompatibility antigen, Q9 alpha chain	↑	0.04879785
Q9R0Q9	Mpdu1	Mannose-P-dolichol utilization defect 1 protein	↑	0.00607583
Q505D7	Opa3	Optic atrophy 3 protein homolog	↑	0.00929756
Q811I0	Atpaf1	ATP synthase mitochondrial F1 complex assembly factor 1	↑	0.02869609
Q9D1T0	Lingo1	Leucine-rich repeat and immunoglobulin-like domain-containing nogo receptor-interacting protein 1	↑	0.01128084
Q9QXK3	Copg2	Coatomer subunit gamma-2	↑	0.02240088
Q7TNV0	Dek	Protein DEK	↑	0.01114445
Q99PW8	Kif17	Kinesin-like protein KIF17	↑	0.00417807
Q8BGR6	Arl15	ADP-ribosylation factor-like protein 15	↑	0.04349161
Q9JKV7	Extl1	Exostosin-like 1	↑	0.0205217
Q6ZWX6	Eif2s1	Eukaryotic translation initiation factor 2 subunit 1	↑	0.0225715
Q61011	Gnb3	Guanine nucleotide-binding protein G(I)/G(S)/G(T) subunit beta-3	↑	0.04322834
Q99M01	Fars2	Phenylalanine--tRNA ligase, mitochondrial	↑	0.04428366
Q8R480	Nup85	Nuclear pore complex protein Nup85	↑	0.01481921
Q02257	Jup	Junction plakoglobin	↑	0.02086963
Q9D0M5	Dynll2	Dynein light chain 2, cytoplasmic	↑	0.03801376
D3YZU1	Shank1	SH3 and multiple ankyrin repeat domains protein 1	↑	0.00364616

Q80TR1	Lphn1	Latrophilin-1	↑	0.00411792
P60521	Gabarapl2	Gamma-aminobutyric acid receptor-associated protein-like 2	↑	0.02088238
P29595	Nedd8	NEDD8	↑	0.02275117
Q62093	Srsf2	Serine/arginine-rich splicing factor 2	↑	0.03561457
Q3UV17	Krt76	Keratin, type II cytoskeletal 2 oral	↑	0.03020346
P12023	App	Amyloid beta A4 protein	↑	0.00677525
P62843	Rps15	40S ribosomal protein S15	↑	0.04605157
Q03137	Epha4	Ephrin type-A receptor 4	↑	0.0459389
Q9CTY5	Micu3	Calcium uptake protein 3, mitochondrial	↑	0.00156141
F8VPU2	Farp1	FERM, RhoGEF and pleckstrin domain-containing protein 1	↑	0.02207905
Q04859	Mak	Serine/threonine-protein kinase MAK	↑	0.00535135
Q9CQ91	Ndufa3	NADH dehydrogenase [ubiquinone] 1 alpha subcomplex subunit 3	↑	0.02285463
Q3UGC7	Eif3j1	Eukaryotic translation initiation factor 3 subunit J-A	↑	0.03125306
Q8CFC2	Myt1	Myelin transcription factor 1	↑	0.03513104
Q9Z1Q9	Vars	Valine--tRNA ligase	↑	0.01517186
P26049	Gabra3	Gamma-aminobutyric acid receptor subunit alpha-3	↑	0.02165176
Q9Z0H4	Celf2	CUGBP Elav-like family member 2	↑	0.02590507
Q9QUP5	Hapln1	Hyaluronan and proteoglycan link protein 1	↑	0.00836603
Q9CR67	Tmem33	Transmembrane protein 33	↑	0.02867992
P56135	Atp5j2	ATP synthase subunit f, mitochondrial	↑	0.02738535
Q3UMR5	Mcu	Calcium uniporter protein, mitochondrial	↑	0.01041182
Q91WJ8	Fubp1	Far upstream element-binding protein 1	↑	0.03899256
P62748	Hpcal1	Hippocalcin-like protein 1	↑	0.01347433
P35282	Rab21	Ras-related protein Rab-21	↑	0.00996353
P56382	Atp5e	ATP synthase subunit epsilon, mitochondrial	↑	0.00091863
Q9R1C6	Dgke	Diacylglycerol kinase epsilon	↑	0.0278891
P53569	Cebpz	CCAAT/enhancer-binding protein zeta	↑	0.04716258
Q8BIG7	Comtd1	Catechol O-methyltransferase domain-containing protein 1	↑	0.00107311

Q61937	Npm1	Nucleophosmin	↑	0.03953225
Q80YE7	Dapk1	Death-associated protein kinase 1	↑	0.01843257
Q9CPQ3	Tomm22	Mitochondrial import receptor subunit TOM22 homolog	↑	0.04575027
Q9CW03	Smc3	Structural maintenance of chromosomes protein 3	↑	0.01206509
P62245	Rps15a	40S ribosomal protein S15a	↑	0.04727436
Q6NS60	Fbxo41	F-box only protein 41	↑	0.00337685
Q91YQ5	Rpn1	Dolichyl-diphosphooligosaccharide--protein glycosyltransferase subunit 1	↑	0.0231123
Q6PDM2	Srsf1	Serine/arginine-rich splicing factor 1	↑	0.02627612
Q69ZK9	Nlgn2	Neuroligin 4-like	↑	0.02606356
Q9JLV5	Cul3	Cullin-3	↑	0.01898442
P62849	Rps24	40S ribosomal protein S24	↑	0.01340028
Q9CQV6	Map1lc3b	Microtubule-associated proteins 1A/1B light chain 3B	↑	0.01601032
P98086	C1qa	Complement C1q subcomponent subunit A	↑	0.0323418
Q62433	Ndrg1	Protein NDRG1	↑	0.01024886
P27659	Rpl3	60S ribosomal protein L3	↑	0.03375718
Q5SNZ0	Ccdc88a	Girdin	↑	0.01792718
P48453	Ppp3cb	Serine/threonine-protein phosphatase 2B catalytic subunit beta isoform	↑	0.04606219
P62315	Snrpd1	Small nuclear ribonucleoprotein Sm D1	↑	0.02323655
P21619	Lmnb2	Lamin-B2	↑	0.03238338
Q80Z38	Shank2	SH3 and multiple ankyrin repeat domains protein 2	↑	0.04793042
Q3UUG6	Tbc1d24	TBC1 domain family member 24	↑	0.02881517
P83882	Rpl36a	60S ribosomal protein L36a	↑	0.04191827
Q9EPJ9	Arfgap1	ADP-ribosylation factor GTPase-activating protein 1	↑	0.0067315
P61804	Dad1	Dolichyl-diphosphooligosaccharide--protein glycosyltransferase subunit DAD1	↑	0.02995337
O09167	Rpl21	60S ribosomal protein L21	↑	0.03414013
Q61990	Pcbp2	Poly(rC)-binding protein 2	↑	0.03952406
Q8VE33	Gdap1l1	Ganglioside-induced differentiation-associated protein 1-like 1	↑	0.00320972

Q6GQS1	Slc25a23	Calcium-binding mitochondrial carrier protein SCaMC-3	↑	0.04394955
Q9Z2U1	Psma5	Proteasome subunit alpha type-5	↓	0.01785697
P10922	H1f0	Histone H1.0;Histone H1.0, N-terminally processed	↓	0.04968211
O55131	Septin7	Septin-7	↓	0.0486011
P15532	Nme1	Nucleoside diphosphate kinase A	↓	0.04715988
P63318	Prkcg	Protein kinase C gamma type	↓	0.0181539
Q9DBP5	Cmpk1	UMP-CMP kinase	↓	0.04487362
Q9ESN6	Trim2	Tripartite motif-containing protein 2	↓	0.02795966
O08807	Prdx4	Peroxiredoxin-4	↓	0.03395507
Q6ZQ38	Cand1	Cullin-associated NEDD8-dissociated protein 1	↓	0.04592688
Q5SQX6	Cyfip2	Cytoplasmic FMR1-interacting protein 2	↓	0.0258467
P51863	Atp6v0d1	V-type proton ATPase subunit d 1	↓	0.04340412
Q9CQV8	Ywhab	14-3-3 protein beta/alpha;14-3-3 protein beta/alpha, N-terminally processed	↓	0.04405799
Q9R0Y5	Ak1	Adenylate kinase isoenzyme 1	↓	0.00492283
Q8BKX1	Baiap2	Brain-specific angiogenesis inhibitor 1-associated protein 2	↓	0.03191857
Q9D8W7	Ociad2	OCIA domain-containing protein 2	↓	0.04200918
Q8BHC4	Dcakd	Dephospho-CoA kinase domain-containing protein	↓	0.04126979
P58281	Opa1	Dynamin-like 120 kDa protein, form S1;Dynamin-like 120 kDa protein, mitochondrial	↓	0.04404092
Q3UHL1	Camkv	CaM kinase-like vesicle-associated protein	↓	0.04033237
Q8BM75	Arid5b	AT-rich interactive domain-containing protein 5B	↓	0.04100581
Q8CI94	Pygb	Glycogen phosphorylase, brain form	↓	0.02420602
Q6ZPK7	Zfyve28	Lateral signaling target protein 2 homolog	↓	0.03626238
P11983	Tcp1	T-complex protein 1 subunit alpha	↓	0.02689479
Q68FD5	Cltc	Clathrin heavy chain 1	↓	0.02262727
Q99104	Myo5a	Unconventional myosin-Va	↓	0.04712614
O08756	Hsd17b10	3-hydroxyacyl-CoA dehydrogenase type-2	↓	0.04637245
Q9DBJ1	Pgam1	Phosphoglycerate mutase 1	↓	0.02414684

Q3UNH4	Gprin1	G protein-regulated inducer of neurite outgrowth 1	↓	0.04108725
P61202	Cops2	COP9 signalosome complex subunit 2	↓	0.03025639
P48722	Hspa4l	Heat shock 70 kDa protein 4L	↓	0.04046754
P35700	Prdx1	Peroxiredoxin-1	↓	0.00936613
P17182	Eno1	Alpha-enolase	↓	0.01067618
Q8R5H1	Usp15	Ubiquitin carboxyl-terminal hydrolase 15	↓	0.04786313
Q8R071	Itpka	Inositol-trisphosphate 3-kinase A	↓	0.03052499
P14115	Rpl27a	60S ribosomal protein L27a	↓	0.04974626
Q9D0J8	Ptms	Parathymosin	↓	0.02266202
Q9Z2H5	Epb41l1	Band 4.1-like protein 1	↓	0.04581872
Q8BIJ6	Iars2	Isoleucine--tRNA ligase, mitochondrial	↓	0.03738588
O08917	Flot1	Flotillin-1	↓	0.01063035
Q9QZQ8	H2afy	Core histone macro-H2A.1	↓	0.00986886
P61226	Rap2b	Ras-related protein Rap-2b	↓	0.0442426
Q8R0Y6	Aldh1l1	Cytosolic 10-formyltetrahydrofolate dehydrogenase	↓	0.04269491
P63085	Mapk1	Mitogen-activated protein kinase 1	↓	0.02654354
Q8CC35	Synpo	Synaptopodin	↓	0.04184601
Q9Z218	Dpp6	Dipeptidyl aminopeptidase-like protein 6	↓	0.02822958
Q9JLK7	Cabp1	Calcium-binding protein 1	↓	0.01355503
Q8C650	Septin10	Septin-10	↓	0.03948762
P00493	Hprt1	Hypoxanthine-guanine phosphoribosyltransferase	↓	0.0301189
Q9Z2I8	Suclg2	Succinyl-CoA ligase [GDP-forming] subunit beta, mitochondrial	↓	0.04698927
P02088	Hbb-b1	Hemoglobin subunit beta-1	↓	0.03733246
Q9Z1B3	Plcb1	1-phosphatidylinositol 4,5-bisphosphate phosphodiesterase beta-1	↓	0.03197723
Q62419	Sh3gl1	Endophilin-A2	↓	0.02672216
Q3UQ44	Iqgap2	Ras GTPase-activating-like protein IQGAP2	↓	0.0492182
P11404	Fabp3	Fatty acid-binding protein, heart	↓	0.02333793
Q4VAE3	Tmem65	Transmembrane protein 65	↓	0.02538482

Q61171	Prdx2	Peroxiredoxin-2	↓	0.0254488
Q9EST5	Anp32b	Acidic leucine-rich nuclear phosphoprotein 32 family member B	↓	0.04340631
Q8BW75	Maob	Amine oxidase [flavin-containing] B	↓	0.02336682
Q9CSP9	Ttc14	Tetratricopeptide repeat protein 14	↓	0.01869053
Q8C0T5	Sipa1l1	Signal-induced proliferation-associated 1-like protein 1	↓	0.04882349
Q8C0E2	Vps26b	Vacuolar protein sorting-associated protein 26B	↓	0.01289939
Q9QZX7	Srr	Serine racemase	↓	0.02664762
Q6R0H7	Gnas	Guanine nucleotide-binding protein G(s) subunit alpha isoforms short;Guanine nucleotide-binding protein G(s) subunit alpha isoforms XLas	↓	0.02653472
Q91VR5	Ddx1	ATP-dependent RNA helicase DDX1	↓	0.02062403
P47809	Map2k4	Dual specificity mitogen-activated protein kinase kinase 4	↓	0.03113635
P62889	Rpl30	60S ribosomal protein L30	↓	0.01558006
P20108	Prdx3	Thioredoxin-dependent peroxide reductase, mitochondrial	↓	0.02782952
Q924N4	Slc12a6	Solute carrier family 12 member 6	↓	0.02434547
Q9QUM9	Psma6	Proteasome subunit alpha type-6	↓	0.00988813
Q63912	Omg	Oligodendrocyte-myelin glycoprotein	↓	0.0118889
P28738	Kif5c	Kinesin heavy chain isoform 5C	↓	0.04976731
O88456	Capns1	Calpain small subunit 1	↓	0.04872616
Q91XL9	Osbpl1a	Oxysterol-binding protein-related protein 1	↓	0.04601445
Q99K67	Aass	Alpha-aminoadipic semialdehyde synthase, mitochondrial	↓	0.01274079
P09041	Pgk2	Phosphoglycerate kinase 2	↓	0.01522495
Q9WVA4	Tagln2	Transgelin-2	↓	0.04956527
Q9QYF9	Ndrg3	Protein NDRG3	↓	0.00325234
Q8BLE7	Slc17a6	Vesicular glutamate transporter 2	↓	0.04878051
Q8BT07	Cep55	Centrosomal protein of 55 kDa	↓	0.03377107
O54962	Banf1	Barrier-to-autointegration factor, N-terminally processed	↓	0.04209268
P62812	Gabra1	Gamma-aminobutyric acid receptor subunit alpha-1	↓	0.04816606
P53810	Pitpna	Phosphatidylinositol transfer protein alpha isoform	↓	0.0368898

Q02248	Ctnnb1	Catenin beta-1	↓	0.04507166
Q62188	Dpysl3	Dihydropyrimidinase-related protein 3	↓	0.01097522
O88844	Idh1	Isocitrate dehydrogenase [NADP] cytoplasmic	↓	0.02465929
P56565	S100a1	Protein S100-A1	↓	0.03087329
P98197	Atp11a	Probable phospholipid-transporting ATPase IH	↓	0.03471471
Q8BHB7		Uncharacterized protein C16orf46 homolog	↓	0.04382347
Q3ULD5	Mccc2	Methylcrotonoyl-CoA carboxylase beta chain, mitochondrial	↓	0.0245239
Q14AX6	Cdk12	Cyclin-dependent kinase 12	↓	0.03940185

Appendix 6. Dysregulated proteins in *Sgsh* D31N heterozygous mouse motor cortex compared to wildtype at 48 Week.

Swiss-Prot Code	Gene Name	Protein Description	Up- or Down-regulation	P-Value
Q80VY2	Fam212b	Protein FAM212B	↑	0.02822207
P70124	Serpinb5	Serpin B5	↑	0.04637105
Q8R1G1	Tasp1	Threonine aspartase 1	↑	0.00833059
Q8VHJ5	Mark1	Serine/threonine-protein kinase MARK1	↑	0.02073254
P35917	Flt4	Vascular endothelial growth factor receptor 3	↑	0.01742689
Q8CIN4	Pak2	PAK-2p27;PAK-2p34;Serine/threonine-protein kinase PAK 2	↑	0.02081995
Q9CY27	Tecr	Very-long-chain enoyl-CoA reductase	↑	0.0140758
Q9Z110	Aldh18a1	Delta-1-pyrroline-5-carboxylate synthase	↑	0.03796618
Q8BH00	Aldh8a1	Aldehyde dehydrogenase family 8 member A1	↑	0.00890673
Q8R0Y8	Slc25a42	Mitochondrial coenzyme A transporter SLC25A42	↑	0.02112063
Q8BTY2	Slc4a7	Sodium bicarbonate cotransporter 3	↑	0.0129491
Q61771	Kif3b	Kinesin-like protein KIF3B;Kinesin-like protein KIF3B, N-terminally processed	↑	0.03954284
Q6P5F9	Xpo1	Exportin-1	↑	0.02020334
Q9EQF6	Dpysl5	Dihydropyrimidinase-related protein 5	↑	0.01650036
O35286	Dhx15	Pre-mRNA-splicing factor ATP-dependent RNA helicase DHX15	↑	0.02622949
Q61502	E2f5	Transcription factor E2F5	↑	0.0271791
Q8CG48	Smc2	Structural maintenance of chromosomes protein 2	↑	0.0081936
Q61851	Fgfr3	Fibroblast growth factor receptor 3	↑	0.04789354
Q9D7X3	Dusp3	Dual specificity protein phosphatase 3	↑	0.02249668
Q8BHC1	Rab39b	Ras-related protein Rab-39B	↑	0.00988546
Q8CGK3	Lonp1	Lon protease homolog, mitochondrial	↑	0.01196023
O08914	Faah	Fatty-acid amide hydrolase 1	↑	0.00842441
Q8C522	Endod1	Endonuclease domain-containing 1 protein	↑	0.04931574
O35864	Cops5	COP9 signalosome complex subunit 5	↑	0.03668858

Q78PY7	Snd1	Staphylococcal nuclease domain-containing protein 1	↑	0.024725
P27601	Gna13	Guanine nucleotide-binding protein subunit alpha-13	↑	0.00894809
Q9DC51	Gnai3	Guanine nucleotide-binding protein G(k) subunit alpha	↑	0.03506095
Q9D1T0	Lingo1	Leucine-rich repeat and immunoglobulin-like domain-containing nogo receptor-interacting protein 1	↑	0.02030554
Q9WVK8	Cyp46a1	Cholesterol 24-hydroxylase	↑	0.01383834
O35114	Scarb2	Lysosome membrane protein 2	↑	0.00534834
O70492	Snx3	Sorting nexin-3	↑	0.01341314
O70589	Cask	Peripheral plasma membrane protein CASK	↑	0.00574913
Q8BFZ9	Erlin2	Erlin-2	↑	0.03767688
Q8VDP6	Cdipt	CDP-diacylglycerol--inositol 3-phosphatidyltransferase	↑	0.02475217
Q03142	Fgfr4	Fibroblast growth factor receptor 4	↑	0.02161162
Q8JZS0	Lin7a;Lin7b	Protein lin-7 homolog A;Protein lin-7 homolog B	↑	0.0039978
Q9QYJ0	Dnaja2	DnaJ homolog subfamily A member 2	↑	0.00573529
Q8CHT1	Ngef	Ephexin-1	↑	0.04322918
Q8C419	Gpr158	Probable G-protein coupled receptor 158	↑	0.00401156
Q9CZJ2	Hspa12b	Heat shock 70 kDa protein 12B	↑	0.0048827
Q8R0S2	Iqsec1	IQ motif and SEC7 domain-containing protein 1	↑	0.02112001
P62843	Rps15	40S ribosomal protein S15	↑	0.04976021
O54946	Dnajb6	DnaJ homolog subfamily B member 6	↑	0.03268675
Q811I0	Atpaf1	ATP synthase mitochondrial F1 complex assembly factor 1	↑	0.04982571
O35316	Slc6a6	Sodium- and chloride-dependent taurine transporter	↑	0.01289581
P26231	Ctnna1	Catenin alpha-1	↑	0.02117177
Q9DBC7	Prkar1a	cAMP-dependent protein kinase type I-alpha regulatory subunit;cAMP-dependent protein kinase type I-alpha regulatory subunit, N-terminally processed	↑	0.02578753
Q920I9	Wdr7	WD repeat-containing protein 7	↑	0.00067597
P19639	Gstm3	Glutathione S-transferase Mu 3	↑	0.00621649

Q91YT0	Ndufv1	NADH dehydrogenase [ubiquinone] flavoprotein 1, mitochondrial	↑	0.01521449
Q148V7	Kiaa1468	LisH domain and HEAT repeat-containing protein KIAA1468	↑	0.00981085
Q9QUR7	Pin1	Peptidyl-prolyl cis-trans isomerase NIMA-interacting 1	↑	0.01762639
Q9JK88	Serpini2	Serpin I2	↑	0.0173695
D3YZU1	Shank1	SH3 and multiple ankyrin repeat domains protein 1	↑	0.03091357
G5E8K5	Ank3	Ankyrin-3	↑	0.00641449
Q9Z1W8	Atp12a	Potassium-transporting ATPase alpha chain 2	↑	0.02312761
Q9DC16	Ergic1	Endoplasmic reticulum-Golgi intermediate compartment protein 1	↑	0.00733064
P20444	Prkca	Protein kinase C alpha type	↑	0.0100152
A3KGB4	Tbc1d8b	TBC1 domain family member 8B	↑	0.02536553
P32848	Pvalb	Parvalbumin alpha	↑	0.00967139
P26049	Gabra3	Gamma-aminobutyric acid receptor subunit alpha-3	↑	0.03279688
Q9D662	Sec23b	Protein transport protein Sec23B	↑	0.01909236
P31324	Prkar2b	cAMP-dependent protein kinase type II-beta regulatory subunit	↑	0.00097587
Q9Z268	Rasal1	RasGAP-activating-like protein 1	↑	0.00262842
Q8JZP2	Syn3	Synapsin-3	↑	0.02685534
A6H6E9	Ttc23l	Tetratricopeptide repeat protein 23-like	↑	0.0440291
P42932	Cct8	T-complex protein 1 subunit theta	↑	0.00953673
P52196	Tst	Thiosulfate sulfurtransferase	↑	0.03487161
Q9CPU4	Mgst3	Microsomal glutathione S-transferase 3	↑	0.02740672
Q9R0N7	Syt7	Synaptotagmin-7	↑	0.02498236
Q922U2	Krt5	Keratin, type II cytoskeletal 5	↑	0.0305756
Q91ZA3	Pcca	Propionyl-CoA carboxylase alpha chain, mitochondrial	↑	0.02071334
Q61656	Ddx5	Probable ATP-dependent RNA helicase DDX5	↑	0.03947439
P14824	Anxa6	Annexin A6	↑	0.04530357
P62911	Rpl32	60S ribosomal protein L32	↑	0.03371312
P03921	Mtnd5	NADH-ubiquinone oxidoreductase chain 5	↑	0.00951583
Q68FL4	Ahcyl2	Putative adenosylhomocysteinase 3	↑	0.03663058

P56379	Mp68	6.8 kDa mitochondrial proteolipid	↑	0.00652535
P97434	Mprip	Myosin phosphatase Rho-interacting protein	↑	0.00114174
Q8K2C9	Hacd3	Very-long-chain (3R)-3-hydroxyacyl-CoA dehydratase 3	↑	0.03563261
Q8VDG6	Mlk4	Mitogen-activated protein kinase kinase kinase MLK4	↑	0.01007847
P20060	Hexb	Beta-hexosaminidase subunit beta	↑	0.01617902
P63034	Cyth2	Cytohesin-2	↑	0.0117385
Q9QZ06	Tollip	Toll-interacting protein	↑	0.03626447
Q61330	Cntn2	Contactin-2	↑	0.04941635
Q9D8W7	Ociad2	OCIA domain-containing protein 2	↑	0.02212595
Q9WUA2	Farsb	Phenylalanine--tRNA ligase beta subunit	↑	0.02133326
Q9Z1P6	Ndufa7	NADH dehydrogenase [ubiquinone] 1 alpha subcomplex subunit 7	↑	0.00598861
Q80Z25	Ofd1	Oral-facial-digital syndrome 1 protein homolog	↑	0.03096962
Q8VCD6	Reep2	Receptor expression-enhancing protein 2	↑	0.00340179
Q9WVK4	Ehd1	EH domain-containing protein 1	↑	0.01980818
P03888	Mtnd1	NADH-ubiquinone oxidoreductase chain 1	↑	0.03193311
P60469	Ppfia3	Liprin-alpha-3	↑	0.04233116
Q80XP8	Fam76b	Protein FAM76B	↑	0.00581409
P55249	Alox12e	Arachidonate 12-lipoxygenase, epidermal-type	↑	0.0161503
P09405	Ncl	Nucleolin	↑	0.01399424
Q32MW3	Acot10	Acyl-coenzyme A thioesterase 10, mitochondrial	↑	0.02207761
Q8CHK3	Mboat7	Lysophospholipid acyltransferase 7	↑	0.03009461
Q8VHW2	Cacng8	Voltage-dependent calcium channel gamma-8 subunit	↑	0.04826676
Q9Z2H5	Epb41l1	Band 4.1-like protein 1	↑	0.03664942
Q6PHZ2	Camk2d	Calcium/calmodulin-dependent protein kinase type II subunit delta	↑	0.02791573
Q8BHE3	Atcay	Caytaxin	↑	0.04422369
Q3UUI3	Them4	Acyl-coenzyme A thioesterase THEM4	↑	0.03824629
P49025	Cit	Citron Rho-interacting kinase	↑	0.02040995
Q8CCK0	H2afy2	Core histone macro-H2A.2	↑	0.04701165

P62264	Rps14	40S ribosomal protein S14	↑	0.00757383
E9Q3L2	Pi4ka	Phosphatidylinositol 4-kinase alpha	↑	0.02483484
P39688	Fyn	Tyrosine-protein kinase Fyn	↑	0.03037907
Q99KB8	Hagh	Hydroxyacylglutathione hydrolase, mitochondrial	↑	0.03895203
Q9WUB3	Pygm	Glycogen phosphorylase, muscle form	↑	0.0354267
Q5SZA1	Slc17a2	Sodium-dependent phosphate transport protein 3	↑	0.0270947
Q3ULJ0	Gpd1l	Glycerol-3-phosphate dehydrogenase 1-like protein	↑	0.01153187
O55131	Septin7	Septin-7	↓	0.03266689
O88384	Vti1b	Vesicle transport through interaction with t-SNAREs homolog 1B	↓	0.04800576
Q91XU3	Pip4k2c	Phosphatidylinositol 5-phosphate 4-kinase type-2 gamma	↓	0.02851004
Q9R111	Gda	Guanine deaminase	↓	0.04209957
Q5SSL4	Abr	Active breakpoint cluster region-related protein	↓	0.02913881
P15532	Nme1	Nucleoside diphosphate kinase A	↓	0.00359108
P63040	Cplx1	Complexin-1	↓	0.04219562
P49722	Psma2	Proteasome subunit alpha type-2	↓	0.02177988
P70349	Hint1	Histidine triad nucleotide-binding protein 1	↓	0.00496053
Q8R5C5	Actr1b	Beta-centractin	↓	0.02540339
O09061	Psmb1	Proteasome subunit beta type-1	↓	0.00696669
Q01768	Nme2	Nucleoside diphosphate kinase B	↓	0.00794823
Q8CI94	Pygb	Glycogen phosphorylase, brain form	↓	0.02308975
Q8BP67	Rpl24	60S ribosomal protein L24	↓	0.01155378
Q8C1B7	Septin11	Septin-11	↓	0.01439375
Q6ZPK7	Zfyve28	Lateral signaling target protein 2 homolog	↓	0.01420112
Q99LR1	Abhd12	Monoacylglycerol lipase ABHD12	↓	0.03690442
Q921F2	Tardbp	TAR DNA-binding protein 43	↓	0.04504175
O35066	Kif3c	Kinesin-like protein KIF3C	↓	0.00322733
Q3THE2	Myl12b	Myosin regulatory light chain 12B	↓	0.00815131
Q9CQV8	Ywhab	14-3-3 protein beta/alpha;14-3-3 protein beta/alpha, N-terminally processed	↓	0.01694216

Q8R1Q8	Dync1li1	Cytoplasmic dynein 1 light intermediate chain 1	↓	0.02295632
Q99PT1	Arhgdia	Rho GDP-dissociation inhibitor 1	↓	0.01195154
P35279	Rab6a	Ras-related protein Rab-6A	↓	0.00294348
Q9R1T4	Septin6	Septin-6	↓	0.03279314
Q9JIF7	Copb1	Coatomer subunit beta	↓	0.02489792
Q9CY58	Serbp1	Plasminogen activator inhibitor 1 RNA-binding protein	↓	0.01614096
Q8BM75	Arid5b	AT-rich interactive domain-containing protein 5B	↓	0.01784087
Q8K596	Slc8a2	Sodium/calcium exchanger 2	↓	0.00397542
P62484	Abi2	Abl interactor 2	↓	0.03648433
Q9WUU9	Mcm3ap	Germinal-center associated nuclear protein	↓	0.0088033
Q60598	Cttn	Src substrate cortactin	↓	0.01961026
Q64511	Top2b	DNA topoisomerase 2-beta	↓	0.03144888
P58771	Tpm1	Tropomyosin alpha-1 chain	↓	0.00257804
P80316	Cct5	T-complex protein 1 subunit epsilon	↓	0.00515904
P62259	Ywhae	14-3-3 protein epsilon	↓	0.03860277
Q11011	Npepps	Puromycin-sensitive aminopeptidase	↓	0.04775768
Q9QUH0	Glrx	Glutaredoxin-1	↓	0.02688917
P61982	Ywhag	14-3-3 protein gamma;14-3-3 protein gamma, N-terminally processed	↓	0.00734427
Q91XA8	Klhdc8a	Kelch domain-containing protein 8A	↓	0.03795375
P47962	Rpl5	60S ribosomal protein L5	↓	0.01028154
P63046	Sult4a1	Sulfotransferase 4A1	↓	0.02634609
P08103	Hck	Tyrosine-protein kinase HCK	↓	0.02243871
Q9CQ69	Uqcrq	Cytochrome b-c1 complex subunit 8	↓	0.04189749
P30677	Gna14	Guanine nucleotide-binding protein subunit alpha-14	↓	0.01490036
P68254	Ywhaq	14-3-3 protein theta	↓	0.02457486
Q62419	Sh3gl1	Endophilin-A2	↓	0.03003755
Q9CZM2	Rpl15	60S ribosomal protein L15	↓	0.04743316
Q9D6U8	Fam162a	Protein FAM162A	↓	0.04793291

P70452	Stx4	Syntaxin-4	↓	0.0451212
Q9QUM9	Psma6	Proteasome subunit alpha type-6	↓	0.04408097
P12367	Prkar2a	cAMP-dependent protein kinase type II-alpha regulatory subunit	↓	0.02208424
Q9DCV7	Krt7	Keratin, type II cytoskeletal 7	↓	0.03665023
Q8R4E6	Purg	Purine-rich element-binding protein gamma	↓	0.02611902
P18572	Bsg	Basigin	↓	0.03730565
P56399	Usp5	Ubiquitin carboxyl-terminal hydrolase 5	↓	0.03504823
Q8BJS8	Mtbp	Mdm2-binding protein	↓	0.04144291
Q6P8J7	Ckmt2	Creatine kinase S-type, mitochondrial	↓	0.0249179
Q80TF4	Klhl13	Kelch-like protein 13	↓	0.04903783
Q9JMH9	Myo18a	Unconventional myosin-XVIIIa	↓	0.04934256
O35660	Gstm6	Glutathione S-transferase Mu 6	↓	0.01502697
P51660	Hsd17b4	(3R)-hydroxyacyl-CoA dehydrogenase;Enoyl-CoA hydratase 2	↓	0.04586453
P22723	Gabrg2	Gamma-aminobutyric acid receptor subunit gamma-2	↓	0.01557893
Q9CR51	Atp6v1g1	V-type proton ATPase subunit G 1	↓	0.01093093
Q66JT0	Wee2	Wee1-like protein kinase 2	↓	0.04168859
Q148W0	Atp8b1	Phospholipid-transporting ATPase IC	↓	0.02492315
O70439	Stx7	Syntaxin-7	↓	0.0060893
Q9ERK4	Cse1l	Exportin-2	↓	0.02532686
Q9D1G1	Rab1b	Ras-related protein Rab-1B	↓	0.04788281
O35215	Ddt	D-dopachrome decarboxylase	↓	0.00367741
P45376	Akr1b1	Aldose reductase	↓	0.03690813
Q8BG32	Psmd11	26S proteasome non-ATPase regulatory subunit 11	↓	0.02235092
O35295	Purb	Transcriptional activator protein Pur-beta	↓	0.02539139
P47876	Igfbp1	Insulin-like growth factor-binding protein 1	↓	0.04333022
Q62393	Tpd52	Tumor protein D52	↓	0.03689092
Q9CWS0	Ddah1	N(G),N(G)-dimethylarginine dimethylaminohydrolase 1	↓	0.03955816
Q04736	Yes1	Tyrosine-protein kinase Yes	↓	0.0426567

Q6A037	N4bp1	NEDD4-binding protein 1	↓	0.03850518
P00416	mt-Co3	Cytochrome c oxidase subunit 3	↓	0.04264393
Q8JZW4	Cpne5	Copine-5	↓	0.01170659
F8VQB6	Myo10	Unconventional myosin-X	↓	0.00170969
P98197	Atp11a	Probable phospholipid-transporting ATPase IH	↓	0.02826024
Q60823	Akt2	RAC-beta serine/threonine-protein kinase	↓	0.03751247
Q8VDB8	Lrrc2	Leucine-rich repeat-containing protein 2	↓	0.02344924
Q9JI46	Nudt3	Diphosphoinositol polyphosphate phosphohydrolase 1	↓	0.02674355
Q8BYZ7	Elmo3	Engulfment and cell motility protein 3	↓	0.01525118
Q7TME2	Spag5	Sperm-associated antigen 5	↓	0.03387448
P47753	Capza1	F-actin-capping protein subunit alpha-1	↓	0.01092168
Q80ZN5	Cst13	Cystatin-13	↓	0.01486246
O35963	Rab33b	Ras-related protein Rab-33B	↓	0.00536558
Q99L88	Sntb1	Beta-1-syntrophin	↓	0.01349644
P09066	En2	Homeobox protein engrailed-2	↓	0.02595967

Appendix 7. Spectral Channels (318, 354).

Spectral Channel	Wavelength			Power (μW)
	Excitation	Emission	Dichroic mirror	
1	348	450-475	442	2.80
2	369	450-475	442	2.90
3	371	450-475	442	2.70
4	376	450-475	442	2.90
5	384	450-475	442	2.00
6	390	450-475	442	3.98
7	394	450-475	442	8.40
8	407	450-475	442	4.11
9	420	450-475	442	8.63
10	423	450-475	442	3.29
11	432	450-475	442	6.90
12	348	532-593	560	2.76
13	369	532-593	560	3.10
14	371	532-593	560	2.10
15	376	532-593	560	0.87
16	384	532-593	560	2.54
17	390	532-593	560	3.14
18	394	532-593	560	2.17
19	407	532-593	560	0.90
20	420	532-593	560	3.02
21	423	532-593	560	4.60
22	432	532-593	560	8.52
23	447	532-593	560	10.19
24	449	532-593	560	6.92
25	471	532-593	560	8.45
26	476	532-593	560	9.20
27	480	532-593	560	4.90
28	499	532-593	560	9.73

Spectral Channel	Wavelength			Power (μW)
	Excitation	Emission	Dichroic mirror	
29	507	532-593	560	13.51
30	522	532-593	560	14.80
31	531	532-593	560	10.21
32	348	690-715	695	14.31
33	369	690-715	695	8.33
34	371	690-715	695	11.89
35	376	690-715	695	12.86
36	384	690-715	695	3.13
37	390	690-715	695	4.84
38	394	690-715	695	8.95
39	407	690-715	695	10.73
40	420	690-715	695	7.26
41	423	690-715	695	8.81
42	432	690-715	695	9.55
43	447	690-715	695	5.30
44	449	690-715	695	10.15
45	471	690-715	695	14.25
46	476	690-715	695	15.49
47	480	690-715	695	10.74
48	499	690-715	695	14.88
49	507	690-715	695	8.62
51	522	690-715	695	12.34
51	531	690-715	695	13.35
52	563	690-715	695	2.47
53	597	690-715	695	3.89
54	625	690-715	695	7.15
55	649	690-715	695	8.62
56	DIC	690-715	695	5.82

References

1. De Duve C, Pressman BC, Gianetto R, Wattiaux R, Appelmans F. Tissue fractionation studies. 6. Intracellular distribution patterns of enzymes in rat-liver tissue. Biochem J. 1955;60(4):604-17.
2. Hesketh GG, Wartosch L, Davis LJ, Bright NA, Luzio JP. The lysosome and intracellular signalling. Prog Mol Subcell Biol. 2018;57:151-80.
3. Saftig P, Klumperman J. Lysosome biogenesis and lysosomal membrane proteins: Trafficking meets function. Nat Rev Mol Cell Biol. 2009;10(9):623-35.
4. Coutinho MF, Prata MJ, Alves S. Mannose-6-phosphate pathway: A review on its role in lysosomal function and dysfunction. Mol Genet Metab. 2012;105(4):542-50.
5. Chen R, Jäättelä M, Liu B. Lysosome as a central hub for rewiring pH homeostasis in tumors. Cancers (Basel). 2020;12(9).
6. Samie M, Wang X, Zhang X, Goschka A, Li X, Cheng X, et al. A TRP Channel in the lysosome regulates large particle phagocytosis via focal exocytosis. Dev Cell. 2013;26(5):511-24.
7. Zhang X, Cheng X, Yu L, Yang J, Calvo R, Patnaik S, et al. MCOLN1 is a ROS sensor in lysosomes that regulates autophagy. Nat Commun. 2016;7:12109.
8. Dell'Angelica EC, Mullins C, Caplan S, Bonifacino JS. Lysosome-related organelles. FASEB J. 2000;14(10):1265-78.
9. Bonam SR, Wang F, Muller S. Lysosomes as a therapeutic target. Nat Rev Drug Discov. 2019;18(12):923-48.
10. Huizing M, Helip-Wooley A, Westbroek W, Gunay-Aygun M, Gahl WA. Disorders of lysosome-related organelle biogenesis: clinical and molecular genetics. Annu Rev Genomics Hum Genet 2008;9:359-86.
11. Ballabio A, Bonifacino JS. Lysosomes as dynamic regulators of cell and organismal homeostasis. Nat Rev Mol Cell Biol. 2020;21(2):101-18.
12. Trivedi PC, Bartlett JJ, Pulinilkunnil T. Lysosomal biology and function: Modern view of cellular debris bin. Cells. 2020;9(5):1131.
13. Schwake M, Schröder B, Saftig P. Lysosomal membrane proteins and their central role in physiology. Traffic. 2013;14(7):739-48.
14. Xiong J, Zhu MX. Regulation of lysosomal ion homeostasis by channels and transporters. Sci China Life Sci. 2016;59(8):777-91.
15. Xu H, Ren D. Lysosomal physiology. Annu Rev Physiol. 2015;77:57-80.

16. Palmieri M, Impey S, Kang H, di Ronza A, Pelz C, Sardiello M, et al. Characterization of the CLEAR network reveals an integrated control of cellular clearance pathways. Hum Mol Genet. 2011;20(19):3852-66.
17. Sardiello M, Palmieri M, Di Ronza A, Medina DL, Valenza M, Gennarino VA, et al. A gene network regulating lysosomal biogenesis and function. Science. 2009;325(5939):473-7.
18. Luzio JP, Pryor PR, Bright NA. Lysosomes: fusion and function. Nat Rev Mol Cell Biol. 2007;8(8):622-32.
19. McIlhinney J, Hooper N, Luzio JP, Pryor PR, Gray SR, Gratian MJ, et al., editors. Membrane traffic to and from lysosomes. Biochemical Society Symposia; 2005: Portland Press.
20. Hu Y-B, Dammer EB, Ren R-J, Wang G. The endosomal-lysosomal system: from acidification and cargo sorting to neurodegeneration. Transl Neurodegener. 2015;4(1):18.
21. Tooze SA, Abada A, Elazar Z. Endocytosis and autophagy: exploitation or cooperation? Cold Spring Harb Perspect Biol. 2014;6(5):a018358.
22. Lamb CA, Dooley HC, Tooze SA. Endocytosis and autophagy: Shared machinery for degradation. Bioessays. 2013;35(1):34-45.
23. Parzych KR, Klionsky DJ. An overview of autophagy: morphology, mechanism, and regulation. Antioxid Redox Signal. 2014;20(3):460-73.
24. Jung S, Jeong H, Yu SW. Autophagy as a decisive process for cell death. Exp Mol Med. 2020;52(6):921-30.
25. Jia R, Guardia CM, Pu J, Chen Y, Bonifacino JS. BORC coordinates encounter and fusion of lysosomes with autophagosomes. Autophagy. 2017;13(10):1648-63.
26. Braulke T, Bonifacino JS. Sorting of lysosomal proteins. Biochim Biophys Acta. 2009;1793(4):605-14.
27. Seaman MN. Cargo-selective endosomal sorting for retrieval to the Golgi requires retromer. J Cell Biol. 2004;165(1):111-22.
28. Doray B, Ghosh P, Griffith J, Geuze HJ, Kornfeld S. Cooperation of GGAs and AP-1 in packaging MPRs at the trans-Golgi network. Science. 2002;297(5587):1700-3.
29. Abubakar YS, Zheng W, Olsson S, Zhou J. Updated insight into the physiological and pathological roles of the retromer complex. Int J Mol Sci. 2017;18(8):1601.
30. Wandinger-Ness A, Zerial M. Rab proteins and the compartmentalization of the endosomal system. Cold Spring Harb Perspect Biol. 2014;6(11):a022616.

31. Rink J, Ghigo E, Kalaidzidis Y, Zerial M. Rab conversion as a mechanism of progression from early to late endosomes. Cell. 2005;122(5):735-49.
32. Bowman SL, Bi-Karchin J, Le L, Marks MS. The road to lysosome-related organelles: Insights from Hermansky-Pudlak syndrome and other rare diseases. Traffic. 2019;20(6):404-35.
33. Ivan V, Martinez-Sanchez E, Sima LE, Oorschot V, Klumperman J, Petrescu SM, et al. AP-3 and Rabip4'coordinately regulate spatial distribution of lysosomes. PLoS One. 2012;7(10):e48142.
34. Platt FM, d'Azzo A, Davidson BL, Neufeld EF, Tifft CJ. Lysosomal storage diseases. Nat Rev Dis Primers. 2018;4(27).
35. Parenti G, Andria G, Ballabio A. Lysosomal storage diseases: from pathophysiology to therapy. Annu Rev Med. 2015;66:471-86.
36. Platt FM, Boland B, Van der Spoel AC. Lysosomal storage disorders: The cellular impact of lysosomal dysfunction. J Cell Biol. 2012;199(5):723-34.
37. Schröder B, Wrocklage C, Pan C, Jäger R, Kösters B, Schäfer H, et al. Integral and associated lysosomal membrane proteins. Traffic. 2007;8(12):1676-86.
38. Sleat DE, Ding L, Wang S, Zhao C, Wang Y, Xin W, et al. Mass spectrometry-based protein profiling to determine the cause of Lysosomal Storage Diseases of unknown etiology. Mol Cell Proteomics. 2009;8(7):1708-18.
39. Poupětová H, Ledvinová J, Berná L, Dvořáková L, Kožich V, Elleder M. The birth prevalence of Lysosomal Storage Disorders in the Czech Republic: comparison with data in different populations. J Inherit Metab Dis. 2010;33(4):387-96.
40. Meikle PJ, Hopwood JJ, Clague AE, Carey WF. Prevalence of Lysosomal Storage Disorders. JAMA. 1999;281(3):249-54.
41. Nalysnyk L, Rotella P, Simeone JC, Hamed A, Weinreb N. Gaucher disease epidemiology and natural history: a comprehensive review of the literature. Hematology. 2016;22(2):65-73.
42. Khan SA, Peracha H, Ballhausem D, Wiesbauer A, Rohrbach M, Gautschi M, et al. Epidemiology of mucopolysaccharidoses. Mol Genet Metab. 2017;121(3):227-40.
43. Zelei T, Csetneki K, Vokó Z, Siffel C. Epidemiology of Sanfilippo syndrome: results of a systematic literature review. Orphanet J Rare Dis. 2018;13(53).
44. Nita DA, Mole SE, Minassian BA. Neuronal ceroid lipofuscinoses. Epileptic Disord. 2016;18(2):73-88.

45. Mistry PK, Kishnani P, Wanner C, Dong D, Bender J, Batista JL, et al. Rare lysosomal disease registries: lessons learned over three decades of real-world evidence. Orphanet Journal of Rare Diseases. 2022;17(1):362.

46. Kingma SDK, Bodamer OA, Wijburg FA. Epidemiology and diagnosis of lysosomal storage disorders; challenges of screening. Best Pract Res Clin Obstet Gynaecol. 2015;29(2):145-57.

47. Ysselstein D, Shulman JM, Krainc D. Emerging links between pediatric lysosomal storage diseases and adult parkinsonism. Mov Disord. 2019;34(5):614-24.

48. Beck M. The Link Between Lysosomal Storage Disorders and More Common Diseases. J Inborn Errors Metab Screen. 2016;4:2326409816682767.

49. Kohlschütter A, Schulz A, Bartsch U, Storch S. Current and emerging treatment strategies for Neuronal Ceroid Lipofuscinoses. CNS Drugs. 2019;33(4):315-25.

50. de Ruijter J, Valstar M, Narajczyk M, et al. Genistein in Sanfilippo disease: a randomized controlled crossover trial. Annals of Neurology. 2012;71(1):110-20.

51. Platt FM, Neises G, Dwek R, Butters T. N-butyldeoxynojirimycin is a novel inhibitor of glycolipid biosynthesis. J Biol Chem. 1994;269:8362-5.

52. Coutinho MF, Santos JI, Alves S. Less is more: Substrate reduction therapy for Lysosomal Storage Disorders. Int J Mol Sci. 2016;17(7):1065.

53. Kay MA, Glorioso JC, Naldini L. Viral vectors for gene therapy: the art of turning infectious agents into vehicles of therapeutics. Nat Med. 2001;7(1):33-40.

54. Tardieu M, Zerah M, Husson B, de Bournonville S, Deiva K, Adamsbaum C, et al. Intracerebral administration of adeno-associated viral vector serotype rh.10 carrying human SGSH and SUMF1 cDNAs in children with mucopolysaccharidosis type IIIA disease: results of a phase I/II trial. Hum Gene Ther. 2014;25(6):506-16.

55. Biffi A, Montini E, Lorioli L, Cesani M, Fumagalli F, Plati T, et al. Lentiviral hematopoietic stem cell gene therapy benefits metachromatic leukodystrophy. Science. 2013;341(6148):1233158.

56. Smith BK, Collins SW, Conlon TJ, Mah CS, Lawson LA, Martin AD, et al. Phase I/II trial of adeno-associated virus–mediated alpha-glucosidase gene therapy to the diaphragm for chronic respiratory failure in pompe disease: initial safety and ventilatory outcomes. Hum Gene Ther. 2013;24(6):630-40.

57. Tardieu M, Zerah M, Gougeon M-L, Ausseil J, Bournonville S, Husson B, et al. Intracerebral gene therapy in children with mucopolysaccharidosis type IIIB syndrome: an uncontrolled phase 1/2 clinical trial. Lancet Neurol. 2017;16(9):712-20.

58. Ohashi T. Gene therapy for lysosomal storage diseases and peroxisomal diseases. J Hum Genet. 2018;64:39-143.
59. Chang D, Nalls MA, Hallgrimsdottir IB, Hunkapiller J, van der Brug M, Cai F, et al. A meta analysis of genome wide association studies identifies 17 new Parkinson's disease risk loci. Nat Genet. 2017;49(10):1511-6.
60. Creese B, Bell E, Johar I, Francis P, Ballard C, Aarsland D. Glucocerebrosidase mutations and neuropsychiatric phenotypes in Parkinson's disease and Lewy body dementias: Review and meta-analyses. Am J Med Genet. 2018;177(2):232-41.
61. Gatto EM, Gustavo Da Prat GD, Etcheverry JL, Guillermo Drelichman G, Cesarini M. Parkinsonisms and glucocerebrosidase deficiency: A comprehensive review for molecular and cellular mechanism of glucocerebrosidase deficiency. Brain Sci. 2019;9(2):30.
62. Ciani M, Benussi L, Bonvicini C, Ghidoni R. Genome wide association study and next generation sequencing: a glimmer of light toward new possible horizons in frontotemporal dementia research. Front Neurosci. 2019;13(506).
63. Clark LN, Chan R, Cheng R, Liu X, Park N, Parmalee N, et al. Gene-wise association of variants in four lysosomal storage disorder genes in neuropathologically confirmed lewy body disease. PLoS ONE. 2015;10(5).
64. Bellettato CM, Scarpa M. Pathophysiology of neuropathic lysosomal storage disorders. J Inherit Metab Dis. 2010;33(4):347-62.
65. Gieselmann V. Fabry Disease: Perspectives from 5 Years of FOS. Oxford: Oxford PharmaGenesis; 2006.
66. Saito Y, Suzuki K, Hulette CM, Murayama S. Aberrant phosphorylation of alpha-synuclein in human Niemann-Pick type C1 disease. J Neuropathol Exp Neurol. 2004;63(4):323-8.
67. Winder-Rhodes S, Garcia-Reitböck P, Ban M, Evans J, Jacques T, Kemppinen A, et al. Genetic and pathological links between Parkinson's disease and the Lysosomal Disorder Sanfilippo Syndrome. Mov Disord. 2012;27(2):312-5.
68. Mazzulli JR, Xu YH, Sun Y, Knight AL, McLean PJ, Caldwell GA, et al. Gaucher disease glucocerebrosidase and α-synuclein form a bidirectional pathogenic loop in synucleinopathies. Cell. 2011;146(1):37-52.
69. Nixon RA. Niemann-Pick Type C disease and Alzheimer's disease: the APP-endosome connection fattens up. Am J Pathol. 2004;164(3):757-61.

70. Chiba Y, Komori H, Takei S, Hasegawa-Ishii S, Kawamura N, Adachi K, et al. Niemann-Pick disease type C1 predominantly involving the frontotemporal region, with cortical and brainstem Lewy bodies: an autopsy case. Neuropathology. 2014;34(1):49-57.

71. Giovedì S, Ravanelli MM, Parisi B, Bettegazzi B, Guarnieri FC. Dysfunctional autophagy and endolysosomal system in neurodegenerative diseases: relevance and therapeutic options. Front Cell Neurosci. 2020;14:602116.

72. Morrill SA, Amon A. Why haploinsufficiency persists. Proc Natl Acad Sci. 2019;116(24):11866-71.

73. Robak LA, Jansen IE, Rooij Jv, Uitterlinden AG, Kraaij R, Jankovic J, et al. Excessive burden of lysosomal storage disorder gene variants in Parkinson's disease. Brain. 2017;140:3191-203.

74. Sidransky E, Nalls MA, Aasly JO, Aharon-Peretz J, Annesi G, Barbosa ER, et al. Multicenter analysis of glucocerebrosidase mutations in Parkinson's disease. N Engl J Med. 2009;361(17):1651-61.

75. Baker M, Mackenzie IR, Pickering-Brown S, Gass J, Rademakers R, Lindholm C, et al. Mutations in progranulin cause tau-negative frontotemporal dementia linked to chromosome 17. Nature. 2006;442(7105):916-9.

76. Kirk EP, Ong R, Boggs K, Hardy T, Righetti S, Kamien B, et al. Gene selection for the Australian Reproductive Genetic Carrier Screening Project ("Mackenzie's Mission"). Eur J Hum Genet. 2021;29(1):79-87.

77. Antonarakis SE. Carrier screening for recessive disorders. Nat Rev Genet. 2019;20(9):549-61.

78. Kaback MM. Population-based genetic screening for reproductive counseling: the Tay-Sachs disease model. Eur J Pediatr. 2000;159 Suppl 3:S192-5.

79. Brady RO, Kanfer J, Shapiro D. The metabolism of glucocerebrosides. I. Purification and properties of a glucocerebroside-cleaving enzyme from spleen tissue. J Biol Chem. 1965;240:39-43.

80. Parkin JL, Brunning RD. Pathology of the Gaucher cell. Prog Clin Biol Res. 1982;95:151-75.

81. Simpson WL, Hermann G, Balwani M. Imaging of Gaucher disease. World J Radiol. 2014;6(9):657-68.

82. Sidransky E. Gaucher disease: complexity in a "simple" disorder. Mol Genet Metab. 2004;83(1-2):6-15.

83. Roshan Lal T, Sidransky E. The Spectrum of Neurological Manifestations Associated with Gaucher Disease. Diseases. 2017;5(1).
84. Wong K, Sidransky E, Verma A, Mixon T, Sandberg GD, Wakefield LK, et al. Neuropathology provides clues to the pathophysiology of Gaucher disease. Mol Genet Metab. 2004;82(3):192-207.
85. Stirnemann J, Belmatoug N, Camou F, Serratrice C, Froissart R, Caillaud C, et al. A review of Gaucher disease pathophysiology, clinical presentation and treatments. Int J Mol Sci. 2017;18(2):441.
86. Lepe-Balsalobre E, Santotoribio JD, Nuñez-Vazquez R, García-Morillo S, Jiménez-Arriscado P, Hernández-Arévalo P, et al. Genotype/phenotype relationship in Gaucher disease patients. Novel mutation in glucocerebrosidase gene. Clin Chem Lab Med. 2020;58(12):2017-24.
87. Neudorfer O, Giladi N, Elstein D, Abrahamov A, Turezkite T, Aghai E, et al. Occurrence of Parkinson's syndrome in type 1 Gaucher disease. QJM: An International Journal of Medicine. 1996;89(9):691-4.
88. Tayebi N, Callahan M, Madike V, Stubblefield BK, Orvisky E, Krasnewich D, et al. Gaucher disease and parkinsonism: a phenotypic and genotypic characterization. Mol Genet Metab. 2001;73(4):313-21.
89. Tayebi N, Walker J, Stubblefield B, Orvisky E, LaMarca ME, Wong K, et al. Gaucher disease with parkinsonian manifestations: does glucocerebrosidase deficiency contribute to a vulnerability to parkinsonism? Mol Genet Metab. 2003;79(2):104-9.
90. Goker-Alpan O, Schiffmann R, LaMarca ME, Nussbaum RL, McInerney-Leo A, Sidransky E. Parkinsonism among Gaucher disease carriers. J Med Genet. 2004;41(12):937-40.
91. Balestrino R, Schapira A. Glucocerebrosidase and Parkinson disease: molecular, clinical and therapeutic implications. Neuroscientist. 2018;5:540-59.
92. Gan-Or Z, Liong C, Alcalay RN. GBA-Associated Parkinson's Disease and Other Synucleinopathies. Curr Neurol Neurosci Rep. 2018;18(8):44.
93. Mitsui J, Mizuta I, Toyoda A, Ashida R, Takahashi Y, Goto J, et al. Mutations for Gaucher Disease Confer High Susceptibility to Parkinson Disease. JAMA Neurology. 2009;66(5):571-6.
94. Neumann J, Bras J, Deas E, O'Sullivan SS, Parkkinen L, Lachmann RH, et al. Glucocerebrosidase mutations in clinical and pathologically proven Parkinson's disease. Brain. 2009;132:1783-94.

95. Gatto EM, Etcheverry JL, Sanguinetti A, Cesarini M, Fernandez EN, Drelichman G. Prodromal Clinical Markers of Parkinson disease in Gaucher Disease Individuals. Eur Neurol. 2016;76(1-2).
96. Riboldi GM, Di Fonzo AB. GBA, Gaucher Disease, and Parkinson's Disease: From Genetic to Clinic to New Therapeutic Approaches. Cells. 2019;8(364).
97. Cerri S, Ghezzi C, Ongari G, Croce S, Avenali M, Zangaglia R, et al. GBA Mutations Influence the Release and Pathological Effects of Small Extracellular Vesicles from Fibroblasts of Patients with Parkinson's Disease. Int J Mol Sci. 2021;22(4).
98. Montfort M, Chabás A, Vilageliu L, Grinberg D. Functional analysis of 13 GBA mutant alleles identified in Gaucher disease patients: Pathogenic changes and "modifier" polymorphisms. Hum Mutat. 2004;23(6):567-75.
99. Shachar T, Lo Bianco C, Recchia A, Wiessner C, Raas-Rothschild A, Futerman AH. Lysosomal storage disorders and Parkinson's disease: Gaucher disease and beyond. Mov Disord. 2011;26(9):1593-604.
100. Maor G, Cabasso O, Krivoruk O, Rodriguez J, Steller H, Segal D, et al. The contribution of mutant GBA to the development of Parkinson disease in Drosophila. Hum Mol Genet. 2016;25(13):2712-27.
101. Ikuno M, Yamakado H, Akiyama H, Parajuli LK, Taguchi K, Hara J, et al. GBA haploinsufficiency accelerates alpha-synuclein pathology with altered lipid metabolism in a prodromal model of Parkinson's disease. Hum Mol Genet. 2019;28(11):1894-904.
102. Tayebi N, Parisiadou L, Berhe B, Gonzalez AN, Vinardell JS, Tamargo RJ, et al. Glucocerebrosidase haploinsufficiency in A53T α-synuclein mice impacts disease onset and course. Mol Genet Metab. 2017;122(4):198-208.
103. Taguchi YV, Liu J, Ruan J, Pacheco J, Zhang XK, Abbasi J, et al. Glucosylsphhingosine promotes apha-synuclein pathology in mutant GBA-associated Parkinson's disease. J Neurosci. 2017;37(40):9617-31.
104. Sardi P, Clarke J, Kinnecom C, Tamsett TJ, Li L, Stanek LM, et al. CNS expression of glucocerebrosidase corrects α-synuclein pathology and memory in a mouse model of Gaucher-related synucleinopathy. PNAS. 2011;108(299):12101-6.
105. Kim D, Hwang H, Choi S, Kwon SH, Lee S, Park JH, et al. D409H GBA1 mutation accelerates the progression of pathology in A53T α-synuclein transgenic mouse model. Acta Neuropathol Commun. 2018;6(1):32.

106. Berge-Seidl V, Pihlstrøm L, Maple-Grødem J, Forsgren L, Linder J, Larsen J, et al. The GBA variant E326K is associated with Parkinson's disease and explains a genome-wide association signal. Neuroscie Lett. 2017;29(658):48-52.
107. Mata IF, Leverenz JB, Weintraub D, Trojanowski JQ, Chen-Plotkin A, Van Deerlin VM, et al. GBA variants are associated with a distinct pattern of cognitive deficits in Parkinson disease. Mov Disord. 2017;31(1):995-102.
108. Lehri-Boufala S, Ouidja M, Barbier-Chassefiere V, Henault E, Raisman-Vozari R, Garrigue-Antar L, et al. New roles of glycosaminoglycans in α-synuclein aggregation in a cellular model of Parkinson disease. PLoS ONE. 2015;10(1).
109. Li H, Ham A, Ma TC, Kuo SH, Kanter E, Kim D, et al. Mitochondrial dysfunction and mitophagy defect triggered by heterozygous GBA mutations. Autophagy. 2019;15(1):113-30.
110. Migdalska-Richards A, Wegrzynowicz M, Rusconi R, Deangeli G, Di Monte DA, Spillantini MG, et al. The L444P Gba1 mutation enhances alpha-synuclein induced loss of nigral dopaminergic neurons in mice. Brain. 2017;140(10):2706-21.
111. Vanier MT. Niemann-Pick diseases. Handbook of Clinical Neurology. 2013;113:1717-21.
112. Pavlů-Pereira H, Asfaw B, Poupctová H, Ledvinová J, Sikora J, Vanier MT, et al. Acid sphingomyelinase deficiency. Phenotype variability with prevalence of intermediate phenotype in a series of twenty-five Czech and Slovak patients. A multi-approach study. J Inherit Metab Dis. 2005;28(2):203-27.
113. Blom TS, Linder MD, Snow K, Pihko H, Hess MW, Jokitalo E, et al. Defective endocytic trafficking of NPC1 and NPC2 underlying infantile Niemann–Pick type C disease. Hum Mol Genet. 2003;12(3):257-72.
114. Garver WS, Heidenreich RA. The Niemann-Pick C Proteins and Trafficking of Cholesterol Through the Late Endosomal / Lysosomal System. Curr Mol Med. 2002;2(5):485-505.
115. Bi X, Liao G. Cholesterol in Niemann-Pick type C disease. Subcell Biochem. 2010;51:319-35.
116. Dagan E, Schlesinger I, Ayoub M, Mory A, Nassar M, Kurolap A, et al. The contribution of Niemann-Pick SMPD1 mutations to Parkinson disease in Ashkenazi Jews. Parkinsonism Relat Disord. 2015;21(9):1067-71.
117. Gan-Or Z, Ozelius LJ, Bar-Shira A, Saunders-Pullman R, Mirelman A, Kornreich R, et al. The p.L302P mutation in the lysosomal enzyme gene SMPD1 is a risk factor for Parkinson disease. Neurology. 2013;80(17):1606-10.

118. Foo J-N, Liany H, Bei J-X, Yu X-Q, Liu J, Au W-L, et al. A rare lysosomal enzyme gene SMPD1 variant (p.R591C) associates with Parkinson's disease. Neurobiol Aging. 2013;34.

119. Gan-Or Z, Orr-Urtreger A, Alcalay RN, Bressman S, Giladi N, Rouleau GA. The emerging role of SMPD1 mutations in Parkinson's disease: Implications for future studies. Parkinsonism Relat Disord. 2015;21(10):1294-5.

120. Schneider SA, Tahirovic S, Hardy J, Strupp M, Bremova-Ertl T. Do heterozygous mutations of Niemann-Pick type C predispose to late-onset neurodegeneration: a review of the literature. J Neurol. 2021;268(6):2055-64.

121. Cupidi C, Frangipane F, Gallo M, Clodomiro A, Colao R, Bernardi L, et al. Role of Niemann-Pick Type C Disease Mutations in Dementia. J Alzheimers Dis. 2017;55(3):1249-59.

122. Kresojević N, Dobričić V, Svetel M, Kostić V. Mutations in Niemann Pick type C gene are risk factor for Alzheimer's disease. Medical Hypotheses. 2014;83(5):559-62.

123. Kluenemann H, Nutt J, Davis M, Bird T. Parkinsonism syndrome in heterozygotes for Nieman-Pick C1. J Neurol Sci. 2013;335(1-2):219-20.

124. Kruth HS, Comly ME, Butler JD, Vanier MT, Fink JK, Wenger DA, et al. Type C Niemann-Pick disease. Abnormal metabolism of low density lipoprotein in homozygous and heterozygous fibroblasts. J Biol Chem. 1986;261(35):16769-74.

125. Benussi A, Cotelli MS, Cantoni V, Bertasi V, Turla M, Dardis A, et al. Clinical and neurophysiological characteristics of heterozygous NPC1 carriers. JIMD Reports. 2019;49(1):80-8.

126. Bremova-Ertl T, Sztatecsny C, Brendel M, Moser M, Möller B, Clevert DA, et al. Clinical, ocular motor, and imaging profile of Niemann-Pick type C heterozygosity. Neurology. 2020;94(16):e1702-e15.

127. Hung YH, Walterfang M, Churilov L, Bray L, Jacobson LH, Barnham KJ, et al. Neurological Dysfunction in Early Maturity of a Model for Niemann–Pick C1 Carrier Status. Neurotherapeutics. 2016;13:614-22.

128. Yu W, Ko M, Yanagisawa K, Michikawa M. Neurodegeneration in heterozygous Niemann-Pick Type C1 (NPC1) mouse: Implication of heterozygous NPC1 mutations being a risk for tauopathy. J Biol Chem. 2005;280.

129. Brown D, Thrall M, Walkley SU, Wurzelmann S, Wenger D, Allison R, et al. Metabolic abnormalities in feline Niemann-Pick type C heterozygotes. J Inherit Metab Dis. 1996;19:319-30.

130. Lefebvre S, Vartanian T. Molecular basis of myelin In: Dangond F, Heinemann B, editors. Disorders of Myelin in the Central and Peripheral Nervous Systems. Woburn: Butterworth Heinemann; 2002.
131. Borda JT, Alvarez X, Mohan M, Ratterree MS, Phillippi-Falkenstein K, Lackner AA, et al. Clinical and immunopathologic alterations in rhesus macaques affected with globoid cell leukodystrophy. Am J Pathol. 2008;172(1):98-111.
132. Suzuki K, Tanaka H, Suzuki K. Studies on the Pathogenesis of Krabbe's Leukodystrophy: Cellular Reaction of the Brain to Exogenous Galactosylsphingosine, Monogalactosyl Diglyceride, and Lactosylceramide. In: Volk BW, Schneck L, editors. Current Trends in Sphingolipidoses and Allied Disorders. Boston, MA: Springer US; 1976. p. 99-114.
133. Cantuti Castelvetri L, Givogri MI, Hebert A, Smith B, Song Y, Kaminska A, et al. The sphingolipid psychosine inhibits fast axonal transport in Krabbe disease by activation of GSK3β and deregulation of molecular motors. J Neurosci. 2013;33(24):10048-56.
134. Lee WC, Kang D, Causevic E, Herdt AR, Eckman EA, Eckman CB. Molecular characterization of mutations that cause globoid cell leukodystrophy and pharmacological rescue using small molecule chemical chaperones. J Neurosci. 2010;30(16):5489-97.
135. Graziano AC, Cardile V. History, genetic, and recent advances on Krabbe disease. Gene. 2015;555(1):2-13.
136. Madsen AMH, Wibrand F, Lund AM, Ek J, Dunø M, Østergaard E. Genotype and phenotype classification of 29 patients affected by Krabbe disease. JIMD Rep. 2019;46(1):35-45.
137. Beltran-Quintero ML, Bascou NA, Poe MD, Wenger DA, Saavedra-Matiz CA, Nichols MJ, et al. Early progression of Krabbe disease in patients with symptom onset between 0 and 5 months. Orphanet J Rare Dis. 2019;14(1):46.
138. Debs R, Froissart R, Aubourg P, Papeix C, Douillard C, Degos B, et al. Krabbe disease in adults: phenotypic and genotypic update from a series of 11 cases and a review. J Inherit Metab Dis. 2013;36(5):859-68.
139. Wenger DA, Rafi MA, Luzi P, Datto J, Costantino-Ceccarini E. Krabbe disease: genetic aspects and progress toward therapy. Mol Genet Metab. 2000;70(1):1-9.
140. Wenger DA, Rafi MA, Luzi P. Krabbe disease: One Hundred years from the bedside to the bench to the bedside. J Neurosci Res. 2016;94(11):982-9.
141. Kolodny EH, Raghavan S, Krivit W. Late-onset Krabbe disease (globoid cell leukodystrophy): clinical and biochemical features of 15 cases. Dev Neurosci. 1991;13(4-5):232-9.

142. Liu Y, Gibson J, Wheeler J, Kwee LC, Santiago-Turla CM, Akafo SK, et al. GALC deletions increase the risk of primary open-angle glaucoma: the role of Mendelian variants in complex disease. PloS one. 2011;6(11):e27134-e.
143. Lee JH, Cho MH, Hersh CP, McDonald ML, Wells JM, Dransfield MT, et al. IREB2 and GALC are associated with pulmonary artery enlargement in chronic obstructive pulmonary disease. Am J Respir Cell Mol Biol. 2015;52(3):365-76.
144. Marshall MS, Bongarzone ER. Beyond Krabbe's disease: The potential contribution of galactosylceramidase deficiency to neuronal vulnerability in late-onset synucleinopathies. J Neurosci Res. 2016;94(11):1328-32.
145. Cruts M, Gijselinck I, van der Zee J, Engelborghs S, Wils H, Pirici D, et al. Null mutations in progranulin cause ubiquitin-positive frontotemporal dementia linked to chromosome 17q21. Nature. 2006;442:920-4.
146. Gass J, Cannon A, Mackenzie IR, Boeve B, Baker M, Adamson J, et al. Mutations in progranulin are a major cause of ubiquitin-positive frontotemporal lobar degeneration. Hum Mol Genet. 2006;15(20):2988-3001.
147. Mackenzie IR, Baker M, Pickering-Brown S, Hsiung G-Y, Lindholm C, Dwosh E, et al. The neuropathology of frontotemporal lobar degeneration caused by mutations in the progranulin gene. Brain. 2006;129(11):3081-90.
148. Bae E-J, Yang N, Lee C, Kim S, Lee H-J, Lee S-J. Haploinsufficiency of cathepsin D leads to lysosomal dysfunction and promotes cell-to-cell transmission of α-synuclein aggregates. Cell Death Dis. 2015;6(10):e1901.
149. Marshall MS, Jakubauskas B, Bogue W, Stoskute M, Hauck Z, Rue E, et al. Analysis of age-related changes in psychosine metabolism in the human brain. PLoS One. 2018;13(2):e0193438.
150. Sawcer S, Franklin RJ, Ban M. Multiple sclerosis genetics. Lancet Neurol. 2014;13(7):700-9.
151. Sawcer S, Hellenthal G, Pirinen M, Spencer CC, Patsopoulos NA, Moutsianas L, et al. Genetic risk and a primary role for cell-mediated immune mechanisms in multiple sclerosis. Nature. 2011;476(7359):214-9.
152. Scott-Hewitt NJ, Folts CJ, Noble MD. Heterozygous carriers of galactocerebrosidase mutations that cause Krabbe disease have impaired microglial function and defective repair of myelin damage. Neural Regen Res. 2018;13(3):393-401.

153. Kresse H. Mucopolysaccharidosis 3A (Sanfilippo A disease): deficiency of a heparan sulfamidase in skin fibroblasts and leucocytes. Biochem Biophys Res Commun. 1973;54:1111-8.
154. Von Figura K. Human alpha-n-acetylglucosaminidase: activity towards natural substrates and multiple recognition forms. Eur J Biochem. 1977;80:535-42.
155. Klein U, Kresse H, von Figura K. Sanfilippo syndrome type C: Deficiency of acetyl-CoA:a-glucosaminide N-acetyltransferase in skin fibroblasts. PNAS. 1978;75(10):5185-9.
156. Kresse H, Paschke E, von Figura K, Gilberg W, Fuchs W. Sanfilippo disease type D: Deficiency of N-acetylglucosamine-6-sulfate sulfatase required for heparan sulfate degradation. PNAS. 1980;77(11):6822-6.
157. Valstar M, Ruijter GJ, van Diggelen OP, Poorthuis BJ, Wijburg FA. Sanfilippo syndrome: a mini-review. J Inherit Metab Dis. 2008;31(2):240-52.
158. Valstar M, Marchal J, Grootenhuis M, Colland V, Wijburg F. Cognitive development in patients with Mucopolysaccharidosis type III (Sanfilippo syndrome). Orphanet J Rare Dis. 2011;6(43).
159. Ruijter G, Valstar M, van de Kamp J, van der Helm R, Durand S, Diggelen O, et al. Clinical and genetic spectrum of sanfilippo type C (MPS IIIC) disease in The Netherlands. Mol Genet Metab. 2007;93(2):104-11.
160. Nalls MA, Blauwendraat C, Vallerga CL, Heilbron K, Bandres-Ciga S, Chang D, et al. Identification of novel risk loci, causal insights, and heritable risk for Parkinson's disease: a meta-analysis of genome-wide association studies. Lancet Neurol. 2019;18(12):1091-102.
161. Douglass ML, Beard H, Shoubridge A, Nazri N, King B, Trim PJ, et al. Is SGSH Heterozygosity a Risk Factor for Early-onset Neurodegenerative Disease? J Inherit Metab Dis. 2021;44(3):763-76.
162. Elia LP, Mason AR, Alijagic A, Finkbeiner S. Genetic regulation of neuronal progranulin reveals a critical role for the autophagy-lysosome pathway. J Neurosci. 2019;39(17):3332-44.
163. Ahmed Z, Mackenzie I, Hutton M, Dickson D. Progranulin in frontotemporal lobar degeneration and neuroinflammation. J Neuroinflammation. 2007;4(7).
164. Gass J, Lee W, Cook C, Finch N, Stetler C, Jansen-West K, et al. Progranulin regulates neuronal outgrowth independent of sortilin. Mol Neurodegener. 2012;7(33).
165. Petkau T, Leavitt B. Progranulin in neurodegenerative disease. Trends Neurosci. 2014;37:388-98.

166. Mole SE, Cotman SL. Genetics of the Neuronal Ceroid Lipofuscinoses (Batten disease). Biochimica et Biophysica Acta. 2015;1852(1000):2237-41.
167. Rabinovici GD, Miller BL. Frontotemporal Lobar Degeneration: Epidemiology, Pathophysiology, Diagnosis and Management. CNS Drugs. 2010;24(5):375-98.
168. Paushter DH, Du H, Feng T, Hu F. The lysosomal function of progranulin, a guardian against neurodegeneration. Acta Neuropathol. 2018;136(1):1-17.
169. Ward ME, Chen R, Huang H-Y, Ludwig C, Telpoukhovskaia M, Taubes A, et al. Individuals with progranulin haploinsufficiency exhibit features of neuronal ceroid lipofuscinosis. Sci Transl Med. 2017;9(385).
170. Neary D, Snowden J, Gustafson L, Passant U, Stuss D, Black S, et al. Frontotemporal lobar degeneration: a consensus on clinical diagnostic criteria. Neurology. 1998;51(6):1546-54.
171. Arrant AE, Onyilo VC, Unger DE, Roberson ED. Progranulin Gene Therapy Improves Lysosomal Dysfunction and Microglial Pathology Associated with Frontotemporal Dementia and Neuronal Ceroid Lipofuscinosis. J Neurosci. 2018;38(9):2341-58.
172. Brouwers N, Nuytemans K, van der Zee J, Gijselinck I, Engelborghs S, Theuns J, et al. Alzheimer and Parkinson Diagnoses in Progranulin Null Mutation Carriers in an Extended Founder Family. Arch Neurol. 2007;64(10):1436-46.
173. Cruchaga C, Fernández-Seara MA, Seijo-Martínez M, Samaranch L, Lorenzo E, Hinrichs A, et al. Cortical atrophy and language network reorganization associated with a novel progranulin mutation. Cereb Cortex. 2009;19(8):1751-60.
174. Guerreiro RJ, Santana I, Bras JM, Revesz T, Rebelo O, Ribeiro MH, et al. Novel progranulin mutation: screening for PGRN mutations in a Portuguese series of FTD/CBS cases. Mov Disord. 2008;23(9):1269-73.
175. Perry DC, Lehmann M, Yokoyama JS, Karydas A, Lee JJY, Coppola G, et al. Progranulin mutations as a risk factor for Alzheimer's Disease. JAMA Neurology. 2013;70(6):774-8.
176. van Swieten JC, Heutink P. Mutations in progranulin (GRN) within the spectrum of clinical and pathological phenotypes of frontotemporal dementia. Lancet Neurol. 2008;7(10):965-74.
177. Le Ber I, Camuzat A, Hannequin D, Pasquier F, Guedj E, Rovelet-Lecrux A, et al. Phenotype variability in progranulin mutation carriers: a clinical, neuropsychological, imaging and genetic study. Brain. 2008;131(3):732-46.

178. Whyte LS, Fourrier C, Hassiotis S, Lau AA, Trim PJ, Hein LK, et al. Lysosomal gene Hexb displays haploinsufficiency in a knock-in mouse model of Alzheimer's disease. IBRO Neurosci Rep. 2022;12:131-41.
179. Filiano AJ, Martens LH, Young AH, Warmus BA, Zhou P, Diaz-Ramirez G, et al. Dissociation of Frontotemporal Dementia–Related Deficits and Neuroinflammation in Progranulin Haploinsufficient Mice. J Neurosci. 2013;33(12):5352-61.
180. Ahmed Z, Sheng H, Xu Y-f, Lin W-L, Innes AE, Gass J, et al. Accelerated Lipofuscinosis and Ubiquitination in Granulin Knockout Mice Suggest a Role for Progranulin in Successful Aging. Am J Pathol. 2010;177(1):311-24.
181. Minami SS, Min SW, Krabbe G, Wang C, Zhou Y, Asgarov R, et al. Progranulin protects against amyloid β deposition and toxicity in Alzheimer's disease mouse models. Nat Med. 2014;20(10):1157-64.
182. Bossù P, Salani F, Alberici A, Archetti S, Bellelli G, Galimberti D, et al. Loss of function mutations in the progranulin gene are related to pro-inflammatory cytokine dysregulation in frontotemporal lobar degeneration patients. J Neuroinflammation. 2011;8(1):65.
183. Yin F, Banerjee R, Thomas B, Zhou P, Qian L, Jia T, et al. Exaggerated inflammation, impaired host defense, and neuropathology in progranulin-deficient mice. J Exp Med. 2010;207(1):117-28.
184. Benes P, Vetvicka V, Fusek M. Cathepsin D--many functions of one aspartic protease. Crit Rev Oncol Hematol. 2008;68(1):12-28.
185. Vidoni C, Follo C, Savino M, Melone MA, Isidoro C. The role of Cathepsin D in the pathogenesis of human neurodegenerative disorders. Med Res Rev. 2016;35(5):845-70.
186. Tavasoli AR, Parvaneh N, Ashrafi MR, Rezaei Z, Zschocke J, Rostami P. Clinical presentation and outcome in infantile Sandhoff disease: a case series of 25 patients from Iranian neurometabolic bioregistry with five novel mutations. Orphanet J Rare Dis. 2018;13(1):130.
187. Tim-Aroon T, Wichajarn K, Katanyuwong K, Tanpaiboon P, Vatanavicharn N, Sakpichaisakul K, et al. Infantile onset Sandhoff disease: clinical manifestation and a novel common mutation in Thai patients. BMC Pediatrics. 2021;21(1):22.
188. Smith NJ, Winstone AM, Stellitano L, Cox TM, Verity CM. GM2 gangliosidosis in a UK study of children with progressive neurodegeneration: 73 cases reviewed. Dev Med Child Neurol. 2012;54(2):176-82.

189. Wang F, Segatori L. Remodeling the proteostasis network to rescue glucocerebrosidase variants by inhibiting ER-associated degradation and enhancing ER folding. PLoS One. 2013;8(4):e61418.
190. Cortés Sanchón A, Santhosh Kumar H, Mantovani M, Osinnii I, Mateos JM, Kaech A, et al. ER-misfolded Proteins become Sequestered with Mitochondria and Impair Mitochondrial Function. Commun Biol. 2021;4(1):1350.
191. Sprenkle NT, Sims SG, Sánchez CL, Meares GP. Endoplasmic reticulum stress and inflammation in the central nervous system. Mol Neurodegener. 2017;12(1):42.
192. Behl T, Kaur G, Fratila O, Buhas C, Judea-Pusta CT, Negrut N, et al. Cross-talks among GBA mutations, glucocerebrosidase, and α-synuclein in GBA-associated Parkinson's disease and their targeted therapeutic approaches: a comprehensive review. Transl Neurodegener. 2021;10(1):4.
193. Cullen V, Sardi SP, Ng J, Xu YH, Sun Y, Tomlinson JJ, et al. Acid β-glucosidase mutants linked to Gaucher disease, Parkinson disease, and Lewy body dementia alter α-synuclein processing. Ann Neurol. 2011;69(6):940-53.
194. Gegg ME, Sweet L, Wang BH, Shihabuddin LS, Sardi SP, Schapira AH. No evidence for substrate accumulation in Parkinson brains with GBA mutations. Mov Disord. 2015;30(8):1085-9.
195. Schöndorf DC, Aureli M, McAllister FE, Hindley CJ, Mayer F, Schmid B, et al. iPSC-derived neurons from GBA1-associated Parkinson's disease patients show autophagic defects and impaired calcium homeostasis. Nat Commun. 2014;5:4028.
196. Lesage S, Condroyer C, Hecham N, Anheim M, Belarbi S, Lohman E, et al. Mutations in the glucocerebrosidase gene confer a risk for Parkinson disease in North Africa. Neurology. 2011;76(3):301-3.
197. Pan X, Taherzadeh M, Bose P, Heon-Roberts R, Nguyen ALA, Xu T, et al. Glucosamine amends CNS pathology in mucopolysaccharidosis IIIC mouse expressing misfolded HGSNAT. J Exp Med. 2022;219(8).
198. Boger HA. Dual-Hit Hypothesis for Dopamine Neurodegeneration and Motor Dysfunction. ProQuest Dissertations Publishing: Medical University of South Carolina; 2006.
199. Maynard TM, Sikich L, Lieberman JA, LaMantia AS. Neural development, cell-cell signaling, and the "two-hit" hypothesis of schizophrenia. Schizophr Bull. 2001;27(3):457-76.
200. Zhu X, Lee HG, Perry G, Smith MA. Alzheimer disease, the two-hit hypothesis: an update. Biochim Biophys Acta. 2007;1772(4):494-502.

201. Patrick KL, Bell SL, Weindel CG, Watson RO. Exploring the "Multiple-Hit Hypothesis" of Neurodegenerative Disease: Bacterial Infection Comes Up to Bat. Front Cell Infect Microbiol. 2019;9:138.
202. Feng G, Mellor RH, Bernstein M, Keller-Peck C, Nguyen QT, Wallace M, et al. Imaging neuronal subsets in transgenic mice expressing multiple spectral variants of GFP. Neuron. 2000;28:41-51.
203. Crawley AC, Gliddon BL, Auclair D, Brodie SL, Hirte C, King BM, et al. Characterization of a C57BL/6 congenic mouse strain of mucopolysaccharidosis type IIIA. Brain Res. 2006;1104:1-17.
204. Puranik N, Yadav D, Yadav SK, Chavda VK, Jin JO. Proteomics and Neurodegenerative Disorders: Advancements in the Diagnostic Analysis. Curr Protein Pept Sci. 2020;21(12):1174-83.
205. Didonna A, Benetti F. Post-translational modifications in neurodegeneration. AIMS Biophysics. 2016;3(1):27-49.
206. Macklin A, Khan S, Kislinger T. Recent advances in mass spectrometry based clinical proteomics: applications to cancer research. Clin Proteomics. 2020;17:17.
207. Peng L, Cantor DI, Huang C, Wang K, Baker MS, Nice EC. Tissue and plasma proteomics for early stage cancer detection. Mol Omics. 2018;14(6):405-23.
208. Corbett JR, Robinson DE, Patrie SM. Robustness and Ruggedness of Isoelectric Focusing and Superficially Porous Liquid Chromatography with Fourier Transform Mass Spectrometry. J Am Soc Mass Spectrom. 2021;32(1):346-54.
209. Cupp-Sutton KA, Wu S. High-throughput quantitative top-down proteomics. Mol Omics. 2020;16(2):91-9.
210. Zhang DY, Ye F, Gao L, Liu X, Zhao X, Che Y, et al. Proteomics, pathway array and signaling network-based medicine in cancer. Cell Div. 2009;4:20.
211. Guerin CL, Guyonnet L, Goudot G, Revets D, Konstantinou M, Chipont A, et al. Multidimensional Proteomic Approach of Endothelial Progenitors Demonstrate Expression of KDR Restricted to CD19 Cells. Stem Cell Rev Rep. 2021;17(2):639-51.
212. Yang L, Cao Y, Zhao J, Fang Y, Liu N, Zhang Y. Multidimensional Proteomics Identifies Declines in Protein Homeostasis and Mitochondria as Early Signals for Normal Aging and Age-associated Disease in Drosophila. Mol Cell Proteomics. 2019;18(10):2078-88.
213. Lai M, Liang L, Chen J, Qiu N, Ge S, Ji S, et al. Multidimensional Proteomics Reveals a Role of UHRF2 in the Regulation of Epithelial-Mesenchymal Transition (EMT). Mol Cell Proteomics. 2016;15(7):2263-78.

214. Buhimschi IA, Zhao G, Rosenberg VA, Abdel-Razeq S, Thung S, Buhimschi CS. Multidimensional proteomics analysis of amniotic fluid to provide insight into the mechanisms of idiopathic preterm birth. PLoS One. 2008;3(4):e2049.

215. Bhaumik M, Muller V, Rozaklis T, Johnson L, Dobrenis K, Bhattacharya R, et al. A mouse model for mucopolysaccharidosis type III A (Sanfilippo syndrome). Glycobiology. 1999;9(12):1389-96.

216. Bhattacharyya R, Gliddon B, Beccari T, Hopwood JJ, Stanley P. A novel missense mutation in lysosomal sulfamidase is the basis of MPS III A in a spontaneous mouse mutant. Glycobiology. 2001;11(1):99-103.

217. Andrade F, Aldamiz-Echevarria L, Llarena M, Couce ML. Sanfilippo syndrome: Overall overview. Pediatr Int. 2015;57(3):331-8.

218. Shoubridge AP. Synaptic morphology, function, and regulation in a paediatric-onset neurodegenerative disorder: University of Adelaide; 2021.

219. Dolgalev I. msigdbr: MSigDB Gene Sets for Multiple Organisms in a Tidy Data Format. R package version 7.5.1.9001, https://igordot.github.io/msigdbr/. 2022.

220. Korotkevich G, Sukhov V, Budin N, Shpak B, Artyomov MN, Sergushichev A. Fast Gene Set Enrichment Analysis. bioRxiv. 2021:060012.

221. Gardner ML, Freitas MA. Multiple Imputation Approaches Applied to the Missing Value Problem in Bottom-Up Proteomics. Int J Mol Sci. 2021;22(17).

222. McGurk KA, Dagliati A, Chiasserini D, Lee D, Plant D, Baricevic-Jones I, et al. The use of missing values in proteomic data-independent acquisition mass spectrometry to enable disease activity discrimination. Bioinformatics. 2020;36(7):2217-23.

223. Anders S, Huber W. Differential expression analysis for sequence count data. Genome Biol. 2010;11(10):R106.

224. Zito A, Lualdi M, Granata P, Cocciadiferro D, Novelli A, Alberio T, et al. Gene Set Enrichment Analysis of Interaction Networks Weighted by Node Centrality. Front Genet. 2021;12.

225. Wilson DF. Oxidative phosphorylation: regulation and role in cellular and tissue metabolism. J Physiol. 2017;595(23):7023-38.

226. Oyarzabal A, Marin-Valencia I. Synaptic energy metabolism and neuronal excitability, in sickness and health. J Inherit Metab Dis. 2019;42(2):220-36.

227. Pshezhetsky AV. Crosstalk between 2 organelles: Lysosomal storage of heparan sulfate causes mitochondrial defects and neuronal death in mucopolysaccharidosis III type C. Rare Dis. 2015;3(1):e1049793.

228. Martins C, Hůlková H, Dridi L, Dormoy-Raclet V, Grigoryeva L, Choi Y, et al. Neuroinflammation, mitochondrial defects and neurodegeneration in mucopolysaccharidosis III type C mouse model. Brain. 2015;138(2):336-55.
229. Lunt SY, Vander Heiden MG. Aerobic Glycolysis: Meeting the Metabolic Requirements of Cell Proliferation. Annu Rev Cell Dev Biol. 2011;27(1):441-64.
230. Tang BL. Glucose, glycolysis, and neurodegenerative diseases. J Cell Physiol. 2020;235(11):7653-62.
231. Langbaum JB, Chen K, Lee W, Reschke C, Bandy D, Fleisher AS, et al. Categorical and correlational analyses of baseline fluorodeoxyglucose positron emission tomography images from the Alzheimer's Disease Neuroimaging Initiative (ADNI). Neuroimage. 2009;45(4):1107-16.
232. Mosconi L, Sorbi S, de Leon MJ, Li Y, Nacmias B, Myoung PS, et al. Hypometabolism Exceeds Atrophy in Presymptomatic Early-onset Familial Alzheimer's Disease. J Nucl Med. 2006;47(11):1778-86.
233. Zhang X, Alshakhshir N, Zhao L. Glycolytic Metabolism, Brain Resilience, and Alzheimer’s Disease. Front Neurosci. 2021;15.
234. Khatri N, Man HY. Synaptic activity and bioenergy homeostasis: implications in brain trauma and neurodegenerative diseases. Front Neurol. 2013;4:199.
235. Mosconi L. Brain glucose metabolism in the early and specific diagnosis of Alzheimer's disease. FDG-PET studies in MCI and AD. Eur J Nucl Med Mol Imaging. 2005;32(4):486-510.
236. Mosconi L, De Santi S, Brys M, Tsui WH, Pirraglia E, Glodzik-Sobanska L, et al. Hypometabolism and altered cerebrospinal fluid markers in normal apolipoprotein E E4 carriers with subjective memory complaints. Biol Psychiatry. 2008;63(6):609-18.
237. De Pasquale V, Costanzo M, Siciliano RA, Mazzeo MF, Pistorio V, Bianchi L, et al. Proteomic Analysis of Mucopolysaccharidosis IIIB Mouse Brain. Biomolecules. 2020;10(3).
238. Nakatsukasa K, Brodsky JL. The recognition and retrotranslocation of misfolded proteins from the endoplasmic reticulum. Traffic. 2008;9(6):861-70.
239. Smith MH, Ploegh HL, Weissman JS. Road to ruin: targeting proteins for degradation in the endoplasmic reticulum. Science. 2011;334(6059):1086-90.
240. Schmidt M, Finley D. Regulation of proteasome activity in health and disease. Biochim Biophys Acta. 2014;1843(1):13-25.
241. Rao G, Croft B, Teng C, Awasthi V. Ubiquitin-Proteasome System in Neurodegenerative Disorders. J Drug Metab Toxicol. 2015;6(4).

242. Bifsha P, Landry K, Ashmarina L, Durand S, Seyrantepe V, Trudel S, et al. Altered gene expression in cells from patients with lysosomal storage disorders suggests impairment of the ubiquitin pathway. Cell Death Differ. 2007;14(3):511-23.
243. Zhan SS, Beyreuther K, Schmitt HP. Neuronal ubiquitin and neurofilament expression in different lysosomal storage disorders. Clin Neuropathol. 1992;11(5):251-5.
244. Higashi Y, Murayama S, Pentchev PG, Suzuki K. Cerebellar degeneration in the Niemann-Pick type C mouse. Acta Neuropathol. 1993;85(2):175-84.
245. Oya Y, Nakayasu H, Fujita N, Suzuki K, Suzuki K. Pathological study of mice with total deficiency of sphingolipid activator proteins (SAP knockout mice). Acta Neuropathol. 1998;96(1):29-40.
246. Heuer GG, Passini MA, Jiang K, Parente MK, Lee VM-Y, Trojanowski JQ, et al. Selective neurodegeneration in murine mucopolysaccharidosis VII is progressive and reversible. Ann Neurol. 2002;52(6):762-70.
247. Lieberman AP, Puertollano R, Raben N, Slaugenhaupt S, Walkley SU, Ballabio A. Autophagy in Lysosomal Storage Disorders. Autophagy. 2012;8(5):719-30.
248. Savas PS, Hemsley KM, Hopwood JJ. Intracerebral injection of sulfamidase delays neuropathology in murine MPS-IIIA. Mol Genet Metab. 2004;82(4):273-85.
249. Beard H, Hassiotis S, Gai WP, Parkinson-Lawrence E, Hopwood JJ, Hemsley KM. Axonal dystrophy in the brain of mice with Sanfilippo syndrome. Exp Neurol. 2017;295:243-55.
250. Gaidarov I, Smith ME, Domin J, Keen JH. The class II phosphoinositide 3-kinase C2α is activated by clathrin and regulates clathrin-mediated membrane trafficking. Mol Cell. 2001;7(2):443-9.
251. Menzies FM, Fleming A, Caricasole A, Bento CF, Andrews SP, Ashkenazi A, et al. Autophagy and neurodegeneration: pathogenic mechanisms and therapeutic opportunities. Neuron. 2017;93(5):1015-34.
252. D'Angelo G, Vicinanza M, Di Campli A, De Matteis MA. The multiple roles of PtdIns (4) P–not just the precursor of PtdIns (4, 5) P 2. J Cell Sci. 2008;121(12):1955-63.
253. Balla T. Phosphoinositides: Tiny Lipids With Giant Impact on Cell Regulation. Physiol Rev. 2013;93(3):1019-137.
254. Volpatti JR, Al-Maawali A, Smith L, Al-Hashim A, Brill JA, Dowling JJ. The expanding spectrum of neurological disorders of phosphoinositide metabolism. Dis Model Mech. 2019;12(8).

255. Zhou X, Wang L, Hasegawa H, Amin P, Han B-X, Kaneko S, et al. Deletion of PIK3C3/Vps34 in sensory neurons causes rapid neurodegeneration by disrupting the endosomal but not the autophagic pathway. PNAS. 2010;107(20):9424-9.

256. Wang L, Budolfson K, Wang F. Pik3c3 deletion in pyramidal neurons results in loss of synapses, extensive gliosis and progressive neurodegeneration. Neuroscience. 2011;172:427-42.

257. Morel E, Chamoun Z, Lasiecka ZM, Chan RB, Williamson RL, Vetanovetz C, et al. Phosphatidylinositol-3-phosphate regulates sorting and processing of amyloid precursor protein through the endosomal system. Nat Commun. 2013;4(1):2250.

258. Nixon RA. Amyloid precursor protein and endosomal–lysosomal dysfunction in Alzheimer's disease: inseparable partners in a multifactorial disease. FASEB J. 2017;31(7):2729.

259. Dickson EJ, Hille B. Understanding phosphoinositides: rare, dynamic, and essential membrane phospholipids. Biochem. 2019;476(1):1-23.

260. Hille B, Dickson EJ, Kruse M, Vivas O, Suh B-C. Phosphoinositides regulate ion channels. Biochim Biophys Acta. 2015;1851(6):844-56.

261. Di Paolo G, Moskowitz HS, Gipson K, Wenk MR, Voronov S, Obayashi M, et al. Impaired PtdIns (4, 5) P2 synthesis in nerve terminals produces defects in synaptic vesicle trafficking. Nature. 2004;431(7007):415-22.

262. Hall PA, Russell SE. The pathobiology of the septin gene family. J Pathol. 2004;204(4):489-505.

263. Nemani VM, Lu W, Berge V, Nakamura K, Onoa B, Lee MK, et al. Increased expression of alpha-synuclein reduces neurotransmitter release by inhibiting synaptic vesicle reclustering after endocytosis. Neuron. 2010;65(1):66-79.

264. Tada T, Simonetta A, Batterton M, Kinoshita M, Edbauer D, Sheng M. Role of Septin Cytoskeleton in Spine Morphogenesis and Dendrite Development in Neurons. Curr Biol. 2007;17(20):1752-8.

265. Kinoshita A, Kinoshita M, Akiyama H, Tomimoto H, Akiguchi I, Kumar S, et al. Identification of septins in neurofibrillary tangles in Alzheimer's disease. Am J Pathol. 1998;153(5):1551-60.

266. Ihara M, Yamasaki N, Hagiwara A, Tanigaki A, Kitano A, Hikawa R, et al. Sept4, a component of presynaptic scaffold and Lewy bodies, is required for the suppression of alpha-synuclein neurotoxicity. Neuron. 2007;53(4):519-33.

267. Zhang Y, Gao J, Chung KK, Huang H, Dawson VL, Dawson TM. Parkin functions as an E2-dependent ubiquitin- protein ligase and promotes the degradation of the synaptic vesicle-associated protein, CDCrel-1. PNAS. 2000;97(24):13354-9.
268. Marttinen M, Kurkinen KMA, Soininen H, Haapasalo A, Hiltunen M. Synaptic dysfunction and septin protein family members in neurodegenerative diseases. Mol Neurodegener. 2015;10(1):16.
269. Musunuri S, Wetterhall M, Ingelsson M, Lannfelt L, Artemenko K, Bergquist J, et al. Quantification of the brain proteome in Alzheimer's disease using multiplexed mass spectrometry. J Proteome Res. 2014;13(4):2056-68.
270. Gillette MA, Carr SA. Quantitative analysis of peptides and proteins in biomedicine by targeted mass spectrometry. Nat Methods. 2013;10(1):28-34.
271. Higdon R, Kolker E. A predictive model for identifying proteins by a single peptide match. Bioinformatics. 2006;23(3):277-80.
272. Bogdanow B, Zauber H, Selbach M. Systematic Errors in Peptide and Protein Identification and Quantification by Modified Peptides. Mol Cell Proteomics. 2016;15(8):2791-801.
273. Flurkey, Currer, Harrison. The mouse in biomedical research. In: Fox J, editor. American College of Laboratory Animal Medicine series. Boston: Elsevier AP: Amsterdam; 2007.
274. Hebda-Bauer EK, Dokas LA, Watson SJ, Akil H. Adaptation to single housing is dynamic: Changes in hormone levels, gene expression, signaling in the brain, and anxiety-like behavior in adult male C57Bl/6J mice. Horm Behav. 2019;114:104541.
275. Kamakura R, Kovalainen M, Leppäluoto J, Herzig KH, Mäkelä KA. The effects of group and single housing and automated animal monitoring on urinary corticosterone levels in male C57BL/6 mice. Physiol Rep. 2016;4(3).
276. Distler U, Schumann S, Kesseler HG, Pielot R, Smalla KH, Sielaff M, et al. Proteomic Analysis of Brain Region and Sex-Specific Synaptic Protein Expression in the Adult Mouse Brain. Cells. 2020;9(2).
277. Hanamsagar R, Bilbo SD. Sex differences in neurodevelopmental and neurodegenerative disorders: Focus on microglial function and neuroinflammation during development. J Steroid Biochem Mol Biol. 2016;160:127-33.
278. Xie Y, Vessey JP, Konecna A, Dahm R, Macchi P, Kiebler MA. The GTP-binding protein Septin 7 is critical for dendrite branching and dendritic-spine morphology. Curr Biol. 2007;17(20):1746-51.

279. Ageta-Ishihara N, Miyata T, Ohshima C, Watanabe M, Sato Y, Hamamura Y, et al. Septins promote dendrite and axon development by negatively regulating microtubule stability via HDAC6-mediated deacetylation. Nat Commun. 2013;4:2532.

280. Hu J, Bai X, Bowen JR, Dolat L, Korobova F, Yu W, et al. Septin-driven coordination of actin and microtubule remodeling regulates the collateral branching of axons. Curr Biol. 2012;22(12):1109-15.

281. Pará C, Bose P, Bruno L, Freemantle E, Taherzadeh M, Pan X, et al. Early defects in mucopolysaccharidosis type IIIC disrupt excitatory synaptic transmission. JCI Insight. 2021;6(15).

282. Dwyer CA, Scudder SL, Lin Y, Dozier LE, Phan D, Allen NJ, et al. Neurodevelopmental Changes in Excitatory Synaptic Structure and Function in the Cerebral Cortex of Sanfilippo Syndrome IIIA Mice. Sci Rep. 2017;7:46576.

283. Spruston N. Pyramidal neurons: dendritic structure and synaptic integration. Nat Rev Neurosci. 2008;9(3):206-21.

284. Egorov AV, Hamam BN, Fransén E, Hasselmo ME, Alonso AA. Graded persistent activity in entorhinal cortex neurons. Nature. 2002;420(6912):173-8.

285. Susloparova A, Halliez S, Begard S, Colin M, Buée L, Pecqueur S, et al. Low impedance and highly transparent microelectrode arrays (MEA) for in vitro neuron electrical activity probing. Sens Actuators B Chem. 2021;327:128895.

286. Patrick KL, Bell SL, Weindel CG, Watson RO. Exploring the "Multiple-Hit Hypothesis" of Neurodegenerative Disease: Bacterial Infection Comes Up to Bat. Frontiers in Cellular and Infection Microbiology. 2019;9(138).

287. Pouchieu C, Piel C, Carles C, Gruber A, Helmer C, Tual S, et al. Pesticide use in agriculture and Parkinson's disease in the AGRICAN cohort study. Int J Epidemiol. 2018;47(1):299-310.

288. Wu AP, He Y, Ye SY, Qi LY, Liu L, Zhong W, et al. Negative effects of a piscicide, rotenone, on the growth and metabolism of three submerged macophytes. Chemosphere. 2020;250:126246.

289. Isman MB. Botanical insecticides, deterrents, and repellents in modern agriculture and an increasingly regulated world. Annu Rev Entomol. 2006;51:45-66.

290. Li N, Ragheb K, Lawler G, Sturgis J, Rajwa B, Melendez JA, et al. Mitochondrial Complex I Inhibitor Rotenone Induces Apoptosis through Enhancing Mitochondrial Reactive Oxygen Species Production. J Biol Chem. 2003;278(10):8516-25.

291. Radad K, Gille G, Rausch WD. Dopaminergic neurons are preferentially sensitive to long-term rotenone toxicity in primary cell culture. Toxicol In Vitro. 2008;22(1):68-74.
292. Giordano S, Lee J, Darley-Usmar VM, Zhang J. Distinct Effects of Rotenone, 1-methyl-4-phenylpyridinium and 6-hydroxydopamine on Cellular Bioenergetics and Cell Death. PLOS ONE. 2012;7(9):e44610.
293. Labbadia J, Morimoto RI. The biology of proteostasis in aging and disease. Annu Rev Biochem. 2015;84:435-64.
294. Kawamata H, Manfredi G. Proteinopathies and OXPHOS dysfunction in neurodegenerative diseases. J Cell Biol. 2017;216(12):3917-29.
295. Shetty PK, Galeffi F, Turner DA. Cellular Links between Neuronal Activity and Energy Homeostasis. Front Pharmacol. 2012;3:43.
296. Abdel-Salam OME, Youssef Morsy SM, Youness ER, Yassen NN, Sleem AA. The effect of low dose amphetamine in rotenone-induced toxicity in a mice model of Parkinson's disease. Iran J Basic Med Sci. 2020;23(9):1207-17.
297. Chou AP, Li S, Fitzmaurice AG, Bronstein JM. Mechanisms of rotenone-induced proteasome inhibition. Neurotoxicology. 2010;31(4):367-72.
298. Beaudoin GMJ, III, Lee S-H, Singh D, Yuan Y, Ng Y-G, Reichardt LF, et al. Culturing pyramidal neurons from the early postnatal mouse hippocampus and cortex. Nat Protoc. 2012;7:1741+.
299. Sahu MP, Nikkilä O, Lågas S, Kolehmainen S, Castrén E. Culturing primary neurons from rat hippocampus and cortex. Neuronal Signal. 2019;3(2):Ns20180207.
300. Edgar JM, Griffiths IR. Chapter 5 - White Matter Structure: A Microscopist's View. In: Johansen-Berg H, Behrens TEJ, editors. Diffusion MRI. San Diego: Academic Press; 2009. p. 74-103.
301. McCarthy MM, Wright CL. Convergence of Sex Differences and the Neuroimmune System in Autism Spectrum Disorder. Biol Psychiatry. 2017;81(5):402-10.
302. McCarthy MM, Nugent BM, Lenz KM. Neuroimmunology and neuroepigenetics in the establishment of sex differences in the brain. Nat Rev Neurosci. 2017;18(8):471-84.
303. Zhang W, Li SS, Han Y, Xu XH. Sex Differences in Electrophysiological Properties of Mouse Medial Preoptic Area Neurons Revealed by In Vitro Whole-cell Recordings. Neurosci Bull. 2021;37(2):166-82.
304. Kolb B, Stewart J. Sex-related differences in dendritic branching of cells in the prefrontal cortex of rats. J Neuroendocrinol. 1991;3(1):95-9.

305. Walsh CT, Tu BP, Tang Y. Eight Kinetically Stable but Thermodynamically Activated Molecules that Power Cell Metabolism. Chem Rev. 2018;118(4):1460-94.
306. Spinelli JB, Haigis MC. The multifaceted contributions of mitochondria to cellular metabolism. Nat Cell Biol. 2018;20(7):745-54.
307. Sazanov LA. A giant molecular proton pump: structure and mechanism of respiratory complex I. Nat Rev Mol Cell Biol. 2015;16(6):375-88.
308. Watt IN, Montgomery MG, Runswick MJ, Leslie AG, Walker JE. Bioenergetic cost of making an adenosine triphosphate molecule in animal mitochondria. PNAS. 2010;107(39):16823-7.
309. Stepien KM, Roncaroli F, Turton N, Hendriksz CJ, Roberts M, Heaton RA, et al. Mechanisms of Mitochondrial Dysfunction in Lysosomal Storage Disorders: A Review. J Clin Med. 2020;9(8).
310. Heaton RA, Heales S, Rahman K, Sexton DW, Hargreaves I. The Effect of Cellular Coenzyme Q(10) Deficiency on Lysosomal Acidification. J Clin Med. 2020;9(6).
311. Montero R, Yubero D, Salgado MC, González MJ, Campistol J, O'Callaghan MDM, et al. Plasma coenzyme Q(10) status is impaired in selected genetic conditions. Sci Rep. 2019;9(1):793.
312. Tillo M, Lamanna WC, Dwyer CA, Sandoval DR, Pessentheiner AR, Al-Azzam N, et al. Impaired mitophagy in Sanfilippo a mice causes hypertriglyceridemia and brown adipose tissue activation. J Biol Chem. 2022;298(8):102159.
313. Mahbub SB, Guller A, Campbell JM, Anwer AG, Gosnell ME, Vesey G, et al. Non-Invasive Monitoring of Functional State of Articular Cartilage Tissue with Label-Free Unsupervised Hyperspectral Imaging. Sci Rep. 2019;9(1):4398.
314. Gosnell ME, Anwer AG, Mahbub SB, Perinchery SM, Inglis DW, Adhikary PP, et al. Quantitative non-invasive cell characterisation and discrimination based on multispectral autofluorescence features. Sci Rep. 2016;6(23453).
315. Gosnell ME, Anwer AG, Cassano JC, Sue CM, Goldys EM. Functional hyperspectral imaging captures subtle details of cell metabolism in olfactory neurosphere cells, disease-specific models of neurodegenerative disorders. Biochim Biophys Acta. 2016;1863(1):56-63.
316. Santos Monteiro CA, Chow DJX, Leal GR, Tan TC, Reis Ferreira AM, Thompson JG, et al. Optical imaging of cleavage stage bovine embryos using hyperspectral and confocal approaches reveals metabolic differences between on-time and fast-developing embryos. Theriogenology. 2021;159:60-8.

317. Staikopoulos V, Gosnell M, Anwer A, Mustafa S, Hutchinson M, Goldys E. Hyperspectral imaging of endogenous fluorescent metabolic molecules to identify pain states in central nervous system tissue: SPIE; 2016.
318. Tan TCY, Mahbub SB, Campbell JM, Habibalahi A, Campugan CA, Rose RD, et al. Non-invasive, label-free optical analysis to detect aneuploidy within the inner cell mass of the preimplantation embryo. Hum Reprod. 2021;37(1):14-29.
319. Sutton-McDowall ML, Gosnell M, Anwer AG, White M, Purdey M, Abell AD, et al. Hyperspectral microscopy can detect metabolic heterogeneity within bovine post-compaction embryos incubated under two oxygen concentrations (7% versus 20%). Hum Reprod. 2017;32(10):2016-25.
320. Sivandzade F, Bhalerao A, Cucullo L. Analysis of the Mitochondrial Membrane Potential Using the Cationic JC-1 Dye as a Sensitive Fluorescent Probe. Bio Protoc. 2019;9(1).
321. Gu X, Ma Y, Liu Y, Wan Q. Measurement of mitochondrial respiration in adherent cells by Seahorse XF96 Cell Mito Stress Test. STAR Protocols. 2021;2(1):100245.
322. Wizenty J, Schumann T, Theil D, Stockmann M, Pratschke J, Tacke F, et al. Recent Advances and the Potential for Clinical Use of Autofluorescence Detection of Extra-Ophthalmic Tissues. Molecules. 2020;25(9).
323. Little AC, Kovalenko I, Goo LE, Hong HS, Kerk SA, Yates JA, et al. High-content fluorescence imaging with the metabolic flux assay reveals insights into mitochondrial properties and functions. Commun Biol. 2020;3(1):271.
324. Mahbub SB, Plöschner M, Gosnell ME, Anwer AG, Goldys EM. Statistically strong label-free quantitative identification of native fluorophores in a biological sample. Sci Rep. 2017;7(1):15792.
325. Divakaruni AS, Paradyse A, Ferrick DA, Murphy AN, Jastroch M. Analysis and interpretation of microplate-based oxygen consumption and pH data. Methods Enzymol. 2014;547:309-54.
326. Arthurs AL, Keating DJ, Stringer BW, Conn SJ. The Suitability of Glioblastoma Cell Lines as Models for Primary Glioblastoma Cell Metabolism. Cancers (Basel). 2020;12(12).
327. Herst PM, Berridge MV. Cell surface oxygen consumption: a major contributor to cellular oxygen consumption in glycolytic cancer cell lines. Biochim Biophys Acta. 2007;1767(2):170-7.
328. Ambrosi G, Ghezzi C, Sepe S, Milanese C, Payan-Gomez C, Bombardieri CR, et al. Bioenergetic and proteolytic defects in fibroblasts from patients with sporadic Parkinson's disease. Biochim Biophys Acta. 2014;1842(9):1385-94.

329. Rodriguez AR, De Sevilla Muller LP, Brecha NC. The RNA Binding Protein RBPMS is a Selective Marker of Ganglion Cells in the Mammalian Retina. J Comp Neurol. 2014;522(6):1411-43.
330. Kirk K, Gennings C, Hupf JC, Tadesse S, D'Aurelio M, Kawamata H, et al. Bioenergetic markers in skin fibroblasts of sporadic amyotrophic lateral sclerosis and progressive lateral sclerosis patients. Ann Neurol. 2014;76(4):620-4.
331. Deus CM, Pereira SP, Cunha-Oliveira T, Pereira FB, Raimundo N, Oliveira PJ. Mitochondrial remodeling in human skin fibroblasts from sporadic male Parkinson's disease patients uncovers metabolic and mitochondrial bioenergetic defects. Biochim Biophys Acta. 2020;1866(3):165615.
332. Pereira SP, Deus CM, Serafim TL, Cunha-Oliveira T, Oliveira PJ. Metabolic and Phenotypic Characterization of Human Skin Fibroblasts After Forcing Oxidative Capacity. Toxicol Sci. 2018;164(1):191-204.
333. Victor Matheus B, Richner M, Hermanstyne Tracey O, Ransdell Joseph L, Sobieski C, Deng P-Y, et al. Generation of Human Striatal Neurons by MicroRNA-Dependent Direct Conversion of Fibroblasts. Neuron. 2014;84(2):311-23.
334. Caiazzo M, Dell'Anno MT, Dvoretskova E, Lazarevic D, Taverna S, Leo D, et al. Direct generation of functional dopaminergic neurons from mouse and human fibroblasts. Nature. 2011;476(7359):224-7.
335. Yang Y, Chen R, Wu X, Zhao Y, Fan Y, Xiao Z, et al. Rapid and Efficient Conversion of Human Fibroblasts into Functional Neurons by Small Molecules. Stem Cell Rep. 2019;13(5):862-76.
336. Yaniv Y, Juhaszova M, Nuss HB, Wang S, Zorov DB, Lakatta EG, et al. Matching ATP supply and demand in mammalian heart: in vivo, in vitro, and in silico perspectives. Ann N Y Acad Sci. 2010;1188:133-42.
337. Zamzami N, Marchetti P, Castedo M, Decaudin D, Macho A, Hirsch T, et al. Sequential reduction of mitochondrial transmembrane potential and generation of reactive oxygen species in early programmed cell death. J Exp Med. 1995;182(2):367-77.
338. Izyumov DS, Avetisyan AV, Pletjushkina OY, Sakharov DV, Wirtz KW, Chernyak BV, et al. "Wages of fear": transient threefold decrease in intracellular ATP level imposes apoptosis. Biochim Biophys Acta. 2004;1658(1-2):141-7.
339. Zorova LD, Popkov VA, Plotnikov EY, Silachev DN, Pevzner IB, Jankauskas SS, et al. Mitochondrial membrane potential. Anal Biochem. 2018;552:50-9.

340. Tessitore A, Pirozzi M, Auricchio A. Abnormal autophagy, ubiquitination, inflammation and apoptosis are dependent upon lysosomal storage and are useful biomarkers of mucopolysaccharidosis VI. Pathogenetics. 2009;2(1):4.
341. Srivastava S, Kashiwaya Y, King MT, Baxa U, Tam J, Niu G, et al. Mitochondrial biogenesis and increased uncoupling protein 1 in brown adipose tissue of mice fed a ketone ester diet. FASEB J. 2012;26(6):2351-62.
342. Tirichen H, Yaigoub H, Xu W, Wu C, Li R, Li Y. Mitochondrial Reactive Oxygen Species and Their Contribution in Chronic Kidney Disease Progression Through Oxidative Stress. Front Physiol. 2021;12.
343. Migdal C, Serres M. [Reactive oxygen species and oxidative stress]. Med Sci (Paris). 2011;27(4):405-12.
344. Monaco A, Fraldi A. Protein aggregation and autophagy dysfunction: new lessons from mucopolysaccharidoses. Autophagy. 2021;17(11):3875-6.
345. Chun Y, Kim J. Autophagy: An Essential Degradation Program for Cellular Homeostasis and Life. Cells. 2018;7(12).
346. Kumar H, Lim HW, More SV, Kim BW, Koppula S, Kim IS, et al. The role of free radicals in the aging brain and Parkinson's Disease: convergence and parallelism. Int J Mol Sci. 2012;13(8):10478-504.
347. Nicholls DG. Spare respiratory capacity, oxidative stress and excitotoxicity. Biochem Soc Trans. 2009;37(Pt 6):1385-8.
348. Desler C, Hansen TL, Frederiksen JB, Marcker ML, Singh KK, Juel Rasmussen L. Is There a Link between Mitochondrial Reserve Respiratory Capacity and Aging? J Aging Res. 2012;2012:192503.
349. Sansbury BE, Jones SP, Riggs DW, Darley-Usmar VM, Hill BG. Bioenergetic function in cardiovascular cells: the importance of the reserve capacity and its biological regulation. Chem Biol Interact. 2011;191(1-3):288-95.
350. Yadava N, Nicholls DG. Spare respiratory capacity rather than oxidative stress regulates glutamate excitotoxicity after partial respiratory inhibition of mitochondrial complex I with rotenone. J Neurosci. 2007;27(27):7310-7.
351. Nicholls DG. Oxidative stress and energy crises in neuronal dysfunction. Ann N Y Acad Sci. 2008;1147(1):53-60.
352. Roszczyc-Owsiejczuk K, Zabielski P. Sphingolipids as a Culprit of Mitochondrial Dysfunction in Insulin Resistance and Type 2 Diabetes. Front Endocrinol. 2021;12:635175.

353. Picard M, Shirihai OS, Gentil BJ, Burelle Y. Mitochondrial morphology transitions and functions: implications for retrograde signaling? Am J Physiol Regul Integr Comp Physiol. 2013;304(6):R393-406.
354. Tan TCY, Brown HM, Thompson JG, Mustafa S, Dunning KR. Optical imaging detects metabolic signatures associated with oocyte quality†. Biol Reprod. 2022;107(4):1014-25.
355. Galeotti T, van Rossum GD, Mayer DH, Chance B. On the fluorescence of NAD(P)H in whole-cell preparations of tumours and normal tissues. Eur J Biochem. 1970;17(3):485-96.
356. Wu S, Huang Y, Tang Q, Li Z, Horng H, Li J, et al. Quantitative evaluation of redox ratio and collagen characteristics during breast cancer chemotherapy using two-photon intrinsic imaging. Biomed Opt Express. 2018;9(3):1375-88.
357. Wallrabe H, Svindrych Z, Alam SR, Siller KH, Wang T, Kashatus D, et al. Segmented cell analyses to measure redox states of autofluorescent NAD(P)H, FAD & Trp in cancer cells by FLIM. Sci Rep. 2018;8(1):79.
358. Chance B, Schoener B, Oshino R, Itshak F, Nakase Y. Oxidation-reduction ratio studies of mitochondria in freeze-trapped samples. NADH and flavoprotein fluorescence signals. J Biol Chem. 1979;254(11):4764-71.
359. Barve G, Sanyal P, Manjithaya R. Septin localization and function during autophagy. Curr Genet. 2018;64(5):1037-41.
360. Ageta-Ishihara N, Kinoshita M. Developmental and postdevelopmental roles of septins in the brain. Neurosci Res. 2021;170:6-12.
361. Kolenc OI, Quinn KP. Evaluating Cell Metabolism Through Autofluorescence Imaging of NAD(P)H and FAD. Antioxid Redox Signal. 2019;30(6):875-89.
362. Bartolomé F, Abramov AY. Measurement of mitochondrial NADH and FAD autofluorescence in live cells. Methods Mol Biol. 2015;1264:263-70.
363. Blanch L, Weber B, Guo X-H, Scott HS, Hopwood JJ. Molecular Defects in Sanfilippo Syndrome Type A. Hum Mol Genet. 1997;6(5):787-91.
364. Hijikata A, Tsuji T, Shionyu M, Shirai T. Decoding disease-causing mechanisms of missense mutations from supramolecular structures. Sci Rep. 2017;7(1):8541.
365. Li L, Chao J, Shi Y. Modeling neurological diseases using iPSC-derived neural cells : iPSC modeling of neurological diseases. Cell Tissue Res. 2018;371(1):143-51.
366. Lowry WE, Richter L, Yachechko R, Pyle AD, Tchieu J, Sridharan R, et al. Generation of human induced pluripotent stem cells from dermal fibroblasts. PNAS. 2008;105(8):2883-8.